Nonequilibrium Fermion Production in Quantum Field Theory

Vom Fachbereich Physik
der Technischen Universität Darmstadt

zur Erlangung des Grades
eines Doktors der Naturwissenschaften
(Dr. rer. nat.)

genehmigte Dissertation von
Dipl.-Phys. Jens Pruschke
aus Dortmund

Darmstadt 2010
D17

Referent:	Prof. Dr. Jürgen Berges
Korreferent:	Prof. Dr. Christian Fischer

Tag der Einreichung:	18.05.2010
Tag der Prüfung:	16.06.2010

Zusammenfassung

Die Erzeugung von Materie im frühen Universum oder in relativistischen Schwerionenkollisionen ist unvermeidbar mit Nichtgleichgewichtsphysik verbunden. Eine der größten Herausforderungen ist es, den dabei auftretenden Thermalisierungsprozess nach Nichtgleichgewichtsinstabilitäten zu beschreiben. Die Bedeutung von fermionischen Quantenfeldern in solchen Szenarien wird in der Literatur in Näherungen untersucht, die wichtige Quantenkorrekturen vernachlässigen. Diese Doktorarbeit geht über derartige Näherungen hinaus.

Es wird eine Quantenfeldtheorie, in der skalare Bosonen mit Fermionen durch eine Yukawa-Wechselwirkung gekoppelt sind, im Formalismus der 2PI effektiven Wirkung untersucht. Es wird eine Näherung gewählt mit der eine korrekte Beschreibung der Dynamik, die Instabilitäten enthält, möglich ist. Insbesondere erlaubt sie, die Wechselwirkung von Fermionen mit großen Bosonfluktuationen zu studieren. Es werden Anfangsbedingungen gewählt, die zu Instabilitäten, wie parametrischer Resonanz oder spinodalen Instabilitäten, führen. Die Bewegungsgleichungen der Korrelationen werden numerisch gelöst. Die Haupteigenschaften der resultierenden Fermiondynamik lassen sich durch analytische Lösungen beschreiben.

Es werden neue Mechanismen der Fermionproduktion entdeckt. Simulationen, in denen spinodale Instabilitäten auftreten, zeigen, dass instabile Bosonfluktuationen, ein exponentielles Wachstum von Fermionmoden induzieren, das approximativ die gleiche Rate der Bosonen hat. Ist die Dauer der instabilen Phase groß genug, dann ist der Infrarot-Bereich der Fermionbesetzungszahlen thermisch. Dies geschieht auf sehr viel kleineren Zeitskalen als eine Thermalisierung der Bosonen. Hinzu kommt, dass Fermionbesetzungszahlen, im Vergleich zur Fermi-Dirac-Statistik, eine höhere Besetzung im Ultraviolett-Bereich haben. Dieser Bereich ist durch ein Potenzgesetz mit dem Exponenten zwei charakterisiert. Liegt parametrische Resonanz vor, so findet eine effiziente Fermionproduktion hauptsächlich nach der instabilen Phase statt. Die Quantenkorrekturen sorgen für die effiziente Fermionproduktion, die durch die Erhöhung der Anzahl von Zerfallsprozessen interpretiert wird. In beiden Mechanismen ist das Verhältnis des Quadrats der Yukawa-Kopplung zur Selbstwechselwirkung der Bosonen, von großer Bedeutung.

Die Dynamik der Bosonen ist für beide Arten von Instabilitäten qualitativ gleich. Die instabile Phase zeigt bekannte Eigenschaften und ist gefolgt von einer quasi-stationären Phase die durch Potenzgesetze in Besetzungszahlen, im Infrarot- und/oder Ultraviolett-Bereich, charakterisiert ist. Das Auftreten von Potenzgesetzen verhindert eine schnelle Thermalisierung. Des Weiteren ist der Einfluss von nicht stark gekoppelten Fermionen auf die Boson Dynamik zu vernachlässigen. Eine Beschleunigung des Thermalisierungsprozesses wird nicht beobachtet.

Abstract

The creation of matter in the early universe or in relativistic heavy-ion collisions is inevitable connected to nonequilibrium physics. One of the key challenges is the explanation of the corresponding thermalization process following nonequilibrium instabilities. The role of fermionic quantum fields in such scenarios is discussed in the literature by using approximations of field theories which neglect important quantum corrections. This thesis goes beyond such approximations.

A quantum field theory where scalar bosons interact with Dirac fermions via a Yukawa coupling is analyzed in the 2PI effective action formalism. The chosen approximation allows for a correct description of the dynamics including nonequilibrium instabilities. In particular, fermion-boson loop corrections allow to study the interaction of fermions with large boson fluctuations. The applied initial conditions generate nonequilibrium instabilities like parametric resonance or spinodal instabilities. The equations of motion for correlation functions are solved numerically and major characteristics of the fermion dynamics are described by analytical solutions.

New mechanisms for the production of fermions are found. Simulations in the case of spinodal instability show that unstable boson fluctuations induce exponentially growing fermion modes with approximately the same growth rate. If the unstable regime lasts long enough a thermalization of the infrared part of the fermion occupation number occurs on time scales much shorter than the time scale on which bosonic quantum fields thermalize. Fermions acquire an excess of occupation in the ultraviolet regime compared to a Fermi-Dirac statistic characterized by a power-law with exponent two. The fermion production mechanism via parametric resonance is found to be most efficient after the instability ends. Quantum corrections then provide a very efficient particle creation mechanism which is interpreted as an amplification of decay processes. The ratio of the Yukawa coupling squared to the boson self-coupling is in both mechanism of great importance.

The boson dynamics is qualitatively the same for both kinds of instabilities. An initially unstable evolution shows well-known characteristics with an ensuing quasi-stationary regime. The latter exhibits infrared and/or ultraviolet power-law behaviors in the occupation number which prevent a fast thermalization. Furthermore, for not too large Yukawa couplings the impact of fermions on the dynamics of highly occupied bosons is weak. An acceleration of the evolution of the whole system towards thermal equilibrium is not observed.

Contents

Chapter 1

Introduction

Nonequilibrium studies in quantum field theory are of great importance in current research. Two main applications are the reheating mechanism of the universe after inflation and the thermalization of the quark-gluon plasma in heavy-ion collisions. They have in common that nonequilibrium instabilities play a major role in understanding the physics. This thesis is about fundamental aspects concerning the role of fermionic quantum fields in those scenarios. We will first introduce these two research areas before we will present the goal of this thesis.

Reheating after Inflation

The necessity for the reheating scenarios arose due to the paradigm of inflationary cosmology [Gut81, Lin83]. Inflation solves serious problems of the standard Big Bang model [KT90, Bra10], like the flatness or the horizon problem [BTW06]. After inflation, the universe acquires a "frozen" vacuum-like state with extremely low entropy. In contrast, a successful description of the thermal history of the universe, within the standard Big Bang model, requires a high density of particles with a certain temperature, called reheating temperature. The currently discussed mechanism for reheating starts with a phase called preheating [KLS94]. It is understood as nonperturbative ("explosive") particle production due to nonequilibrium instabilities like tachyonic/spinodal instabilities or parametric resonance (cf. Sec. 2.3). It sets the origin of matter creation. This results into enormously high occupation numbers being far from thermal equilibrium. During this epoch perturbative decays of particles [DL82, AFW82] are suppressed and only become relevant at a subsequent stage of the reheating process [KLS94]. The preheating mechanism was believed to produce a reheating temperature which is in agreement with those estimated from the Big Bang model. In general all known kinds of particles must have been produced by this mechanism. Since models which contain many different particles are practically impossible to handle one restricts the discussion of a few or even only one species.

There exists an enormous amount of publications in which preheating is studied. Purely boson field models in leading order large-N or Hartree-type approx-

imations can be found, e.g. in [BDdV$^+$95, Yos95, FKYY96a, FKYY96b, Kai96, BdVHS96, KLS97, GKLS97, GBL98, Kai98, Kai97, RH97, FKL99, CPR02, F$^+$01, FKL01, BH04, BR05, DFKL05, DFK$^+$06, AMPEC08, GBFR09]. Studies of fermion production usually consider interactions to classical macroscopic ("inflaton") fields, see e.g. Refs. [KES$^+$92, BDdV$^+$95, RHS98, BHP98, GTR99, GPRT99, GRT99, AS00, GBMR00, PS00, TBV00, BGM00, GK99, GK00, NPS01a, NPS01b, BKP07]. All these investigations have in common that the energy density is most efficiently transferred from the inflaton field to the bosonic degrees of freedom while only a small fraction is stored into the fermions. This leads to the argumentation that fermions do not contribute significantly to the thermalization process.

Mean-field-type approximations such as leading order large-N or Hartree-types fail to describe thermalization [BC01, Ber02] and are even quantitatively incorrect if quantum fluctuations become of the order of the inverse coupling constant. In the latter regime re-scattering of produced particles become important and consequently Hartree-type approximations are invalid [Son96]. Thermalization requires scattering and off-shell processes. Thermalization in a scalar quantum field theory was shown for the first time in Ref. [BC01] within a Born collision approximation. In Ref. [Ber02] a 2PI $1/N$-expansion up to next-to-leading order (NLO) (cf. Sec. 2.2) was employed and the occupation numbers approached the Bose-Einstein distribution. In the case of fermionic quantum fields interacting with bosonic quantum fields thermalization was shown in Ref. [BBS03]. These publications did not consider instabilities in their dynamics.

The first analysis of the resonant particle production mechanism taking into account re-scattering and off-shell effects was done in Ref. [BS03]. There, a scalar field theory was considered by using the 2PI $1/N$-expansion up to next-to-leading order. Besides the well known initial exponential growth of fluctuations, it was found that due to nonlinear source effects a second even faster stage (during preheating) of efficient exponential amplification of fluctuation modes occurs. The subsequent evolution is found to be quasi-stationary, i.e. is remarkably slow. They did not follow the evolution till thermalization sets in. In Ref. [AST04] a similar behavior was observed for a tachyonic instability in a scalar $O(N)$ theory within the same approximation.

Similar phenomena are observed in classical-statistical calculations. It was realized that classical statistical simulations on a lattice can be used to describe the evolution from the onset of preheating towards thermal equilibrium [KT96, PR97, FK01, PFKP06]. Note that at late times classical-statistical simulations fail to describe a quantum field theory since it cannot reproduce a Bose-Einstein or Fermi-Dirac distribution. In general a quantum field theory where large fluctuations dominate the dynamics is well described by classical statistics for not too late times [AB02, BG07]. This is only valid for bosonic degrees of freedom and the inclusion of fermionic degrees of freedom is under discussion [BH09b].

The quasi-stationary evolutions in quantum field theory are characterized by power-law behaviors in correlation functions (scaling solutions) as it is well known from, e.g. turbulence [Fri95, ZLF92]. The origins of a power-law can be different. It was pointed out that the thermalization of bosonic particles after preheating exhibits the phenomenon of turbulence [KT96, Son96, MT03, MT04], i.e. power-laws emerge in a finite ultraviolet regime of a particle number spectrum. In Ref. [BRS08] for the first time infrared scaling solutions were observed in a classical statistical simulation of a scalar field theory. They found a power-law behavior for infrared modes with an exponent higher than those known from turbulence. This leads to strongly enhanced long wavelength fluctuations, a phenomenon known as critical slowing down. An infrared power-law correspond to divergent correlation lengths, thus is different to turbulence. This shows the possibility of critical phenomena out of equilibrium. With renormalization group techniques for a scalar field theory a hierarchy of fixed point solutions were found [BH09a]. The existence of such nonthermal fixed points for a wide class of initial conditions prevents a fast thermalization.

While current studies of the bosonic reheating dynamics provide a rich amount of information on specific characteristics of the early and subsequent intermediate stages (see above) it is still puzzling how a fast thermalization with a phenomenological realistic temperature is obtained. In Refs. [KT96, Son96, MT03, MT04] only kinetic estimates of the reheating temperature were discussed and showed that the slow evolution leads to low temperatures which are also obtained by perturbative estimates. Consequently, the evolution towards thermal equilibrium after instabilities is, so far, only barely understood. Including fermions and taking into account re-scattering processes requires an approximation of a corresponding quantum field theory which is not done so far. The presence of such re-scattering effects are expected to change the evolution.

Most discussed phenomenological applications are gravitino (over-) production which has consequences on leptogenesis [GTR99]. Furthermore, the production of supermassive fermions is interesting in connection with the dark matter problem and the problem of ultra-high energy cosmic rays [GK00], as well as for leptogenesis [GPRT99]. For an overview of applications see e.g. Ref. [ABCRM10].

Thermalization of the Quark-Gluon Plasma

Heavy-ion collisions are suitable for the study of strongly interacting matter. Describing the latter by quantum chromodynamics (QCD) is a challenge for current research. Experiments, like the Relativistic Heavy Ion Collider (RHIC) at Brookhaven National Laboratory (BNL) or in the future the Large Hadron Collider (LHC) at CERN and the Facility for Antiproton and Ion Research (FAIR) at GSI, investigate heavy-ion collisions. Such “Little Bangs” [Hei01] can probe, e.g., the deconfined phase of QCD. The deconfined state is characterized by a medium called quark-

gluon plasma. The question of thermalization of the quark-gluon plasma after heavy-ion collisions became an actively discussed topic. Experimental results are well described by hydrodynamical calculations [Hei05] which require a very rapid thermalized plasma. There exist several ideas for an explanation of a fast thermalization, for an overview see e.g. [Mro06]. The applicability of hydrodynamics may also be possible if the prethermalization of the equation of state is given [BBW04]. In Ref. [ALMY05] it was argued that an isotropized plasma supports the conditions used for hydrodynamical modelling. An isotropization on time scales much shorter than the typical equilibration time occurs due to the existence of nonequilibrium instabilities in anisotropic plasma [Mro88]. Many authors studied plasma instabilities in nonequilibrium gauge theories with different approaches [BSS08, BGSS09, RV06a, RV06b, RS03, ALM03, ALMY05, DN05, DNS07, FII09, FI08, XG05]. Often, a priori assumptions like the separation of momentum scales are employed which corresponds to the weak coupling limit. In order to tackle the problem without such assumptions, a proper nonperturbative treatment of quantum fields out of equilibrium is required.

A complete nonperturbative calculation of nonequilibrium QCD is so far impossible to handle. Classical-statistical real-time calculations of pure non-Abelian gauge theories were made in Refs. [BSS08, BGSS09]. Weibel instabilities [Mro88] lead to a rapid isotropization of the pressure in a limited low-momentum regime. Characteristics of unstable momentum modes were found which are known from scalar field theories often used in cosmology (see last section). In addition those kind of simulations show the phenomenon of turbulence which emerges in the dynamics after the plasma instability terminates [BSS09a]. This quasi-stationary evolution phase, as in cosmology, prevents a system from thermalizing quickly. Turbulent spectra of occupation numbers (or energy) were also observed in different approaches to gauge field dynamics after plasma instabilities [AM06a, AM06b, MSW07, DNS07, MSW07, Kha08]. The characterization of this quasi-stationary evolution regime is far from being unique. Different power-laws which characterize the spectra were found. Their analytic predictions are diverse.

The above mentioned real-time simulations in non-Abelian gauge theories do not contain fermionic degrees of freedom (e.g. quarks). A consideration of quark production in anisotropic plasma can be found in Ref. [SS06, Mro02]. The authors analyzed dispersion relations of fermion modes and did not find an unstable behavior (nonvanishing imaginary part). Quark production from classical gluon fields, which corresponds to solving the Dirac equation with a time dependent mass, was investigated in Ref. [GKL06]. The authors claim that a gluon domination after heavy-ion collisions should be questioned. Thus impact of fermions might not be negligible and thus could lead to important phenomenological implications.

Goal of this Thesis

Understanding the dynamics of fermionic quantum fields out of equilibrium is a challenging task. The presence of nonequilibrium instabilities leads to complex phenomena which need to be investigated. This thesis is a contribution to research in order to understand basic fundamental aspects of the interaction between fermionic and bosonic quantum fields.

As pointed out in the last two sections, instabilities were thought to lead to a fast thermalization (isotropization). However, this did not turn out to be the case. In all studies done before the interaction between fermionic and bosonic fluctuations were neglected. In contrast, in the applications described above fermion quantum fields naturally have to play a nonnegligible role. In our studies presented here for the first time this restriction is relaxed.

In this thesis we investigate a generic quantum field theoretical model in $3 + 1$ dimensions with interacting scalar boson and Dirac fermion fields. They interact via a Yukawa coupling. This model can act as a toy model for reheating dynamics in the early universe as well as an effective theory for low energy QCD. For massless fermions it obeys the chiral symmetry of two-flavor QCD.

Our program requires a certain approximation since boson fluctuations with amplitudes of the order of the inverse coupling appear. The 2PI $1/N$-expansion up to next-to-leading order (NLO) in the boson sector is an appropriate tool which we used. The amplitudes of fermion fluctuations are limited by the Pauli principle, therefore it is reliable, for a not too large Yukawa coupling, to employ a loop-expansion with the Yukawa coupling as the expansion parameter.

This approximation includes scattering and off-shell effects between bosons and fermions. This is necessary to study the dynamics leading to the thermalization of both kinds of quantum fields.

Two kinds of instabilities are analyzed which serves for the possibility to point out similarities between the corresponding dynamics and thus get hints of a universal behavior out of equilibrium. On the one hand we consider the tachyonic/spinodal instability and on the other hand parametric resonance is analyzed. The initial conditions are completely different (cf. Sec. 3.4). Observing similar characteristics in the dynamics of the quantum fields is very interesting.

We focus on the characterization of the evolution of fermionic quantum fields in the presence of large boson fluctuations. Since we go beyond mean-field-type approximations where fermions only interact with a macroscopic classical (background) field, this leads to a dramatic change of the known dynamical evolutions and thus to a new picture of fermionic preheating.

We employ numerical simulations of the dynamics governed by the evolution equations. Adapting and extending analytical considerations of the evolution equations known from purely scalar field theories gives us an understanding of the character-

istics of the fermion dynamics observed in numerical simulations.

Moreover, we consider spectral functions out of equilibrium in the presence of an instability. Nonequilibrium spectral functions are barely understood and so far not discussed in real-time evolutions including instabilities.

With our model we can answer the question if the interaction between fermion and boson fluctuations lead to an acceleration of the thermalization dynamics. Furthermore we can judge whether or not quasi-stationary evolutions (scaling solutions) in presence of fermionic quantum fields are still stable as observed previously. This should lead to an impulse to study real-time evolutions of more realistic models for early universe cosmology and heavy-ion collisions.

Structure of this Thesis

This first Chapter is devoted to the introduction of the research area and the presentation of the goal of this thesis with its structure.

In the following chapter we will discuss the key aspects of nonequilibrium quantum field theory. We will explain the basics of the closed time path and the functional formalism in Sec. 2.1. We will introduce in Sec. 2.2 the 2PI effective action method which we used with certain approximations. The description of the two instabilities used in this work is presented in Sec. 2.3. The ensuing section reports about the important phenomenon of nonthermal fixed points.

Chapter 3 concerns the set-up of our investigations. In Sec. 3.1 we introduce the model and discuss the employed symmetries. Sec. 3.2 presents the equations of motion which were solved on a computer. In the subsequent section the applied approximations are considered, before we turn to the specifications of the initial conditions in Sec. 3.4. In Sec. 3.5 we introduce our definition of a particle number. The Chapter ends with the presentation of the energy-momentum tensor of the model.

Chapter 4 reports about a new mechanism of fermion production in the presence of a tachyonic/spinodal instability. The Chapter is divided into two large sections where we consider massless and massive fermion production respectively. In the first section we consider the boson and fermion dynamics separately for the sake of organization. In both parts there exist subsections where the fast unstable evolution regime and the ensuing slow quasi-stationary evolution is analyzed. In Sec. 4.1.1.3 and Sec. 4.1.2.4 spectral functions in four dimensional Fourier space are discussed. In Sec. 4.1.2.3 we have a close look on the approach of the fermions towards thermal equilibrium. Sec. 4.2 where we consider the production of massive fermions is divided into two subsections. The first treats the amplification of massive fermion modes via fluctuations. The second investigates the impact of nonvanishing field expectation values. In the latter case the resulting spectral functions are studied too.

Chapter 5 is devoted to the fermion production mechanism occurring in the pres-

ence of parametric resonance. In Sec. 5.1 we consider the resulting boson dynamics important to understand the fermion evolution. This section is separated into two subsections, one which reports about the pure boson dynamics and the second contains the study of the fermion impact. In the ensuing section we analyze the fermion dynamics in different approximations. We point out the difference between approximations used in the past and the extension of those advocated in this work. The latter shows new phenomena which are described and explained.

In Chapter 6 we will present a summary of our results together with our conclusions and give an outlook to what should be done in the future.

There are six appendices. Appendix A considers the chiral decomposition of the fermionic two-point functions. In Appendix B we present a detailed calculation of the energy-momentum tensor. The ensuing appendix shows that our used particle number definition is formally equivalent to a mode function formulation used in the literature. The method of how spectral functions are calculated in the Wigner representation is presented in Appendix D. In Appendix E we discuss the calculation of the fermionic parts of the self-energies. The last appendix is devoted to the explanation of the numerical methods and the check of cut-off insensitivity of our results.

Most parts of Chapter 4 have been already published in Ref. [BPR09]. A forthcoming publication about results of this thesis is in progress.

Chapter 2

Nonequilibrium Quantum Field Theory

In this chapter we present the major aspects of nonequilibrium quantum field theory. Sec. 2.1 reviews the general formalism typically used to describe quantum fields out of equilibrium. The subsequent section introduces the so called 2PI effective action with possible approximations often used in calculations. Sec. 2.3 briefly comments on the types of instabilities which are present in our simulations. The last section explains the nature of nonthermal fixed points which usually emerge in out-of-equilibrium evolutions.

2.1 General Formalism

In nonequilibrium quantum field theory one is typically interested in the time evolution of correlation functions. Correlation functions contain all information one needs in order to describe a system. For example a one-point correlation function can be interpreted as a macroscopic (inflaton) field which may play a fundamental role in early time cosmology. Two-point correlation functions provide basic information about field excitations, interpreted as particles, like their mass and life time. Especially important for this work is that they can be used to define occupation numbers which are often used to describe the production of particles.

Time evolution is an initial value problem, i.e. it is specified by the evolution equations together with initial conditions.

In the following sections we are going to present the most important facts about the construction of a set up of an initial value problem which is used to analyze a quantum field theory out of equilibrium.

Closed Time Path

Initial value problems in quantum field theory are best formulated within the closed time path (CTP) formalism introduced by Schwinger [Sch61] and later considerable

developed by Keldysh by introducing a corresponding diagram technique [Kel64]. Therefore this formalism is often referred to as the Schwinger-Keldysh formalism. This formalism is discussed in detail in the literature, see e.g. [C$^+$94, CH87, CSHY85, Kel64, BM63a, BM63b, Sch61]. In this section we only briefly explain the necessity of the CTP. For the sake of simplicity we consider scalar fields, however the arguments also hold for spinor fields.

The fundamental quantity of the statistical aspects of a quantum field theory is the density matrix. Knowing this quantity one has all relevant information about the system present. Out of equilibrium this knowledge is required at all times t. The evolution of the density matrix $\rho(t)$ is governed by the Von-Neumann equation

$$i\frac{\partial\rho(t)}{\partial t} = [H(t), \rho(t)] \ , \tag{2.1}$$

with $H(t)$ as the Hamiltonian of the system. Here and in the whole work we set $\hbar = c = k_B = 1$ and omit the indication of operators with a hat. In thermal equilibrium the commutator on the right hand side of Eq. (2.1) vanishes and there exists the unique solution $\rho_{eq} \sim e^{-H/T}$ for a given temperature T. Out of equilibrium the form of the time dependent density matrix is in general not known. A formal solution of (2.1) is given by

$$\rho(t) = U(t, t_0)\rho(t_0)U^{-1}(t, t_0) \, , \tag{2.2}$$

with the unitary time evolution operator $U(t, t_0)$ which evolves the density matrix from the initial time t_0 to t. We are interested in correlation functions which are expectation values of field operators which are calculated by use of the density matrix. For example the one-point correlation function in the Schrödinger picture is defined by

$$\langle\mathcal{O}(t)\rangle = \frac{\mathrm{Tr}\,[\rho(t)\mathcal{O}]}{\mathrm{Tr}\,[\rho(t)]} \, , \tag{2.3}$$

for an arbitrary field operator $\mathcal{O}$. Using (2.2) and the identity $U(t_0, t')U(t', t) = U(t_0, t)$ the expectation value can be written in the form

$$\langle\mathcal{O}(t)\rangle = \frac{\mathrm{Tr}\,[\rho(t_0)U(t_0, t')U(t', t)\mathcal{O}U(t, t_0)]}{\mathrm{Tr}\,[\rho(t_0)]} \, , \tag{2.4}$$

i.e. the time is evolved first from t_0 to t, then to an intermediate time t' and back to t_0. This is the origin of the closed time path. A sketch of a closed time path in the complex time plane is displayed in Fig. 2.1. Once the initial configuration of the density matrix is specified one can calculate the expectation value for all times t with Eq. (2.4).

For a practical way of calculating arbitrary correlation functions it is more convenient to switch from the operator formalism to the path integral formalism. In

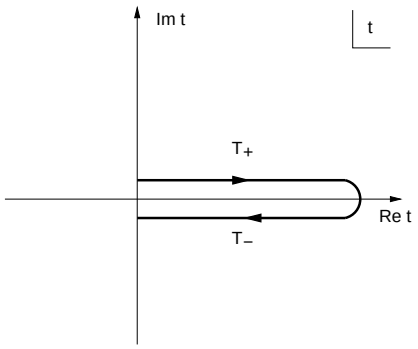

Figure 2.1: Sketch of a closed time path in the complex time plane used in initial value problems in quantum field theory. Note that the path is shifted away from the real axis in order to illustrate the forward and backward time branches T_+ and T_-.

the latter correlation functions are given by functional derivatives of the generating functional which will be introduced in the next section. Further it turned out that it is more suitable in nonequilibrium quantum field theory to rephrase the Von-Neumann equation with the help of functionals into equations of motion for the correlation functions directly.

Generating Functional for Correlation Functions

Having explained the necessity for a closed time path we can proceed and introduce the functional formalism for calculating correlation functions from the generating functional. Moreover it is the starting point for the derivation of the effective action which in turn is used to construct self-consistent evolution equations for correlation functions (see Sec. 2.2). We will go along the lines presented in the Refs. [Ber05, C$^+$94].

The generating functional for a scalar quantum field theory is defined by (we omit internal symmetry indices)

$$Z[J,R] \;=\; \int \mathcal{D}\varphi \exp\left[i\left(\mathcal{S}[\varphi] + \int d^4x J(x)\varphi(x) + \frac{1}{2}\int d^4x\, d^4y\, \varphi(x) R(x,y)\varphi(y) \right)\right], \quad (2.5)$$

with so called local and bi-local sources $J(x)$ and $R(x,y)$ respectively. The classical action $\mathcal{S}[\varphi]$ contains also an integration over space-time with $x = x^0, \mathbf{x}$. The connected one and two-point functions, $\phi(x)$ and $G(x,y)$, are defined by the derivative

of $W[J,R] \equiv -i \log Z[J,R]$ with respect to the sources, i.e.[1]

$$\phi(x) = \frac{\delta W[J,R]}{\delta J(x)}\,, \qquad G(x,y) = 2\frac{\delta W[J,R]}{\delta R(x,y)} - \phi(x)\phi(y) \tag{2.6}$$

The definition of the nonequilibrium generating functional defined on a closed time path is given by

$$\begin{aligned} Z[J,R,\rho] \;&=\; \int \mathcal{D}\varphi_0^1 \mathcal{D}\varphi_0^2 \langle \varphi_0^1|\rho(t_0)|\varphi_0^2\rangle \times \\ &\int_{\varphi_0^1}^{\varphi_0^2} \mathcal{D}\varphi \exp\left[i\left(\mathcal{S}[\varphi] + \int_{\mathrm{CTP}} d^4x J(x)\varphi(x) + \frac{1}{2}\int_{\mathrm{CTP}} d^4x\, d^4y\, \varphi(x) R(x,y)\varphi(y)\right)\right], \end{aligned} \tag{2.7}$$

where φ_0^1 and φ_0^2 correspond to field configurations at initial time t_0 on the forward (T^+) and backward (T^-) time branch, respectively, cf. Fig. 2.1. Thus the expectation value of the density matrix is taken with respect to the initial states and decouple from the time evolution. Note that in (2.7) the time integration in the exponential function goes over the CTP. Conceptually one could also choose another way of obtaining the generating functional by introducing fields defined on the forward and backward time branch separately. For a nice explanation of this approach see [C$^+$94]. Both methods are equivalently, for details see [Ber05, C$^+$94, Jor86]. We would like to emphasize that the structure of (2.7), i.e. the initial density matrix as a factor of a functional integration which in turn has the same form as in equilibrium is fundamental for the practicability of nonequilibrium quantum field theory.

In (2.7) the density matrix still needs to be determined and we have to understand its effect on the correlation functions. The density matrix can always be expressed as an exponential function of a polynomial in the fields [C$^+$94], i.e.

$$\begin{aligned} \langle \varphi_0^1|\rho(t_0)|\varphi_0^2\rangle \;&=\; \mathcal{N}\exp\left\{ A^{(0)} + \int d^3\mathbf{x}\left[A^1_{(1)}(\mathbf{x})\varphi_0^1(\mathbf{x}) + A^2_{(1)}(\mathbf{x})\varphi_0^2(\mathbf{x})\right]\right. \\ &+\frac{1}{2}\int d^3\mathbf{x}\, d^3\mathbf{y}\left[A^{1,1}_{(2)}(\mathbf{x},\mathbf{y})\varphi_0^1(\mathbf{x})\varphi_0^1(\mathbf{y}) + A^{1,2}_{(2)}(\mathbf{x},\mathbf{y})\varphi_0^1(\mathbf{x})\varphi_0^2(\mathbf{y})\right. \\ &\left.\left. A^{2,1}_{(2)}(\mathbf{x},\mathbf{y})\varphi_0^2(\mathbf{x})\varphi_0^1(\mathbf{y}) + A^{2,2}_{(2)}(\mathbf{x},\mathbf{y})\varphi_0^2(\mathbf{x})\varphi_0^2(\mathbf{y})\right] + \mathcal{O}\left[\left(\varphi_0^{1,2}\right)^3\right]\right\}. \end{aligned} \tag{2.8}$$

The last term in the exponential represents higher order terms in the initial field configurations φ_0^1 and φ_0^2. In this work we consider systems where the initial density matrix is parametrized by an expansion as in (2.8) up to second order in the fields, i.e. it is Gaussian. One can show [Ber05, CHKM97, C$^+$94] that the parameters

[1] $W[J,R]$ is called the generating functional of connected correlation functions.

of the Gaussian initial density matrix are directly related to the initial values of the one and two-point correlation functions. This gives us a notion which role the density matrix plays in nonequilibrium quantum field theory. An experimental set-up can be chosen in such a way that it is described by a Gaussian initial density matrix. Moreover the initial conditions in cosmology right after the end of inflation are believed to be well described by a Gaussian density matrix [CH08]. Inserting (2.8) into (2.7) we observe that the generating functional can be written in a form resembling equilibrium quantum field theory

$$Z[J,R,\rho] \;=\; \int \mathcal{D}\varphi \exp\left[i\left(\mathcal{S}[\varphi] + \int_{\mathrm{CTP}} d^4x J'(x)\varphi(x) + \frac{1}{2}\int_{\mathrm{CTP}} d^4x\, d^4y\, \varphi(x) R'(x,y)\varphi(y) \right)\right], \tag{2.9}$$

where we have defined the modified sources J' and R' by shifting the old ones (they could be set to zero) by the parameter functions $A_{(1)}$ and $A_{(2)}$ respectively. This is possible since the parameter functions are only nonvanishing at initial time and the different field configurations on the time branches in (2.8) become at that time equivalent. Most important is the observation that with (2.9) we have a generating functional suitable for the construction of the well known effective action [DJ74, Sch74, CJP74] which is the basis for obtaining evolution equations for correlation functions. This is explained in the next Section.

Thus we can describe nonequilibrium quantum field theories by the usual methods known from equilibrium with the only specification of the time integration over the closed time path. The information of the density matrix is contained in the initial conditions of the correlation functions. We mention again that the arguments given above can be repeated for spinor fields despite the fact that they are Grassmann valued quantities, see e.g. [C$^+$94, Jor86]. Hence a quantum field theory out of equilibrium with fermionic fields can be described along the same lines as it is possible for scalar fields.

2.2 2PI Effective Action

There exist many approaches to study nonequilibrium quantum field theories. Depending on the situation one is confronted with, a certain way is preferable or even necessary. Since we are dealing with initial value problems we should ensure that no secularity[2] occurs. If one would like to start from first principles the effective action [DJ74, Sch74, CJP74] provides a reasonable tool. In our work there is the need for a special nonperturbative description because of the emergence of instabilities which lead to large fluctuations of the order of the inverse coupling. A standard perturbative expansion would fail in this scenario. A powerful tool which provides all

[2]Secularity means that solutions of equations of motion grow unbounded in time.

demanded features in nonequilibrium studies is the two-particle irreducible[3] (2PI) effective action [LW60, Bay62, CJT74]. Secularity is avoided [Ber02] and special approximations allow to analyze evolutions of systems where an instability is present. We do not want to present a complete derivation of the 2PI effective action here, for this we refere the reader to the literature [Ber05, CJT74][4]. We rather explain the most important ingredients and explain how the evolution equations of correlation functions are obtained. Along this we introduce our notation of correlation functions and self-energies which will be used later when we will consider a specific model. Since we will consider a model where scalar boson and fermion fields appear we will here restrict ourselves to these kinds of fields and do not include for example gauge fields[5].

The 2PI effective action is a functional of the one-point correlation function $\phi(x)$ and of the connected two-point correlation functions $G(x,y)$ and $D(x,y)$ in the case of bosonic and fermionic fields respectively. Note that there does not exist an expectation value of a fermion field, i.e. $\langle\psi(x)\rangle = \langle\bar{\psi}(x)\rangle = 0$ ($\bar{\psi} = \psi^\dagger\gamma^0$). Further we will denote two-point correlation functions as propagators and vice versa. The 2PI effective action is defined by a Legendre transformation of the generating functional for connected Green functions (cf. Eqs.2.6) with respect to the local and bi-local sources of the fields. The resulting explicit expression for the 2PI effective action is

$$\begin{aligned}\Gamma[\phi,G,D] &= \mathcal{S}[\phi] + \frac{i}{2}\mathrm{Tr}\ln\left(G^{-1}\right) + \frac{i}{2}\mathrm{Tr}\left(G_0^{-1}G\right) \\ &\quad -i\mathrm{Tr}\ln\left(D^{-1}\right) - i\mathrm{Tr}\left(D_0^{-1}D\right) + \Gamma_2[\phi,G,D] + \text{const.}\,, \quad (2.10)\end{aligned}$$

where $G_0 = G_0(x,y)$ and $D_0 = D_0(x,y)$ are the free boson and fermion propagator respectively, whereas $G = G(x,y)$ and $D = D(x,y)$ are the corresponding exact propagators with $x = \{x^0, \mathbf{x}\}$ and $y = \{y^0, \mathbf{y}\}$ as the space-time coordinates in Minkowski space. The free propagators might depend on the macroscopic field $\phi = \phi(x)$ explicitly which we did not indicate in order to avoid confusion. Here we omitted possible indices of the functions which could represent additional degrees of freedom. The trace, the logarithm and the products of two-point functions have to be understood in the functional sense.

Each term in (2.10) has a special meaning. The first term represents the classical action, the following four terms correspond to the expansion of the effective action to one loop order and $\Gamma_2[\phi,G,D]$ contains all higher orders starting with two-loop contributions. The constant in (2.10) can be used for normalization. $\Gamma_2[\phi,G,D]$ leads to the proper self-energies with one-particle-irreducible propagator lines, per

[3] "Two-particle-irreducible" means that only diagrams are taken into account which do not become disconnected whenever one cuts two propagator lines.

[4] 2PI effective action methods are sometimes also called "Φ-derivable" methods [Bay62].

[5] For a discussion of gauge fields see for example [Ber04].

definition, which in turn proofs that Γ_2 only contains diagrams which are two-particle-irreducible, for details of this argumentation see e.g. [Ber05, CJT74]. The bosonic and fermionic self-energies are defined by

$$\Pi(x,y;\phi,G,D) = 2i\frac{\delta\Gamma_2[\phi,G,D]}{\delta G(x,y)}\,, \tag{2.11}$$

$$\Sigma(x,y;\phi,G,D) = -i\frac{\delta\Gamma_2[\phi,G,D]}{\delta D(y,x)}\,, \tag{2.12}$$

respectively. One typically decomposes the propagators into

$$D(x,y) = F(x,y) - \frac{i}{2}\rho(x,y)\,\mathrm{sign}(x^0-y^0)\,, \tag{2.13}$$

$$G(x,y) = F^\phi(x,y) - \frac{i}{2}\rho^\phi(x,y)\,\mathrm{sign}(x^0-y^0)\,, \tag{2.14}$$

where $F^{(\phi)}$ are called statistical two-point functions and contain the information about the occupation of states, whereas $\rho^{(\phi)}$ are called spectral two-point functions which give the information about the allowed states. They are defined by[6]

$$F(x,y) = \frac{1}{2}\Big\langle\big[\psi(x),\bar\psi(y)\big]\Big\rangle\,, \qquad \rho(x,y) = i\Big\langle\big\{\psi(x),\bar\psi(y)\big\}\Big\rangle\,, \tag{2.15}$$

$$F^\phi(x,y) = \frac{1}{2}\Big\langle\{\varphi(x),\varphi(y)\}\Big\rangle - \phi(x)\phi(y)\,, \qquad \rho^\phi(x,y) = i\Big\langle[\varphi(x),\varphi(y)]\Big\rangle\,. \tag{2.16}$$

The self-energies can be decomposed similarly

$$\Sigma(x,y) = C(x,y) - \frac{i}{2}A(x,y)\,\mathrm{sign}(x^0-y^0)\,, \tag{2.17}$$

$$\Pi(x,y) = \Pi^F(x,y) - \frac{i}{2}\Pi^\rho(x,y)\,\mathrm{sign}(x^0-y^0)\,. \tag{2.18}$$

The boson self-energy typically can be separated into a local and a non-local part. The local part is usually put into an effective mass in the equation of motion, see Sec. 3.1. Out of equilibrium $F^{(\phi)}$ and $\rho^{(\phi)}$ are independent from each other, whereas in equilibrium they are related by the virtue of the fluctuation-dissipation relation[7] [Ber05]

$$F(p)|_{\text{thermal. eq.}} = i\left(\frac{1}{2} - n_{\mathrm{FD}}(p^0)\right)\rho(p)|_{\text{thermal. eq.}}\,, \tag{2.19}$$

$$F^\phi(p)|_{\text{thermal. eq.}} = -i\left(\frac{1}{2} + n_{\mathrm{BE}}(p^0)\right)\rho^\phi(p)|_{\text{thermal. eq.}}\,, \tag{2.20}$$

[6] This definition is equivalent to the one which uses the Wightman functions $D^{\lessgtr}(x,y)$ and $G^{\lessgtr}(x,y)$ [Ber02, BBS03].

[7] Also known as the Kubo-Martin-Schwinger (KMS) periodicity condition [Kub57, MS59]. Here we wrote the condition in four dimensional Fourier space. Analog relations exist also for the self-energies.

where $p = \{p^0, \mathbf{p}\}$ and $n_{\mathrm{FD/BE}}$ is the Fermi-Dirac and Bose-Einstein distribution respectively. This simplifies many calculations in thermal equilibrium considerably. Sometimes a generalized relation to (2.19) and (2.20) is employed known as Kadanoff-Baym ansatz [Ber05] where instead of the equilibrium distribution $n_{\mathrm{FD/BE}}$ an out-of-equilibrium distribution is inserted.

The stationarity conditions of the 2PI effective action, i.e.

$$\frac{\delta\Gamma[\phi, G, D]}{\delta\phi(x)} = 0\,, \quad \frac{\delta\Gamma[\phi, G, D]}{\delta G(x,y)} = 0\,, \quad \frac{\delta\Gamma[\phi, G, D]}{\delta D(x,y)} = 0\,, \tag{2.21}$$

yield the equations of motion for $\phi(x)$, $G(x,y)$ and $D(x,y)$, respectively. Note that in (2.21) the sources vanish. The equations of motion for the corresponding statistical and spectral parts are obtain by plugging in (2.15) and (2.16) into (2.21). The stationarity condition for the two-point functions can be written in a compact notation. By using (2.10) we get

$$G^{-1}(x,y) = G_0^{-1}(x,y) - \Pi(x,y;\phi,G,D)\,, \tag{2.22}$$
$$D^{-1}(x,y) = D_0^{-1}(x,y) - \Sigma(x,y;\phi,G,D)\,, \tag{2.23}$$

which are nothing but Schwinger-Dyson equations suitable for boundary value problems in equilibrium. They are also the starting point of the derivation of the equations of motion for the two-point correlation functions, which result into partial integro-differential equations. In the following we will present the main steps of this derivation. The method in the case of the fermion correlators is the same as in the case of the boson correlators, thus we consider here only the case of the fermions and just present the solution for the bosons.

In order to obtain partial differential equations suitable for initial value problems we have to apply a convolution in the Schwinger-Dyson equations (2.22) and (2.23). We use $\int_{z,\mathrm{CTP}} D_{ik}^{-1}(x,z)D_{kj}(z,y) = \delta(x-y)\delta_{ij}$ with $\delta(x-y) = \delta_{\mathrm{CTP}}(x^0-y^0)\delta(\mathbf{x}-\mathbf{y})$ where in the time direction the CTP orientation has to be respected. We also introduced flavor indices i,k,j. The same rules hold for $G_{ab}(x,y)$ with internal symmetry indices a and b. With this (2.23) becomes

$$\int_{z,\mathrm{CTP}} D_{0,ik}^{-1}(x,z)D_{kj}(z,y) - \int_{z,\mathrm{CTP}} \Sigma_{ik}(x,z;\phi,G,D)D_{kj}(z,y) = \delta(x-y)\delta_{ij}$$

$$\Rightarrow \left[i\gamma^\mu\partial_\mu^x - M_\psi(x)\right] D_{ij}(x,y) + i\int_{z,\mathrm{CTP}} \Sigma_{ik}(x,z;\phi,G,D)D_{kj}(z,y) = -i\delta(x-y)\delta_{ij}\,, \tag{2.24}$$

where $M_\psi(x)$ is a possible space-time dependent fermion mass coming from the interaction with the classical (macroscopic) field $\phi(x)$. Inserting the decomposition into statistical and spectral part of the propagator (2.15) and self-energies (2.17) and

equating real and imaginary part we get the equation of motion for the statistical and spectral components separately

$$\begin{aligned}\left[i\gamma^\mu\partial^x_\mu - M_\psi(x)\right] F_{ij}(x,y) &= \int_0^{x^0} dz\, A_{ik}(x,z)F_{kj}(z,y) \\ &\quad - \int_0^{y^0} dz\, C_{ik}(x,z)\rho_{kj}(z,y)\,, \qquad (2.25)\end{aligned}$$

$$\left[i\gamma^\mu\partial^x_\mu - M_\psi(x)\right] \rho_{ij}(x,y) = \int_{y^0}^{x^0} dz\, A_{ik}(x,z)\rho_{kj}(z,y), \qquad (2.26)$$

with the abbreviation $\int dz = \int dz^0 \int d^3z$. In obtaining (2.25) and (2.26) one respects the CTP prescription which leads to the integral limits given here.

Solving these equations means solving the equation for each Dirac component of $F_{ij}(x,y)$ and $\rho_{ij}(x,y)$. If there are certain symmetries the number of independent (nonvanishing) components can be reduced. In this case it is convenient to apply a Lorentz decomposition[8] of the fermion correlation functions and consider the resulting equations of motions for them [BBS03].

For the boson correlators we can go through each step in an analogous way. The resulting equations of motion have the same structure as in (2.25) and (2.26), however the corresponding functions have to be replaced by their bosonic counterparts, as well as the differential operator and the effective mass. Accordingly, one has

$$\begin{aligned}\left[\Box_x\delta_{ac} + M^2_{ac}(x)\right] F^\phi_{cb}(x,y) &= -\int_0^{x^0} dz\, \Pi^\rho_{ac}(x,z)F^\phi_{cb}(z,y) \\ &\quad + \int_0^{y^0} dz\, \Pi^F_{ac}(x,z)\rho^\phi_{cb}(z,y)\,, \qquad (2.27)\end{aligned}$$

$$\left[\Box_x\delta_{ac} + M^2_{ac}(x)\right] \rho^\phi_{cb}(x,y) = -\int_{y^0}^{x^0} dz\, \Pi^\rho_{ac}(x,z)\rho^\phi_{cb}(z,y)\,. \qquad (2.28)$$

The derivation of the equation of motion of the macroscopic field is straightforward once the classical action is specified. We will present the result in Sec. 3.2

[8] Projecting out the scalar, pseudo-scalar, vector, axial-vector and tensor components of a fermion two-point function one can represent the latter by a linear combination of the components (16 bilinear forms) [PS95]. The components have special properties under Lorentz transformations therefore this is called a Lorentz decomposition.

together with the other equations of motion for the model we are going to consider. We would like to emphasize that the form of the equations of motion presented here are completely general. The degree of approximation of the effective action is incorporated in a special form of the self-energies. Of course certain employed symmetries could change the most general structure.

The solution of the equations of motion is the aim in order to know the correlation function at every time, this gives us the complete information about the system under consideration. Without any approximation of $\Gamma[\phi, G, D]$ solving the equations becomes practically impossible. Hence we need to apply a certain approximation. We will see that the resulting equations are still very complicated and so far only numerical solutions are known.

In the following two subsections we will discuss two approximations which are often used in nonequilibrium quantum field theory.

2.2.1 2PI Loop-Expansion

The 2PI loop-expansion is similar to the corresponding 1PI loop-expansion, which corresponds to a perturbative coupling expansion. The difference is that, due to the fact that we have the propagator as a second variable of the effective action, each line in a loop-diagram corresponds to the resummed propagator and only 2PI diagrams are present. The convergence of the loop-expansion requires a small coupling, which is effectively the expansion parameter. Hence practically one employs a Taylor expansion in the coupling and sums up each contribution with the same number of loops, where one has to be careful with the possible combinatorial factors of diagrams.

The 2PI loop-expansion contains less topological distinct diagrams than the 1PI loop-expansion. For example, in the symmetric scalar ϕ^4-theory, there in the first four orders in the 2PI case only one diagram contributes to each order, whereas in the fifth order two different diagrams appear [Ber05].

We have to consider a 2PI loop-expansion instead of a 1PI loop-expansion since it cures the problem of secularity. Further it includes diagrams which yield nonlocal self-energy contributions in order to respect scattering and off-shell effects which are responsible for a thermalization of the system.

2.2.2 2PI $1/N$-Expansion

In this section we introduce the 2PI $1/N$-expansion [Ber02, AAB$^+$02] where N stands for the number of field components of an underlying theory. In the next chapter we will present an explicit representation when we introduce the model considered in this work. The idea is to arrange the 2PI effective action into terms $\sim N$, $\sim N^0$, $\sim N^{-1}$, ..., where one identifies the contributions $\sim N$ as leading order

(LO), $\sim N^0$ as next-to-leading order (NLO) and so on. With this one has a coupling independent expansion parameter $1/N$ and is thus not restricted to small couplings for a sufficiently large N. Each order in such an expansion could have infinitely many terms contributing to the action, hence to have a useful expansion one should be able to take all of them into account, e.g. by a resummation. In the case of an $O(N)$ symmetric model this is possible by considering $O(N)$-invariants of the effective action with a certain scaling with N [Ber02]. For a detailed description of the practical identification of the different orders we refer to Refs. [Ber05, AAB$^+$02, Ber02]. In general this method is independent of the kinds of the fields under consideration.

Symmetries like time reflection or energy conservation are respected at any order in the expansion. In addition, if one considers spontaneous symmetry breaking one can show that the Goldstone theorem is fulfilled at any order of the 2PI $1/N$-expansion [AAB$^+$02]. However, note that for a given approximation of the 2PI effective action, with the solution of the stationary equation (2.21) for the two-point function, the transversal modes not necessarily have to be massless.

One has to distinguish a 2PI $1/N$-expansion from a 1PI $1/N$-expansion [CJP74, BW98]. The derivation of the expansions are similar, however, the 1PI $1/N$-expansion shows secular behavior [MDC97].

If instabilities of quantum fields are present like in preheating dynamics after inflation, or, more general, if fluctuations have got large amplitudes of the order of the inverse coupling like at the critical point in a second order phase transition, one has to take NLO contributions into account in order to have a reasonable description of the dynamics [BS03, Ber05].

Alternative Approaches to Nonequilibrium Dynamics

In this subsection we would like to briefly mention different approaches for studying nonequilibrium dynamics of quantum fields. This little subsection has no demand to comprise a complete overview over all possible methods.

At first there has to be named kinetic transport theory with its various applications in many areas in physics. The major part in this approach comes from the so called Boltzmann transport equations. For an overview of specific applications and approximations we refer to the introduction of Ref. [Cas09]. Boltzmann-like transport equations can also be derived from 2PI evolution equations with certain restrictions [Ber05].

There also exist classical-statistical simulations which can be very efficiently used in situations where the quantum fields have large amplitudes so that they become "classical". This turns out to be the case if the classicality condition $F^2(x,y) \gg \rho^2(x,y)$ is satisfied [AB02, Ber05]. This is only possible for bosonic fields such as scalar or gauge fields. Attempts to include fermions in such simulations were made

in Ref. [BH09b, AS99]. The advantage of this method is that they are numerically cheap since no time integrals over the whole history in the simulation exist as in 2PI simulations.

Ref. [BS05] initiated the method of real-time simulation on a lattice. While lattice simulations are popular and often used in equilibrium [MM94], out of equilibrium such an approach is not trivial. Using stochastic quantization methods the authors in Ref. [BS05] opened a door towards a realization of the latter. In Ref. [Aar09] an example with stochastic quantization methods was presented where the well-known sign-problem in lattice calculations did not have a negative effect.

A relatively new way to study quantum fields out of equilibrium is followed by the authors in Ref. [GP08]. They use renormalization group methods in order to derive dynamical equations for correlation functions. The aim is to go beyond the well-known 2PI $1/N$-expansion approximations.

2.3 Instabilities

Instabilities in nonequilibrium quantum field theory are defined as physical solutions of evolution equations which grow exponentially over a finite time regime. Typically one or two-point correlation functions are the quantities under consideration which acquire such an behavior. There exist many physical situations in which exponential growing correlations can occur. Some of the most famous and discussed instabilities in nonequilibrium physics are parametric resonance with its main application in reheating the universe [KLS94] after the Big Bang, where also tachyonic or spinodal (decomposition) instabilities[9] play an important role [FKL01]. The latter is frequently discussed in (sub-)nuclear physics as well [SFR07]. The so called (Chromo-) Weibel instabilities emerge in anisotropic (quark-gluon) plasma [Mro88]. Related to this, color magnetic fields can generate Nielsen-Olesen instabilities [FII09, NO78]. Rayleigh-Taylor instabilities are considered to be important to understand the mechanism of core-collapse supernovae [KPJM03, JLM$^+$07].

In this section we are going to introduce the types of instabilities investigated in the work in hand. We start with the spinodal instability before we turn to the parametric resonance phenomenon.

Spinodal Instability

In general a spinodal instability is connected to the coexistence of phases in thermal equilibrium [CCR04]. The most famous example where such a situation occurs is the first-order liquid-gas phase transition. This results in a special structure of

[9] In cosmology the name "tachyonic" instability [FKL01] is used. However, it stands for the same. We prefer to denote it with "spinodal" instability.

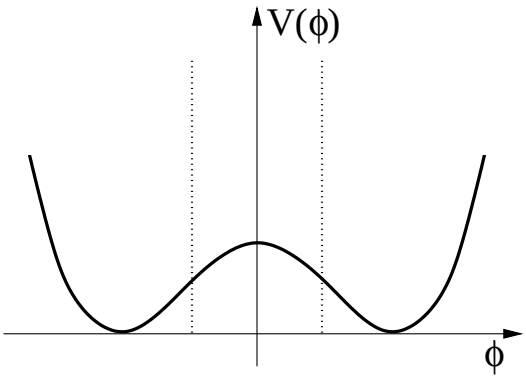

Figure 2.2: Sketch of a typical classical potential in which a spinodal instability can occur. The vertical dotted lines enclose the so called spinodal region in which the potential has negative curvature.

thermodynamical potentials which has to be treated with care. Thermodynamical potentials, like the Gibbs free energy, are counterparts of the effective action in quantum field theory [PS95]. This is the link to the situation in our framework. Note that in nonequilibrium evolutions there exists no unique definition of an effective potential, however the theory is defined by its classical action which has a well defined potential. The specific initial configuration of the classical potential is the origin of spinodal instabilities.

A spinodal instability in the context considered here occurs whenever the classical potential, which defines the theory, exhibits a concave region, i.e. a region with negative curvature. In Fig. 2.2 a sketch of a typical shape of a potential is displayed. The dotted vertical lines enclose the region with negative curvature, also called spinodal region. In the simplest case such a shape is realized by a potential of the form $V(\phi) = -m^2\phi^2 + \lambda\phi^4$ with $m^2 > 0$, $\lambda > 0$. Consequently a quantum field φ would acquire a leading order dispersion relation of the form $\omega_{|\mathbf{p}|} = \sqrt{|\mathbf{p}|^2 - m^2}$. The positive frequency solution $\sim e^{-i\omega_{|\mathbf{p}|}\,t}$ of the evolution equations results in an exponential growing function for modes with $|\mathbf{p}| < m$, i.e. $\varphi(t, \mathbf{p}) \sim e^{\gamma_{|\mathbf{p}|}\,t}$ with a positive growth rate $\gamma_{|\mathbf{p}|} = \sqrt{m^2 - |\mathbf{p}|^2}$. Hence an unstable behavior exists for a certain interval of time till it terminates by the virtue of next-to-leading (and higher) order contributions to the evolution. The latter yield a non-imaginary dispersion relation which causes a stable evolution in time.

A physical situation we have in mind is for example a (quantum) gas which is suddenly cooled down by a certain mechanism. This is called a quench. Other situations where a classical potential could acquire a shape of the kind described above is the exit of the inflationary phase in early-time cosmology. In inflation models from hybrid type the shape is generated dynamically which sets the beginning of preheating [Lin94]. Also in heavy-ion collisions quench-like situations may play an important role [RW93].

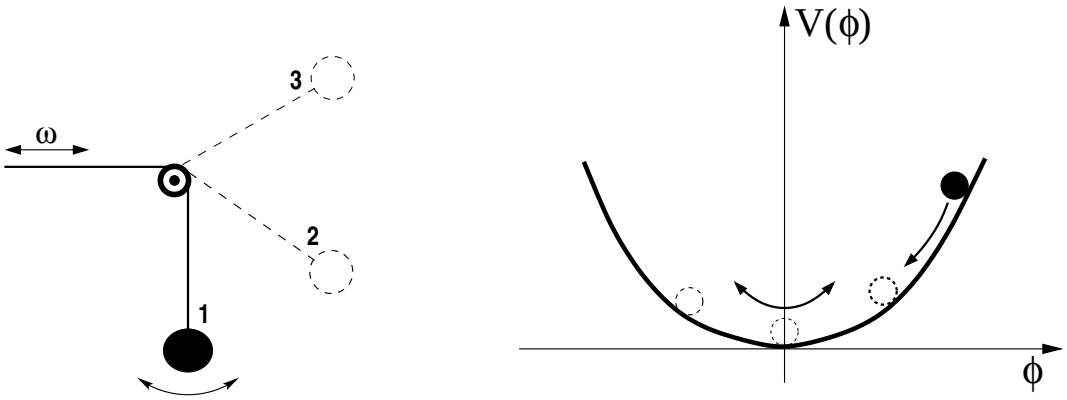

Figure 2.3: Left: Mechanical example of the phenomenon of parametric resonance. Right: Sketch of a typical classical potential which can lead to parametric resonance. The ball represent a possible field dynamics.

Parametric Resonance

Parametric resonance is a well known phenomenon in many areas of physics. In general the characteristics is a time dependence of parameters caused by (external) interaction. The simplest realization is a classical pendulum, like the one displayed in the right sketch of Fig. 2.3. Suppose it oscillates with a certain frequency where the pendel length is periodically changed during a short time, e.g. due to a fast pull on the pendel rope. The change of the pendel length has to act in the moment when the pendel has the temporary position 1 in Fig. 2.3. This causes an increase of the oscillation amplitude. If the maximal amplitude at the beginning lead to an inflection point 2, after a few oscillations the amplitude increases which yields an inflection point 3. If this mechanism continues the pendel performs a loop and the oscillation is no longer stable. This unstable evolution is called resonance. Another famous example of a resonance effect is a bridge which was destroyed by periodically emerging gusts of wind. Such macroscopic phenomena are well described and understood. The resonant amplitude is described by an exponential function [LL62].

A similar mechanism in quantum field theory got a lot attention since quite a long time. If quantum fields interact with a classical (background) field ϕ, their energy (frequency) is affected by ϕ. Solutions of ϕ might be periodic functions with a certain frequency and amplitude. This is visualized in the right sketch of Fig. 2.3 where the ball represents the classical field amplitude. The shape of the corresponding potential causes a certain frequency. This oscillation causes a periodically time dependent frequency of the quantum fields (fluctuations) which in turn yields an exponential growing solution. Hence, there is an unstable evolution of fluctuations. The growing quantum field amplitude is interpreted as particle excitations (production). The unstable evolution is stopped due to the back-reaction of the fluctuations on the

classical field, the behavior of the classical field changes which then is no longer able to amplify the quantum fields.

The most important application of this mechanism in quantum field theory is the preheating stage of the early-time evolution in cosmology [KLS94, BS03].

2.4 Nonthermal Fixed Points

Out-of-equilibrium studies in bosonic field theories with instabilities like resonant particle production in early-time cosmology after inflation typically lead to nonperturbative large fluctuations. Accordingly, spectra of occupation numbers are far from equilibrium and can be described by classical statistical field theories [KT96, BG07, AB02]. It was realized that the subsequent evolution enters a quasi-stationary phase which delays thermalization considerably. The characteristics of such systems are nonthermal power-law behaviors in the occupation number spectra[10], i.e. $n_{\mathbf{p}} \sim |\mathbf{p}|^{-\kappa}$ with an "occupation number exponent" κ and $n_{\mathbf{p}}$ the occupation number.

An ultraviolet power-law behavior with $n_{\mathbf{p}} \sim |\mathbf{p}|^{-3/2}$ of (effectively) classical spectra is connected with the phenomenon known as (wave) turbulence [ZLF92, Fri95]. In reheating dynamics the phenomenon of turbulence was observed[11], see e.g. [MT04, MT03, FK01, PFKP06, GC02]. As well as in gauge theories with application in relativistic heavy-ion collisions [AM06b, AM06a, Kha08, BSS09a, MSW07].

Recently it was shown analytically and numerically for scalar field theories that nonthermal power-law behaviors can also show up in the infrared part of spectra [BRS08, BPR09] with exponents larger than those known from turbulence. In Ref. [BH09a] in a renormalization group approach for scalar field theories infrared and ultraviolet (turbulence) exponents were derived from first principles.

Whereas ultraviolet power-laws are connected to turbulence which cease to exist once quantum effects become important, infrared scaling solutions are associated to critical phenomena with large enhanced infrared fluctuations, which distinguishes these two types of "nonthermal fixed points".

In the following we would like to present the most important facts about how to determine power-law exponents of nonthermal fixed points from first principles. We closely follow parts out of [BH09a]. We do not restrict ourselves to a specific type of fields in this discussion. Once a system described by an effective action enters a

[10] Generically the power-laws emerge in the statistical (spectral) two-point functions, however, typically one considers occupation numbers which are connected to the statistical two-point functions.

[11] Note that there is a difference in specifying occupation (particle) number exponents between "particle cascades" and "energy cascades" [MT04]. $n_{\mathbf{p}} \sim |\mathbf{p}|^{-3/2}$ corresponds to "particle cascades" whereas "energy cascades" yield e.g. $n_{\mathbf{p}} \sim |\mathbf{p}|^{-5/3}$.

quasi-stationary state it can be shown that the following identity holds [BH09a]

$$\Pi^{\rho}(\omega,\mathbf{p})F(\omega,\mathbf{p}) - \Pi^{F}(\omega,\mathbf{p})\rho(\omega,\mathbf{p}) = 0\,, \tag{2.29}$$

which is known as the stationarity condition. The functions $\Pi^{\rho}(\omega,\mathbf{p})$ and $\Pi^{F}(\omega,\mathbf{p})$ are self-energies in 4-dimensional Fourier space with $p^0 = \omega$ and the $F(\omega,\mathbf{p})$ and $\rho(\omega,\mathbf{p})$ as statistical and spectral parts of the resummed propagator, respectively. Solutions of (2.29) for $F(\omega,\mathbf{p})$ and $\rho(\omega,\mathbf{p})$ with a certain scaling behavior define a fixed point of the theory. Note that the self-energies can be expressed in terms of the statistical and spectral functions if an approximation is applied. Eq. (2.29) is reminiscent of the "gain-" and "loss-term" structure in Boltzman-type equations [Ber05]. It can also be derived from 2PI nonequilibrium evolution equations with a generalized gradient expansion up to leading order [Ber05].

In equilibrium equation (2.29) is fulfilled by virtue of the fluctuation-dissipation relation[12]. In the limit $\omega \ll T$ where $n(\omega) \sim T\,\omega^{-\kappa_{\mathrm{therm}}}$ there is $\kappa_{\mathrm{therm}} = 1$. Thus κ_{therm} characterizes the thermal fixed point. For a general discussion one typically makes an ansatz for the propagator parts in (2.29) which is [BH09a]

$$F(\omega,\mathbf{p}) = s^{2+\kappa}F(s^z\omega, s\mathbf{p})\,, \qquad \rho(\omega,\mathbf{p}) = s^{2-\eta}\rho(s^z\omega, s\mathbf{p})\,, \tag{2.30}$$

with a positive real scaling parameter s, the anomalous dimension η, the standard dynamical scaling exponent z and the "occupation number exponent" κ which is defined by the above relation. With the help of the fluctuation-dissipation relation one finds for the case of vacuum physics ($T = 0$) $\kappa = -\eta$, whereas for thermal equilibrium $\kappa = -\eta + z$ [BH09a]. For example, a relativistic 3+1 dimensional scalar theory has $z \simeq 1$ and $\eta \simeq 0$. The authors in Ref. [BH09a] found for nonthermal systems the relation $\kappa = -\eta + z + d$, where d is the number of spatial dimensions. They used renormalization group methods within a nonperturbative large-N expansion up to next-to-leading order. With this one has a hierarchy of exponent relations with increasing complexity from vacuum to nonequilibrium physics.

What has to be done practically is, with a specific theory on hand, find the representation of the self-energies in (2.29) for a given approximation in terms of F and ρ, insert the ansatz for the scaling solution (2.30) into (2.29) and find the exponents for which different terms in (2.29) cancel so that the identity is fulfilled.

With this method in the case of a scalar ϕ^4-theory with initial conditions which lead to parametric resonance an out-of-equilibrium study showed an infrared exponent $\kappa_{\mathrm{IR}} = 4$ [BRS08]. Further, with a similar method in a $SU(2)$ gauge theory a turbulent spectrum with $\kappa_{\mathrm{UV}} = 4/3$ was found numerically and analytically[13] [BSS09a].

So far quantum field theories with fermionic degrees of freedom have not been investigated under the aspect of nonthermal fixed points. It is clear that infrared

[12] In Eq. (2.20) and (2.19) we showed the examples of the relation for scalar and Dirac fields. Analog relations can be found for the self-energies [Ber05].

[13] In both cases one analytically finds other solutions as well.

fixed points in fermion occupation numbers are forbidden by the Pauli principle. However ultraviolet scaling solutions are not excluded, but cannot be identified with classical turbulence. The existence of "quantum turbulence" in this context is speculative. If fermions coupled to other degrees of freedom which could exhibit infrared scaling solutions they may prevent the system from approaching nonthermal fixed points or, they may accelerate the evolution towards thermal equilibrium. With the model and its approximation considered in this work it is possible to learn something about the influence of fermionic degrees of freedom on the bosonic sector. Moreover, the fermion dynamics by itself in the presence of large bosonic fluctuations can be studied. These topics are addressed in Chapters 4 and 5.

Chapter 3

Model with Yukawa-Type Interaction

In this chapter we discuss the model which is used in this work. In Sec. 3.1 the model is introduced and its symmetries and their consequences are considered. In the ensuing section we display the resulting equations of motion which we implemented on a computer in order to solve the dynamics. In Sec. 3.3 we present the explicit expressions for the self-energies. Sec. 3.4 discusses the initial conditions we used for the simulations. A central quantity in our investigations is the occupation number which we are going to define in Sec. 3.5. The last section of this chapter is devoted to the energy-momentum tensor of our system.

3.1 Action and Symmetries

The model we are going to investigate is a generic model in which scalar bosons interact with Dirac fermions via a Yukawa coupling. It could have many applications in different areas in particle physics, for instance in early-time cosmology for reheating studies, or it could serve as an effective theory for low-energy hadron physics in QCD[1]. The model is defined by its classical action

$$\begin{aligned}\mathcal{S}[\varphi,\psi,\bar{\psi}] \;=\; & \int d^4x \left\{ \bar{\psi}\left[i\gamma^\mu\partial_\mu - m_\psi\right]\psi - \frac{g}{N_f}\bar{\psi}\left[\sigma + i\gamma_5\tau^l\pi^l\right]\psi \right. \\ & + \frac{1}{2}\left[\partial_\mu\sigma\partial^\mu\sigma + \partial_\mu\pi^l\partial^\mu\pi^l\right] \\ & \left. - \frac{1}{2}m^2\left[\sigma^2+\pi^l\pi^l\right] - \frac{\lambda}{4!N_s}\left[\sigma^2+\pi^l\pi^l\right]^2 \right\}, \end{aligned} \tag{3.1}$$

where τ^l $(l = 1, 2, 3)$ are the standard Pauli matrices and γ^μ $(\mu = 0, 1, 2, 3)$ denote the Dirac matrices. We employ a metric with components $\eta_{\mu\nu} = \mathrm{diag}(1, -1, -1, -1)$.

[1] The model is also known as the linear-sigma model or "quark-meson model" [GML60] which has been extensively studied in thermal equilibrium.

Summation over repeated indices is implied. The fermion fields $\psi(x)$ are coupled via the Yukawa coupling g to the scalars $\varphi_a(x) = \{\sigma(x), \pi^1(x), \pi^2(x), \pi^3(x)\}$, whose self-coupling is λ. The mass parameters are m and m_ψ for the scalars and fermions respectively. Below we will use $h \equiv g/N_f$ for convenience.

If $m_\psi = 0$ the model is invariant under $SU(2)_L \times SU(2)_R$ transformations, i.e. it exhibits chiral symmetry. Chiral symmetry is spontaneously broken if at least one of the scalar fields acquires a nonvanishing expectation value, i.e. $\langle\varphi_a(x)\rangle \neq 0$. In the case $m_\psi \neq 0$ the symmetry is explicitly broken. Our studies include all variants of the model (3.1) with different scopes. We will present the parametrization of the effective action and the equations of motion for the case with explicitly broken symmetry where in addition we assume that not all expectation values vanish. This results in the most complex structure of the equations for our purposes. The reduction to the $SU(2)_L \times SU(2)_R$ symmetric theory is straightforward and will be described in Sec. 3.3.2.

We will use the 2PI effective action to calculate the evolution equations for the one- and two-point functions. The 2PI effective action was introduced in Sec. 2.2. It is parametrized by the one-point function $\langle\varphi_a(x)\rangle = \{\langle\sigma(x)\rangle \equiv \phi(x), 0, 0, 0\}$ and the two-point functions $D_{ij}(x,y)$ and $G_{ab}(x,y)$, cf. Sec. 2.2.

In our model the free inverse propagator of the bosonic quantum field is defined by

$$iG^{-1}_{0,ab}(x,y) \;=\; -\left[\partial_\mu\partial^\mu\delta_{ab} + m^2_{ab}(x)\right]\delta^{(4)}(x-y)\,, \tag{3.2}$$

for $a, b = 1, \ldots, N_s$. The free inverse fermion propagator is

$$iD^{-1}_{0,ij}(x,y) \;=\; \left[i\gamma^\mu\partial_\mu - M_\psi(x)\right]\,\delta^{(4)}(x-y)\delta_{ij}\,, \tag{3.3}$$

for $i, j = 1, \ldots, N_f$. The boson mass in (3.2) is defined by

$$m^2_{ab}(x) = m^2\delta_{ab} + \frac{\lambda}{6N_s}\langle\varphi_a(x)\rangle^2\delta_{ab} + \frac{\lambda}{3N_s}\langle\varphi_a(x)\rangle\langle\varphi_b(x)\rangle\,, \tag{3.4}$$

while the fermion mass is given by

$$M_\psi(x) = m_\psi + h\phi(x)\,. \tag{3.5}$$

It is convenient to decompose the resummed propagators into a statistical and spectral part, cf. (2.13) and (2.14),

$$D_{ij}(x,y) \;=\; F_{ij}(x,y) - \frac{i}{2}\rho_{ij}(x,y)\,\mathrm{sign}(x^0-y^0)\,, \tag{3.6}$$

$$G_{ab}(x,y) \;=\; F^\phi_{ab}(x,y) - \frac{i}{2}\rho^\phi_{ab}(x,y)\,\mathrm{sign}(x^0-y^0)\,, \tag{3.7}$$

where the statistical and spectral parts are defined in (2.15) and (2.16). The self-energies can be decomposed in a similar fashion

$$\Sigma_{ij}(x,y) \;=\; C_{ij}(x,y) - \frac{i}{2}A_{ij}(x,y)\,\mathrm{sign}(x^0-y^0)\,, \tag{3.8}$$

$$\Pi_{ab}(x,y) \;=\; -i\Pi^{\mathrm{local}}_{ab}(x)\,\delta^{(4)}(x-y) + \Pi^{F}_{ab}(x,y) - \frac{i}{2}\Pi^{\rho}_{ab}(x,y)\,\mathrm{sign}(x^0-y^0)\,. \tag{3.9}$$

Here we take into account a possible space-time dependent local term $\Pi^{\mathrm{local}}_{ab}(x)$ for the boson self-energy, which is not present for the fermion self-energy. Since only the field expectation value $\langle\sigma(x)\rangle = \phi(x)$ is nonvanishing the boson propagator can be written in the form

$$G_{ab}(x,y) = \mathrm{diag}(G_{\parallel}(x,y), G_{\perp}(x,y), G_{\perp}(x,y), G_{\perp}(x,y))\,. \tag{3.10}$$

Accordingly the expectation values of the fields $\pi_l(x)$ ("pions") vanish and there is no flavor mixing, thus the fermion propagator becomes proportional to the unity matrix in flavor space and we can write (we omit Dirac indices)

$$D_{ij}(x,y) = D(x,y)\delta_{ij}\,. \tag{3.11}$$

Corresponding representations are valid for the self-energies. The boson propagator is fully described by the four components given in (3.10). For the fermion propagator, not all 16 Dirac components are independent. By symmetry arguments we can reduce the number of independent components significantly. It is convenient to decompose the fermion correlators into a sum of components which have special properties under Lorentz transformations. Such a decomposition is known as the Lorentz decomposition. For the statistical function we have (omitting Dirac and flavor indices)

$$F(x,y) = F_S(x,y) + F_P(x,y) + \gamma_\mu F^\mu_V(x,y) + \gamma_\mu\gamma_5 F^\mu_A(x,y) + \frac{1}{2}\sigma_{\mu\nu}F^{\mu\nu}_T(x,y)\,, \tag{3.12}$$

with $F_S, F_P, F^\mu_V, F^\mu_A, F^{\mu\nu}_T$ as the scalar, pseudo-scalar, vector, axial-vector and tensor component, respectively, with $\sigma_{\mu\nu} \equiv \frac{i}{2}[\gamma^\mu,\gamma^\nu]$. An analog decomposition can be made for the spectral function as well as for the self-energies. For convenience we will call $F_S, F_P, F^\mu_V, F^\mu_A, F^{\mu\nu}_T$ the "Lorentz components" in the following.

We will consider spatially homogeneous and isotropic systems. This implies that the one-point function only depends on time $x^0 = t$, i.e. $\phi(x) = \phi(t)$, consequently the masses (3.4) and (3.5) do. Using parity and CP invariance the only non-vanishing components of the fermion propagator are the scalar-, vector- and $0i$-tensor-components[2]. For a general two-point function $\mathcal{T} = \mathcal{T}(x,y)$ they are defined by

$$\mathcal{T}_S = \frac{1}{4}\mathrm{tr}\,\{\mathcal{T}\}\;,\quad \mathcal{T}^\mu_V = \frac{1}{4}\mathrm{tr}\,\{\gamma^\mu\mathcal{T}\}\;,\quad \mathcal{T}^{\mu\nu}_T = \frac{1}{4}\mathrm{tr}\,\{\sigma_{\mu\nu}\mathcal{T}\}\;. \tag{3.13}$$

[2]One may call the $0i$-tensor-components "temporal-spatial" components.

To obtain the corresponding Lorentz components for the propagators and self-energies one simply inserts for $\mathcal{T}(x,y)$ the functions $F(x,y)$, $\rho(x,y)$, $C(x,y)$ and $A(x,y)$. If in addition we apply chiral symmetry we would be left with only the vector part. We will consider this case in detail in Sec. 3.3.2. Each Lorentz component can be decomposed in spatial Fourier space as

$$F_\Xi(x,y) = \int_{\mathbf{p}} F_\Xi(x^0,y^0;\mathbf{p})\, e^{i\mathbf{p}(\mathbf{x}-\mathbf{y})}\,, \tag{3.14}$$

where we use the abbreviation $\int_{\mathbf{p}} = \int d^3p/(2\pi)^3$ and $\Xi = \{S,V,T\}$ represents the index for the Lorentz components. Corresponding decompositions hold for all other correlations.

Due to isotropy the dependence of the two-point functions on the momentum can be described by[3]

$$\begin{aligned} &F_S(x^0,y^0;\mathbf{p}) = F_S(x^0,y^0;|\mathbf{p}|)\,, \quad F_V^0(x^0,y^0;\mathbf{p}) = F_V^0(x^0,y^0;|\mathbf{p}|)\,,\\ &\mathbf{F}_V(x^0,y^0;\mathbf{p}) = \frac{\mathbf{p}}{|\mathbf{p}|}\,F_V(x^0,y^0;|\mathbf{p}|)\,, \quad \mathbf{F}_T^0(x^0,y^0;\mathbf{p}) = \frac{\mathbf{p}}{|\mathbf{p}|}\,F_T(x^0,y^0;|\mathbf{p}|)\,, \end{aligned} \tag{3.15}$$

for the statistical fermion correlators, and

$$F^\phi_{\parallel,\perp}(x^0,y^0;\mathbf{p}) \;=\; F^\phi_{\parallel,\perp}(x^0,y^0;|\mathbf{p}|)\,, \tag{3.16}$$

for the statistical boson correlators. Eqs. (3.15) and (3.16) can be written in an analogous way for the spectral functions as well as for the corresponding self-energies. An important information is the behavior of the two-point functions under interchanging their time arguments and whether they are complex or real valued. Applying CP symmetry and using

$$F_{ij}^{(\Xi)}(x,y) = \Big[F_{ji}^{(\Xi)}(y,x)\Big]^*\,, \quad \rho_{ij}^{(\Xi)}(x,y) = -\Big[\rho_{ji}^{(\Xi)}(y,x)\Big]^*\,, \tag{3.17}$$

[3]Note that it has to be understood $\mathbf{F}_V = \big(F_V^1, F_V^2, F_V^3\big)$ and $\mathbf{F}_T^0 = \big(F_T^{01}, F_T^{02}, F_T^{03}\big)$. For convenience we denote the tensor component which only depends on $|\mathbf{p}|$ with F_T. For the spectral function and the self-energies the same holds.

we find the following properties

$$F_S(x^0, y^0; |\mathbf{p}|),\, C_S(x^0, y^0; |\mathbf{p}|): \quad \text{real, symmetric}, \tag{3.18}$$
$$\rho_S(x^0, y^0; |\mathbf{p}|),\, A_S(x^0, y^0; |\mathbf{p}|): \quad \text{real, antisymmetric}, \tag{3.19}$$

$$F_V^0(x^0, y^0; |\mathbf{p}|),\, C_V^0(x^0, y^0; |\mathbf{p}|): \quad \text{imaginary, antisymmetric}, \tag{3.20}$$
$$\rho_V^0(x^0, y^0; |\mathbf{p}|),\, A_V^0(x^0, y^0; |\mathbf{p}|): \quad \text{imaginary, symmetric}, \tag{3.21}$$

$$F_V(x^0, y^0; |\mathbf{p}|),\, C_V(x^0, y^0; |\mathbf{p}|): \quad \text{real, symmetric}, \tag{3.22}$$
$$\rho_V(x^0, y^0; |\mathbf{p}|),\, A_V(x^0, y^0; |\mathbf{p}|): \quad \text{real, antisymmetric}, \tag{3.23}$$

$$F_T(x^0, y^0; |\mathbf{p}|),\, C_T(x^0, y^0; |\mathbf{p}|): \quad \text{real, symmetric}, \tag{3.24}$$
$$\rho_T(x^0, y^0; |\mathbf{p}|),\, A_T(x^0, y^0; |\mathbf{p}|): \quad \text{real, antisymmetric}, \tag{3.25}$$

for the fermion sector and

$$F^\phi(x^0, y^0; |\mathbf{p}|): \quad \text{real, symmetric}, \tag{3.26}$$
$$\rho^\phi(x^0, y^0; |\mathbf{p}|): \quad \text{real, antisymmetric}, \tag{3.27}$$

$$\Pi_F(x^0, y^0; |\mathbf{p}|): \quad \text{real, symmetric}, \tag{3.28}$$
$$\Pi_\rho(x^0, y^0; |\mathbf{p}|): \quad \text{real, antisymmetric}, \tag{3.29}$$

for the boson sector. We now have all important properties of the two-point functions presented. In the next section we will consider the equations of motion for each nonvanishing correlation function.

3.2 Equations of Motion

In this section we will present all relevant evolution equations. The formal way of getting the equations of motion in the 2PI framework was presented in Sec. 2.2. Since the self-energies of the various fields are still not specified the following equations have the most general form in combination with the applied symmetries. In the numerical calculations we solve the equations in spatial Fourier space (cf. Appendix F). Hence, we prefer to present the equations in terms of Fourier modes.

The complete equations of motions (2.25) and (2.26) for the fermion two-point

functions are

$$
\begin{aligned}
i\partial_t F_S(t,t';|\mathbf{p}|) &= -i|\mathbf{p}|F_T(t,t';|\mathbf{p}|) + M_\psi(t)\, F_V^0(t,t';|\mathbf{p}|) \\
&\quad + \int_0^t dt'' \Big\{ A_S(t,t'';|\mathbf{p}|)\, F_V^0(t'',t';|\mathbf{p}|) + A_V^0(t,t'';|\mathbf{p}|)\, F_S(t'',t';|\mathbf{p}|) \\
&\qquad + i\Big(A_V(t,t'';|\mathbf{p}|)\, F_T(t'',t';|\mathbf{p}|) - A_T(t,t'';|\mathbf{p}|)\, F_V(t'',t';|\mathbf{p}|) \Big) \Big\} \\
&\quad - \int_0^{t'} dt'' \Big\{ C_S(t,t'';|\mathbf{p}|)\, \rho_V^0(t'',t';|\mathbf{p}|) + C_V^0(t,t'';|\mathbf{p}|)\, \rho_S(t'',t';|\mathbf{p}|) \\
&\qquad + i\Big(C_V(t,t'';|\mathbf{p}|)\, \rho_T(t'',t';|\mathbf{p}|) - C_T(t,t'';|\mathbf{p}|)\, \rho_V(t'',t';|\mathbf{p}|) \Big) \Big\},
\end{aligned}
\tag{3.30}
$$

$$
\begin{aligned}
i\partial_t F_V^0(t,t';|\mathbf{p}|) &= |\mathbf{p}|\, F_V(t,t';|\mathbf{p}|) + M_\psi(t)\, F_S(t,t';|\mathbf{p}|) \\
&\quad + \int_0^t dt'' \Big\{ A_S(t,t'';|\mathbf{p}|)\, F_S(t'',t';|\mathbf{p}|) \quad - A_T(t,t'';|\mathbf{p}|)\, F_T(t'',t';|\mathbf{p}|) \\
&\qquad + A_V^0(t,t'';|\mathbf{p}|)\, F_V^0(t'',t';|\mathbf{p}|) - A_V(t,t'';|\mathbf{p}|)\, F_V(t'',t';|\mathbf{p}|) \Big\} \\
&\quad - \int_0^{t'} dt'' \Big\{ C_S(t,t'';|\mathbf{p}|)\, \rho_S(t'',t';|\mathbf{p}|) \quad - C_T(t,t'';|\mathbf{p}|)\, \rho_T(t'',t';|\mathbf{p}|) \\
&\qquad + C_V^0(t,t'';|\mathbf{p}|)\, \rho_V^0(t'',t';|\mathbf{p}|) - C_V(t,t'';|\mathbf{p}|)\, \rho_V(t'',t';|\mathbf{p}|) \Big\},
\end{aligned}
\tag{3.31}
$$

$$
\begin{aligned}
\partial_t F_V(t,t';|\mathbf{p}|) &= -i|\mathbf{p}|\, F_V^0(t,t';|\mathbf{p}|) + M_\psi(t) F_T(t,t';|\mathbf{p}|) \\
&\quad + \int_0^t dt'' \Big\{ -i\Big(A_V^0(t,t'';|\mathbf{p}|)\, F_V(t'',t';|\mathbf{p}|) - A_V(t,t'';|\mathbf{p}|)\, F_V^0(t'',t';|\mathbf{p}|) \Big) \\
&\qquad + A_S(t,t'';|\mathbf{p}|)\, F_T(t'',t';|\mathbf{p}|) + A_T(t,t'';|\mathbf{p}|)\, F_S(t'',t';|\mathbf{p}|) \Big\} \\
&\quad - \int_0^{t'} dt'' \Big\{ -i\Big(C_V^0(t,t'';|\mathbf{p}|)\, \rho_V(t'',t';|\mathbf{p}|) - C_V(t,t'';|\mathbf{p}|)\, \rho_V^0(t'',t';|\mathbf{p}|) \Big)
\end{aligned}
$$

$$+C_S(t,t'';|\mathbf{p}|)\,\rho_T(t'',t';|\mathbf{p}|)+C_T(t,t'';|\mathbf{p}|)\,\rho_S(t'',t';|\mathbf{p}|)\Big\}\,, \tag{3.32}$$

$$\begin{aligned}
\partial_t F_T(t,t';|\mathbf{p}|) \;=\;& |\mathbf{p}|F_S(t,t';|\mathbf{p}|)-M_\psi(t)\,F_V(t,t';|\mathbf{p}|)\\
&+\int_0^t dt''\Big\{-A_S(t,t'';|\mathbf{p}|)\,F_V(t'',t';|\mathbf{p}|)-A_V(t,t'';|\mathbf{p}|)\,F_S(t'',t';|\mathbf{p}|)\\
&\quad -i\Big(A_V^0(t,t'';|\mathbf{p}|)\,F_T(t'',t';|\mathbf{p}|)-A_T(t,t'';|\mathbf{p}|)\,F_V^0(t'',t';|\mathbf{p}|)\Big)\Big\}\\
&-\int_0^{t'} dt''\Big\{-C_S(t,t'';|\mathbf{p}|)\,\rho_V(t'',t';|\mathbf{p}|)-C_V(t,t'';|\mathbf{p}|)\,\rho_S(t'',t';|\mathbf{p}|)\\
&\quad -i\Big(C_V^0(t,t'';|\mathbf{p}|)\,\rho_T(t'',t';|\mathbf{p}|)-C_T(t,t'';|\mathbf{p}|)\,\rho_V^0(t'',t';|\mathbf{p}|)\Big)\Big\}\,,
\end{aligned} \tag{3.33}$$

for the statistical two-point functions and

$$\begin{aligned}
i\partial_t\rho_S(t,t';|\mathbf{p}|) \;=\;& -i|\mathbf{p}|\rho_T(t,t';|\mathbf{p}|)+M_\psi(t)\,\rho_V^0(t,t';|\mathbf{p}|)\\
&+\int_{t'}^t dt''\Big\{A_S(t,t'';|\mathbf{p}|)\,\rho_V^0(t'',t';|\mathbf{p}|)+A_V^0(t,t'';|\mathbf{p}|)\,\rho_S(t'',t';|\mathbf{p}|)\\
&\quad +i\Big(A_V(t,t'';|\mathbf{p}|)\,\rho_T(t'',t';|\mathbf{p}|)-A_T(t,t'';|\mathbf{p}|)\,\rho_V(t'',t';|\mathbf{p}|)\Big)\Big\}\,,
\end{aligned} \tag{3.34}$$

$$\begin{aligned}
i\partial_t\rho_V^0(t,t';|\mathbf{p}|) \;=\;& |\mathbf{p}|\,\rho_V(t,t';|\mathbf{p}|)+M_\psi(t)\,\rho_S(t,t';|\mathbf{p}|)\\
&+\int_{t'}^t dt''\Big\{A_S(t,t'';|\mathbf{p}|)\,\rho_S(t'',t';|\mathbf{p}|)-A_T(t,t'';|\mathbf{p}|)\,\rho_T(t'',t';|\mathbf{p}|)\\
&\quad +A_V^0(t,t'';|\mathbf{p}|)\,\rho_V^0(t'',t';|\mathbf{p}|)-A_V(t,t'';|\mathbf{p}|)\,\rho_V(t'',t';|\mathbf{p}|)\Big\}\,,
\end{aligned} \tag{3.35}$$

$$\begin{aligned}\partial_t\rho_V(t,t';|\mathbf{p}|) \;=\; & -i|\mathbf{p}|\,\rho_V^0(t,t';|\mathbf{p}|) + M_\psi(t)\rho_T(t,t';|\mathbf{p}|) \\ & + \int_{t'}^{t} dt''\Big\{-i\Big(A_V^0(t,t'';|\mathbf{p}|)\,\rho_V(t'',t';|\mathbf{p}|) - A_V(t,t'';|\mathbf{p}|)\,\rho_V^0(t'',t';|\mathbf{p}|)\Big) \\ & \qquad + A_S(t,t'';|\mathbf{p}|)\,\rho_T(t'',t';|\mathbf{p}|) + A_T(t,t'';|\mathbf{p}|)\,\rho_S(t'',t';|\mathbf{p}|)\Big\}, \end{aligned} \tag{3.36}$$

$$\begin{aligned}\partial_t\rho_T(t,t';|\mathbf{p}|) \;=\; & |\mathbf{p}|\rho_S(t,t';|\mathbf{p}|) - M_\psi(t)\,\rho_V(t,t';|\mathbf{p}|) \\ & + \int_{t'}^{t} dt''\Big\{-A_S(t,t'';|\mathbf{p}|)\,\rho_V(t'',t';|\mathbf{p}|) - A_V(t,t'';|\mathbf{p}|)\,\rho_S(t'',t';|\mathbf{p}|) \\ & \qquad -i\Big(A_V^0(t,t'';|\mathbf{p}|)\,\rho_T(t'',t';|\mathbf{p}|) - A_T(t,t'';|\mathbf{p}|)\,\rho_V^0(t'',t';|\mathbf{p}|)\Big)\Big\}, \end{aligned} \tag{3.37}$$

for the spectral two-point functions. The complete equations of motion for the boson two-point functions (2.27) and (2.28) are

$$\begin{aligned}\Big[\big(\partial_t^2+\mathbf{p}^2\big)+M_\parallel^2(t)\Big]F_\parallel^\phi(t,t';|\mathbf{p}|) \;=\; & -\int_0^t dt''\,\Pi_\parallel^\rho(t,t'';|\mathbf{p}|)\,F_\parallel^\phi(t'',t';|\mathbf{p}|) \\ & + \int_0^{t'} dt''\,\Pi_\parallel^F(t,t'';|\mathbf{p}|)\,\rho_\parallel^\phi(t'',t';|\mathbf{p}|)\,, \end{aligned} \tag{3.38}$$

$$\begin{aligned}\Big[\big(\partial_t^2+\mathbf{p}^2\big)+M_\perp^2(t)\Big]F_\perp^\phi(t,t';|\mathbf{p}|) \;=\; & -\int_0^t dt''\,\Pi_\perp^\rho(t,t'';|\mathbf{p}|)\,F_\perp^\phi(t'',t';|\mathbf{p}|) \\ & + \int_0^{t'} dt''\,\Pi_\perp^F(t,t'';|\mathbf{p}|)\,\rho_\perp^\phi(t'',t';|\mathbf{p}|)\,, \end{aligned} \tag{3.39}$$

$$\Big[\big(\partial_t^2+\mathbf{p}^2\big)+M_\parallel^2(t)\Big]\rho_\parallel^\phi(t,t';|\mathbf{p}|) \;=\; -\int_{t'}^t dt''\,\Pi_\parallel^\rho(t,t'';|\mathbf{p}|)\,\rho_\parallel^\phi(t'',t';|\mathbf{p}|)\,, \tag{3.40}$$

$$\Big[\big(\partial_t^2+\mathbf{p}^2\big)+M_\perp^2(t)\Big]\rho_\perp^\phi(t,t';|\mathbf{p}|) \;=\; -\int_{t'}^t dt''\,\Pi_\perp^\rho(t,t'';|\mathbf{p}|)\,\rho_\perp^\phi(t'',t';|\mathbf{p}|)\,, \tag{3.41}$$

where we used the diagonal matrix representation (3.10). The time dependent masses are defined by

$$\begin{aligned} M_{\parallel}^2(t) &= \left(m^2 + \frac{\lambda}{2N_s}\phi^2(t) + \Pi_{\parallel}^{\text{local}}(t) \right) , \\ M_{\perp}^2(t) &= \left(m^2 + \frac{\lambda}{6N_s}\phi^2(t) + \Pi_{\perp}^{\text{local}}(t) \right) . \end{aligned} \tag{3.42}$$

Note that a coupling between longitudinal and transversal components in (3.38)–(3.41) are solely given due to the self-energies.

The equation of motion for the expectation value $\phi(t)$ is

$$\left[\partial_t^2 + \frac{\lambda}{6N_s}\phi^2(t) + M_{\parallel}^2(\phi = 0, t) \right] \phi(t) = 4\, g \int \frac{d^3p}{(2\pi)^3} F_S(t, t; \mathbf{p}) + \frac{\delta \Gamma_2[\phi, G, D]}{\delta\, \phi(t)} , \tag{3.43}$$

where the first term on the right-hand side corresponds to the backreaction of the fermion field. The last term represents nonlocal contributions of the interaction between the boson field with the macroscopic field ϕ. It contains memory integrals similar to those in the equations for the two-point functions. The explicit form will be specified in the next section when we will consider the approximation used in this work.

The above equations have to be regularized, which we do by implementing a momentum cut-off following Ref. [BPR09, BBS03], further details can be found in Appendix F. Hence, we consider a cut-off theory where we subtract leading order divergences at initial time, such as "tadpole-like" contributions in (3.42) as well as the fermion backreaction term in (3.43). Renormalized ("physical") quantities like the oscillation frequency and damping/growth rates are extracted from the simulation results. Note that subtracting the fermion backreaction term at initial time preserves the fact that the fermion backreaction only starts if fermions are produced [GPRT99].

3.3 Approximations

In this section we are going to consider the explicit parametrization of the Γ_2-part of the 2PI effective action in terms of statistical and spectral two-point functions as well as the macroscopic field expectation value ϕ. First we discuss the case where the $SU(2)_L \times SU(2)_R$ symmetry is broken. In Sec. 3.3.2 we apply chiral symmetry which results in simplified equations.

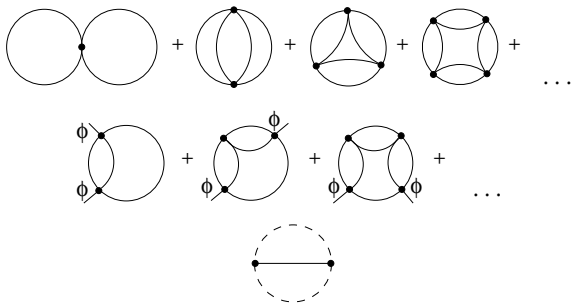

Figure 3.1: Diagrammatic representation of the employed approximation for Γ_2. Solid lines are associated to self-consistently dressed boson propagators G and dashed lines to fermion propagators D. External legs indicate the interaction with the macroscopic field ϕ. The dots indicate an infinite series of diagrams, each obtained from the previous one by adding another loop in the bubble ring.

3.3.1 Nonvanishing Field Expectation Value

As we know from Sec. 2.2, the self-energies are defined by the variation of the Γ_2 part of the effective action with respect to the two-point functions, see (2.11) and (2.12). $\Gamma_2[G, D, \phi]$ depends on the approximation. Here we consider the nonperturbative 2PI $1/N$-expansion to next-to-leading order (NLO) in the number of boson fields N_s, see Sec. 2.2.2. For bosons the physics of nonequilibrium instabilities cannot be described by an expansion in the coupling λ even for weak couplings, since occupation numbers can grow parametrically large of order $1/\lambda$. This requires to sum an infinite series of boson diagrams, which can be classified into two parts, one with purely self-interacting boson fluctuations and the other with interactions with the background field ϕ. These parts are displayed in Fig. 3.1 by two sums. The upper line corresponds to the former part and the second line represents the latter part. Note that the first diagram in the upper sum is local and corresponds to the local self-energy contributions entering the effective masses (3.42), see below. In contrast to the boson sector, occupation numbers for fermions are bounded due to the Pauli principle and a 2PI coupling expansion (see Sec. 2.2.1) in powers of the Yukawa coupling g will be employed to describe the fermion fluctuations. In the last row of Fig. 3.1 the diagram which is responsible for the nonlocal fermion-boson interaction is shown. The mathematical expression of $\Gamma_2[\phi, D, G]$ in our approximation, in terms of the resummed propagators, consequently acquires the form[4] (summation

[4]In this expression, as in some others, we did not applied $\langle\varphi_a(x)\rangle = \{\phi(x), 0, 0, 0\}$ which is sometimes useful in order to get compact expressions. Nevertheless it should be always understood that only the first component is nonvanishing.

over repeated indices is implied)

$$\begin{aligned}\Gamma_2[\phi, D, G] &= -\frac{\lambda}{4!N_s}\int_x G_{aa}(x,x)G_{bb}(x,x) + \frac{i}{2}\mathrm{Tr}\ln\left[B(G)\right] \\ &\quad +i\frac{\lambda}{6N_s}\int_x\int_y I(x,y;G)\langle\varphi_a(x)\rangle G_{ab}(x,y)\langle\varphi_b(y)\rangle \\ &\quad -i\,h^2\frac{N_f}{2}\int_x\int_y \mathrm{tr}\left[D(x,y)D(y,x)\right]G_{aa}(x,y) \end{aligned} \tag{3.44}$$

where the trace acts on Dirac space and [Ber05]

$$B(x,y;G) = \delta^{(4)}(x-y) + i\frac{\lambda}{6N_s}G_{ab}(x,y)G_{ab}(x,y) \tag{3.45}$$

and

$$I(x,y;G) = \frac{\lambda}{6N_s}G_{ab}(x,y)G_{ab}(x,y) - i\frac{\lambda}{6N_s}\int_z I(x,z;G)G_{ab}(z,y)G_{ab}(z,y)\,, \tag{3.46}$$

which encodes the infinite sum of boson 2PI diagrams without macroscopic field insertions, cf. Fig. 3.1. The expression (3.46) can be, analog to (3.7), decomposed into a part I_F, and a part I_ρ, see below for a representation in spatial Fourier space.

With (3.44)–(3.46) we are now able to determine the self-energies via (2.11) and (2.12) of the fermion and boson fields respectively. In Fig. 3.2 we display the topology of the Feynman diagrams for the fermion (left) and boson (right) self-energy contributions which result due to the fermion-boson loop in Fig. 3.1. These self-energy contributions play an essential role in our studies. In the equations of motion, see Sec. 3.2, the Fourier components of the self-energies enter, therefore we will present in the following all expressions in the spatial Fourier space representation. A detailed calculation of the fermion parts of the self-energies can be found in Appendix E.

We obtain for the statistical parts of the fermion self-energy (3.8)

$$\begin{aligned}C_S(t,t';\mathbf{p}) &= -h^2\int_{\mathbf{q}}\Big\{F_S(t,t';\mathbf{q})\left[F^\phi_\parallel(t,t';\mathbf{p}-\mathbf{q}) + (N_s-1)F^\phi_\perp(t,t';\mathbf{p}-\mathbf{q})\right] \\ &\quad -\frac{1}{4}\rho_S(t,t';\mathbf{q})\left[\rho^\phi_\parallel(t,t';\mathbf{p}-\mathbf{q}) + (N_s-1)\rho^\phi_\perp(t,t';\mathbf{p}-\mathbf{q})\right]\Big\}\,, \end{aligned} \tag{3.47}$$

$$\begin{aligned}C^\mu_V(t,t';\mathbf{p}) &= -h^2\int_{\mathbf{q}}\Big\{F^\mu_V(t,t';\mathbf{q})\left[F^\phi_\parallel(t,t';\mathbf{p}-\mathbf{q}) + (N_s-1)F^\phi_\perp(t,t';\mathbf{p}-\mathbf{q})\right] \\ &\quad -\frac{1}{4}\rho^\mu_V(t,t';\mathbf{q})\left[\rho^\phi_\parallel(t,t';\mathbf{p}-\mathbf{q}) + (N_s-1)\rho^\phi_\perp(t,t';\mathbf{p}-\mathbf{q})\right]\Big\}\,, \end{aligned} \tag{3.48}$$

Figure 3.2: Left: fermion self-energy contribution: "fermion-boson loop". Right: fermion part of the boson self-energy contribution. The dotted lines correspond to fermion propagators, the solid lines represent boson propagators.

$$\begin{aligned} C_T^{0i}(t,t';\mathbf{p}) \;=\; -h^2\int_{\mathbf{q}}\Big\{ & F_T^{0i}(t,t';\mathbf{q})\left[F_\parallel^\phi(t,t';\mathbf{p}-\mathbf{q})+(N_s-1)F_\perp^\phi(t,t';\mathbf{p}-\mathbf{q})\right] \\ & -\frac{1}{4}\rho_T^{0i}(t,t';\mathbf{q})\left[\rho_\parallel^\phi(t,t';\mathbf{p}-\mathbf{q})+(N_s-1)\rho_\perp^\phi(t,t';\mathbf{p}-\mathbf{q})\right]\Big\}, \end{aligned} \tag{3.49}$$

and for the spectral parts

$$\begin{aligned} A_S(t,t';\mathbf{p}) \;=\; -h^2\int_{\mathbf{q}}\Big\{ & F_S(t,t';\mathbf{q})\left[\rho_\parallel^\phi(t,t';\mathbf{p}-\mathbf{q})+(N_s-1)\rho_\perp^\phi(t,t';\mathbf{p}-\mathbf{q})\right] \\ & +\rho_S(t,t';\mathbf{q})\left[F_\parallel^\phi(t,t';\mathbf{p}-\mathbf{q})+(N_s-1)F_\perp^\phi(t,t';\mathbf{p}-\mathbf{q})\right]\Big\}, \end{aligned} \tag{3.50}$$

$$\begin{aligned} A_V^\mu(t,t';\mathbf{p}) \;=\; -h^2\int_{\mathbf{q}}\Big\{ & F_V^\mu(t,t';\mathbf{q})\left[\rho_\parallel^\phi(t,t';\mathbf{p}-\mathbf{q})+(N_s-1)\rho_\perp^\phi(t,t';\mathbf{p}-\mathbf{q})\right] \\ & +\rho_V^\mu(t,t';\mathbf{q})\left[F_\parallel^\phi(t,t';\mathbf{p}-\mathbf{q})+(N_s-1)F_\perp^\phi(t,t';\mathbf{p}-\mathbf{q})\right]\Big\}, \end{aligned} \tag{3.51}$$

$$\begin{aligned} A_T^{0i}(t,t';\mathbf{p}) \;=\; -h^2\int_{\mathbf{q}}\Big\{ & F_T^{0i}(t,t';\mathbf{q})\left[\rho_\parallel^\phi(t,t';\mathbf{p}-\mathbf{q})+(N_s-1)\rho_\perp^\phi(t,t';\mathbf{p}-\mathbf{q})\right] \\ & +\rho_T^{0i}(t,t';\mathbf{q})\left[F_\parallel^\phi(t,t';\mathbf{p}-\mathbf{q})+(N_s-1)F_\perp^\phi(t,t';\mathbf{p}-\mathbf{q})\right]\Big\}. \end{aligned} \tag{3.52}$$

Analog for the statistical part of the boson self-energy (3.9) we get

$$\begin{aligned}
\Pi^F_{ab}(t,t';\mathbf{p}) = \\
&-\frac{\lambda}{3N_s}\int_{\mathbf{q}}\Big\{\Big(F^\phi_{ab}(t,t';\mathbf{p}-\mathbf{q})+\delta(\mathbf{p}-\mathbf{q})\langle\varphi_a(t)\rangle\langle\varphi_b(t')\rangle\Big)\,I_F(t,t';\mathbf{q}) \\
&\qquad -\frac{1}{4}\rho^\phi_{ab}(t,t';\mathbf{p}-\mathbf{q})I_\rho(t,t';\mathbf{q}) \\
&\qquad +P_F(t,t';\mathbf{q})F^\phi_{ab}(t,t';\mathbf{p}-\mathbf{q})-\frac{1}{4}P_\rho(t,t';\mathbf{q})\rho^\phi_{ab}(t,t';\mathbf{p}-\mathbf{q})\Big\} \\
&-4h^2N_f\delta_{ab}\int_{\mathbf{q}}\Big\{F^\mu_V(t,t';\mathbf{q})F_{V,\mu}(t,t';\mathbf{p}-\mathbf{q})-F_S(t,t';\mathbf{q})F_S(t,t';\mathbf{p}-\mathbf{q}) \\
&\qquad -F^{0i}_T(t,t';\mathbf{q})F^{0i}_T(t,t';\mathbf{p}-\mathbf{q}) \\
&\qquad -\frac{1}{4}\Big[\rho^\mu_V(t,t';\mathbf{q})\rho_{V,\mu}(t,t';\mathbf{p}-\mathbf{q})-\rho_S(t,t';\mathbf{q})\rho_S(t,t';\mathbf{p}-\mathbf{q}) \\
&\qquad\quad -\rho^{0i}_T(t,t';\mathbf{q})\rho^{0i}_T(t,t';\mathbf{p}-\mathbf{q})\Big]\Big\}\,, \qquad (3.53)
\end{aligned}$$

and for the spectral part

$$\begin{aligned}
\Pi^\rho_{ab}(t,t';\mathbf{p}) = \\
&-\frac{\lambda}{3N_s}\int_{\mathbf{q}}\Big\{\Big(F^\phi_{ab}(t,t';\mathbf{p}-\mathbf{q})+\delta(\mathbf{p}-\mathbf{q})\langle\varphi_a(t)\rangle\langle\varphi_b(t')\rangle\Big)\,I_\rho(t,t';\mathbf{q}) \\
&\qquad +\rho^\phi_{ab}(t,t';\mathbf{p}-\mathbf{q})I_F(t,t';\mathbf{q}) \\
&\qquad +P_\rho(t,t';\mathbf{q})F^\phi_{ab}(t,t';\mathbf{p}-\mathbf{q})+P_F(t,t';\mathbf{q})\rho^\phi_{ab}(t,t';\mathbf{p}-\mathbf{q})\Big\} \\
&-8h^2N_f\delta_{ab}\int_{\mathbf{q}}\Big\{\rho^\mu_V(t,t';\mathbf{q})F_{V,\mu}(t,t';\mathbf{p}-\mathbf{q})-\rho_S(t,t';\mathbf{q})F_S(t,t';\mathbf{p}-\mathbf{q}) \\
&\qquad -\rho^{0i}_T(t,t';\mathbf{q})F^{0i}_T(t,t';\mathbf{p}-\mathbf{q})\Big\}\,. \qquad (3.54)
\end{aligned}$$

The local contributions read

$$\Pi^{\text{local}}_\parallel(t)=\frac{\lambda}{6N_s}\int\frac{d^3p}{(2\pi)^3}\Big[3\,F^\phi_\parallel(t,t;|\mathbf{p}|)+(N_s-1)F^\phi_\perp(t,t;|\mathbf{p}|)\Big] \qquad (3.55)$$

and

$$\Pi^{\text{local}}_\perp(t)=\frac{\lambda}{6N_s}\int\frac{d^3p}{(2\pi)^3}\Big[F^\phi_\parallel(t,t;|\mathbf{p}|)+(N_s+1)F^\phi_\perp(t,t;|\mathbf{p}|)\Big] \qquad (3.56)$$

In (3.55) and (3.56) we used the decomposition of (3.46) into their real and imaginary parts which have in spatial Fourier space the following expressions

$$\begin{aligned} I_F(t,t';\mathbf{p}) &= \frac{\lambda}{6N_s}\int_{\mathbf{q}}\Bigg\{F^{\phi}_{ab}(t,t';\mathbf{p}-\mathbf{q})F^{\phi}_{ba}(t,t';\mathbf{q}) \\ &\quad -\frac{1}{4}\rho^{\phi}_{ab}(t,t';\mathbf{p}-\mathbf{q})\rho^{\phi}_{ba}(t,t';\mathbf{q}) - \int_0^t dt'' I_\rho(t,t'';\mathbf{p}) \\ &\quad \times\left[F^{\phi}_{ab}(t'',t';\mathbf{p}-\mathbf{q})F^{\phi}_{ba}(t'',t';\mathbf{q}) - \frac{1}{4}\rho^{\phi}_{ab}(t'',t';\mathbf{p}-\mathbf{q})\rho^{\phi}_{ba}(t'',t';\mathbf{q})\right] \\ &\quad +2\int_0^{t'} dt'' I_F(t,t'';\mathbf{p})F^{\phi}_{ab}(t'',t';\mathbf{p}-\mathbf{q})\rho^{\phi}_{ba}(t'',t';\mathbf{q})\Bigg\}, \end{aligned} \tag{3.57}$$

and

$$\begin{aligned} I_\rho(t,t';\mathbf{p}) &= \frac{\lambda}{3N_s}\int_{\mathbf{q}}\Bigg\{F^{\phi}_{ab}(t,t';\mathbf{p}-\mathbf{q})\rho^{\phi}_{ba}(t,t';\mathbf{q}) \\ &\quad -\int_{t'}^t dt'' I_\rho(t,t'';\mathbf{p})F^{\phi}_{ab}(t'',t';\mathbf{p}-\mathbf{q})\rho^{\phi}_{ba}(t'',t';\mathbf{q})\Bigg\}. \end{aligned} \tag{3.58}$$

The functions $P_{F,\rho}(t,t';\mathbf{p})$ encode the interaction of the fluctuations with the macroscopic field, they have the following expressions

$$\begin{aligned} P_F(t,t';\mathbf{p}) = -\frac{\lambda}{3N_s}\Bigg\{ & H_F(t,t';\mathbf{p}) \\ & -\int_0^t dt''\ [H_\rho(t,t'';\mathbf{p})I_F(t'',t';\mathbf{p}) + I_\rho(t,t'';\mathbf{p})H_F(t'',t';\mathbf{p})] \\ & +\int_0^{t'} dt''\ [H_F(t,t'';\mathbf{p})I_\rho(t'',t';\mathbf{p}) + I_F(t,t'';\mathbf{p})H_\rho(t'',t';\mathbf{p})] \\ & -\int_0^t dt''\int_0^{t'} ds\, I_\rho(t,t'';\mathbf{p})H_F(t'',s;\mathbf{p})I_\rho(s,t';\mathbf{p}) \\ & +\int_0^t dt''\int_0^{t''} ds\, I_\rho(t,t'';\mathbf{p})H_\rho(t'',s;\mathbf{p})I_F(s,t';\mathbf{p}) \end{aligned}$$

$$+\int_0^{t'} dt'' \int_{t''}^{t'} ds\, I_F(t,t'';\mathbf{p}) H_\rho(t'',s;\mathbf{p}) I_\rho(s,t';\mathbf{p}) \Bigg\}, \tag{3.59}$$

and

$$\begin{aligned} P_\rho(t,t';\mathbf{p}) &= -\frac{\lambda}{3N_s}\Bigg\{ H_\rho(t,t';\mathbf{p}) \\ &\quad -\int_{t'}^{t} dt''\, \left[H_\rho(t,t'';\mathbf{p}) I_\rho(t'',t';\mathbf{p}) + I_\rho(t,t'';\mathbf{p}) H_\rho(t'',t';\mathbf{p})\right] \\ &\quad +\int_{t'}^{t} dt'' \int_{t'}^{t''} ds\, I_\rho(t,t'';\mathbf{p}) H_\rho(t'',s;\mathbf{p}) I_\rho(s,t';\mathbf{p}) \Bigg\}, \end{aligned} \tag{3.60}$$

with the functions

$$H_F(t,t';\mathbf{p}) = -\phi(t) F_\parallel^\phi(t,t';\mathbf{p}) \phi(t')\,, \tag{3.61}$$

$$H_\rho(t,t';\mathbf{p}) = -\phi(t) \rho_\parallel^\phi(t,t';\mathbf{p}) \phi(t')\,. \tag{3.62}$$

In calculating the P-functions numerically one is confronted with "nested" memory integrals due to the double time integral in (3.59) and (3.60), this can be either numerically expensive or very slow, see Appendix F.

Finally we have to specify the second term on the right-hand side in Eq. (3.43), it is given by

$$\frac{\delta\Gamma_2[\phi,G,D]}{\delta\,\phi(t)} = \frac{\lambda}{3N_s}\int_0^t dt' \int_{\mathbf{p}} \Big[I_\rho(t,t';|\mathbf{p}|) F_\parallel^\phi(t,t';|\mathbf{p}|) + I_F(t,t';|\mathbf{p}|) \rho_\parallel^\phi(t,t';|\mathbf{p}|) \Big]\, \phi(t')\,, \tag{3.63}$$

with the functions I_F and I_ρ defined above.

Now we have all the ingredients which enter the equations of motion. Before we proceed with the specification of the initial conditions we consider the characteristics of the chiral symmetric theory of the model (3.1).

3.3.2 $SU(2)_L \times SU(2)_R$ Symmetry

As stated in the beginning of Sec. 3.1 we will also consider the chirally invariant version of the model (3.1). Therefore we have to discuss the corresponding differences of the equations of motions and self-energies introduced so far. Since all equations are obtained by neglecting terms in the above equations we will not list the reduced equations and just explain the differences.

If the expectation value $\phi(x)$ of the scalar fields and the fermion mass m_ψ vanish the model (3.1) becomes $SU(2)_L \times SU(2)_R$ symmetric. This simplifies the equations of motion enormously. In particular, it leads to vanishing scalar and tensor components of the Lorentz decomposition (3.12). Thus we are left with the equations of motion (3.31), (3.32), (3.35) and (3.36) with $F_S(t,t';\mathbf{p}) = 0$ and $F_T(t,t';\mathbf{p}) = 0$ at all times. Consequently the corresponding self-energies (3.47), (3.49), (3.50) and (3.52) vanish, too. Since $\phi(x) = 0$ we have no spontaneously broken symmetry, hence the components of the boson propagator (3.10) are all equal and we can write $G_{ab} = \delta_{ab} G$. This transfers to the self-energies. Consequently we can omit the subscripts $\parallel$ and $\perp$ and write for the statistical two-point function $F_\parallel^\phi = F_\perp^\phi = F_\phi$ and analog for the spectral functions as well as for the self-energies. Accordingly we simply write $M(t)$ for the effective masses in (3.42). Further, because of $\phi(x) = 0$, the functions $P_F(t,t';\mathbf{p})$ and $P_\rho(t,t';\mathbf{p})$ vanish, cf. (3.59) and (3.60), whereas the functions $I_F(t,t';\mathbf{p})$ and $I_\rho(t,t';\mathbf{p})$ remain the same.

In summary all expressions introduced so far define the chiral symmetric theory as long as we set $\phi(x) = 0$ and $m_\psi = 0$. This holds also for the initial conditions which we will consider in Sec. 3.4.

Nomenclature

In Chapter 4 and 5 we compare different forms of the evolution equations which has implications on the dynamics. It is convenient to define names for different approximations of the above equations of motion, for this reason this little subsection is invented.

If we consider the complete equations of motions presented above in Sec. 3.2 and 3.3 without any further restrictions, we speak about the 2PI$^+$ approximation (or just 2PI$^+$). If we only neglect the fermion-boson loop[5] shown in Fig. 3.2 we speak about the 2PI$^-$ approximation (2PI$^-$). In the latter case the macroscopic field takes part in the full nonlinear dynamics in the boson sector, this leads to a certain evolution of $\phi(t)$ which influences the fermion dynamics via the time dependent mass term $\sim g\phi(t)$. We will denote this fermion-boson interaction with "tree-level" interaction. For some considerations of the fermion dynamics it it useful to assume a simple periodic behavior of the macroscopic field, like a cosine, in this case together with neglecting the fermion-boson loop in Fig. 3.2 the equations of motion of the fermion two-point functions acquire the form of a Dirac equation with a simple time dependent mass. We will call this case the "Dirac-type" approximation.

[5]Whenever we talk about a fermion-boson loop it is meant to be the one in Fig. 3.2. Sometimes we just say "loop" or quantum correction, the context should not allow for confusion.

3.4 Initial Conditions

Nonequilibrium dynamics is an initial value problem. As described in Sec. 2.1 the initial values of the two-point correlation functions parametrize the initial Gaussian density matrix of the system. We will consider two different types of instabilities which require distinct set-ups. These two set-ups are defined by the initial value of ϕ and the shape of the classical potential. Accordingly the form of the initial two-point functions are the same, however with a dependence on ϕ.

In the following we will consider the initial conditions for the two-point functions and discuss afterwards, separately, the special configurations leading to the different instabilities.

The initial conditions for the boson and fermion spectral functions are completely determined by their commutation and anti-commutation relation, respectively. We will denote the initial time by $t = 0$. Since the fermion equations of motion are of first order and the boson equations are of second order we have in the case of the fermions for each flavor

$$\gamma_0 \rho(t,t;|\mathbf{p}|) = i\,, \tag{3.64}$$

which yields for the different Lorentz components

$$\begin{aligned}
\rho_S(t,t;|\mathbf{p}|) &= 0\,, && (3.65)\\
\rho_V^0(t,t;|\mathbf{p}|) &= i\,, && (3.66)\\
\rho_V(t,t;|\mathbf{p}|) &= 0\,, && (3.67)\\
\rho_T(t,t;|\mathbf{p}|) &= 0\,, && (3.68)
\end{aligned}$$

whereas for the boson spectral function we have

$$\rho_\phi(t,t;|\mathbf{p}|) = 0\,, \quad \partial_t \rho_\phi(t,t';|\mathbf{p}|)|_{t=t'} = 1\,. \tag{3.69}$$

Note that the conditions (3.64)–(3.69) actually are valid for all times t.

The initial conditions for statistical functions are in general free to choose as long as they correspond to a parametrization of an Gaussian initial density matrix, cf. Sec. 2.1. We employ initial free-field conditions with a given initial particle occupation number. The free-field Dirac matrix for F is (we omit flavor and Dirac indices)

$$F(t,t;\mathbf{p}) = \frac{-\boldsymbol{\gamma}\cdot\mathbf{p} + M_\psi(t)}{\sqrt{\mathbf{p}^2 + M_\psi^2(t)}} \left(\frac{1}{2} - n_\psi(t;\mathbf{p})\right)\,, \tag{3.70}$$

for a given fermion occupation number n_ψ which corresponds in thermal equilibrium to the Fermi-Dirac distribution. The Lorentz components are obtained by

projection, this leads to

$$F_S(t,t';|\mathbf{p}|)|_{t=t'=0} = \frac{M_\psi(t=0)}{\sqrt{|\mathbf{p}|^2+M_\psi^2(t=0)}}\left(\frac{1}{2}-n_\psi(t=0;|\mathbf{p}|)\right), \quad (3.71)$$

$$F_V^0(t,t';|\mathbf{p}|)|_{t=t'=0} = 0, \quad (3.72)$$

$$F_V(t,t';|\mathbf{p}|)|_{t=t'=0} = \frac{|\mathbf{p}|}{\sqrt{|\mathbf{p}|^2+M_\psi^2(t=0)}}\left(\frac{1}{2}-n_\psi(t=0;|\mathbf{p}|)\right), \quad (3.73)$$

$$F_T(t,t';|\mathbf{p}|)|_{t=t'=0} = 0, \quad (3.74)$$

with M_ψ given in Eq. (3.5). For the bosonic statistical two-point function we also employ free-field expressions, i.e. at initial time

$$F^\phi_{\parallel/\perp}(t,t';|\mathbf{p}|)|_{t=t'=0} = \frac{1}{\epsilon_{\parallel/\perp}(t=0;|\mathbf{p}|)}\left(\frac{1}{2}+n^\phi_{\parallel/\perp}(t=0;|\mathbf{p}|)\right), \quad (3.75)$$

$$\partial_t F^\phi_{\parallel/\perp}(t,t';|\mathbf{p}|)|_{t=t'=0} = 0, \quad (3.76)$$

$$\partial_t\partial_{t'} F^\phi_{\parallel/\perp}(t,t';|\mathbf{p}|)|_{t=t'=0} = \epsilon_{\parallel/\perp}(t=0;|\mathbf{p}|)\left(\frac{1}{2}+n^\phi_{\parallel/\perp}(t=0;|\mathbf{p}|)\right), \quad (3.77)$$

with $\epsilon_{\parallel/\perp}(t,|\mathbf{p}|)$ as an effective quasi particle energy defined by [Ber05]

$$\epsilon_{\parallel/\perp}(t,|\mathbf{p}|) \equiv \sqrt{\left.\frac{\partial_t\partial_{t'}F^\phi_{\parallel/\perp}(t,t';|\mathbf{p}|)}{F^\phi_{\parallel/\perp}(t,t';|\mathbf{p}|)}\right|_{t=t'}}. \quad (3.78)$$

It is important to note that (3.77) is needed in order to fully specify the density matrix. The right hand side of (3.77) is obtained by using the free-field equation of motion together with (3.75). We choose a vacuum initial state so that $n_\psi = n^\phi_{\parallel/\perp} = 0$.

In the following two sections we present the special initial conditions for the macroscopic field together with the specific shape of the classical potential responsible for the nature of the instability.

Spinodal Instability

The spinodal instability is induced via a so-called quench [AST04], i.e. at initial time the classical potential has positive curvature with a vanishing expectation value, $\phi(t=0)=0$, see left-hand side of Fig. 3.3, and in the next time step a sign flip in front of the boson mass squared m^2 renders the shape of the potential in such a way that a region with negative curvature appears, see the right-hand side of Fig. 3.3. This corresponds to supercooling a system in condensed matter physics or

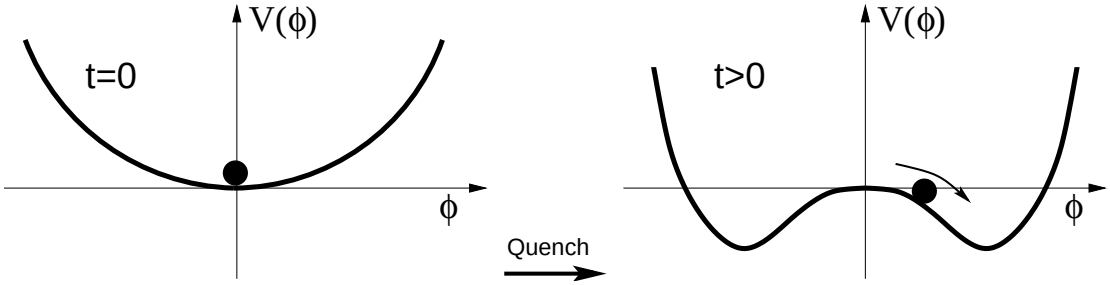

Figure 3.3: Sketch of the initial situation in the case of a spinodal instability. The ball corresponds to the value of the macroscopic field. For $t > 0$ the potential acquires a region with negative curvature which leads to exponentially growing modes, cf. Sec. 4.1. For certain initial conditions $\phi(t > 0)$ can become nonvanishing.

to situations which can appear in early time cosmology at the end of the inflationary era in certain inflation models like hybrid inflation [Lin94, BKP07]. The sign flip is in our case introduced by hand.

The local effective boson mass at initial time becomes

$$\begin{aligned} M_\parallel^2(t=0) &= m^2 + \frac{\lambda}{2N_s}\phi^2(t{=}0)\,, \\ M_\perp^2(t=0) &= m^2 + \frac{\lambda}{6N_s}\phi^2(t{=}0)\,, \end{aligned} \tag{3.79}$$

$$\begin{aligned} M_\parallel^2(t>0) &= -m^2 + \frac{\lambda}{2N_s}\phi^2(t) \\ &+\frac{\lambda}{6N_s}\int_{\mathbf{p}}\left[3\left(F_\parallel^\phi(t,t;|\mathbf{p}|) - \frac{1}{2\epsilon_\parallel(0;\mathbf{p})}\right) + (N_s{-}1)\left(F_\perp^\phi(t,t;|\mathbf{p}|) - \frac{1}{2\epsilon_\perp(0;\mathbf{p})}\right)\right], \end{aligned} \tag{3.80}$$

$$\begin{aligned} M_\perp^2(t>0) &= -m^2 + \frac{\lambda}{6N_s}\phi^2(t) \\ &+\frac{\lambda}{6N_s}\int_{\mathbf{p}}\left[\left(F_\parallel^\phi(t,t;|\mathbf{p}|) - \frac{1}{2\epsilon_\parallel(0;\mathbf{p})}\right) + (N_s{+}1)\left(F_\perp^\phi(t,t;|\mathbf{p}|) - \frac{1}{2\epsilon_\perp(0;\mathbf{p})}\right)\right], \end{aligned}$$

where we subtracted the quadratically divergent terms in the momentum integrals in (3.80) which ensures with $\phi(t = 0^+) \simeq 0$ for a vacuum initial state $M_{\parallel/\perp}^2(t = 0^+) = -m^2$. We set m as our scale in each simulation starting with a quench.

In Sec. 4.1 we consider the $SU(2)_L \times SU(2)_R$ symmetric theory which requires $\phi(t) = 0$ for all times t. The above listed initial conditions acquire the corresponding values.

In Sec. 4.2 the restriction to $SU(2)_L \times SU(2)_R$ symmetry is absent. In this case the initial conditions require some explanation. The symmetry of the evolution equation of the macroscopic field, Eq. (3.43), without fermion backreaction term $\sim F_S$ keeps $\phi(t)$ at its initial value $\phi(t = 0) = 0$, as long as there is no symmetry breaking mechanism. Then the whole simulation would be exactly the same as in Sec. 4.1[6]. If one is interested in the "rolling down the potential" of the macroscopic field and the phenomena connected with this evolution one is forced to slightly change the initial conditions in order to have a broken symmetry and be able to observe a nonvanishing macroscopic field evolution. However, so far in this discussion we neglected the fermion backreaction which naturally arises. It does not vanish for massive fermions and thus would lead to symmetry breaking which causes $\phi(t > 0) \neq 0$ automatically. This could be in general induced dynamically by a time dependent mass due to another (third) field, or directly by a nonvanishing fermion bare mass m_ψ[7]. In our approximation only the latter case is possible. The important thing is that we do not have to introduce by hand an initial displacement or initial velocity in order to have $\phi(t > 0) \neq 0$, which is often used because of the lack of backreaction [GBMR00, TBV00]. We emphasize that due to the subtraction of the leading order divergence in the fermion backreaction, cf. the statement below Eq. (3.43), the latter vanishes at $t = 0$. This represents the fact that there should be no backreaction if no fermions are created.

That means if F_S does not vary in time there is no backreaction at all and thus no symmetry breaking. The scalar component of the fermion statistical two-point function indeed does not vary (starting with $\phi(t = 0) = 0$) if there is no loop-correction. Consequently, ϕ remains zero if the fermion-boson loop is neglected and hence there is no particle production at all. We will consider this situation in Sec. 4.2 in detail.

If we want to compare the influence of the tree-level interaction with the loop-correction in the case of the initial condition described above we need to employ an initial displacement or initial velocity, otherwise the loop always dominates[8]. Therefore we will consider in Sec. 4.2 a few cases with an initial displacement and vanishing velocity in order to learn about the effect of the fermion-boson loop compared to the tree-level term in the equation of motion. The actual displacement we chose will be presented below in connection with the description of the emerging phenomena.

[6]Note that boson fluctuations do not push $\phi(t)$ away from zero since they are always multiplied by $\phi(t)$ in Eq. (3.43).

[7]If fermions have a nonvanishing mass m_ψ, the classical potential acquires a linear term $\sim \bar{\psi}\psi$ and the Z_2 symmetry is broken. This leads to a non-vanishing $\phi(t > 0)$. Hence the initial displacement is generated naturally and does not have to be put in by hand.

[8]Since in this case the tree-level term vanishes the domination of the loop is trivial.

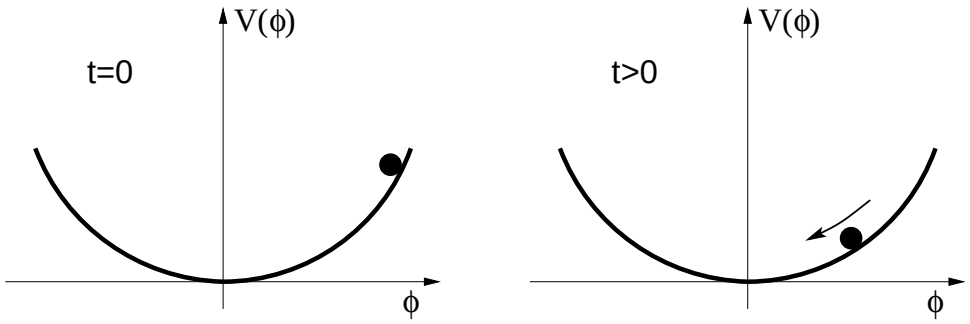

Figure 3.4: Sketch of the initial situation in the case of parametric resonance. The ball corresponds to the value of the macroscopic field. For $t = 0$ (left) some nonzero initial value for ϕ is chosen without any velocity. For $t > 0$ potential energy converts into kinetic energy and the field "rolls down" the potential before it starts to oscillate around the minimum.

Parametric Resonance

In the case of parametric resonance the potential has a symmetric shape as sketched in Fig. 3.4 and $\phi(t = 0)$ has some nonvanishing value. The resonance effect arises due to the subsequent oscillating macroscopic field $\phi(t)$ with a certain amplitude and frequency. We employ chaotic inflation [Lin83] initial conditions in which the macroscopic field has a large initial amplitude and all energy is stored in ϕ. We choose the positive value[9]

$$\phi(t=0) = \phi_0 \sqrt{\frac{6\,N_s}{\lambda}}\,, \qquad \partial_t \phi(t)|_{t=0} = 0\,, \tag{3.81}$$

with a dimensionful parameter $\phi_0 \sim \mathcal{O}(1)$ and a small self-coupling λ. Since in our theory the frequency of the macroscopic field depends on its amplitude, higher values of ϕ_0 lead to a higher frequency which in turn causes a faster development of an instability. Accordingly ϕ_0 can be used as a scale as it is done in Chapter 5. In Sec. F.2 of Appendix F we show simulation results which confirm the reliability of this choice. The precise values of the self-coupling will be given when we present our results. In the parametric resonance case the masses shown in (3.80) have the same form except for the sign of the bare mass squared. The initial conditions presented in this section will be applied in Chapter 5.

[9] A negative value would also be possible because of Z_2-symmetry.

3.5 Particle Number

If one is interested in the production of a certain kind of particle one should clarify what is meant by "particle number". In a quantum field theory there exists no clear uniquely defined expression which is associated to a particle number. Field excitations with an on-shell energy-momentum relation are interpreted as "quasi-particles" [PS95], therefore typically expectation values of particle (occupation) number operators are used in order to describe the particle content of a given system.

A famous commonly used way to define an occupation number out of equilibrium is given by a Bogoliubov transformation of a mode function basis [CH08, BD82, GPS04]. However, also those approaches are not rigorously uniquely well defined. Nevertheless it is common to use such a concept if one is interested in the evolution of quantum fields out of equilibrium, as was done for instance in [BdVH$^+$95, BHP97, BHP98, GK00]. The quality of a given definition is usually measured by how well one can describe the results within a quasi-particle picture.

In our case we have to deal with two-point functions and we are not restricted to mean-field type dynamics. However, we choose initial conditions which are connected to free-field (equilibrium) expressions (3.71)–(3.74) and (3.75)–(3.77) in order to have a link to an occupation number. To define a corresponding quantity out of equilibrium we assume that this connection should hold at each time point, which then defines an occupation number far from equilibrium, i.e. far from a Fermi-Dirac or Bose-Einstein distribution. Eventually, due to the dynamical evolution, the system should approach thermal equilibrium and thus the particle distribution should converge to a Fermi-Dirac or Bose-Einstein distribution. That this concept works was shown in Ref. [BBS03, BC01]. However, in Refs. [BBS03, BC01] the authors did not consider instabilities at the beginning of the evolution which typically drive the system into a quasi-stationary regime and thus delay the thermalization. Hence one might not be able to observe an equilibrium distribution on numerical accessible time scales given in this work.

To find an expression of an occupation number for fermions with (3.71)–(3.74) we have so solve these equations for n_ψ. A possible way to solve (3.73) and (3.71) is given by multiplying (3.73) with $|\mathbf{p}|$ and (3.71) with $M_\psi(t)$ and sum the two equations. Accordingly we obtain

$$n_\psi(t,|\mathbf{p}|) = \frac{1}{2} - \frac{1}{\sqrt{|\mathbf{p}|^2 + M_\psi^2(t)}}\left[|\mathbf{p}| F_V(t,t;|\mathbf{p}|) + M_\psi(t) F_S(t,t;|\mathbf{p}|)\right]. \tag{3.82}$$

This expression agrees formally with the one used in [GK00] in an approximation which corresponds to solving the Dirac equation with a time dependend macroscopic background field within a mode function analysis. The equivalence between both definitions is shown in Appendix C. Note that, since the equation of motion of

$F_V(t,t;|\mathbf{p}|)$ and $F_S(t,t;|\mathbf{p}|)$ contain the next-to-leading order quantum corrections, the definition (3.82) is not restricted to the mean-field case. Rather one is able to study directly the influence of the quantum corrections on the evolution of n_ψ. This is what we will do in the next two chapters. One might argue that the emergence of the leading order mass term in (3.82) is a relic of the mean-field approximation and thus one should not use this expression for an approximation beyond leading order, but rather switch to a definition where only correlation functions determine the particle number[10]. However, in all simulations we performed we found that both definitions yield the same results. To get an understanding of the quantitative influence of higher order quantum correction to the fermion dynamics, it is reasonable to study (3.82). We explicitly mention that for chiral fermions the definition (3.82) reduces to

$$n_\psi(t,|\mathbf{p}|) \;=\; \frac{1}{2} - F_V(t,t;|\mathbf{p}|)\,. \tag{3.84}$$

In Sec. 4.1 we will consider the model (3.1) in the chiral limit, hence (3.84) plays a central role.

For the boson particle number only one equation exists which connects the equal time correlator with the particle distribution, i.e. (3.75). Therefore we immediately have the definition of $n^{\phi}_{\parallel/\perp}$, namely

$$n^{\phi}_{\parallel/\perp}(t,|\mathbf{p}|) = \epsilon_{\parallel/\perp}(t,|\mathbf{p}|)F^{\phi}_{\parallel/\perp}(t,t;|\mathbf{p}|) - \frac{1}{2}\,. \tag{3.85}$$

Consequently for large occupation numbers, which are typically present if an instability acts, the main characteristics are also given by $F^{\phi}_{\parallel/\perp}(t,t;|\mathbf{p}|) \simeq n^{\phi}_{\parallel/\perp}(t,|\mathbf{p}|)$.

We emphasize that the underlying equations of motion for boson and fermion fields and their numerical solutions presented in this work do not depend on the definition of a particle number.

[10] A possible definition is

$$n_\psi(t,|\mathbf{p}|) = \frac{1}{2} - \mathrm{sign}[F_V(t,t;|\mathbf{p}|)]\,\sqrt{F_V^2(t,t;|\mathbf{p}|) + F_S^2(t,t;|\mathbf{p}|)}\,, \tag{3.83}$$

where we squared (3.73) and (3.71) and build the sum out of the resulting two equations. The solution of the quadratically equation for n_ψ yields (3.83). The signum function accounts for the $\pm$ in front of the square root. F_V determines the sign of $(1/2 - n_\psi(t,|\mathbf{p}|))$, see 3.73. For massless fermions $F_S(t,t;\mathbf{p})$ vanishes and thus (3.83) reduces to the expression used in Refs. [BBS03, BPR09].

3.6 Energy-Momentum Tensor

The energy-momentum tensor, $T_{\mu\nu}(x)$, contains the information about the energy density of a system gained from first principles. The energy density is the "time-time" component $T_{00}(x)$ of $T_{\mu\nu}(x)$. In a spatially homogeneous system the total energy is hence given by

$$\frac{E_{\rm tot}(t)}{V} = T_{00}(t)\,, \tag{3.86}$$

with the spatial volume V. Since the energy-momentum tensor is a conserved quantity it is useful to check the accuracy of the numerical calculation. It is possible to define a classical and quantum (fluctuation) part, which are defined by

$$E_{\rm tot}(t) = E_{\rm class}(t) + E_{\rm fluct}(t) = E_{\rm class}(t) + E_{\phi}(t) + E_{\psi}(t)\,. \tag{3.87}$$

The specific distribution of the energy over different kinds of particles have important implications in applications such as in cosmology or in relativistic heavy-ion collisions.

The calculation of the energy density is presented in detail in Appendix B. Here we merely present the results of both quantities. We find:

Classical part

$$E^{\rm class}(t)/V = \frac{1}{2}\dot{\phi}^2(t) + \frac{1}{2}m_\phi^2\,\phi^2(t) + \frac{\lambda}{4!N_s}\phi^4(t)\,. \tag{3.88}$$

Boson part of quantum fluctuations

$$\begin{aligned} E^{\phi}(t)/V \;=\; & \frac{1}{2}\int\frac{d^3p}{(2\pi)^3}\Big\{\partial_t\,\partial_{t'}\,F_{aa}(t,t';\mathbf{p})|_{t'=t} + \;\mathbf{p}^2\,F_{aa}(t,t;\mathbf{p}) + M^2_{ab}(t)F_{ba}(t,t;\mathbf{p})\Big\} \\ & + \frac{\lambda}{4!N_s}\left(\int\frac{d^3p}{(2\pi)^3}F_{aa}(t,t;\mathbf{p})\right)^2 + \frac{1}{2}\int\frac{d^3p}{(2\pi)^3}I_F(t,t;\mathbf{p}) \\ & + \frac{1}{2}\int\frac{d^3p}{(2\pi)^3}\left[P_F(t,t;\mathbf{p}) + \frac{\lambda}{3N_s}H_F(t,t;\mathbf{p})\right]\,. \end{aligned} \tag{3.89}$$

Fermion part of quantum fluctuations

$$E^{\psi}(t)/V \;=\; -16\int\frac{d^3p}{(2\pi)^3}\Big[|\mathbf{p}|F_V(t,t;|\mathbf{p}|) + M_\psi(t)\,F_S(t,t;|\mathbf{p}|) + R(t,t;|\mathbf{p}|)\Big]\,. \tag{3.90}$$

Here $R(t,t;|\mathbf{p}|)$ represents the right-hand side of the equation of motion for F_V, i.e. the memory integrals.

One can in addition define the pressure by the average of the spatial diagonal components $T_{ii}(x)$, that is

$$\frac{P_{\rm tot}(t)}{V} = \frac{1}{3}\sum_{i=1}^{3} T_{ii}(t)\,. \tag{3.91}$$

Using the same partition as for the energy we have for the pressure

$$P_{\rm tot}(t) = P_{\rm class}(t) + P_{\rm fluct}(t) = P_{\rm class}(t) + P_\phi(t) + P_\psi(t)\,. \tag{3.92}$$

The corresponding results are:

Classical part

$$P^{\rm class}(t)/V = \frac{1}{2}\dot{\phi}^2(t) - \frac{1}{2}m_\phi^2\,\phi^2(t) - \frac{\lambda}{4!N_s}\phi^4(t)\,. \tag{3.93}$$

Boson part of quantum fluctuations

$$\begin{aligned} P^\phi(t)/V \;=\; & \frac{1}{2}\int\frac{d^3p}{(2\pi)^3}\left\{\partial_t\,\partial_{t'}\,F_{aa}(t,t';\mathbf{p})|_{t'=t} + \frac{\mathbf{p}^2}{3}\,F_{aa}(t,t;\mathbf{p}) - M^2_{ab}(t)F_{ba}(t,t;\mathbf{p})\right\} \\ & -\frac{\lambda}{4!N_s}\left(\int\frac{d^3p}{(2\pi)^3}F_{aa}(t,t;\mathbf{p})\right)^2 - \frac{1}{2}\int\frac{d^3p}{(2\pi)^3}I_F(t,t;\mathbf{p}) \\ & -\frac{1}{2}\int\frac{d^3p}{(2\pi)^3}\left[P_F(t,t;\mathbf{p}) + \frac{\lambda}{3N_s}H_F(t,t;\mathbf{p})\right]\,. \end{aligned} \tag{3.94}$$

Fermion part of quantum fluctuations

$$P^\psi(t)/V = 16\int\frac{d^3p}{(2\pi)^3}\frac{|\mathbf{p}|}{3}F_V(t,t;|\mathbf{p}|)\,. \tag{3.95}$$

Knowing the energy and pressure we can determine an equation of state out of equilibrium. That this concept is useful was shown in Ref. [BBW04]. In hydrodynamical applications[11] this concept is standard and used for example to decide whether or not ultra-relativistic particles characterize the system. In cosmology the universe is typically approximated by an ideal dilute gas and the explicit form of the equation of state describes different (thermal) phases of the evolution of the universe after the Big Bang [KT90].

[11] If one considers a diagonal energy-momentum tensor as given above one deals with ideal gas approximations. However, often one is interested in more complex systems in which shear/bulk-viscosity play an important role, like in QCD [Hei05].

Chapter 4

Instability-Induced Fermion Production

Starting from first principles most of the mechanisms known for fermion production are based on an interaction with a macroscopic (background) field. In this chapter we introduce a new mechanism which has its origin in the interaction between quantum fluctuations. We consider initial conditions which lead to a spinodal instability.

In the first part we will consider the production of massless fermions starting with the chirally symmetric version of the model (3.1). Therefore each expectation value of the scalar fields has to be set equal to zero. We will analyze the corresponding dynamics of the boson and fermion fields in separate subsections which does not mean that the dynamics is independent. Actually, the specific dynamics of the boson fields is the basis for the understanding of the mechanism of fermion production in this framework.

Naturally the question arises: what if not all expectation values vanish? This question will be attacked in Sec. 4.2, where we consider the model (3.1) with a nonvanishing expectation value. We additionally allow for a nonvanishing fermion mass parameter m_ψ which breaks chiral symmetry and discuss its consequences. Here as in the first section of this chapter the knowledge of the behavior of the participating bosons is important for the understanding of the fermion dynamics. Again we consider the boson and fermion dynamics in separate subsections. In this Chapter we use m as our scale, cf. Sec. 3.4. Hence, the dimensionful quantities shown in figures have to be understood in units of m.

4.1 Production of Massless Fermions

In this section we are going to investigate the nonequilibrium dynamics of massless Dirac fermions coupled to massive scalar bosons in the chiral model introduced in Sec. 3.3.2. More precisely we study the model in the presence of a spinodal instability (cf. Sec. 2.3). We use vacuum initial conditions where we have to set $m_\psi = 0$ as well as $\phi(t) = 0$ for all times t in the equations of motion in order to

respect chiral symmetry. The detailed initial conditions were reported in Sec. 3.4. We used the energy density defined in Eq. (3.86) to control the accuracy of our numerical calculations. For all shown results the deviation from the initial total energy density did not exceed the order of one percent over the whole simulation time. In most cases, depending on the couplings, the calculations have a deviation of less than one percent. In the following we will discuss the results of the boson and fermion dynamics separately in the next two subsections.

4.1.1 Boson Dynamics

In this subsection we analyze the evolution of the bosonic quantum fields in the chiral model (3.1). The first part is devoted to the unstable early-time evolution. The ensuing part discusses the emergence of power-law behaviors and the phenomenon of self-similarity. The third and last part considers the out-of-equilibrium spectral function as a function of energy.

4.1.1.1 Early-Time Evolution

The evolution starts from a vacuum-like state, thus at very early times almost no fluctuations are present for weak couplings. Accordingly, neglecting the self-energy corrections in (3.38)[1] and (3.42) the initial evolution for the Fourier modes of the boson statistical propagator may be approximately described by

$$\left[\partial_t^2 + \mathbf{p}^2 - m^2\right] F_\phi(t,t';|\mathbf{p}|) \;=\; 0\,. \tag{4.1}$$

Thus modes with $|\mathbf{p}| < m$ exhibit exponential growth and the dominant solution behaves as[2]

$$F_\phi(t,t';\mathbf{p}) \;=\; A_0\, e^{\gamma(\mathbf{p})\,(t+t')}\,, \tag{4.2}$$

where the inverse amplitude $A_0 m \simeq 1/4$ for our initial conditions. The momentum dependent growth rate is given by

$$\gamma(\mathbf{p}) = \sqrt{m^2 - \mathbf{p}^2}\,. \tag{4.3}$$

This classical instability leads to a strongest amplification with rate $\gamma_0 \equiv \gamma(\mathbf{p}=0)$ for the mode with the smallest momentum. The range of momenta $|\mathbf{p}| < m$ for which such a "primary" amplification can be observed is limited. During the subsequent exponential growth the fluctuations become larger and the self-energy corrections

[1] Recall that in the chiral symmetric model $F_\parallel^\phi = F_\perp^\phi = F_\phi$ with identical equations of motion, see Sec.3.3

[2] The complete solution contains as well an exponentially decreasing term which plays a subdominant role.

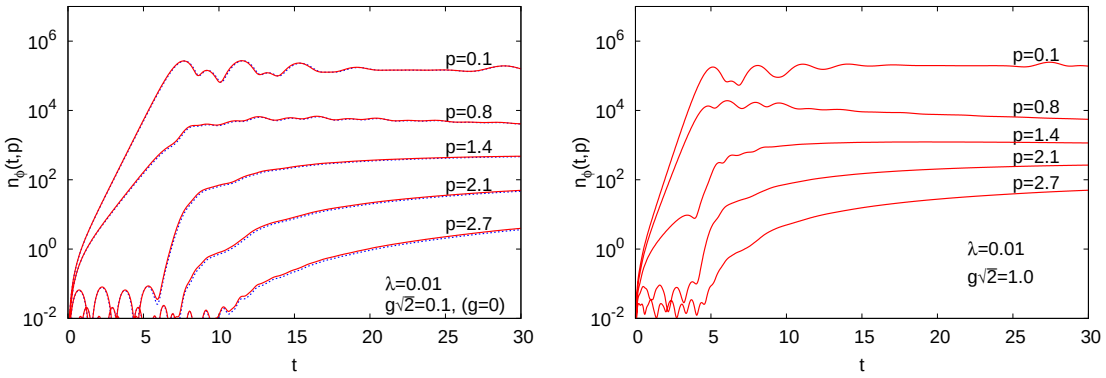

Figure 4.1: Occupation numbers of boson modes as a function of time for given boson self-coupling λ and different values of the Yukawa coupling g to fermions. The left graph shows the results for the purely bosonic theory with no fermions, $g = 0$ (dashed lines), compared to a weakly coupled theory with $g\sqrt{2} = 0.1$ (solid lines). The right graph shows the behavior for $g\sqrt{2} = 1$. Here and in all following figures in this Chapter the quantities are given in units of the mass parameter m.

in (3.38), (3.40) and (3.42) become relevant. These self-energy corrections incorporate non-linear effects, such as scattering and off-shell dynamics. For scalar bosonic models, in the absence of fermions, this has been discussed in detail for parametric resonance as well as spinodal instabilities in Refs. [BS03, Ber05, AST04], respectively.

In the left graph of Fig. 4.1 we show our result for the evolution of different boson occupation number modes (3.85) as a function of time for a scalar self-coupling $\lambda = 10^{-2}$. The graph compares two runs, one without fermions ($g = 0$) and the other with a weak Yukawa coupling of $g\sqrt{2} = 0.1$. On the logarithmic plot one observes that the boson occupation numbers are practically not affected by the weak coupling with fermions. Hence they can be viewed as independent in the weak coupling regime. The time evolution exhibits the characteristic stages explained in detail in the purely bosonic studies of Refs. [BS03, Ber05, AST04]. Low-momentum modes with $|\mathbf{p}| < m$ show primary exponential growth with decreasing rate, whereas higher momentum modes become exponentially amplified at a later ("secondary") stage with faster growth rates due to nonlinearities that were built up by primary modes. After the fast exponential growth period the dynamics slows down considerably. At this stage the nonlinearities are nonperturbatively large, i.e. parametrically $F^{\phi}(t, t; \mathbf{p}) \sim \mathcal{O}(1/\lambda)$ and all processes become of order unity. This happens at the time t_{ϕ}. As a consequence, in this nonperturbative regime higher-order loop diagrams are no longer suppressed by powers of the coupling and a 2PI $1/N$ expansion becomes necessary for a reliable description. The subsequent dynamics approaches a quasi-

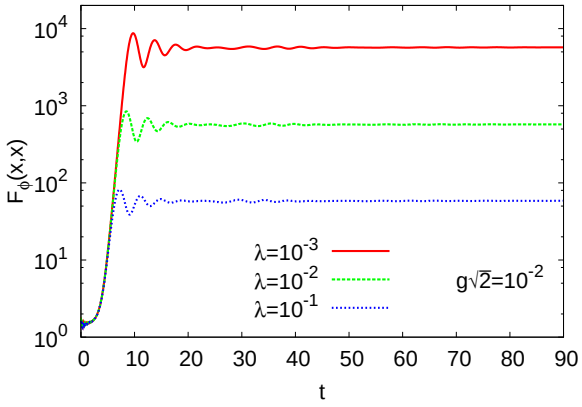

Figure 4.2: Time evolution of the function $F_\phi(x,x)$ for different self-couplings λ. After the unstable evolution the amplitude becomes of the order $1/\lambda$.

stationary evolution phase which will be considered in the next section. Note that parametrically $F^\phi(t,t;\mathbf{p}) \sim \mathcal{O}(1/\lambda)$ means that in a certain momentum range of $F^\phi(t,t;\mathbf{p})$ the amplitude is of the order $1/\lambda$. For lower momenta the amplitude can be larger and for higher momenta smaller. However the integration over all momenta, i.e. $F^\phi(x,x)$, is of the order $1/\lambda$, as can be seen in Fig. 4.2 for different values of the boson self-coupling.

If the Yukawa coupling g is increased in the presence of fermions, the dynamics of the bosons becomes substantially affected and their behavior can no longer be understood separately. This is demonstrated in the right plot of Fig. 4.1 for $g\sqrt{2} = 1$. We emphasize that for $g \approx 1$ it may not be quantitatively justified to neglect higher loop-orders including fermion propagators beyond the two-loop graph taken into account in Γ_2 as shown in Fig. 3.1. However, the observed increase of the growth rates comes from a negative mass-squared contribution for the boson self-energies, which is induced by fermion fluctuations. The very same mechanism operates already for small couplings with $g \ll 1$ and just the quantitative corrections are not sizeable enough in this case to be visible in the figures. The induced negative mass-squared contribution has been analyzed in great detail also in the context of nonperturbative renormalization group studies of this model in thermal equilibrium [BJW99]. In summary the boson dynamics is not much influenced by a weak coupling to fermions whereas sizeable effects occur for stronger couplings. In Sec.4.1.2 we will see that this is not the case for the fermion dynamics. The latter is always significantly affected by highly occupied boson modes, since even for weak Yukawa couplings they induce an exponential growth in the fermion correlation functions as is explained in Sec. 4.1.2.

In the following two paragraphs we present crucial properties of the boson dynam-

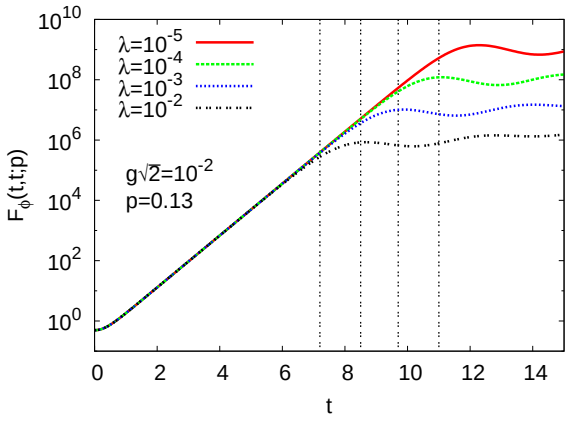

Figure 4.3: Early time evolution of $F_\phi(t,t;|\mathbf{p}|)$ for different couplings λ and fixed g. The different vertical dotted lines correspond to the times $t_\phi = 7.2/m$, $t_\phi = 8.5/m$, $t_\phi = 9.7/m$, $t_\phi = 11.0/m$, respectively.

ics which will be important in Sec. 4.1.2 in order to understand the specific fermion dynamics.

The time scale t_ϕ can be estimated with the condition that the local self-energy contribution ("tadpole") of the masslike term (3.42) becomes of order one. This was done in Ref. [Ber05] in the case of parametric resonance and we can adopt the method. For the evaluation of the momentum integral we take (4.2) and apply a saddle-point approximation around $|\mathbf{p}| = 0$. We find the solution

$$\frac{\lambda(N_s+2)}{6\,N_s}\int\frac{d^3p}{(2\pi)^3}\,F^\phi(t,t;\mathbf{p}) \simeq \lambda\frac{A_0\,e^{2\gamma_0 t}}{32(\gamma_0^{-1}\,\pi\,t)^{3/2}}\,. \tag{4.4}$$

Requiring that the right hand side should be of order one, at $t = t_\phi$, generates an expression for t_ϕ which is

$$t_\phi \simeq \frac{1}{2\gamma_0}\ln\left(\frac{32}{\lambda}\right) + \frac{3}{4\gamma_0}\ln\left(\frac{\pi\,t_\phi}{A_0^{2/3}\,\gamma_0^{-1/3}}\right)\,. \tag{4.5}$$

Using $\gamma_0 = m$ and $A_0 m \simeq 1/4$ we find the solutions $t_\phi \simeq 7.2/m$ for $\lambda = 10^{-2}$, $t_\phi \simeq 8.5/m$ for $\lambda = 10^{-3}$, $t_\phi \simeq 9.7/m$ for $\lambda = 10^{-4}$ and $t_\phi \simeq 11.0/m$ for $\lambda = 10^{-5}$. These solutions agree with the numerical simulations as it is shown in Fig. 4.3.

In the following we consider the evolution of the unequal-time boson spectral function $\rho^\phi(t,t';|\mathbf{p}|)$ and statistical function $F^\phi(t,t';|\mathbf{p}|)$. We will use this to explain in more detail some estimates based on the dominance of contributions coming from the equal-time correlator $F^\phi(t,t;|\mathbf{p}|)$. According to (3.69) the equal-time spectral function $\rho_\phi(t,t;|\mathbf{p}|)$ vanishes identically. The time evolution of $F_\phi(t,t';|\mathbf{p}|)$ in the

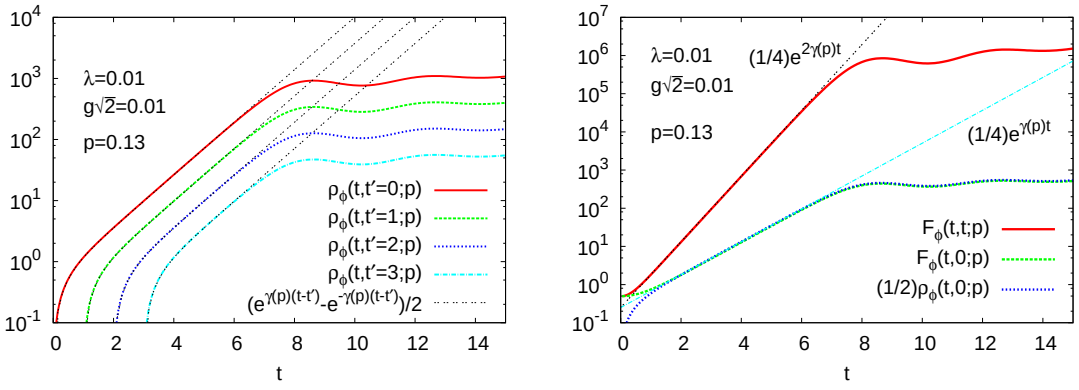

Figure 4.4: Left: Time evolution of the unequal-time correlation function $\rho_\phi(t,t';|\mathbf{p}|)$ for different t' with couplings and momentum as indicated in the figure. For each t' the analytical expression (4.6) is plotted for comparison. Right: Comparison of the time evolution of the statistical and spectral function together with the analytical expressions discussed in the text. Couplings and the chosen momentum are indicated in the figure.

linear regime can be approximated by (4.2). Similar considerations for the spectral function lead to

$$\rho_\phi(t,t';|\mathbf{p}|) = \frac{1}{2m}\left(e^{\gamma(\mathbf{p})(t-t')} - e^{-\gamma(\mathbf{p})(t-t')}\right), \tag{4.6}$$

with $\gamma(\mathbf{p})$ defined in (4.3). In the left plot of Fig. 4.4 we present results from simulations together with the corresponding analytical expression (4.6) for couplings and momentum as indicated in the figure. We show simulations for a low-momentum mode with $|\mathbf{p}| = 0.13m$. The agreement before the exponential amplification terminates is remarkably good for low-momentum modes. For momenta $|\mathbf{p}| \gtrsim m$ the approximation becomes worse. These results show that not only equal time correlations grow exponentially if an instability is present, also correlations between current and initial time get strongly amplified, however not as much as the the former ones, as will be shown in the following. With (4.6) and (4.2) for the statistical function one observes that for not too early times $F_\phi(t,t;|\mathbf{p}|)$ dominates over $F_\phi(t,t';|\mathbf{p}|)$ and $\rho_\phi(t,t';|\mathbf{p}|)$. Moreover one can find in this time regime the relation

$$F_\phi(t,0;|\mathbf{p}|) \simeq \frac{1}{2}\rho_\phi(t,0;|\mathbf{p}|)\,, \tag{4.7}$$

which holds also for large times. In the right graph of Fig. 4.4 the correlation functions $F_\phi(t,t;|\mathbf{p}|)$, $F_\phi(t,0;|\mathbf{p}|)$ and $\rho_\phi(t,0;|\mathbf{p}|)$ are plotted together with (4.2) and the dominant part of (4.6) with a factor 1/2. This confirms (4.7) and the dominance

of $F_\phi(t,t;|\mathbf{p}|)$ is well established for not too early times. We note that for $t' > 0$ the correlator $F_\phi(t,t';|\mathbf{p}|)$ becomes larger than $F_\phi(t,0;|\mathbf{p}|)$, whereas $\rho_\phi(t,t';|\mathbf{p}|)$ becomes smaller than $\rho_\phi(t,0;|\mathbf{p}|)$ as Fig. 4.4 shows. However, $F_\phi(t,t;|\mathbf{p}|)$ exhibits always the largest amplitude. These findings justify the neglection of terms proportional to $\rho_\phi(t,t';|\mathbf{p}|)$ in the self-energy contributions in the equation of motion (3.32), as will be important for the analytical estimates in Sec. 4.1.2.

The results of $n_\phi(t,|\mathbf{p}|)$ as a function of $\mathbf{p}$, i.e. the spectrum of the occupation number, is shown in Fig. 4.5. There we present boson spectra for different couplings indicated in the figure. Different lines represent snapshots at different times. At times $t < 10/m$, the fast change of $n_\phi(t,\mathbf{p})$ due to the "primary" exponential growth is clearly visible. Later the nonlinear "secondary" growth causes a broadening of the spectrum. We would like to emphasize that the occupation of modes with $|\mathbf{p}| > m$ could not be observed in a mean-field or Hartree-type approximation since in those approximations the nonlinear effects are missing.

Even though the Yukawa coupling changes one order of magnitude from $g\sqrt{2} = 0.1$ to $g\sqrt{2} = 0.01$ the graphs with $\lambda = 0.01$ do not show any significant differences. This confirms that weakly coupled fermions have no significant affect on the boson dynamics.

Comparison With Classical-Statistical Simulations

If only the boson dynamics is considered in the absence of fermions, alternative nonperturbative approximation schemes are available that can be used to test the 2PI $1/N$-expansion [AB02, AST04, BG07, BRS08]. Since the exponential growth is induced by an instability of the free-field-type equation (4.1) at sufficiently early times quantum corrections play no role. Furthermore, occupation numbers become large at later times because of the exponential growth and one expects an accurate description of the quantum dynamics using the classical-statistical field theory approximation for highly occupied modes. The classical-statistical simulation result is obtained[3] from repeatedly solving the classical field equation of motion numerically and Monte Carlo sampling of the initial conditions. Fig. 4.6 shows a comparison of the purely bosonic dynamics, represented by $F_\phi(t,t;|\mathbf{p}|)$, from the quantum 2PI $1/N$-expansion and the classical-statistical simulation for the initial conditions (3.75)-(3.77) and $\lambda = 0.1$. The level of agreement between both calculations is remarkable. For low momenta, where occupation numbers are high, the classical-statistical simulation represents the exact result up to controlled statistical errors and the comparison points out the accuracy of the NLO approximation to describe the strongly nonlinear dynamics. On the other hand, from the comparison one also

[3]The classical-statistical computations shown in Fig. 4.6 and 4.7 are taken from [BPR09] and were made by Dipl.-Phys. Alexander Rothkopf. I am very grateful to him for being allowed to use these results here.

$\underline{\lambda < g \;\; (2\xi = 1)}$:

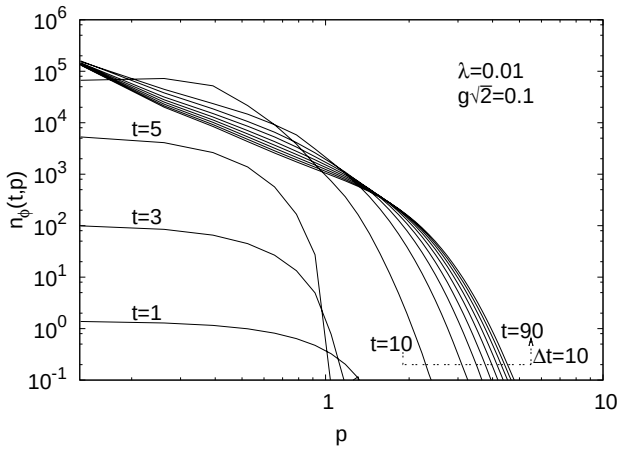

$\underline{\lambda = g \;\; (2\xi = 10^{-2})}$:

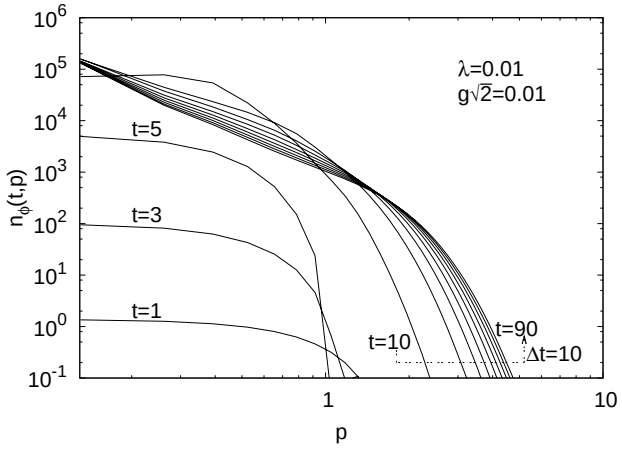

$\underline{\lambda > g \;\; (2\xi = 10^{-3})}$:

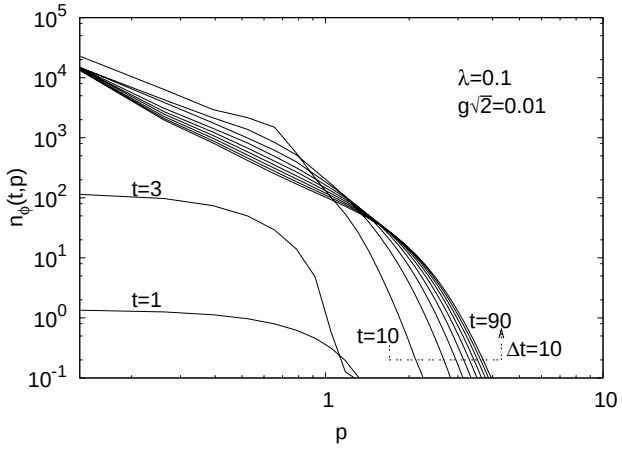

Figure 4.5: Occupation numbers for bosons as a function of momentum at different times. Different graphs correspond to different couplings as indicated in the figures. Here we anticipate $\xi = g^2/\lambda$, cf. Eq. (4.27).

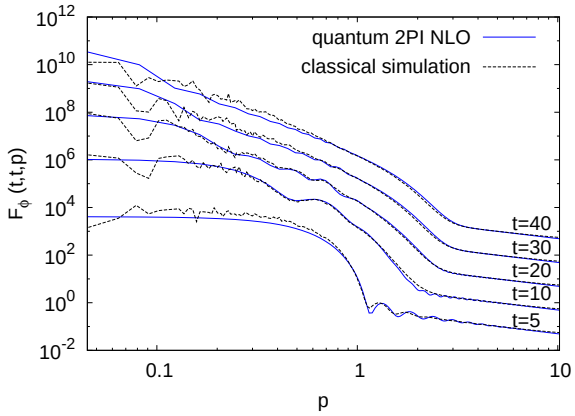

Figure 4.6: Left: Comparison between spectra of the boson correlation function $F_\phi(t,t;|\mathbf{p}|)$ in a 2PI (solid lines) and a classical-statistical (dotted lines) simulation at different times for $\lambda = 0.1$. The spectra for times larger than $t = 5/m$ are multiplied by a factor of 10 in order to make separate lines better visible.

observes that for the considered small coupling the quantum corrections are small even for lower-occupied modes at higher momenta.

4.1.1.2 Subsequent Power-Law Behavior

The asymptotic approach to quantum thermal equilibrium characterized by a Bose-Einstein distribution is impossible in a classical-statistical approximation. The quantum evolution using the 2PI $1/N$-expansion to NLO approaches a Bose-Einstein distribution as was shown in [Ber02, AB02, AST04, BG07]. We emphasize that the approach to thermal equilibrium can be significantly delayed in the presence of a nonequilibrium instability. This happens because after the period of exponential growth the evolution is driven towards a nonthermal infrared fixed point. This was pointed out in Ref. [BRS08] for the case of a parametric resonance instability. In order to demonstrate that a similar behavior also occurs starting from a spinodal or tachyonic instability, we present in Fig. 4.7 simulation results for much later times. Shown are snapshots of the occupation number as a function of momenta for different times, where the black dots are taken at the latest time $t = 4900/m$. A straight line on the double-logarithmic plot corresponds to a power-law behavior

$$n_\phi(t,|\mathbf{p}|) \sim \frac{1}{|\mathbf{p}|^\kappa}\,, \tag{4.8}$$

where the occupation number exponent κ at low-momenta is well approximated by $\kappa_{\rm IR} \simeq 4$ in agreement with the analytical estimates in Refs. [BRS08, BH09a] for the nonthermal fixed point as well as the numerical results starting from parametric

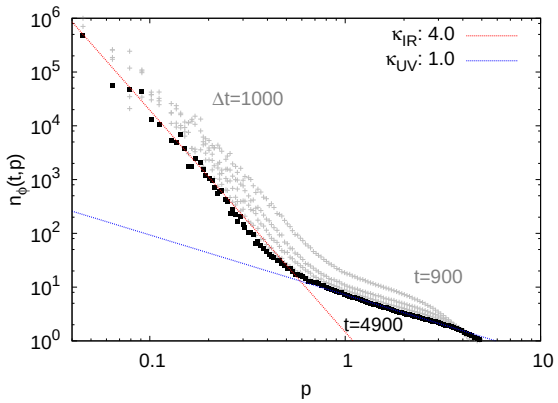

Figure 4.7: The boson occupation numbers $n_\phi(t, |\mathbf{p}|)$ from classical-statistical simulations for $\lambda = 0.1$. Shown are in gray the distributions starting at time $t = 900/m$ (from right), continuing with a time step of $\Delta t = 1000/m$ to the black dots which correspond to $t = 4900/m$.

resonance [BRS08]. At higher momenta, where parametrically $n_\phi(t, |\mathbf{p}|) \lesssim 1/\lambda$, one observes the transition to a classical-statistical thermal distribution for which the occupation number exponent becomes $\kappa_{\rm UV} \simeq 1$. Towards higher momenta than those shown in Fig. 4.7 the distribution still drops rapidly. The classical-statistical theory will finally occupy all high-momentum modes according to a power-law with $\kappa_{\rm UV} \simeq 1$, which corresponds to the Rayleigh-Jeans ultraviolet divergence. In contrast, quantum corrections in the 2PI $1/N$ approximation prevent a power-law distribution at high momenta and lead to finite results [Ber02, AB02, AST04, BG07, BH09a].

Another feature of the quasi-stationary evolution of the system is the self-similarity of the occupation number spectra [MT03]. If the evolution of $n_\phi(t, |\mathbf{p}|)$ is self-similar then it should hold that [MT03]

$$n_\phi(\tilde{t}, |\mathbf{p}|) = \tau^{-q} n_\phi(t, |\mathbf{p}|\tau^{-p}) \,, \tag{4.9}$$

with $\tau = t/\tilde{t}$. $\tilde{t}$ denotes some (arbitrary) reference time point and p and q are real positive parameters. Although the 2PI simulations do not get far in time and on the accessible time scales do not show a clear power-law behavior[4] they nevertheless fulfill the relation (4.9). In order to show that this is indeed the case we present the following simulation results. In the left plot of Fig. 4.8 we show $|\mathbf{p}|^4 n_\phi(t, |\mathbf{p}|)$ as a function of $|\mathbf{p}|$ at different times indicated in the figure where the self-coupling is $\lambda = 10^{-3}$. The growth of amplitude indicates the movement of the fall-off of the

[4]In Fig. 4.5 one might identify a range with a power-law with an exponent approximately equal to 2.2, however the range is small and the time scale is too short in order to be sure that this indicates a proper stable power-law.

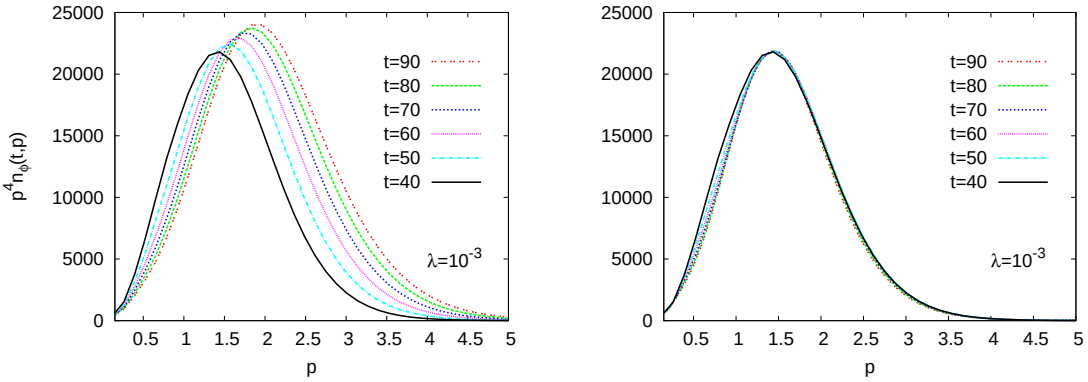

Figure 4.8: Left: $|\mathbf{p}|^4 n_\phi(t, |\mathbf{p}|)$ for $\lambda = 10^{-3}$ as a function of $|\mathbf{p}|$ at different times indicated in the figure. Right: the same graphs as on the left but transformed according to Eq. (4.9). The spectra lie on top of each other which is a signature of a self-similar evolution.

spectrum at high momenta, cf. Fig. 4.5, towards higher momenta. This is sometimes called a "cascade". In the right plot we show the same spectra transformed according to (4.9) where the reference time point was chosen to be $t = 40/m$. This means all spectra at times $t > 40/m$ are mapped onto the spectrum at $t = 40/m$.[5] In our case $q \simeq 0.35$ and $p \simeq 0.12$. This result obviously confirms the fact that the 2PI simulations already entered the quasi-stationary regime without showing a clear power-law in the occupation number spectrum. The values $q \simeq 0.35$ and $p \simeq 0.12$ are similar to those found in Ref. [MT03, MT04]. In Ref. [MT03, MT04] the values of q and p were used to estimate with a kinetic theory approach the time at which the system enters thermal equilibrium. With this the reheating temperature was estimated. Those results yield an extremely long thermalization time with a far to low reheating temperature compared to the one required for the standard hot big bang model [KT90]. Accordingly, with our results we would get similar values within the same approach. However, this does not mean that in general a theory with interacting bosons and fermions lead to too low reheating temperatures. At the latest, when the boson occupation becomes of order one to ten it is expected that the fermion interaction cause an acceleration which would change the results. Additionally a full quantum theory may behave very differently from what is assumed in a kinetic approach.

[5] Note that it is not necessary to choose $t = 40/m$. We could also have mapped all spectra onto the one at $t = 90/m$ or even some other reference time point.

4.1.1.3 Spectral Function

Deviations from a free-field spectral function $\rho(\omega)$ with a well defined (Breit-Wigner) peak, cf. Fig. D.3, for instance a very broad peak or an additional bump in the shape of the peak, are usually interpreted as a signature of different decay channels of particles [AB01]. Though one cannot speak of particles in a classical sense in nonequilibrium the observation of similar spectra lead to the notion of the presence of (off-shell) multiparticle processes out of equilibrium on the way towards a thermal state. In the approximation considered in this work such processes, like $2 \longleftrightarrow 2$ or $1 \longleftrightarrow 3$, are included via the $1/N$-expansion to next-to-leading order. The contribution beyond leading order become very important in scenarios where an instability acts. One expects a strong signal from such effects in the spectral function in those cases. In other words, it would be useful to have a signature of multiparticle scattering far from thermal equilibrium.

In this section we are going to consider the spectral function $\rho_\phi(\omega, \mathbf{p})$ as a function of ω, known as the Wigner representation, typically used in quantum transport theory [ZH98, GPS04]. The calculation of $\rho_\phi(\omega, \mathbf{p})$ in the theoretical framework given here is of great interest since standard kinetic approaches to nonequilibrium processes like heavy-ion collisions often use on-shell δ-functions as an approximation for the spectral function. They may, however, not describe the underlying physics sufficiently well. A computation from the 2PI effective action in a $1/N$-expansion goes beyond such approximations. In Sec. 4.1.2.4 we will also consider fermionic spectral functions. We concentrate on the influence of an instability in the evolution on the spectral function. $\rho_\phi(\omega, \mathbf{p})$ is obtained by a Fourier transformation with respect to the relative time coordinate $s = t - t'$ with a fixed center of mass coordinate $X^0 = \frac{t+t'}{2}$. Hence the spectral function depends on X^0. In Appendix D we explain the corresponding calculation method.

In Fig. 4.9 we show results[6] of $\rho_\phi(X^0; \omega, |\mathbf{p}|)$ for different momenta $|\mathbf{p}|$ indicated in the figure at $X^0 = 45/m$. At that time the system is already in the quasi-stationary evolution phase. It is important to recognize the special values of the momenta in Fig. 4.9. In the left plot of Fig. 4.9 two modes, $|\mathbf{p}| = 0.3$ and $|\mathbf{p}| = 0.7$, are out of the initially unstable momentum regime. The other two modes ($|\mathbf{p}| = 1.4$ and $|\mathbf{p}| = 4.1$) were amplified due to nonlinear effects, cf. Sec. 4.1.1.1. We will first discuss the former two momenta. The results show a peak at $\omega \approx |\mathbf{p}|$ and next to it large oscillations which are symmetric around zero. We comment about the peak positions at $\omega \approx |\mathbf{p}|$ below since it is also observed for higher momenta. Negative values of the spectral function are usually caused by finite-time effects [AB01], see also App. D. That those large effects only occur for modes which were initially unstable seems to be a special property of the spectral function in a system with an instability.

[6] Note that $\rho_\phi(X^0; \omega, |\mathbf{p}|)$ is per definition imaginary, cf. Appendix D. Therefore we plot $-i\rho_\phi(X^0; \omega, |\mathbf{p}|)$.

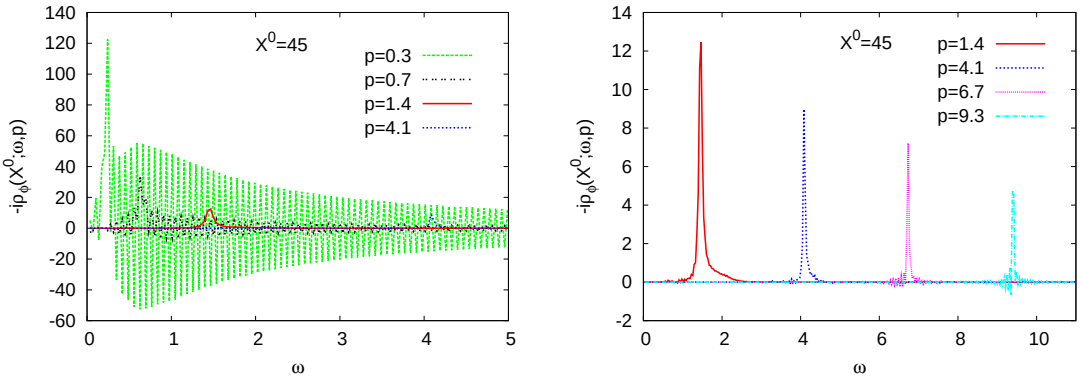

Figure 4.9: Wigner transformed spectral function at center of mass coordinate $X^0 = 45$ for different momenta $|\mathbf{p}|$ and couplings $\lambda = 0.01$, $g\sqrt{2} = 0.1$. Left: modes with $\mathbf{p} > m$, i.e. $\mathbf{p} = 0.3m$ and $\mathbf{p} = 0.7m$ show unexpected spectra, see main text. For comparison with the right plot $\mathbf{p} = 1.4m$ and $\mathbf{p} = 4.1m$ are included. Right: only modes with $\mathbf{p} > m$ are shown, clear peaks with decreasing amplitude are observed.

We observe such a behavior in other simulations with different parameters too. Those effects become larger for smaller self-couplings λ which is equivalent to a larger amplitude of the occupation number due to the instability. It is tempting to interpret the shape of the envelope function of the oscillations as an enhancement of the spectrum. This again could be interpreted as a signature of multiparticle processes [AB01] which are present in calculations given here.

We now consider the modes with $|\mathbf{p}| = 1.4$ and $|\mathbf{p}| = 4.1$ in Fig. 4.9. In the left plot the results are almost not visible, they correspond to the little peaks at $\omega \approx |\mathbf{p}|$. The special position may be interpreted in a quasi-particle picture where $\omega = \sqrt{|\mathbf{p}|^2 + m_{\text{eff}}^2}$ with an effective mass $m_{\text{eff}}^2 \approx 0$ which includes self-energy contributions coming from the next to leading order in a 2PI $1/N$-expansion. If such a result is a signature of the convexity of the effective potential has to be discussed elsewhere[7]. Note that the initial (classical) potential was not convex at $\phi = 0$ since the boson bare mass $m \neq 0$. These two modes are also shown in the right plot of Fig. 4.9 together with two high-momentum modes ($|\mathbf{p}| = 6.7$ and $|\mathbf{p}| = 9.3$). For the latter two the same findings hold. The decrease of the amplitude comes from the fact that these modes seem to be well described by "quasi-free fields" since the factor $1/E_{\mathbf{p}}$ in (D.5) is responsible for such a decrease, see Appendix. D. Moreover, with higher momenta the width of the peaks decrease which can be interpreted as stable

[7] In that context it is worth to note that we observed that $\epsilon(t, \mathbf{p})$, as defined in (3.78), approaches approximately zero for $|\mathbf{p}| = 0$.

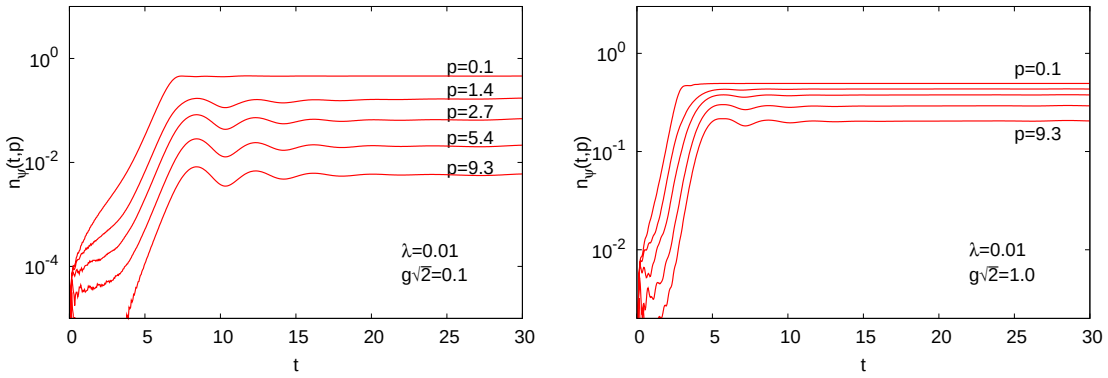

Figure 4.10: Occupation numbers of fermion modes as a function of time with couplings as indicated in the graphs. The observed growth rate of modes is approximately independent of momenta. In the right graph only two modes are labeled, the three other modes correspond to the same momenta as in the left graph.

particles.

In conclusion we think that we found first signatures of nonequilibrium instability characteristics in the spectral function calculated in a 2PI $1/N$-expansion up to next-to-leading order.

4.1.2 Fermion Dynamics

In this section we will analyze the fermion dynamics in detail. First we will concentrate on the early-time evolution where the instability acts. After that we will consider the occurrence of a power-law behavior in the fermion occupation number as a function of momentum. In the last but one part we will turn to the late time evolution of the fermion occupation number $n_\psi(t, \mathbf{p})$ with its fast approach towards thermal equilibrium. The last part is devoted to a discussion of the spectral function as a function of energy.

4.1.2.1 Early-Time Evolution

The results of an out-of-equilibrium simulation of the fermion occupation number defined in Eq. (3.84) is displayed in Fig. 4.10. Different modes are presented as a function of time for two different Yukawa couplings, $g\sqrt{2} = 0.1$ and $g\sqrt{2} = 1$, for $\lambda = 0.01$. The figure shows the behavior of the fermions, which corresponds to the evolution of the bosons presented in Fig. 4.1. After a short initial period one observes an exponential growth of fermion modes. The fast dynamics then slows down rather abruptly and approaches a quasi-stationary evolution phase. A most

characteristic property of the fast period is that the different momentum modes get exponentially amplified with approximately the same growth rate for a wide momentum range $|\mathbf{p}|/m \approx 0.1$ – 9.3, which can be seen from the slopes of the curves in Fig. 4.10. Higher-momentum fermion modes are amplified at later times. Recall the amplification of boson modes, where the primary growth rates show a significant momentum dependence according to (4.3) and the secondary rates equal multiples of the maximum primary growth rate (see Fig. 4.1). Consequently in the system under consideration fermions behave very differently compared to bosons. Though fermion production occurs practically over the whole spectrum, the high-momentum delay leads to a decrease of the amplitude of the occupation number modes with increasing momenta. In Sec. 4.1.2.2 we will consider the spectrum in detail. One also notes that in our simulations $n_\psi(t, \mathbf{p})$ never exceeds $1/2$, despite the fact that its definition allows occupancies in the range $0 \leq n_\psi(t, \mathbf{p}) \leq 1$ in accordance with the Pauli principle. We note that $n_{\mathrm{FD}}(t, \mathbf{p} = 0) = 1/2$ corresponds to the value of the low-momentum distribution in thermal equilibrium, which is discussed in more detail in Sec. 4.1.2.3. In the right graph of Fig. 4.10 we show the evolution with a stronger Yukawa coupling $g\sqrt{2} = 1$. One observes a more efficient fermion production over the spectrum, i.e. the decrease of the amplitude with higher momentum is less pronounced than for weak couplings. The growth rate is larger and the system enters the quasi-stationary evolution phase earlier. Exponentially growing fermion modes were also observed in a multi-field model [TBV00]. However, the authors did not explained the origin of the exponential growth.

In the following we present an analytical description of the phenomenon of exponential growing fermion modes. Moreover the analysis provides information about the main characteristics of the dynamics. As stated above, for weak Yukawa couplings the boson dynamics can be viewed as independent of the fermion dynamics. This is an important point in our consideration. We have to have a close look at the equation of motion (3.32) for the equal time correlation $F_V(t, t; \mathbf{p})$ since this correlator is connected to the occupation number (3.84) in the chiral limit. In (3.32) scalar and tensor correlations vanish because we investigate in this chapter the chirally symmetric model introduced in Sec.3.3.2. The term proportional to $|\mathbf{p}|$ is zero at equal times because of the symmetry relation in (3.20). With the definition of the self-energies (3.48) and (3.51) in the chiral limit there are eight terms, each coming with a product of two fermion and one boson two-point function. The self-energy contributions can be visualized by a loop diagram as shown in Fig. 4.11, where internal lines represent the different propagators as indicated in the diagram. Since $F_\phi(t, t; \mathbf{p})$ grows exponentially fast it quickly becomes larger than any other quantity, especially larger than $\rho_\phi(t, t'; \mathbf{p})$. That this is indeed the case was shown in Sec.4.1.1.1. Thus each term in which $F_\phi(t, t'; \mathbf{p})$ enters dominates the self-energy contributions in (3.32). The dominance is best realized if we have a small boson self-coupling because the amplitude of F_ϕ becomes parametrically of order $1/\lambda$, see

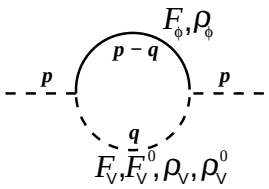

Figure 4.11: The fermion self-energy diagram. The internal lines represent the various propagators indicated in the diagram.

4.1.1.1. With this we proceed and neglect all terms in (3.32) which do not contain F_ϕ. It follows that the equation of motion acquires the form

$$
\begin{aligned}
i\left\{\partial_t F_V(t,t';|\mathbf{p}|)\right\}|_{t'=t} \simeq \\
&- g^2\int_0^t dt''\int\frac{d^3q}{(2\pi)^3}\Big[\rho_V^0(t,t'';|\mathbf{q}|)F_\phi(t,t'';|\mathbf{p}-\mathbf{q}|)F_V(t'',t;|\mathbf{p}|) \\
&\quad -\frac{\mathbf{p}}{|\mathbf{p}|}\frac{\mathbf{q}}{|\mathbf{q}|}\rho_V(t,t'';|\mathbf{q}|)F_\phi(t,t'';|\mathbf{p}-\mathbf{q}|)F_V^0(t'',t;|\mathbf{p}|)\Big] \\
&+ g^2\int_0^t dt''\int\frac{d^3q}{(2\pi)^3}\Big[F_V^0(t,t'';|\mathbf{q}|)F_\phi(t,t'';|\mathbf{p}-\mathbf{q}|)\rho_V(t'',t;|\mathbf{p}|) \\
&\quad -\frac{\mathbf{p}}{|\mathbf{p}|}\frac{\mathbf{q}}{|\mathbf{q}|}F_V(t,t'';|\mathbf{q}|)F_\phi(t,t'';|\mathbf{p}-\mathbf{q}|)\rho_V^0(t'',t;|\mathbf{p}|)\Big]\,. \quad (4.10)
\end{aligned}
$$

Since we are interested in the evolution of the equal-time correlation function, we write for the derivative on the left hand side of (4.10)

$$
\begin{aligned}
\partial_t F_V(t,t;\mathbf{p}) &= \left\{\partial_{t'}F_V(t',t;\mathbf{p})\right\}|_{t'=t} + \left\{\partial_{t'}F_V(t,t';\mathbf{p})\right\}|_{t'=t} \\
&= 2\left\{\partial_{t'}F_V(t',t;\mathbf{p})\right\}|_{t'=t}\,, \quad (4.11)
\end{aligned}
$$

where we used in the second equation that $F_V(t',t;\mathbf{p})$ is symmetric under time exchange according to (3.22). In the spinodal instability case the mode with the smallest momentum grows fastest, see (4.1) with (4.3). Thus the momentum integrals in (4.10) are dominated by momenta $\mathbf{q} \simeq \mathbf{p}$. For small momenta $\mathbf{p} \ll m$ we can write

$$
\gamma(\mathbf{p}) \simeq \gamma_0 + \frac{1}{2}\gamma''(\mathbf{p}=0)\,\mathbf{p}^2 = m - \frac{\mathbf{p}^2}{2m}\,. \quad (4.12)
$$

where we used $\gamma_0 = m$ and the second derivative of (4.3) with respect to $\mathbf{p}$. Consequently the low momentum bosonic modes behave like

$$
F_\phi(t,t;\mathbf{p}-\mathbf{q}) \simeq A_0\, e^{2\gamma_0 t}\, e^{-\gamma_0^{-1}(\mathbf{p}-\mathbf{q})^2\, t}\,, \quad (4.13)
$$

such that the integrand of (4.10) is dominated by $\mathbf{q} \simeq \mathbf{p}$ for sufficiently large t. This also holds in the presence of additional powers of momenta in the integrand, such as those coming from the measure of the integral. The sum appearing in the integrand of (4.10) consists of pairs of terms, which are the same if $\mathbf{q} = \mathbf{p}$. Accordingly, the equation of motion may be approximated by

$$\begin{aligned} i\partial_t F_V(t,t;|\mathbf{p}|) \;\simeq\; -4g^2 \int_0^t dt'' \int \frac{d^3q}{(2\pi)^3} F_\phi(t,t'';|\mathbf{p}-\mathbf{q}|) \\ \times \Big[\rho_V^0(t,t'';|\mathbf{p}|) F_V(t'',t;|\mathbf{p}|) - \rho_V(t,t'';|\mathbf{p}|) F_V^0(t'',t;|\mathbf{p}|) \Big]. \end{aligned} \tag{4.14}$$

During the time interval in which F_ϕ grows exponentially the time evolution is dominated by the near past, hence the memory integrals on the right hand side in (4.10) get the largest contribution from the latest times. In other words, the memory integrals become approximately local in time [Ber05]. The typical time scale for these dominant contributions is given by the primary growth rate γ_0. Following similar calculations for boson dynamics in Refs. [BS03, Ber05], we will employ a "memory expansion" for an approximate analytical description of the fermion evolution. That means that we employ a Taylor expansion of the integrand in (4.14) around the latest time of the memory integrals up to the lowest order. Since $F_V^0(t,t';|\mathbf{p}|)$ and $\rho_V(t,t';|\mathbf{p}|)$ are antisymmetric in time as described by (3.20) and (3.23) their equal-time correlation functions vanish such that the corresponding terms in (4.14) can be neglected to lowest order in the expansion. Note that $\rho_V^0(t,t;|\mathbf{p}|) = i$ for all momenta and times, see (3.66). Integrals over the entire past, $\int_0^t dt''$, are replaced by integrals with a finite time range, $\int_{t-c/\gamma_0}^t dt''$. We will see that during the growth period this memory restriction leads to a good description of the full numerical results even for rather short memory intervals with $c \lesssim 1$. In particular, the estimate for the fermion growth rate will be insensitive to the value of c. Applying all these approximations the equation of motion (4.10) reads

$$\partial_t F_V(t,t;|\mathbf{p}|) + K(t) F_V(t,t;|\mathbf{p}|) \;\simeq\; 0\,, \tag{4.15}$$

where we define

$$K(t) \;=\; \frac{4g^2 c}{\gamma_0} \int_{\mathbf{q}} F_\phi(t,t;|\mathbf{p}-\mathbf{q}|) \;\simeq\; g^2 \frac{A_0 \sqrt{\gamma_0} c}{2(\pi t)^{3/2}} e^{2\gamma_0 t}\,. \tag{4.16}$$

In the second step we used (4.13) under the integral such that it becomes a Gaussian integral. We emphasize that the equations in our argumentation always respect chiral symmetry. In Appendix A we present a decomposition of the relevant correlation functions into left and right handed components. We find that a mixture of the two

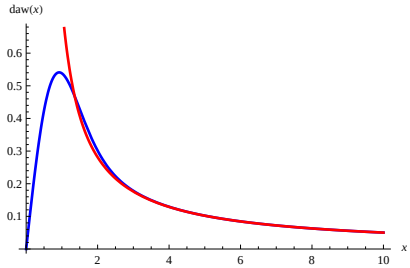

Figure 4.12: A plot of the Dawson function (blue) appearing in the solution (4.17) together with its asymptotic expansion given in (4.20).

different types cannot appear in the above equations. Note that the approximation is only valid for times $2\gamma_0 t \gg 1$ since $F_\phi(t,t';\mathbf{p})$ is not large initially, moreover $K(t)$ is not defined at $t=0$. Nevertheless we will find that the results describe the numerical simulations quite well if we proceed and integrate the equation (4.15) with the initial condition $F_V(t,t;|\mathbf{p}|)|_{t=0^+} = 1/2$ which is taken from (3.73). The solution of (4.15) can be determined analytically[8] and is given by

$$F_V(t,t;|\mathbf{p}|) \;=\; \frac{1}{2}\exp\left\{-g^2 a\, e^{2\,\gamma_0\, t}\left[2\,\mathrm{daw}(\sqrt{2\gamma_0 t}) - \frac{1}{\sqrt{2\gamma_0 t}}\right]\right\}\,, \tag{4.17}$$

with the dimensionless constant

$$a \;=\; \frac{A_0\gamma_0\sqrt{2}c}{\pi^{3/2}}\,. \tag{4.18}$$

The Dawson function appearing in (4.17) is defined as

$$\mathrm{daw}(x) \;=\; e^{-x^2}\int_0^x \mathrm{d}y\, e^{y^2}\,. \tag{4.19}$$

It is an odd function and its derivative is $\mathrm{daw}'(x) \;=\; 1-2x\,\mathrm{daw}(x)$ such that it grows linearly at $x=0$. In Fig. 4.12 we show a plot of the Dawson function compared to its asymptotic series

$$\mathrm{daw}(x) \;=\; \frac{1}{2x} + \frac{1}{2^2x^3} + \ldots \tag{4.20}$$

with which the expression (4.17) can be simplified for not too early times by using

$$2\,\mathrm{daw}(\sqrt{2\gamma_0 t}) - \frac{1}{\sqrt{2\gamma_0 t}} \;=\; \frac{1}{2(2\gamma_0 t)^{3/2}} + \ldots\,. \tag{4.21}$$

[8] A straightforward integration may lead to a different expression containing the well-known error function. However, using the relation between the latter and the Dawson function [AS64] one ends up at (4.17). It turns out that the representation in (4.17) is more convenient.

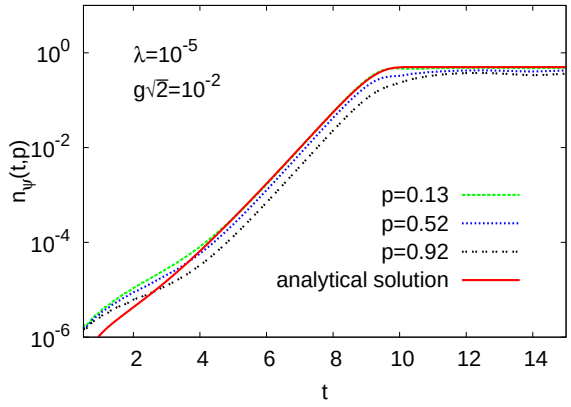

Figure 4.13: Evolution of $n_\psi(t, |\mathbf{p}|)$ as a function of time for different momenta and $g = 10^{-2}$. The boson self-coupling is $\lambda = 10^{-5}$. The solid line represents the analytical solution and the dotted lines show the results from simulations.

One finds that (4.21) provides a rather good description already for times $2\gamma_0 t \gtrsim \mathcal{O}(1)$, which may also deduced from Fig. 4.12.

We are now able to present the solution of the fermion occupation number. Inserting the solution (4.17) into the definition of $n_\psi(t, \mathbf{p})$ (3.84) we obtain

$$n_\psi(t, |\mathbf{p}|) = \frac{1}{2} - \frac{1}{2} \exp\left\{ -g^2 a \, e^{2\gamma_0 t} \left[2\,\mathrm{daw}(\sqrt{2\gamma_0 t}) - \frac{1}{\sqrt{2\gamma_0 t}} \right] \right\} . \tag{4.22}$$

In order to compare this solution with numerical simulations we take $A_0\gamma_0 = 1/4$ with which $a \simeq 0.05c$ and plug this into (4.22). We find the best agreement with simulations for $c \simeq 0.48$, we comment on this later again. Note that the growth rate of (4.22) does not depend on c. In Fig. 4.13 we show simulations together with the analytical solution (4.22) of $n_\psi(t, \mathbf{p})$ for different momenta indicated in the figure. The couplings are $\lambda = 10^{-5}$ and $g\sqrt{2} = 10^{-2}$. We find a remarkably good description of the numerical results for small $\mathbf{p}$. This we anticipated during the derivation of (4.22). The analytical result shows no momentum dependence where the simulations exhibit a decreasing amplitude for higher modes, as mentioned above. This leads to considerable deviations already for $\mathbf{p} \approx m$. On the other hand, the major characteristic of an approximate momentum independent growth rate (cf. Fig. 4.10) is reproduced. As expected, at early times deviations are present.

It is instructive to consider the analytical solution in detail. We will concentrate on two main aspects. On the one hand there is the fact that (4.22) exhibits approximately the same growth rate as the boson counterpart. On the other hand there is the abrupt stop of exponential growth when the value 1/2 is reached. To understand these properties let us divide the time evolution into two parts: (I) $2\gamma_0 t \gtrsim \mathcal{O}(1)$ and

(II) $2\gamma_0 t \gg 1$. We consider weak Yukawa couplings g. In the range (I) we can expand the first exponential function in (4.22) and get

$$\begin{aligned} \textbf{(I):} \qquad \mathrm{n}_\psi(\mathrm{t},|\mathbf{p}|) &\simeq \frac{g^2 a}{2}\, e^{2\,\gamma_0\, t}\left[2\,\mathrm{daw}(\sqrt{2\gamma_0 t}) - \frac{1}{\sqrt{2\gamma_0 t}}\right] \\ &\simeq \frac{g^2 a}{4(2\gamma_0 t)^{3/2}} e^{2\,\gamma_0\, t}\,. \end{aligned} \tag{4.23}$$

for the second step we used the asymptotic expansion of the Dawson function (4.20). This immediately tells us that $n_\psi(t,|\mathbf{p}|)$ has effectively the same growth rate as F_ϕ. We conclude that the fermions are produced by induction due to the boson dynamics. The time dependent factor $\sim t^{-3/2}$ in (4.23) reduces the actual fermion growth rate γ_ψ. If one measures the growth rate of $n_\psi(t,|\mathbf{p}|)$, e.g. with a fit by an exponential function in Fig. 4.13, one finds $\gamma_\psi \simeq 0.85\gamma_0$. In the second time regime the expansion of the exponential is not valid. However, using the asymptotic expansion (4.20) in the first exponent in (4.22), we find an effective solution for the range (II) of the form

$$\textbf{(II):} \qquad \mathrm{n}_\psi(\mathrm{t},|\mathbf{p}|) \simeq \frac{1}{2} - \frac{1}{2}\exp\left\{-\frac{\mathrm{g}^2\mathrm{a}}{2(2\gamma_0\mathrm{t})^{3/2}}\,\mathrm{e}^{2\,\gamma_0\,\mathrm{t}}\right\}. \tag{4.24}$$

Accordingly, the first exponent grows exponentially, which causes the second term to vanish quickly once the first exponent becomes of order one. This is the reason for the abrupt stop of the growth of $n_\psi(t,|\mathbf{p}|)$, see e.g. Fig. 4.13. From this we learn result that the solution $n_\psi(t,|\mathbf{p}|) = 1/2$ is incorporated in the equation of motion with quantum corrections for the fermion correlator F_V.

We get further inside into the properties of the mechanism observed here if we consider the time scale at which the exponential growth of $n_\psi(t,|\mathbf{p}|)$ stops. This time scale, denoted by t_ψ, can be estimated by requiring the absolute value of the first exponent in (4.24) to be of order one[9]. Thus we have the condition

$$\frac{g^2 a}{2(2\,\gamma_0\,t)^{3/2}}\, e^{2\,\gamma_0\, t} \overset{t=t_\psi}{\simeq} 1\,, \tag{4.25}$$

which can be rewritten in a more convenient form as

$$t_\psi \simeq \frac{1}{2\gamma_0}\ln\left(\frac{2}{g^2 a}\right) + \frac{3}{4\gamma_0}\ln\left(2\,\gamma_0\, t_\psi\right)\,. \tag{4.26}$$

Since $a \simeq 0.05c$ we observe a logarithmically dependence of t_ψ on the parameter c. Taking $c \simeq 0.48$ as above we find the solutions $t_\psi \simeq 11.8$ for $g\sqrt{2} = 0.001$, $t_\psi \simeq 9.2$ for $g\sqrt{2} = 0.01$, and $t_\psi \simeq 6.7$ for $g\sqrt{2} = 0.1$. In the left plot of Fig. 4.14 we present

[9]This is equivalent to the estimate of the function $K(t)$ in (4.16) to be of order one.

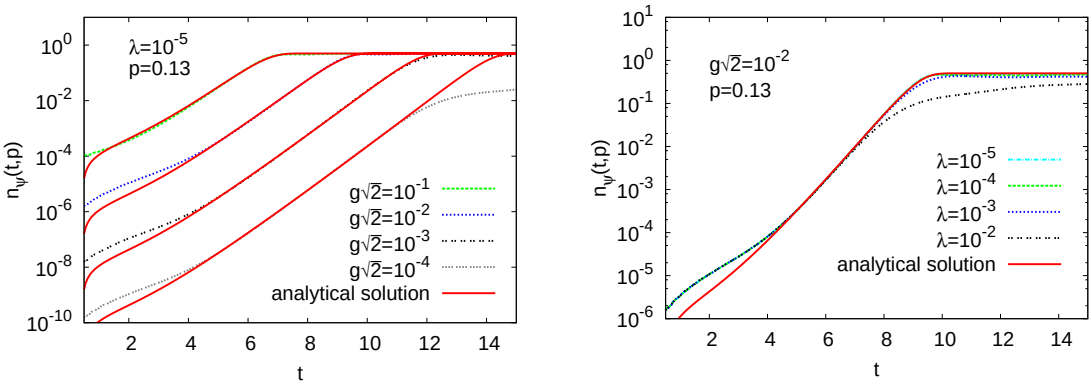

Figure 4.14: Evolution of $n_\psi(t, |\mathbf{p}|)$ as a function of time. The analytical solution (solid lines) is compared to the result from numerical simulations (dotted lines) for different values of the Yukawa coupling g (left) and different values for the boson self-coupling λ (right) as indicated in the plots. For the numerical simulations the lowest available momentum $|\mathbf{p}| = 0.13m$ is chosen.

comparisons between simulations and analytical solutions (4.22) for the lowest momentum $|\mathbf{p}| = 0.13m$ and different Yukawa couplings but fixed $\lambda = 10^{-5}$. The end of the exponential regime agrees rather well with the analytical results for t_ψ from above. This holds for a wide range of Yukawa couplings. However for $g\sqrt{2} = 10^{-4}$ the numerical simulation exhibits an earlier stop compared to the corresponding analytical solution. We find considerable deviations between numerical and analytical solutions for $g < 10^{-3}$ with $\lambda = 10^{-5}$. In the right plot of Fig. 4.14 we expose simulations with different boson self-couplings λ and fixed $g\sqrt{2} = 10^{-2}$ compared to the corresponding analytical solution. The same statements apply as before, and similar deviations after the exponential growth terminates occur for $\lambda > 10^{-3}$ with $g = 10^{-2}$. In general we observe that the ratio

$$\xi = \frac{g^2}{\lambda} \tag{4.27}$$

is responsible for the efficiency of the fermion production. If $2\xi \lesssim 0.1$, significant deviations appear, as reported above. If $2\xi \gtrsim 0.1$, the occupation number reaches $1/2$ in the small momentum regime and thus agrees very well with our analytical solution. This structure is explained by the fact that in our analytical derivation we assumed everlasting exponentially growing boson modes. However this can only lead to a good description at time scales $t \leq t_\phi$, cf. (4.5). The equations of motion in the fermion sector respect the Pauli principle, hence the amplitude of the solution grows until the maximal occupation is obtained[10]. Consequently, if $t_\phi \geq t_\psi$ the

[10]That $n_\psi(t, \mathbf{p}) = 1/2$ is the maximal occupation was already stated above and will be explained

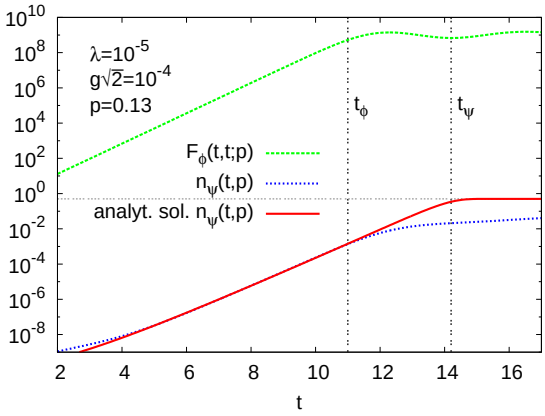

Figure 4.15: Time evolution of $F_\phi(t,t;|\mathbf{p}|)$, $n_\psi(t,|\mathbf{p}|)$ and the analytical solution (4.22) for momentum and couplings indicated in the figure. The vertical lines represent the time scales t_ϕ and t_ψ determined with (4.5) and (4.26). The horizontal line displays 1/2.

maximal occupancy is reached and the analytical solution does not show sizeable deviations for small momenta. Whereas if $t_\phi \leq t_\psi$ the exponential growth stops before $n_\psi(t,|\mathbf{p}|) \simeq 1/2$.

In Fig. 4.15 we illustrate the latter case. We display the time evolution of $F_\phi(t,t;\mathbf{p})$, $n_\psi(t,\mathbf{p})$ and the analytical solution (4.22) together in one plot with vertical lines which indicates the time scales $t_\phi \simeq 11.0/m$ and $t_\psi \simeq 14.2/m$. The couplings are $g\sqrt{2} = 10^{-4}$ and $\lambda = 10^{-5}$, so that $2\xi < 0.1$. If $F_\phi(t,t;\mathbf{p})$ stops growing the numerical $n_\psi(t,\mathbf{p})$ stops growing as well and $n_\psi(t,|\mathbf{p}|) < 1/2$. If $t_\phi \geq t_\psi$ the vertical lines would be interchanged and thus numerical and analytical solutions would agree over almost the whole simulation.

Now the condition $t_\phi \gtrsim t_\psi$ can be translated into a condition for ξ with the use of (4.5) and (4.26). It turns out that the corresponding inequality reads $\xi \gtrsim 1/(8c)$, which fits with the numerical findings. If we define efficient fermion production occurs if the occupation number reaches 1/2 at least in a small range, then we can state that for efficient fermion production ξ must be larger than $1/(8c)$.

It is a general fact that the ratio (4.27) plays an important role for the fermion dynamics for $t \gtrsim t_\phi$. This can be understood as follows. According to the discussion in Sec. 4.1.1.1 at the time t_ϕ the parametric coupling-dependence of the boson correlation function becomes $F_\phi \sim \mathcal{O}(1/\lambda)$. The fermion-boson loop contribution to the fermion propagators shown in Fig. 4.11 is proportional to g^2. Since the dominant term in the boson propagator line appearing in the loop is associated to F_ϕ, this leads to the parametric $g^2/\lambda = \xi$ dependence. In order to verify this we have plotted

in Sec. 4.1.2.2.

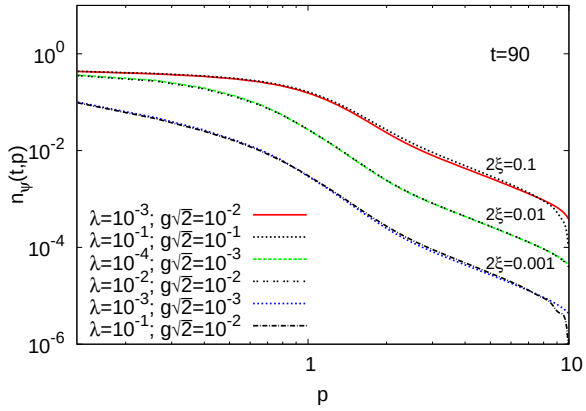

Figure 4.16: Fermion occupation numbers as a function of momentum at fixed time $t = 90/m$ after the exponential growth period. Compared are simulations with different λ and g but equal $\xi = g^2/\lambda$.

in Fig. 4.16 fermion occupation number distributions for different values of g and λ. Compared are simulations with different λ and g but same ratio ξ for $\xi = 0.1$, 0.01 and 0.001 at fixed time $t = 90/m$ after the exponential growth period. The agreement is remarkably good. We emphasize that at early times they differ in general for the same ξ. In particular, the time t_ϕ itself depends on λ and is insensitive to g for the considered weak couplings (see Sec. 4.1.1.1).

4.1.2.2 Emergence of Power-Law Behavior

In Section 4.1.1 we have seen that infrared scaling solution of $n_\phi(\mathbf{p})$ exist. This has dramatically consequences on the evolution of the bosons occupation number since it implies a diverging time scale on which the system thermalize. By the virtue of the Pauli principle the fermion occupation number cannot exceed one. Consequently an infrared scaling solution is forbidden. This leads to the fact that the phenomenon of critical-slowing down is absent in the fermion sector.

However, this does not exclude a power-law behavior at all. In the high-momentum regime there may be the opportunity for a scaling solution. Power-laws in the ultraviolet regime of the fermion occupation number spectrum were observed in Refs. [NPS01a, NPS01b, GRT99], in the context of gravitino production. They were interpreted as a shut-off of fermion production at high momenta which indicates a cut-off at a certain momentum in the spectrum [NPS01a, NPS01b]. Modes beyond the cut-off should be associated with plane-waves [GRT99]. However, as we will see, the power-law we observed has a different origin. In Fig. 4.17 fermion spectra $n_\psi(\mathbf{p})$ are shown for different couplings indicated in the figure. More precisely, snapshots of spectra at different times are shown. The straight lines represent a

$\underline{\lambda < g \;\; (2\xi = 1)}$:

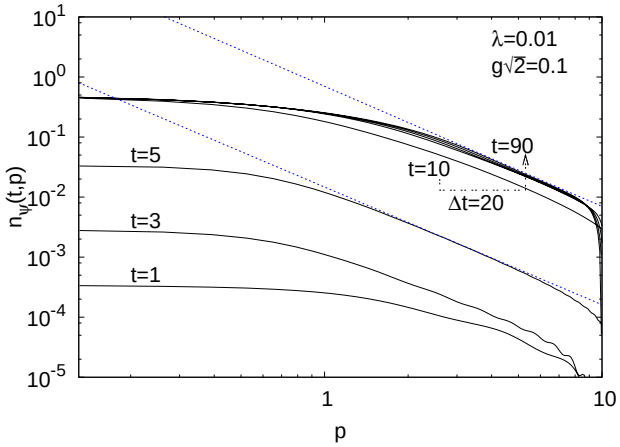

$\underline{\lambda = g \;\; (2\xi = 10^{-2})}$:

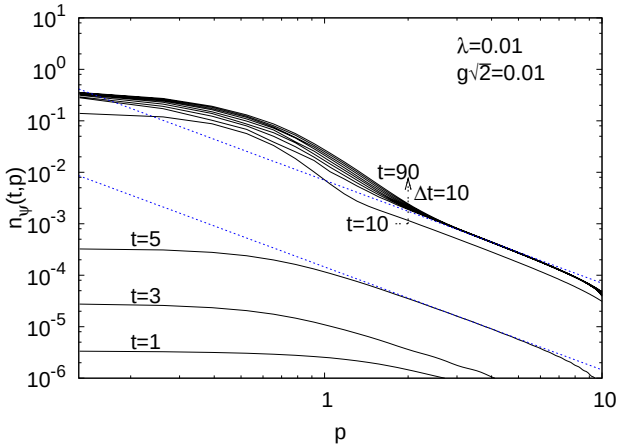

$\underline{\lambda > g \;\; (2\xi = 10^{-3})}$:

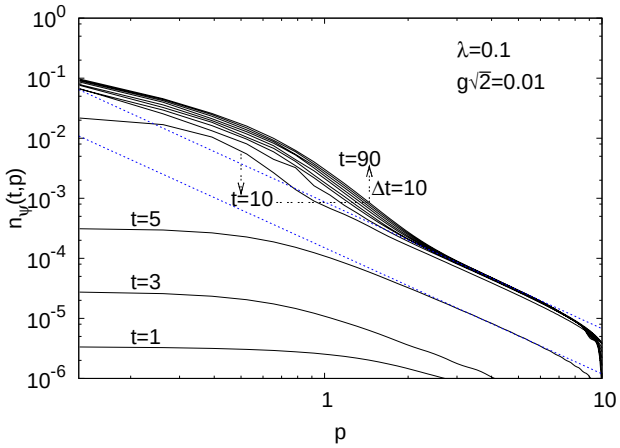

Figure 4.17: Fermion occupation numbers as a function of momentum at different times. Different graphs correspond to different couplings as indicated in the figures. The dotted lines display power-law behavior $n_\psi(|\mathbf{p}|) \sim |\mathbf{p}|^{-\kappa_\psi}$ with the exponent $\kappa_\psi = 2$ for comparison (see Sec. 4.1.2).

power-law behavior $n_\psi(\mathbf{p}) \sim 1/|\mathbf{p}|^{\kappa_\psi}$ with $\kappa_\psi = 2$ for momenta $|\mathbf{p}| \gtrsim m$. We have verified that the very sharp fall-off of the distribution at later times close to the cut-off, i.e. $|\mathbf{p}| \approx 10m$ in Fig. 4.17, is removed if we enlarge the momentum cut-off and accordingly the power-law behavior extends to larger momenta. For a check of insensitivity of our results against cut-off changes see Appendix F. We also observe that the emergence of the power-law in the high-momentum regime occurs quite early, i.e. around the time $t \approx 3/m$, and it is well established already around $t \approx 5/m$. This means the origin of the power-law lies in early-time physics and cannot be connected with subsequent scaling behavior as in the case of the boson power-laws explained in Sec. 4.1.1. The time scale at which the power-law arises is the same for all ξ. During the unstable evolution phase the amplitude of the spectrum changes dramatically, however the power-law remains stable with the same exponent. At the end of the exponential growth high-momentum modes exit the unstable evolution simultaneously. Thus the already established power-law becomes "frozen-in" in time during the subsequent quasi-stationary evolution. This may be observed in the left plot of Fig. 4.10 where modes with $|\mathbf{p}| \geq 1.4m$ exit the unstable evolution simultaneously, and, accordingly, around the exit time $n_\psi(t, |\mathbf{p}|)$ exhibits a power-law in the region $|\mathbf{p}| \geq 1.4m$, see Fig. 4.5. The region where the fermionic power-law remains after the instability decreases slowly with time due to nonlinear effects which eventually drive the system into thermal equilibrium.

In the following we are going to explain the origin of the fermion power-law behavior. As already stated in Sec. 4.1.2.1 the delayed growth of high-momentum modes is the reason for a special momentum dependence of $n_\psi(t, \mathbf{p})$. We are mainly interested in a momentum-dependent part of the occupation number, which we call $A(|\mathbf{p}|)$, i.e. we write

$$n_\psi(t, |\mathbf{p}|) \;=\; A(|\mathbf{p}|)\, B(t). \tag{4.28}$$

The time dependent part was determined in Sec. 4.1.2.1 in the low-momentum regime and has the form of $B(t) \sim e^{2\gamma_0 t}/t^{3/2}$, accordingly $A(|\mathbf{p}|) = \text{const.}$, cf. Eq. (4.23). Now we are interested in the actual momentum dependence of $A(|\mathbf{p}|)$ and the time dependence plays a subordinate role.

The starting point of our analysis is the approximate equation of motion for $F_V(t, t; |\mathbf{p}|)$ (4.10). The boson two point function $F_\phi(t, t'; |\mathbf{p}|)$ in Eq. (4.10) can be approximated by

$$F_\phi(t, t'; |\mathbf{p}|) \simeq A_0 m\, e^{\gamma(\mathbf{p})\,(t+t')} \theta(m - |\mathbf{p}|)\,, \tag{4.29}$$

with $\gamma(\mathbf{p})$ defined in (4.3) and a constant factor $A_0 m \simeq 1/4$. This approximation is similar to the one in (4.2) with the difference that we here restrict the occupation to be present only up to momenta $|\mathbf{p}| < m$. Of course this is only arguable up to a certain time scale at which nonlinearities start to cause an occupation for momenta $|\mathbf{p}| > m$. That (4.29) is a reliable approximation in a certain time regime

was observed in Fig. 4.5. In the Sec. 4.1.2.1 we argued that the momentum integration we have to carry out receives its main contribution from values of $\mathbf{q} \approx \mathbf{p}$ for which $F_\phi(t,t';|\mathbf{p}-\mathbf{q}|)$ takes on its largest values since the momentum argument is small. This is also valid in the case considered here where we are interested in the high momentum regime. The reason for this lies in the special shape of $F_\phi(t,t';|\mathbf{p}|)$, i.e. a high occupation in a narrow momentum regime at low momenta. Applying a memory expansion as in Sec. 4.1.2.1 would lead to the same form of the equation as in (4.15). However, as we observed in that analysis, the momentum dependence of the solution gets lost since the equation of motion is reduced to a local differential equation with respect to the momentum. In this section we are interested in the momentum dependence of $n_\psi(t,|\mathbf{p}|)$. Therefore we have to keep the memory integration and evaluate it.

In order to make analytical progress in the large $|\mathbf{p}|$ limit we use free-field solutions which correspond to zero order (in the coupling g) solutions of the equation of motion. With vanishing boson field expectation value the next order in g is the loop contribution in (3.32) which is proportional to g^2 [11]. Such a perturbative approach should be reliable in the large momentum limit. Accordingly with the replacements

$$F_V(t,t'';|\mathbf{p}|) \;\to\; \frac{1}{2}\cos\Big(|\mathbf{p}|(t-t'')\Big)\,, \tag{4.30}$$

$$F^0_V(t,t'';|\mathbf{p}|) \;\to\; -\frac{i}{2}\sin\Big(|\mathbf{p}|(t-t'')\Big)\,, \tag{4.31}$$

$$\rho_V(t,t'';|\mathbf{p}|) \;\to\; \sin\Big(|\mathbf{p}|(t-t'')\Big)\,, \tag{4.32}$$

$$\rho^0_V(t,t'';|\mathbf{p}|) \;\to\; i\cos\Big(|\mathbf{p}|(t-t'')\Big)\,. \tag{4.33}$$

we get a form of the equation of motion which is

$$\partial_t F_V(t,t;|\mathbf{p}|) \simeq -2g^2\int_0^t dt''\int_{\mathbf{q}} F_\phi(t,t'';|\mathbf{p}-\mathbf{q}|)\cos\Big(2|\mathbf{p}|(t-t'')\Big)\,. \tag{4.34}$$

With (4.29) the momentum integral in (4.34) can be directly evaluated. We simplify the approximation by using $\gamma(\mathbf{p}) \simeq \gamma_0$ in the momentum integral. This will give us the correct $|\mathbf{p}|$-dependence. This avoids the occurrence of a polynomial time dependence which renders the analysis difficult to handle analytically. We will comment on the additional time dependence later again. The integral in our case gives ($\gamma_0 = m$)

$$\int_{\mathbf{q}} F_\phi(t,t'';|\mathbf{p}-\mathbf{q}|) \simeq \frac{A_0\,\gamma_0^3}{6\pi^2}e^{\gamma_0(t+t'')}\,. \tag{4.35}$$

[11] In the chiral limit considered here Eq. (3.32) is simplified as mentioned in Sec. 3.3.2. Of course the proportionality to g^2 remains.

With (4.35) the integral is roughly approximated and the amplitude of the solution of $n_\psi(t,|\mathbf{p}|)$ will be overestimated, however, the difference to the solution similar to the one in (4.16) is given by a time dependent factor $\sim (t+t'')^{-3/2}$. The time integrations we have to carry out lead to different time dependencies for these two approximations. We have verified that the $|\mathbf{p}|$-dependence remains the same. For a clear presentation of the relevant physics we stick to the approximate solution (4.35) with which the equation of motion becomes

$$\partial_t F_V(t,t;|\mathbf{p}|) \simeq -\frac{g^2 A_0 \gamma_0^3}{3\pi^2} \int_0^t dt''\, e^{\gamma_0 (t+t'')} \cos\Big(2|\mathbf{p}|(t-t'')\Big)\,. \tag{4.36}$$

Evaluating the memory integral we get

$$\partial_t F_V(t,t;|\mathbf{p}|) \simeq -\frac{g^2 A_0 \gamma_0^3}{3\pi^2} \frac{\gamma_0 e^{2\gamma_0 t} - e^{\gamma_0 t}\Big[\gamma_0 \cos\big(2|\mathbf{p}|t\big) - 2|\mathbf{p}| \sin\big(2|\mathbf{p}|t\big)\Big]}{4|\mathbf{p}|^2+\gamma_0^2}\,. \tag{4.37}$$

The next step is to integrate the equation in order to find the solution for $F_V(t,t;|\mathbf{p}|)$ which is connected to the fermion occupation number (3.82) (in the chiral limit). Using the initial condition $F_V(0,0;|\mathbf{p}|) = 1/2$, cf. Sec. 3.4, we find

$$F_V(t,t;|\mathbf{p}|) \simeq \frac{1}{2} - \frac{g^2 A_0 \gamma_0^3}{6\pi^2} \frac{e^{2\gamma_0 t} - 2e^{\gamma_0 t}\cos\big(2|\mathbf{p}|t\big) + 1}{4|\mathbf{p}|^2+\gamma_0^2}\,. \tag{4.38}$$

On first sight it seems to be astonishing that the denominator is the same after the integration. However, the special structure of the numerator leads to (4.38). For the occupation number we have immediately

$$n_\psi(t,|\mathbf{p}|) \;\simeq\; \frac{g^2 A_0 \gamma_0^3}{6\pi^2} \frac{e^{2\gamma_0 t} - 2e^{\gamma_0 t}\cos\big(2|\mathbf{p}|t\big) + 1}{4|\mathbf{p}|^2+\gamma_0^2} \;\approx\; \frac{g^2 A_0 \gamma_0^3}{6\pi^2} \frac{e^{2\gamma_0 t}}{4|\mathbf{p}|^2+\gamma_0^2}\,. \tag{4.39}$$

The second line follows from the fact that the first term quickly dominates the solution and thus the oscillatory behavior becomes suppressed for intermediate and late times. With this we find for the momentum dependent amplitude in Eq. (4.28) the expression

$$A(|\mathbf{p}|) \;\sim\; \frac{1}{4|\mathbf{p}|^2+\gamma_0^2}\,, \tag{4.40}$$

which reflects the observed behavior in the simulations in Fig. 4.17, i.e. $\sim 1/|\mathbf{p}|^2$. Especially, (4.40) points out that the power-law emerges for sufficiently large $|\mathbf{p}|$ compared to $\gamma_0 = m$.

Now we will have a closer look at the time dependence of (4.39). If we had used the same approximation for F_ϕ as in Sec. 4.1.2.1 (see (4.12) and (4.13)) in (4.34) the momentum integral would have lead to a time dependence as in (4.16) with $2t$

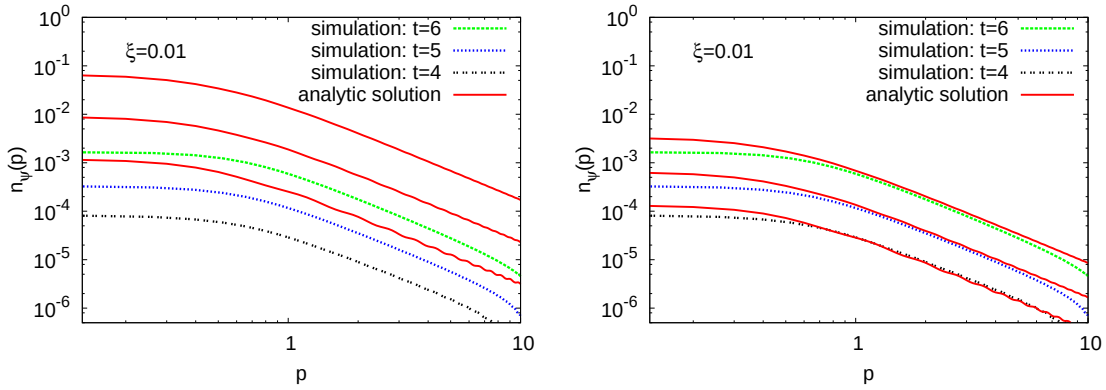

Figure 4.18: Comparison between the analytic solution and simulation of fermion spectra at times $t = 4/m$, $t = 5/m$ and $t = 6/m$ for $\xi = 0.01$, with $g = 0.01$ and $\lambda = 0.01$. Left: without correction factor. Right: with the correction factor $\sim t^{-2}$ in (4.39).

replaced by $t + t''$. The following t''-integration would lead to an expression which is impossible to handle. Neglecting a polynomial time dependence in the memory integral suggests to try to compensate the missing time dependence in the solution (4.39) with a polynomial factor $\sim t^{-\alpha}$ with some positive exponent α.

In the left plot of Fig. 4.18 we present a comparison of the analytical solution (4.39) with a simulation for $\xi = 0.01$ ($\lambda = 0.01$ and $g = 0.01$) at different early times. The shape of the analytical spectra agree quite well with the simulations, but the amplitude is wrong. This was already anticipated in the derivation of (4.39). In the right plot of Fig. 4.18 the same is shown as in the left plot, however in the analytical solution we used a $t^{-\alpha}$-factor with $\alpha = 2$. We observe that the difference becomes smaller and the solution describes the spectrum in a small time regime quite well. This confirms our analytical approach. The fact that our solution is not bounded in time reflects the range of validity of our approximation which is restricted to early times.

4.1.2.3 Approaching Thermal Equilibrium

In this subsection we will discuss and explain the statement made in Sec. 4.1.2.1 where we mentioned that $n_\psi(t, \mathbf{p}) = 1/2$ corresponds to a thermal spectrum for $\mathbf{p} \to 0$. In order to explicitly show that this is true consider the Fermi-Dirac distribution of massless fermions with zero net charge and vanishing chemical potential

$$n_{\mathrm{FD}}(|\mathbf{p}|) \;=\; \frac{1}{e^{|\mathbf{p}|/T}+1} \;\overset{|\mathbf{p}|\to 0}{\longrightarrow}\; \frac{1}{2}\,. \tag{4.41}$$

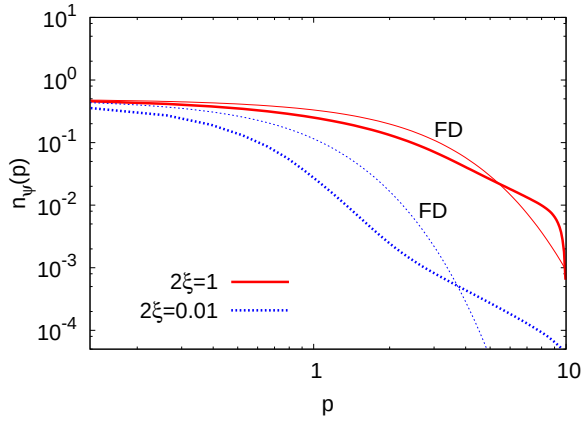

Figure 4.19: Comparison between Fermi-Dirac distribution (thin) and simulation of the fermion occupation number at $t = 90/m$ (thick) for $2\xi = 1$ (solid line) and $2\xi = 0.01$ (dotted line).

Hence, in the infrared limit we have $n_{\mathrm{FD}}(|\mathbf{p}|) = 1/2$ regardless of the temperature T. In Sec. 4.1.2.1 we learned that for $2\xi \gtrsim 0.1$ the infrared part of the fermion occupation number takes on the thermal value $1/2$ on a time scale smaller than t_ϕ. In Fig. 4.19 we compare a Fermi-Dirac distribution with $n_\psi(t, \mathbf{p})$ at $t = 90/m$. The results for $2\xi = 1$ are obtained from $g\sqrt{2} = 0.01$ and $\lambda = 10^{-4}$, whereas $2\xi = 0.01$ results from $g\sqrt{2} = 0.01$ and $\lambda = 0.01$. There we determine the temperature for $n_{\mathrm{FD}}(|\mathbf{p}|)$ by equating the energies obtained in a quasi-particle picture from the Fermi-Dirac statistics and our simulation respectively,

$$\int \frac{d^3p}{(2\pi)^3} \, |\mathbf{p}| \, n_{\mathrm{FD}}(|\mathbf{p}|) \; = \int \frac{d^3p}{(2\pi)^3} \, |\mathbf{p}| \, n_\psi(t, |\mathbf{p}|) \, . \tag{4.42}$$

For $2\xi = 1$ we observe that the infrared region of the spectrum indeed is close to a thermal spectrum. In contrast, at the same time the boson occupation number exhibits a nonperturbatively large amplitude and evolves orders of magnitudes in time towards a nonthermal fixed point, cf. Sec. 4.1.1. This leads to the conclusion that the fermion sector approaches thermal equilibrium faster than the boson sector. The presence of a fermionic thermal "heat bath" may cause interesting features in the subsequent evolution of the boson sector. In the case of $2\xi = 0.01$ Fig. 4.19 demonstrates that the thermal spectrum is not reached on a relatively small time scale and the deviations for high momenta are even larger. However, in general the pronounced excess of the occupation number with a power-law in the ultraviolet region compared to a thermal distribution may have phenomenologically interesting consequences.

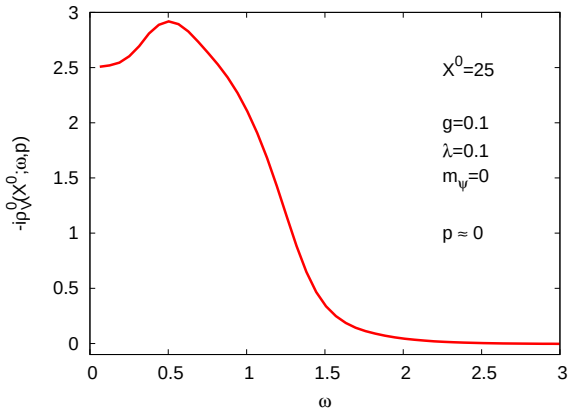

Figure 4.20: Spectral function $\rho_V^0(X^0;\omega,|\mathbf{p}|)$ as a function of ω for the smallest momentum $|\mathbf{p}| \approx 0$. A broad enhancement up to energies $\omega \approx m$ is present. The peak at $\omega \approx 0.5m$ is interpreted as an effective mass.

4.1.2.4 Spectral Function of Massless Fermions

In Sec. 4.1.1.3 we considered the boson spectral function as a function of ω. In this section we will discuss the fermionic counterparts $\rho_V^0(X^0;\omega,|\mathbf{p}|)$ and $\rho_V(X^0;\omega,|\mathbf{p}|)$ in the chirally symmetric version of the model (3.1). The motivation was stated in Sec. 4.1.1.3. For details of the calculation of the spectral function we refer to Appendix. D.

There exists a sum rule for the temporal vector part $\rho_V^0(X^0;\omega,|\mathbf{p}|)$, cf. Appendix D. This gives us a normalized quantity. It contains the information which (mass) state can be occupied. In Fig. 4.20 ρ_V^0 at $X^0 = 25/m$ for the smallest available momentum is displayed. We observe a broad spectrum up to energies $\omega \approx m$. It is interesting that this is also the case in the fermin occupation number as a function of momentum. For momenta $|\mathbf{p}| \lesssim m$ a highly occupied spectrum was observed and for $|\mathbf{p}| \gtrsim m$ a fall-off with a power-law behavior emerges. The occupation number $n_\psi(t,\mathbf{p})$ is defined for definite mass states, like it is the case in a free-field theory. Mass contributions coming from quantum corrections are not a priori respected by $n_\psi(t,\mathbf{p})$. In contrast the spectral function ρ_V^0 contains such information. It is interesting that the enhancements in both quantities qualitatively agree. The peak in Fig. 4.20 is interpreted as an effective mass $m_\psi^{\text{eff}} \simeq 0.5m$. The spectral function for higher momenta exhibits peaks at positions $\omega_{|\mathbf{p}|} = \sqrt{|\mathbf{p}|^2 + (m_\psi^{\text{eff}})^2}$. The amplitude of such high-momentum peak is very high and it would not fit into the figure above, therefore we skip the presentation.

The general peak structure can also be inferred from $\rho_V(X^0;\omega,|\mathbf{p}|)$. In the left plot of Fig. 4.21 we present the spatial vector part of the fermion spectral function for different momenta at center of mass time coordinate $X^0 = 45/m$. The right plot of

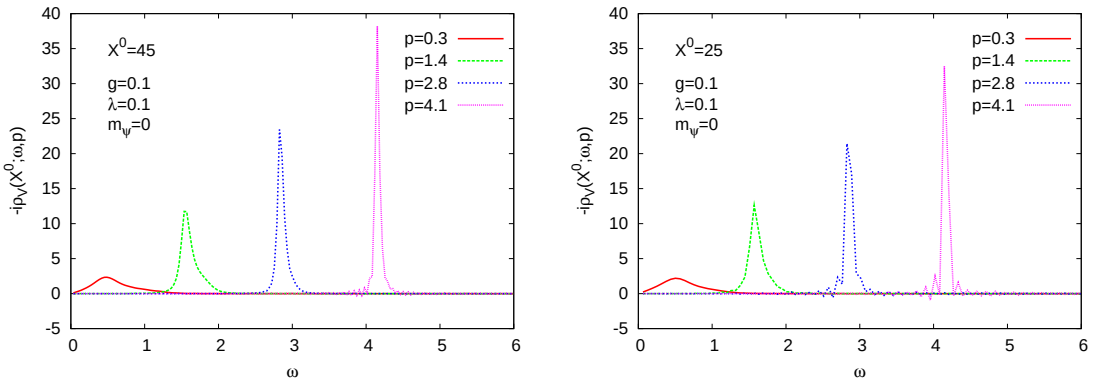

Figure 4.21: Fermion spectral function $\rho_V(X^0;\omega,|\mathbf{p}|)$ as a function of ω for different momenta indicated in the figure. In the left plot the center of mass time coordinate is $X^0 = 45/m$, in the right plot it is $X^0 = 25/m$ for comparison.

Fig. 4.21 corresponds to the left one but for a smaller X^0, i.e. $X^0 = 25/m$. We find the same results except for larger finite-time effects, however the qualitative shape of the spectra are both the same which reassures the reliability of the calculations which do not reach $X^0 = 45/m$. This will be the case in simulations with massive fermions. The coupling parameters correspond to $\xi = 0.1$. In the following we consider the left plot. Some minor finite-time effects are present for high modes. The width of the peaks differ significantly. The momentum mode with $|\mathbf{p}| = 0.3m$ shows a broad enhancement rather than a clear peak. Similar to the boson case, cf. Sec. 4.1.1.3, this is a signature of the domination of multiparticle processes. Deviations from a clear peak structure are in general observed for momenta $|\mathbf{p}| < m$. This region in the occupation number spectrum shows no power-law and has the largest amplitude, and thus the largest occupation. Hence the instability acts more efficient in this part of the spectrum. We conclude that there is a connection between strong deviations from a peak structure and the virtue of enhanced quantum corrections coming from an unstable evolution. This is supported by the fact that for smaller ξ all modes exhibit a clear peak structure. Since ξ can be seen as the strength of the instability, statements from above are confirmed. The positions of the well defined peaks are again describable in a quasi-particle picture with energy $\omega = \sqrt{\mathbf{p}^2 + m_{\text{eff}}^2}$. We find a small effective mass $m_{\text{eff}} \approx 0.5m$ generated by nonlocal self-energy contributions of the 2PI $1/N$-expansion[12]. This was also observed in ρ_V^0. The increase in the amplitude with higher momenta is interpreted as an approach towards a δ-function shape, which corresponds to stable particles.

[12]Note that this does not violate the fact that we have a chirally symmetric model.

4.2 Production of Massive Fermions

In the last section we studied the $SU(2)_L \times SU(2)_R$ symmetric model (3.1) which implies that only chiral fermions can be produced. The macroscopic field vanishes for all times and the $O(4)$-symmetry in the boson sector does not become broken. This is the generic case of spontaneous symmetry breaking in models with applications in the early universe [F$^+$01, FKL01] like in scalar hybrid inflation models. There, no (known) external force can push a field expectation value away from its origin ("false vacuum") so that it can "roll down" the potential hill towards the "true vacuum".

In this section we relax the chiral constraint and consider massive fermions. Due to the fermion backreaction term in the equation of motion (3.43) of the macroscopic field ϕ, the initially vanishing field ϕ becomes nonzero.Due to a nonvanishing fermion mass chiral symmetry is explicitly broken.

The consequences may play an important role, because now $\phi(t > 0) \neq 0$, and hence the fermion modes acquire a time dependent mass term $\sim g\phi(t)$. This could also be an origin of particle production similar to the well known case of parametric resonance, which we will consider in the next chapter.

The initial conditions were presented in Sec. 3.4 where we already discussed the implications of the value $\phi(t = 0)$ in combination with the presence of a fermion bare mass. There we stated that without fluctuations there is no fermion production if $\phi(t = 0) = 0$. Consequently the production mechanism, even in the case of massive fermions, is completely governed by the phenomenon explained in Sec. 4.1.

In this section we first consider the implication of the presence of a mass on the production mechanism reported in Sec. 4.1. Subsequently we will employ initial conditions which allow for a comparison of the tree-level production mechanism to the fluctuation induced counterpart. In both parts we concentrate on the early time evolution. We used the energy density, defined in Eq. (3.86), to control the accuracy of our numerical calculations. For all shown results the deviation from the initial total energy density did not exceed the order of one percent over the whole simulation time. In most cases the calculations have a deviation of less than one percent.

4.2.1 Fluctuation Induced Massive Fermion Production

If in the model (3.1) the fermion mass m_ψ is nonvanishing the field ϕ acquires a nonvanishing value $\phi(t)$ due to the fermion backreaction. In Fig. 4.22 we present the time evolution of $\phi(t)$ starting with $\phi(t = 0) = 0$ for different fermion masses, $m_\psi = 0$, $m_\psi = 0.15m$ and $m_\psi = 1m$. We observe that indeed, for $m_\psi \neq 0$ there is $\phi(t > 0) \neq 0$. The larger the fermion mass the bigger the backreaction. This is simply because $F_S(t, t; \mathbf{p}) \sim M_\psi(t)$ which is responsible for the symmetry breaking. The negative values of $\phi(t)$ are expected due to the sign in front of the Yukawa

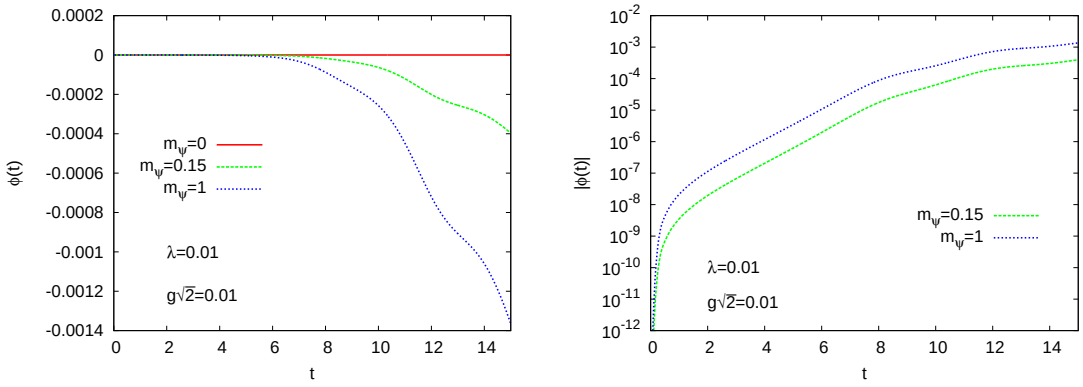

Figure 4.22: Fermion backreaction effect on the macroscopic field $\phi(t)$ for different masses m_ψ indicated in the figures. The left plot shows the actual evolution, the right plot shows the time evolution of the absolute value of $\phi(t)$ which illustrates that there is an exponential growth.

coupling in $M_\psi(t)$[13]. This has no further relevant implications. In the right plot we show the evolution of the absolute value on a logarithmic plot which shows an exponential growth which is $\sim e^{\gamma_\phi t}$ with an approximate growth rate $\gamma_\phi \approx m$. More important, the absolute value of $\phi(t)$ is very small, so that we observe on our simulated time scales $\phi(t) \approx 0$. In contrast the boson fluctuations become of order $1/\lambda$, see Fig. 4.23, and dominate the dynamics. This implies that there is no significant difference in the evolution compared to the chiral case, especially for the boson dynamics.

We emphasize that this tells us that the most natural set-up of the initial conditions in evolutions starting with a spinodal instability, i.e. $\phi(t=0)=0$, leads to the dynamics reported and explained in Sec. 4.1.

Now we would like to discuss the influence of the mass m_ψ on the generated fermion occupation number $n_\psi(t,|\mathbf{p}|)$.

The left plot Fig. 4.24 displays the time evolution of $n_\psi(t,|\mathbf{p}|)$ for $|\mathbf{p}|=0.1m$ in the three different cases $m_\psi=0,\ m_\psi=0.15m,\ m_\psi=1m$. For light fermions ($m_\psi=0.15m$) the evolution is practically the same. For heavier fermions the exponential growth starts later, however with the same growth rate. This delay causes a special shape of the corresponding spectrum (right plot) which we will consider below in detail. After the initial exponential growth the system enters a quasi-stationary evolution phase as was reported and explained in Sec. 4.1.2. In summary we infer from these results that the main characteristics of the time evolution are the same for massive fermions, except for the amplitude.

Now we turn to the discussion of $n_\psi(t,|\mathbf{p}|)$ as a function of the momentum. In the

[13]The Lagrangian contains a term $\sim -g\bar{\psi}\psi$. This produces a tilt with positive slope, cf. (3.1).

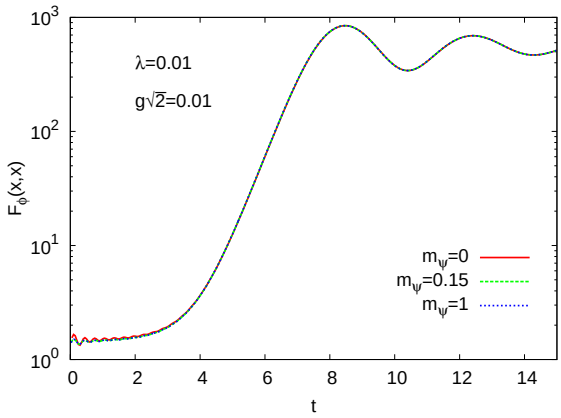

Figure 4.23: Time evolution of the boson statistical two-point correlation function $F_\phi(x,x)$ for different fermion masses. It illustrates the independence of the boson dynamics on the fermion dynamics in the case of massive fermions. Note that here effectively $F^\phi_\parallel(x,x) = F^\phi_\perp(x,x) = F_\phi(x,x)$.

right plot of Fig. 4.24 we present simulation results of the corresponding spectra, at time $t = 8/m$, which corresponds to the time at which the unstable growth stops, cf. the left plot. We observe that in the high momentum regime the spectra approach each other whereas in the low-momentum regime the deviations become large. The characteristic ultraviolet power-law $n_\psi(|\mathbf{p}|) \sim |\mathbf{p}|^{-2}$ is well established, cf. Sec. 4.1.2. The spectra with nonvanishing fermion mass show a very specific shape. There is a slight fall-off for momenta $|\mathbf{p}| < m_\psi$ which yields a maximum around $|\mathbf{p}| \approx m_\psi$. The amplitude decreases with larger masses which is expected since it needs more energy to create heavier fermions than light ones. The characteristic shape of the spectra of massive fermions become comprehensible if we consider the difference to tree-level results, i.e. produced fermions via the time dependent mass term $\sim g\phi(t)$. In the case of parametric resonance this is the typical mechanism known from the literature. In Chapter 5 we will consider such scenarios and go beyond tree-level dynamics by including the fermion-boson loop. If $\phi(t)$ is changing in time the corresponding term in the equation of motion for the correlators acts like a source. This yields a nonvanishing $n_\psi(t, |\mathbf{p}|)$ even without loop corrections.

Naturally, the question arises, in which situations the loop correction dominates the dynamics. We already learned in the last section that this is the case if $\phi(t = 0) = 0$, no matter if it is kept fixed at zero or if it is dynamically pushed away from the origin by fermion fluctuations.

Since there are also physical situations where an external force can cause an initial displacement of $\phi(t = 0)$ and this might lead to larger values of $\phi(t)$ during the evolution as compared to the results above, it is worth to consider such situations

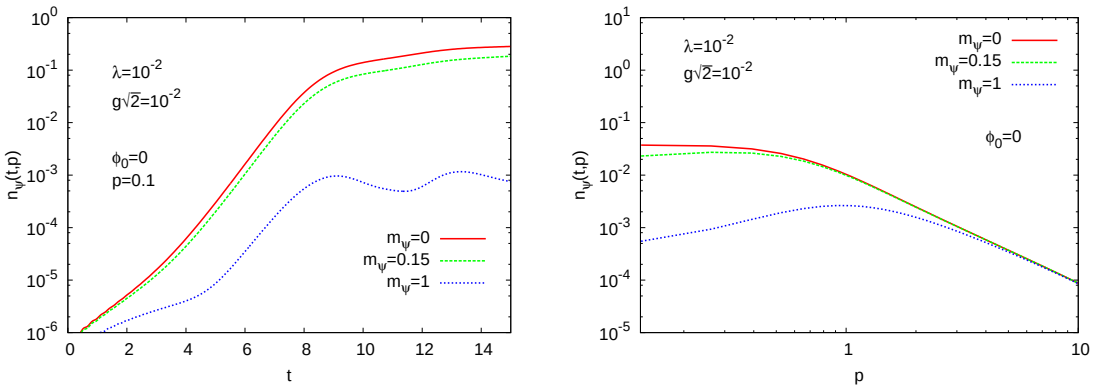

Figure 4.24: Simulation results of $n_\psi(t, |\mathbf{p}|)$ for different masses indicated in the figure. Left: time evolution for $|\mathbf{p}| = 0.1m$. Right: corresponding spectrum at $t = 8/m$. A new feature is the decreasing amplitude of the spectrum for small momenta.

and determine the conditions where the loop correction dominates. A possible physical situation might be the cooling of a ferromagnet with a nonnegligible external magnetic field.

4.2.2 Implications of a Nonnegligible Field Expectation Value

In this section we will consider situations where initial displacements yield larger values for the macroscopic field and discuss the competition between tree-level and loop corrections. In the first part we discuss the major aspects of a nonnegligible $\phi(t)$. We are going to present the results for the boson and fermion dynamics in two separate subsections. In the second part we focus on the fermion dynamics and analyze the different influences of the tree-level and loop contributions. We concentrate on the early-time behavior, i.e. the evolution phase where the instability acts and the onset of the transition to the quasi-stationary regime.

Boson Dynamics

We learned in Sec. 4.1 that the boson dynamics is independent from the fermion dynamics if the Yukawa coupling is not too high. In order to show that this is also the case if the symmetry is broken and $\phi(t)$ is not approximately zero, we display in the left plot of Fig. 4.25 simulation results of the boson occupation number $n_\phi(t, \mathbf{p})$ as a function of time for different momenta. Due to the initially small macroscopic field

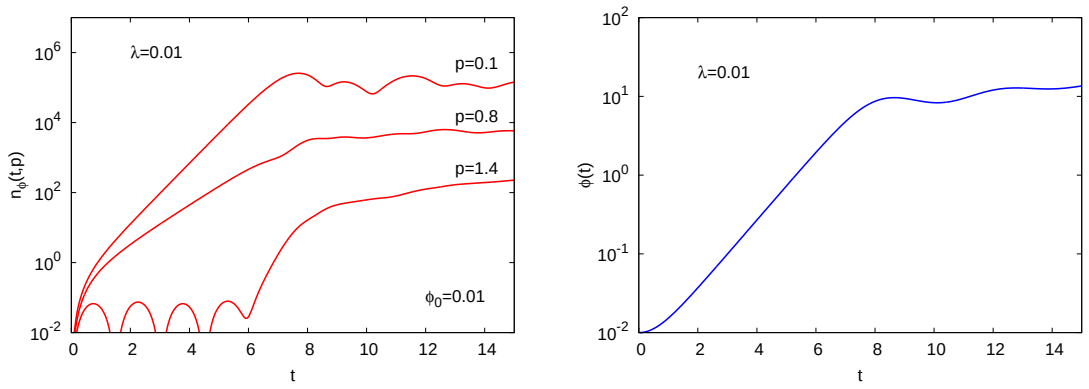

Figure 4.25: Left: time evolution of $n_\phi(t, \mathbf{p})$ for different momenta as indicated in the figure with $\lambda = 0.01$. The Yukawa coupling is $g\sqrt{2} = 0.01$. Right: evolution of the macroscopic field with an initial value of $\phi(t = 0) = 0.01m$, the parameters are the same as in the left plot.

ϕ longitudinal and transversal components are amplified equally[14]. The couplings are $\lambda = 0.01$ and $g\sqrt{2} = 0.01$[15]. Here the fermions have a vanishing mass $m_\psi = 0$, however, we would like to emphasize that there is no qualitative change in the boson results if $m_\psi \neq 0$, which was checked numerically too. The initial value of the macroscopic field was chosen to be $\phi(t = 0) = 0.01m$, this small displacement causes a nonvanishing evolution of $\phi(t)$ which is also shown in Fig. 4.25[16]. The corresponding evolutions for the fermion occupation number are given in Fig. 4.27 below.

We observe practically the same results as in Fig. 4.1 in Sec. 4.1, although the expectation value $\phi(t)$ is not negligible as can be seen in the right plot. The macroscopic field also grows exponentially as expected and stops at some point where the fluctuations become parametrically of order $1/\lambda$. Here a nonvanishing fermion mass m_ψ would not change anything. Since each mode shows the same result as in Sec. 4.1 the shape of the occupation number spectrum looks the same as the corresponding ones (up to $t \approx 10/m$) in Fig. 4.5.

Recall that the origin of the unstable evolution phase lies in a negative mass squared, cf. Sec. 4.1.1. A nonvanishing $\phi(t)$ yields positive contributions to the effective mass, as can be seen in Eq. (3.42). For small $\phi(t)$ (and small λ) these contributions are suppressed. Larger values would correspondingly lead to nonnegligible contributions. If $\phi(t = 0)$ would be larger than the spinodal point $\phi_s = m\sqrt{4/\lambda}$, the

[14] Accordingly in Fig. 4.25 we used the label $n^\phi_\parallel(t, \mathbf{p}) = n^\phi_\perp(t, \mathbf{p}) = n_\phi(t, \mathbf{p})$

[15] Recall that the exact value of the Yukawa coupling is not relevant for the boson dynamics as mentioned in Sec. 4.1.

[16] Here we chose a positive $\phi(t = 0)$ without loss of generality.

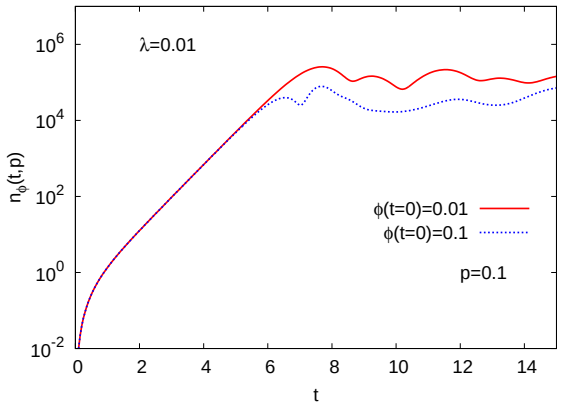

Figure 4.26: Time evolution of the boson occupation number with a momentum of $|\mathbf{p}| = 0.1m$ for two different initial values of the macroscopic field indicated in the figure. Couplings are the same as in Fig. 4.25.

initial conditions for an instability would be violated. If $\phi(t = 0)$ is not too small the exponential growth of $\phi(t)$ is responsible for large values of the macroscopic field. This causes a leading order contribution to the earlier end of the unstable phase. Of course the nonlinearly generated fluctuations are responsible, too, and without a macroscopic field the unstable phase terminates at some point, as was discussed and explained in Sec. 4.1. For a confirmation of these statements see Fig. 4.26 where a time evolution of boson occupation number modes are shown, where in one case $\phi(t = 0) = 0.01m$ and in the other $\phi(t = 0) = 0.1m$. The growth rate is the same because at the beginning the positive mass contributions are negligible and the rate can be determined as done at the beginning of Sec. 4.1.1. That means, the smaller the initial value of ϕ the larger is the duration of the unstable evolution phase. This implies a more efficient fermion production in those cases where $t_\phi > t_\psi$, cf. Sec. 4.1.2. The time scale t_ϕ parametrizes the duration of the unstable evolution phase. In Sec. 4.1.2 we were confronted with the maximally efficient case, i.e. $\phi(t) = 0$. Actually for $\phi(t = 0) = 0.01m$ there are no differences in t_ϕ as compared to $\phi(t = 0) = 0$, so for $\phi(t = 0) \lesssim 0.01$ we can adopt the main results of Sec.4.1.

The subsequent evolution of $\phi(t)$ (i.e. for $t \gtrsim 10/m$) turns out to be highly influenced by infrared fluctuation modes. Shifting the cut-off Λ_{IR} towards smaller values changes the evolution after the stop of exponential growth in ϕ. However, correlation function modes are not affected in the first place by cut-off changes. In our study here we are interested in the early-time evolution where everything is quite insensitive against cut-off changes, for details see Appendix F. Nevertheless we would like to mention that independently from the cut-off value, the characteristics of the late-time evolution of the macroscopic field seems to be a nonoscillating evolution. We observed at most one half of an oscillation of $\phi(t)$ before it starts to show a

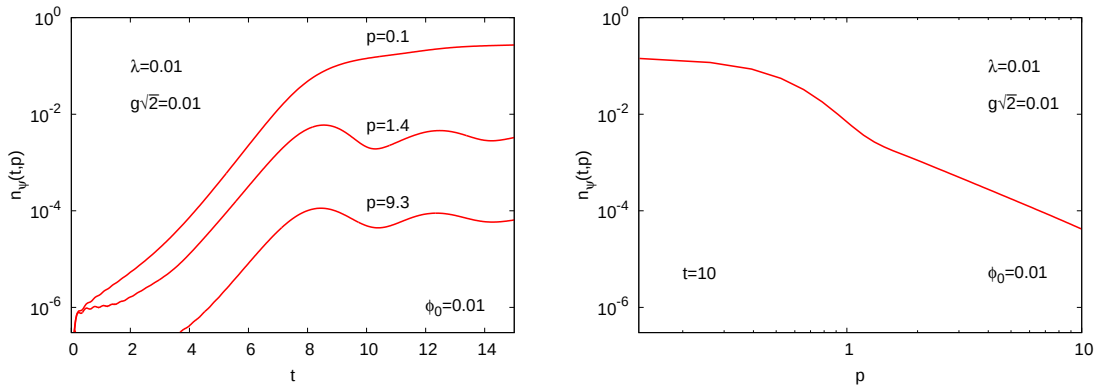

Figure 4.27: Time evolution (left) of $n_\psi(t, |\mathbf{p}|)$ for different momenta and couplings indicated in the figure, $m_\psi = 0$. The right plot shows the corresponding spectrum after $(t = 10/m)$ the unstable evolution.

evolution reminiscent of a drift, cf. Fig. 4.25. Qualitatively the same phenomenon was observed in a supersymmetric hybrid model in Ref. [BKP07]. This might be a nonequilibrium signature that the effective potential of the system acquires a convex shape[17]. This is expected but, to our knowledge, was not yet observed in a 2PI simulation. Moreover there are no parametric resonance effects ensuing the spinodal instability.

In summary we learned that also in the broken symmetry case the early time dynamics of the bosons is not altered qualitatively. This points out that the results obtained in Sec. 4.1.1 are quite general. Long time simulations need to be taken with care because of the strong influence of infrared fluctuations on the dynamics of the macroscopic case.

Equipped with the knowledge of the boson dynamics we can now turn to the analysis of the fermion evolution in the presence of broken symmetry.

Fermion Dynamics

We first discuss the results of the time evolution of $n_\psi(t, \mathbf{p})$ for different momenta, i.e. the results corresponding to those considered in Fig. 4.25. The results of $n_\psi(t, \mathbf{p})$ are given in Fig. 4.27. Recall that $\lambda = 0.01$, $g\sqrt{2} = 0.01$, $m_\psi = 0$ and $\phi_0 = 0.01$. Again we observe qualitatively the same result as for the chiral case in Sec. 4.1.2. The whole spectrum gets amplified with approximately the same growth rate, cf. Sec. 4.1.2. After the initial exponential growth the system enters a quasi-stationary phase which will not discussed here, as it was mentioned above. In the last subsection we already observed that with $\phi_0 = 0.01m$ we practically obtain the boson dynamics

[17] Note that for a proper convex potential all infrared fluctuations have to be taken into account[BTW02].

for $\phi_0 = 0$. This leads to the same production mechanism for the fermions which is confirmed by the results in Fig. 4.27.

The corresponding spectrum right after the exponential growth terminates is given in the right plot of Fig. 4.27. The characteristic shape already observed in Fig. 4.17 is present. The power-law with exponent two for momenta $|\mathbf{p}| > m$ is well established and the infrared is not far away from the thermal value 1/2, cf. Sec. 4.1.2. We conclude that the tree-level term in this case just plays a subdominant role.

With these results we have shown that even if the expectation value is not vanishing during the unstable evolution phase the fermion production mechanism reported in Sec. 4.1 is still valid.

4.2.2.1 Fermion-Boson Loop vs. Tree-Level

In the following we will present a study of different sets of parameters with which we are able to determine the initial condition of ϕ for which the quantum loop corrections dominate or, on the other hand do not lead to a change compared to tree-level physics[18]. We will consider light fermions with $m_\psi = 0.15m$ and employ three different initial conditions of ϕ within two different sets of couplings, ($\lambda = 0.01, g = 0.01$) and ($\lambda = 10^{-6}, g = 10^{-3}$). First we will focus on the time evolution of different modes in both sets and afterwards we will turn to the discussion of the spectra.

Early-Time Evolution

In Fig. 4.28 we present simulations of the time evolution of the fermion occupation number $n_\psi(t; \mathbf{p})$. These plots show the characteristic early-time dynamics. The coupling parameters are $g = 10^{-2}$, $\lambda = 10^{-2}$ in the left column and $g = 10^{-3}$, $\lambda = 10^{-6}$ in the right column. The initial value of the macroscopic field $\phi(t)$ is changed from top to bottom in each parameter set, i.e. $\phi_0 = 10^{-2}m, 10^{-1}m, 1m$ respectively. The fermion mass is $m_\psi = 0.15m$[19]. In each plot we present the time evolution for two values of the momentum including the fermion-boson loop (red lines, 2PI$^+$) and neglecting it (2PI$^-$). The specific values of the momenta become clear later. The first observation is the qualitatively equal evolution in each parameter set. In the following we will describe the main features of the dynamics which consequently holds for both sets.

We first discuss the case $\phi_0 = 10^{-2}m$ (first row). We observe an exponential growth in both types of approximations with the same growth rate in a certain

[18] Note that the set of parameters is arbitrary and the information we will gain could also be gained from other parameter sets.

[19] In order to resolve the main characteristics of the spectrum we have to consider a certain momentum regime. It is sufficient to consider a range of $|\mathbf{p}| \approx \{0.01, 1\}$, therefore we chose $a_s = 1$ and $N = 256$.

time interval. That the 2PI$^-$ approximation also shows an exponential growth is expected. However, the difference of the two approximations is clearly visible. The amplitude of the occupation number in 2PI$^+$ is at least one order of magnitude larger. Thus the quantum correction due to the loop has a significant impact on the dynamics, more precisely, it dominates the evolution.

Now we turn to the case $\phi_0 = 10^{-1}m$ (middle row). The development of an exponential growth is less pronounced as in the previous case and stops earlier. The large difference of the two approximations is only observable at very early times. During the exponential growth the modes with $|\mathbf{p}| = 0.15m$ are almost identical and the difference in the case of $|\mathbf{p}| = 0.02m$ becomes less. The amplitude of the occupation number in 2PI$^-$ increases compared to the plot on the top. The mode with $|\mathbf{p}| = 0.02m$ in 2PI$^+$ acquires a smaller amplitude as in the case with $\phi_0 = 10^{-2}m$. Consequently we observe that the properties of the dynamics for the two approximations approach each other for certain momenta. Effects of the macroscopic field and the loop enter the dynamics as a mixture, which becomes clear below when we consider the spectra.

In the case with $\phi_0 = 1m$ during the unstable evolution there is almost no difference between the two approximations visible except for extremely early or late times. More important, there is no exponential growth visible, however the overall amplitude is larger as in the other two simulations. The growth behaves approximately polynomially with a large exponent ($\gtrsim 4$). The exponential growth ends even earlier compared to $\phi_0 = 10^{-1}m$. Accordingly, the dynamics with $\phi_0 = 1m$ is governed by the macroscopic field interaction.

In summary we learned that for large values of ϕ_0 the loop becomes less important. Below we will confirm this with analytical estimates of the contributions to the equations of motion for the corresponding two-point correlation function. We stress that the conclusion here is restricted to the early-time evolution, i.e. it is valid for the unstable evolution phase and the transition to the quasi-stationary regime. We expect that afterwards the loop always has an important impact in the low- and high-momentum regime.

Spectra

In Fig. 4.29 we present the corresponding spectra for both approximations (red lines, 2PI$^+$) belonging to the simulations in Fig. 4.28. We took snapshots of the spectra at time $t = 5/m$ (left column) and $t = 8/m$ at which occupation number modes exhibit exponential growth or just exit this regime (this is the case for $\phi_0 = 1m$). Note that the amplitudes are rather small because the production at that time has not yet finished. In the first row of Fig. 4.29 the spectra of the 2PI$^+$ simulations show the typical shape which emerges in the case of fluctuation induced massive fermion production, cf. Sec. 4.2.1. In the high-momentum regime we also observe a

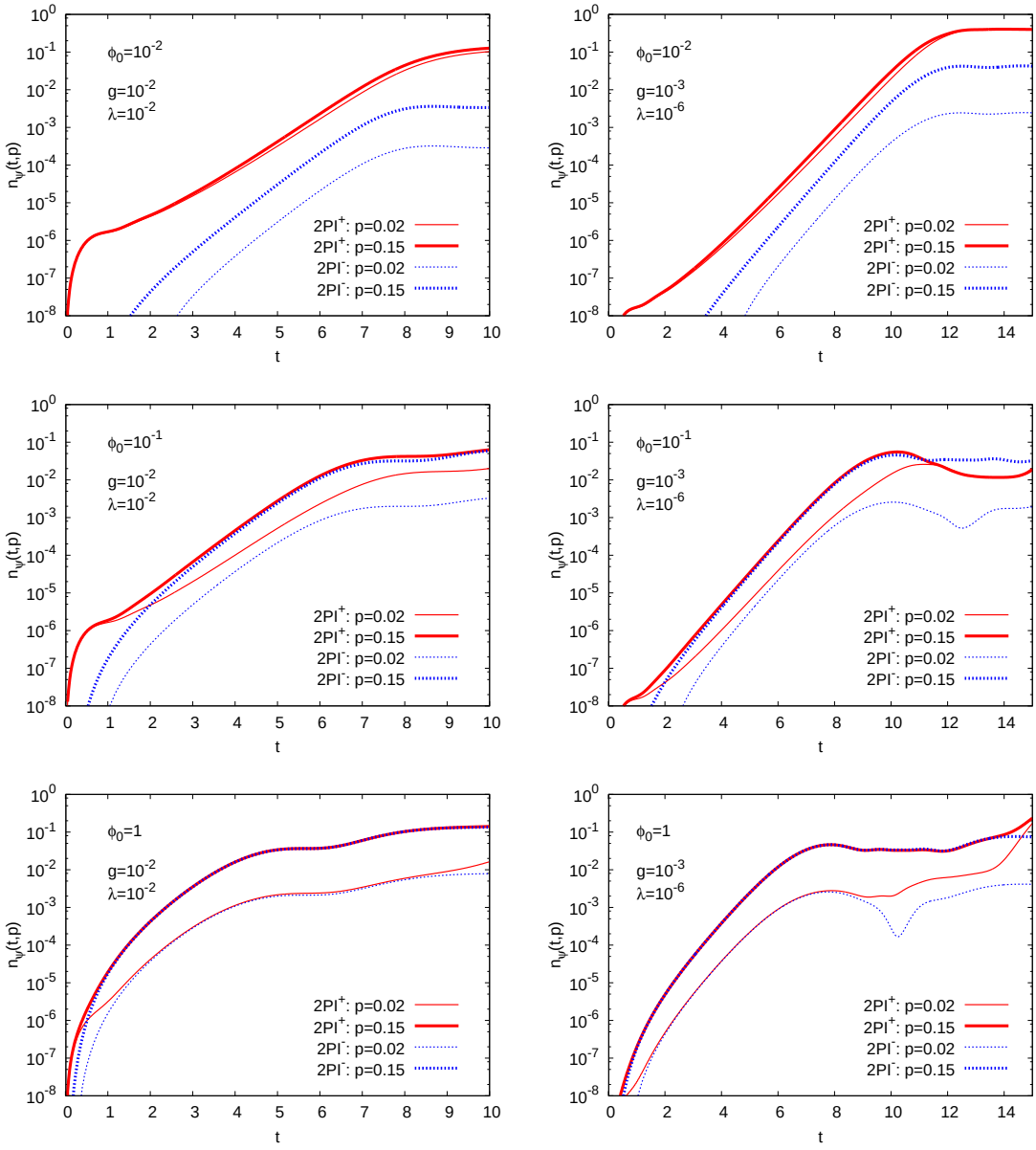

Figure 4.28: Time evolutions of $n_\psi(t, |\mathbf{p}|)$ where only tree-level (2PI$^-$) interactions are taken into account compared to the corresponding simulations where the loop correction is included (2PI$^+$). We compare in each plot two momenta indicated in the figure, respectively. In the left and right column one coupling set is presented for different ϕ_0.

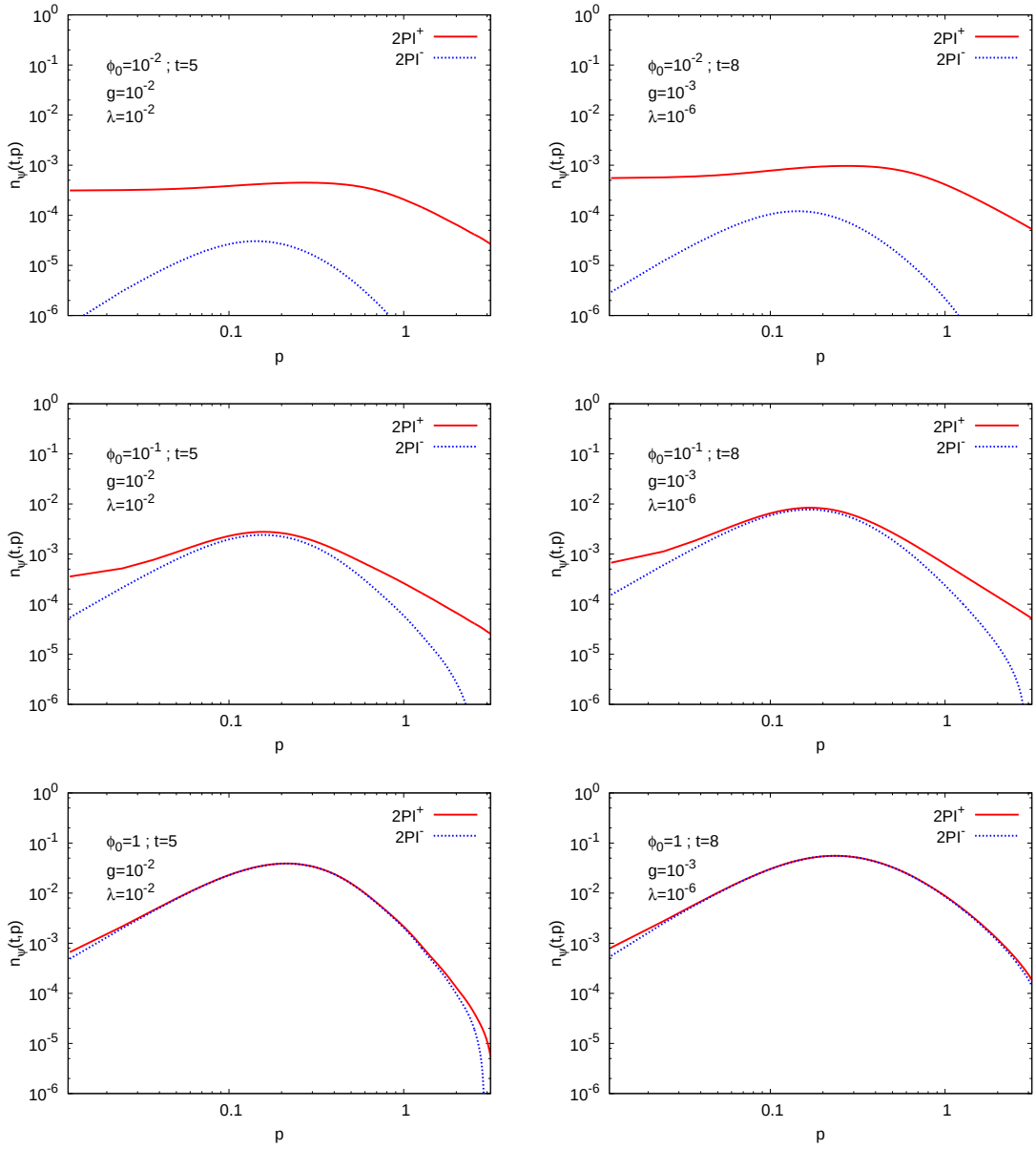

Figure 4.29: Comparison between tree-level (2PI^-) and loop-correction (2PI^+) simulations of $n_\psi(t, |\mathbf{p}|)$ as a function of momentum for different ϕ_0 (from top to bottom) and two different sets of couplings (left and right column).

power-law with exponent minus two. In the low-momentum regime the amplitude first falls of slightly and then saturates at a certain value. Since we have massive fermions the amplitude of the deep infrared part of the spectrum does not have to have the characteristic value 1/2 at the end of the evolution, as in Sec. 4.1. The corresponding spectra in the 2PI$^-$ simulations have an amplitude which is at least one order of magnitude smaller. Those spectra acquire a special form which shows a maximum at the position $|\mathbf{p}| \approx m_\psi$. On the left side of this peak the spectrum increases with a power-law with an exponent approximately equal to two. On the right side the shape behaves approximately like[20] $1/|\mathbf{p}|^4$. Consequently the 2PI$^+$ simulations show a considerable excess of occupation in the infrared and ultraviolet.

In the middle row of Fig. 4.29, where $\phi_0 = 10^{-1}m$, we observe that the results of both approximations approach each other. The 2PI$^+$ simulations now have a maximal value at $|\mathbf{p}| \approx m_\psi$ too, however there is no fall-off towards smaller momenta. The spectrum again exhibits a power-law with exponent minus two for $|\mathbf{p}| > m_\psi$. Thus the slope of the high momentum fall-off is lower compared to 2PI$^-$ and again we observe that the fermion-boson loop quantum correction yields an excess of occupation.

In the lowest row of Fig. 4.29, where $\phi_0 = 1m$, 2PI$^+$ and 2PI$^-$ qualitatively yield the same results. The excess due to the loop is no longer present. The spectrum is entirely determined by the interaction with the macroscopic field. However, the amplitudes are larger compared to the two previous cases.

Now it becomes clear why we have chosen $|\mathbf{p}| = 0.02m_\phi$ and $|\mathbf{p}| = 0.15m_\phi$ as two examples of the time evolution in Fig. 4.28. They correspond to modes in the deep infrared and the peak position. This is the reason why in the case of $\phi_0 = 10^{-1}m$ one pair of modes is almost identical and the other is not. Hence the main characteristics of both approximations can be deduced from both figures.

In conclusion the spectra confirm the results stated above. The initial value of the background field judges which kind of dynamics has the dominating impact on the dynamics. We want to emphasize that the choice of the initial value ϕ_0 has no physical reasoning. In the case of massive fermions there is no need of an initial displacement since the fermion interaction breaks the Z_2-symmetry. Hence one can choose the natural value $\phi_0 = 0$. With the above results it is clear that in those situations the fermion-boson loop quantum correction dominates the dynamics and neglecting it would lead to a failure of the description.

In the following we want to derive a condition which states for which initial value ϕ_0 the dynamics is governed by the classical (macroscopic background field) or quantum (fermion-boson loop) contribution. A similar consideration in the case of a pure scalar field model was done in [BCdV$^+$98]. We have to consider the equations of motion of the equal time two-point functions $F_V(t,t;|\mathbf{p}|)$, $F_S(t,t;|\mathbf{p}|)$

[20] A $1/|\mathbf{p}|^4$ behavior for large momenta was also observed in Refs. [NPS01a, GRT99] where fermions interact with a classical background field.

and $F_T(t,t;|\mathbf{p}|)$, since they are coupled. Following the arguments in Sec. 4.1.2 we can write (3.30), (3.32) and (3.33) in the form

$$\partial_t F_S(t,t;|\mathbf{p}|) = -2|\mathbf{p}|F_T(t,t;|\mathbf{p}|)\,, \tag{4.43}$$

$$\partial_t F_V(t,t;|\mathbf{p}|) = 2M_\psi(t)F_T(t,t;|\mathbf{p}|) + \mathrm{K}_V(t)F_V(t,t;|\mathbf{p}|)\,, \tag{4.44}$$

$$\partial_t F_T(t,t;|\mathbf{p}|) = 2|\mathbf{p}|F_S(t,t;|\mathbf{p}|) - 2M_\psi(t)F_V(t,t;|\mathbf{p}|) + \mathrm{K}_T(t)F_T(t,t;|\mathbf{p}|)\,, \tag{4.45}$$

where[21] $\mathrm{K}_{V,S,T}(t)$ is proportional to g^2 and contain the information of the quantum correction represented by the loop in Fig. 3.2. We want to stress that although $\mathrm{K}_{V,S,T}(t)$ contains a loop integral it is not cut-off dependent, since the integrand is dominated by the infrared part[22]. The unstable behavior in the boson sector consequently produces exponentially growing "source" terms in (4.44), (4.45) and indirectly in (4.43). Compared to the approximated equation of motion in Sec. 4.1.2 we have additional nontrivial time dependent terms which prohibits an analytical description similar to the one in Sec. 4.1.2. Hence we proceed by estimating the impact of the macroscopic field and the loop correction.

We expect to have situations where either the loop corrections (see left diagram in Fig. 3.2) or the macroscopic field ϕ dominate the equations of motion and hence the dynamics of the occupation number or a mixture of both aspects, see Fig. 4.28. In the above equations (4.43)–(4.45) there is a "classical source" $g\phi(t)$ coming from the time dependent mass $M_\psi(t)$ and a "quantum source" $K_{V,S,T}(t)$ coming from the fermion-boson loop. The time dependence of both during the unstable evolution can be described by

$$g\phi(t) = g\phi_0\, e^{mt}; \quad \mathrm{K}_{V,S,T}(t) = K_0\, e^{2mt}, \tag{4.46}$$

where K_0 has the dimension of a mass and is defined by

$$K_0 = g^2\tilde{\mathrm{K}} \equiv g^2 A_0(\pi t)^{-3/2}\sqrt{mc}/2\,, \tag{4.47}$$

with $A_0 m = 1/4$ and c a constant of approximately order one. We take in $\tilde{K}$ the time $t \sim \mathcal{O}(1)$ with which we have $\tilde{K} \approx 0.01$. This means that we concentrate on the evolution where the polynomial time dependence is suppressed, which does not alter our conclusions below. The dominance of one of the sources in the equations requires a larger value of the corresponding source, and consequently we can estimate parametrically the impact by determining the time scale at which they become of the order one. A lower time scale yields an earlier impact and thus to the corresponding characteristic behavior of the dynamics. We denote the timescale at which the

[21] The Lorentz subscripts V, S, T on the K-functions just indicates the affiliation to the corresponding equation.

[22] The domination becomes pronounced at not too early times.

background field contribution becomes of order one by t_{class} and the time scale at which the quantum corrections become of order one by t_ψ[23]. Expressing everything in units of the boson mass, we get

$$g\,\phi_0\,e^{mt} \sim m \quad \Rightarrow \quad t_{\text{class}} \sim \frac{1}{m}\log\left(\frac{m}{g\phi_0}\right)\,, \tag{4.48}$$

$$g^2\tilde{K}e^{2mt} \sim m \quad \Rightarrow \quad t_\psi \sim \frac{1}{2m}\log\left(\frac{m}{g^2\tilde{K}}\right)\,. \tag{4.49}$$

So we obtain the following result:

$$t_{\text{class}} \gg t_\psi \quad \Rightarrow \quad \frac{\phi_0}{m} \ll \sqrt{\frac{\tilde{K}}{m}} : \qquad \text{loop dominates}\,, \tag{4.50}$$

$$t_{\text{class}} \ll t_\psi \quad \Rightarrow \quad \frac{\phi_0}{m} \gg \sqrt{\frac{\tilde{K}}{m}} : \qquad \text{background field dominates}\,. \tag{4.51}$$

This means that, $\phi_0 \gg 0.1\,m$ for a classical evolution and $\phi_0 \ll 0.1\,m$ for a quantum evolution. For $\phi_0 \approx 0.1\,m$ we expect that the dynamics shows features of both kinds of sources. Accordingly we find that the initial value of the background field determines if we have a classically dominated evolution or if the dynamics is governed by quantum fluctuations. This is what is observed in the simulations in Fig. 4.28 and Fig. 4.29.

The reason for the classical dominance in the case $\phi_0 \gtrsim 0.1$ is that the derivative of $\phi(t)$, due to the "rolling down", is larger as for smaller values of ϕ_0. A large derivative means a strong violation of the adiabatic condition, which is interpreted as the origin of the particle production via a classical background field [GK00]. Thus a strong violation causes an efficient particle production. One can explicitly show with the equations of motion for the fermion correlation function without loop contributions that a nonvanishing derivative is needed for a particle production.

We close this section with the conclusion that the loop contribution, i.e. fluctuation effects, dominate the fermion production dynamics for a wide range of initial conditions in the case of a spinodal instability. More precisely, for all natural initial conditions, i.e. $\phi_0 \approx 0$, the loop always dominates. Furthermore the fermion production induced by fluctuations is more efficient than due to a classical background field. This could have a large impact on phenomenological results if it is respected in more realistic models.

[23] This is the same time scale t_ψ as in Sec.4.1.2, except from numerical factors which are irrelevant for our purposes here.

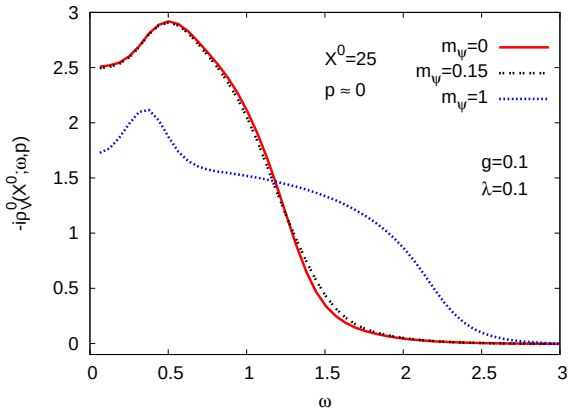

Figure 4.30: Comparison of the spectral function $\rho_V^0(X^0;\omega,|\mathbf{p}|)$ for $|\mathbf{p}| \approx 0$. Simulations with three different masses (indicated in the figure) are compared.

4.2.2.2 Spectral Function of Massive Fermions

Considering the spectral function requires simulations which reach late times in order to minimize finite-time effects. We observed in Sec. 4.2.2 that the late time dynamics suffers from infrared cut-off dependencies. Therefore it does not make sense to consider corresponding spectral functions. However the actual late time dynamics is characterized by a nonoscillating background field ϕ since it approaches its minimum slowly, cf. Sec. 4.2.2. Therefore the leading order fermion mass would be constant anyway. A mass contribution coming from the next-to-leading order contribution is included due to the fermion-boson loop. Boson fluctuations in the presence of a nonvanishing constant ϕ are assumed to be not much different compared to the case $\phi = 0$. Consequently it is worth to consider simulations of the dynamics of the type as in Sec. 4.1, but with a nonvanishing fermion mass m_ψ. If we consider massive fermions we have to consider $\rho_V^0(X^0;\omega,|\mathbf{p}|)$, $\rho_V(X^0;\omega,|\mathbf{p}|)$ and the scalar component $\rho_S(X^0;\omega,|\mathbf{p}|)$ which vanishes in the chiral case.

We first consider the normalized function $\rho_V^0(X^0;\omega,|\mathbf{p}|)$. In Fig. 4.30 we present a comparison of results with different masses, i.e. $m_\psi/m = 0,\ 0.15,\ 1$. The result for $m_\psi = 0$ was already discussed in Sec. 4.1.2.4. We see that a small mass qualitatively does not change anything. A larger mass leads to a broadening of the spectrum along with a decrease of the amplitude. Further, the peak at $\omega = 0.5m$ moves slightly towards a smaller value. Consequently we observe that for a higher mass more high energy state can be occupied, whereas the low energy states are less pronounced. This is plausible. If we have a look at the occupation number for $m_\psi = m$, see Fig. 4.24, we observe less occupied low-momentum modes. The high-momentum region is not very different from that for massless particles. The overall amplitude of $n_\psi(t,\mathbf{p})$ for $m_\psi = m$ is smaller. This is expected since the initial energy in

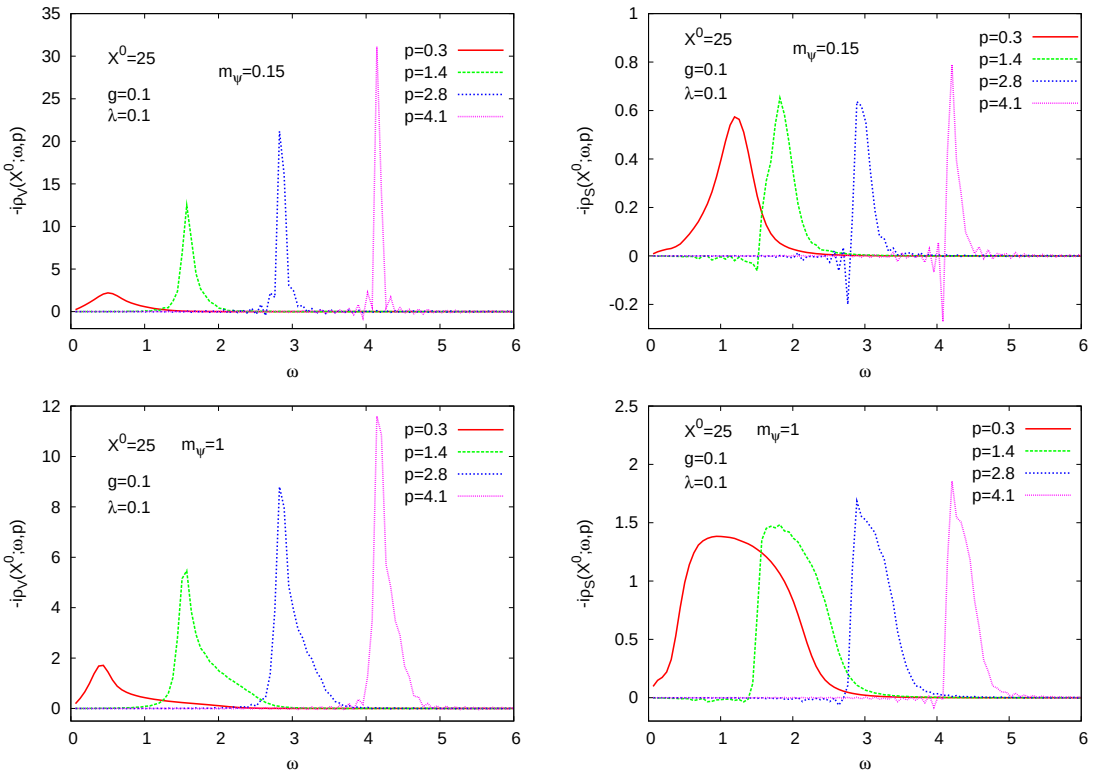

Figure 4.31: Fermion spectral functions in the case of spinodal instability. The left plots show $\rho_V(X^0;\omega,|\mathbf{p}|)$ the right plots the corresponding $\rho_S(X^0;\omega,|\mathbf{p}|)$. The upper row considers $m_\psi = 0.15m$, the lower row shows $m_\psi = m$.

those simulations is the same. Results of $\rho_V(X^0;\omega,|\mathbf{p}|)$ and $\rho_S(X^0;\omega,|\mathbf{p}|)$ for light fermions with $m_\psi = 0.15m$ and heavier fermion with $m_\psi = m$ are presented in Fig. 4.31. The left plots show the vector component $\rho_V(X^0;\omega,|\mathbf{p}|)$ and the right plots show $\rho_S(X^0;\omega,|\mathbf{p}|)$ as functions of ω. The upper line belongs to $m_\psi = 0.15m$, the lower to $m_\psi = m$. The vector component for $m_\psi = 0.15m$ almost does not change compared to the massless case. It is interesting that the peaks of $\rho_S(X^0;\omega,|\mathbf{p}|)$ are located at a slightly higher energy compared to the vector component which is more pronounced for low-momentum modes. This is a signature of the presence of an effective mass contribution since in the free field case the peaks of $\rho_V(X^0;\omega,|\mathbf{p}|)$ and $\rho_S(X^0;\omega,|\mathbf{p}|)$ coincide. If we increase the fermion bare mass to $m_\psi = m$, the shape of the vector and scalar components changes significantly. Although the positions of the peaks are approximately the same, they become broader. This is more pronounced for $\rho_S(X^0;\omega,|\mathbf{p}|)$. The broadening occurs typically on the right side of the peaks whereas for low-momentum modes of $\rho_S(X^0;\omega,|\mathbf{p}|)$ the whole peak

changes. A broader width is connected to a faster decay of states, thus is expected for heavier particles. Hence, we find a typical behavior of spectral functions even out of equilibrium after an instability acts.

Chapter 5

Amplified Fermion Production by Quantum Corrections

In this chapter we will study the model (3.1) with a nonvanishing macroscopic field and initial conditions leading to parametric resonance. With the inclusion of the nonlocal interaction between bosonic and fermionic fluctuations sketched in Fig. 3.2 we go beyond approaches known from the literature.

The equations of motion which will be solved are (3.30)-(3.37) and (3.38)-(3.41) for the fermionic and bosonic two-point functions, respectively. The initial values of the correlation functions are explained in Sec. 3.4. The fermion self-energies entering the equations of motion are defined in Eqs. (3.47)-(3.52) and the bosonic counterparts are given in Eqs. (3.53) and (3.54). The equation of motion for the macroscopic field is given by (3.43). We used the energy density, defined in Eq. (3.86), to control the accuracy of our numerical calculations. For all shown results the deviation from the initial total energy density is less than one percent.

Results known from the literature on fermion production where the quantum corrections were not included can be obtained by solving the Eqs. (3.30) and (3.37) with vanishing right-hand side and a periodic behavior of the background field ϕ. This corresponds to solving the Dirac equation with a time dependent mass, which is what we call "Dirac-type approximation", cf. Sec. 3.3.2. If the background field interacts with fluctuations the dynamics of ϕ is affected. In this case the boson sector exhibits the full nonlinear dynamics of the 2PI $1/N_s$-expansion up to NLO. Especially the amplitude of $\phi(t)$ is damped which leads to a different fermion evolution. The approximation where we include the nonlinear equations in the boson sector and only neglect the quantum correction in Fig. 3.2 is called "2PI$^-$ approximation" (2PI$^-$) [1], and the inclusion of the fermion-boson loop will be denoted by "2PI$^+$ approximation" (2PI$^+$), cf. Sec. 3.3.2.

In order to embed our results into the current picture of fermion production due to parametric resonance, typically used in preheating, we will summarize the most

[1] Since in the fermion sector still only a local mass contribution enters the equation of motion this approximation is also from "Dirac-type", however the damped amplitude of $\phi(t)$ results in a different evolution of the system.

important facts about the state of the art in Sec. 5.2.1. For further details we refer the reader to the literature, e.g. [GK00]. The results shown in this short review nevertheless will be those calculated by us, which confirms a reliable transition if we extend the approximation. It should be noted that in our calculation also the backreaction of the fermions onto the dynamics of the macroscopic field is taken into account which is often not done in other publications. In [BHP98, GPRT99] the authors paid special attention to the backreaction. A significant impact of that kind of interaction only emerges in the case if the coupling is not too small or the resonance parameter has very large values. In our simulations both is not the case and thus the backreaction plays a subdominant role.

Before we start with the explanation of the fermion production mechanism in the case of parametric resonance we present the situation in the boson sector. In order to understand major features of the fermion production it is necessary to be familiar with the characteristics of the boson dynamics. Recall that this was also the case for spinodal instabilities, cf. Sec. 4.1. Furthermore we discuss whether or not the fermions have significant impact on the dynamics of the bosons. Note that we use ϕ_0, cf. Eq. (3.81), as the scale in this Chapter. That this is reliable is discussed in Sec. F.2 of Appendix F.

5.1 Boson Dynamics

In this section we describe the dynamics of bosonic quantum fields in the presence of parametric resonance. We will first consider the dynamics of self-coupled scalar fields only, i.e. without fermions. Afterwards we consider the impact of fermionic degrees of freedom on the boson dynamics.

5.1.1 Structure of Parametric Resonance

A time dependent frequency of the fluctuations due to an oscillating macroscopic (background) field ϕ is the origin of resonance effects. The special properties of the background oscillations causes qualitatively and quantitatively different resonance effects. The solution of the dynamics of ϕ defines the class of the equations for the fluctuations since it shows up in the time dependent frequency due to the effective mass, cf. (3.42). The form of the equation of motion of the fluctuations tells us the qualitative structure of the resonance. Determining the structure of the resonance analytically is only possible for a few types of equations which are all certain approximations of the complete underlying quantum field theory. Detailed analytical studies of parametric resonance in the context of reheating can be found in Refs. [KLS94, BdVHS96, GKLS97, Kai98, Kai97]. Nevertheless it is worth to know the basic facts of those approximations since they play an important role in

the early time physics of the full theory. Further, some features, like the growth rate of amplified momentum modes, remain valid even in the full theory. Therefore we would like to explain some elementary topics in the following.

There are two classes of equations widely discussed in the literature which also play an important role in our studies. First, there are Mathieu type equations [AS64] which are characterized by a harmonic periodic time dependence of the frequency, like a cosine. The other class contains Lamé-type equations [WW58] which are characterized by a double-periodic[2] time dependence which is present, for instance, in the case of the Jacobian elliptic functions. This makes the treatment somewhat more difficult compared to the former equations. The main difference in view of the resonance structure is that the Mathieu equations lead to several (infinitely many) physical resonance bands [KLS97], whereas Lamé equations only comprise a finite number of physical resonance bands[3]. In certain models (or approximation of models) the Lamé equation can be reduced to a Mathieu equation [KLS97, GKLS97].

In our case the equations of motion of the statistical two-point functions at early times can be approximated by (cf. Eqs. (3.38) and (3.39))

$$\left[\partial_t^2 + \mathbf{p}^2 + m^2 + \frac{\lambda}{2N_s}\phi^2(t)\right] F_{\parallel}^{\phi}(t,t';|\mathbf{p}|) \;=\; 0\,, \tag{5.1}$$

$$\left[\partial_t^2 + \mathbf{p}^2 + m^2 + \frac{\lambda}{6N_s}\phi^2(t)\right] F_{\perp}^{\phi}(t,t';|\mathbf{p}|) \;=\; 0\,, \tag{5.2}$$

whereas the background field equation in this time regime is (cf. Eq. (3.43))

$$\partial_t^2\phi(t) + m^2\phi(t) + \frac{\lambda}{6N_s}\phi^3(t) = 0\,, \tag{5.3}$$

which is a valid approximation if there are no fluctuations. In the case $\lambda = 0$ the solution is given by a cosine with frequency m. This would lead to a Mathieu-type equation for the correlation functions $F_{\parallel/\perp}(t,t';\mathbf{p})$. If $\lambda \neq 0$, which is the case considered in this work, the solution, after rescaling $\tau = \phi_0\, t$ and $\tilde{\phi}(\tau) = \sqrt{\lambda/(6N_s)}\phi(\tau)/\phi_0$, has the form $\tilde{\phi}(\tau) = \mathrm{cn}\left[\tau\sqrt{1+\phi_0^2}\,,\, \phi_0^2/(2+2\phi_0^2)\right]$ where the function cn is the Jacobian elliptic cosine. Inserting this solution into the equations of motion (5.1) and (5.2) gives us Lamé-type equations. Hence we expect one unstable resonance for each equation, i.e. solutions $\sim e^{2\gamma_{\mathbf{p}}t}$ for certain momenta $\mathbf{p}$ with a certain growth rate $\gamma_{\mathbf{p}}$. The only difference in the equations for the longitudinal and transversal components is the factor three in front of the $\phi^2(t)$ term. However this factor causes

[2] Double-periodic has to be understood in the complex plane, it means periodic along the real and imaginary direction.

[3] In general there are at least two resonance bands where one of those lies in the range of unphysical values of the considered variable like the momentum.

significantly different evolutions of the two correlation functions. In equation (5.2) one finds one unstable band for physical momenta $|\mathbf{p}|$ in the range $0 \leq |\mathbf{p}|^2 \leq \phi_0^2/2$. Equation (5.1) shows a comparably narrow physical resonance band for momenta $3\,\phi_0^2/2 + 3 \leq |\mathbf{p}|^2 \leq \sqrt{3\phi_0^4 + 6\phi_0^2 + 4} + 1$. The growth rate as a function of the momentum is for general ϕ_0 a highly nontrivial expression which cannot be presented in a compact form. Since our focus does not lie on the analytic description of the solution to (5.1) and (5.2) we drop this derivation here. We will later give specific examples when we compare them to the numerical results and refer to Ref. [BCdV$^+$98] for the details. Fact is that the growth rate of the narrow band is approximately one order of magnitude smaller than the one from the broad band[4], thus the longitudinal unstable modes are significantly less amplified than the transversal modes and would only play a role on a time scale where the approximation is already invalid and nonlinear effects dominate. Note that the growth rate for the maximally amplified momentum $|\mathbf{p}_0|$ of the transversal fluctuations can be determined analytically and has the approximate value $|\mathbf{p}_0| \simeq \phi_0/2$ [BCdV$^+$98].

In order to show that the above results are reproduced by the numerical simulations, we present in Fig. 5.1 spectra of the boson occupation number at different times of the longitudinal (left plot) and transversal components on a double logarithmic plot. The simulation was done with a boson self-coupling of $\lambda = 10^{-4}$ and an initial value of the rescaled background field $\phi_0 = 2$. In the left panel we observe a little peak at $|\mathbf{p}|/\phi_0 \approx 1.5$ (best seen at $t\phi_0 = 60$, bold line), this is exactly the narrow resonance band analytically predicted above. Moreover, it becomes clear that at the shown time scale nonlinearities already start to become dominating in the low-momentum regime. At later times they cause the broadening of the whole spectrum which leads to the disappearance of the resonance peak. Hence, this resonance band plays a subdominant role in the evolution. Additionally one sees the different rates of change of the dynamics. At early times the spectrum changes fast whereas at late times is becomes quasi-stationary. The quasi-stationary evolution phase exhibits qualitatively the same characteristics as for a spinodal instability, cf. Sec. 4.1.

The transversal component of the occupation number shows the broad resonance peak discussed above with the maximally amplified mode with $|\mathbf{p}_0|/\phi_0 \approx 1/2$. The peak is best developed around $t\phi_0 = 60$ (bold line), note that this is a double logarithmic plot which causes the special shape of the peak. Already at $t\phi_0 = 40$ there is an enhancement of low momentum modes due to nonlinearities. In the subsequent evolution these nonlinearities start to wash out the peak structure and lead to a broad enhanced spectrum. The fast and slow evolution of the modes at early and late times is clearly visible. At even later times both spectra would approach a unique shape. This is expected since the amplitude of the background

[4]The notations "broad" and "narrow" are sometimes also referred to as strong and weak resonances. In the cases considered here they coincide.

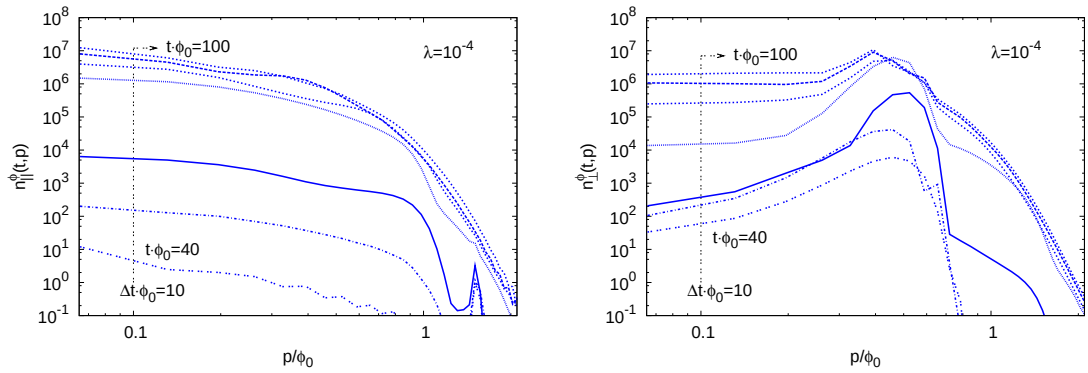

Figure 5.1: Snapshots at different times of the longitudinal (left) and transversal components of $n_\phi(t, \mathbf{p})$ as a function of the momentum $|\mathbf{p}|$. Different lines correspond to different times as indicated in the figure.

field oscillations eventually vanishes and the final value of the classical field becomes $\phi(t \to \infty) = 0$, thus the $O(N_s)$ symmetry is restored. The main features of the spectrum can also be deduced from the time evolution of modes to which we will turn now.

In Fig. 5.2 we plotted the corresponding time evolution for the longitudinal and transversal components of the bosonic occupation number for different modes. All characteristics of the whole dynamics are observable[5]. At early times low-momentum transversal modes ($0 \leq |\mathbf{p}|^2 \leq \phi_0^2/2$) grow exponentially. This lasts up to a time t_ϕ where the instability stops[6]. On this time scale the amplitudes of fluctuations grow till they reach values[7] $\sim 1/\lambda$ and thus all processes become of order one, cf. Sec. 4.1. After t_ϕ the dynamics slows down and the system enters into a quasi-stationary phase, as was also observed in the case of a spinodal instability, cf. Sec. 4.1.1, with the same characteristics. At a certain time $s_\phi^\perp < t_\phi$ nonlinearities lead to a second exponential growth with multiples of the "primary" growth rate. The longitudinal components do not show an exponential growth from the beginning on, except the modes which lie in the narrow resonance band which have a very small growth rate. We plotted one mode of the this band, i.e. $|\mathbf{p}|/\phi_0 = 1.5$, which demonstrates the subdominant role of the resonance band[8]. At some time point $s_\phi^\parallel$ also $n_\parallel^\phi$ shows

[5] Qualitatively the same results were already obtained and reported earlier in Refs. [BS03, Ber05]

[6] t_ϕ has the same interpretation as in the case of spinodal instabilities, cf. Sec. 4.1.1. We will consider this time in detail later.

[7] This is always meant to be parametrically. For small momenta the spectrum shows even higher amplitudes, and smaller ones for large momenta. However, the integration over all modes scales like $\sim 1/\lambda$

[8] Our mode shown does not exhibit an exponential growth right from the beginning, however this band is rather narrow. The single mode which would show exponential growth from the very

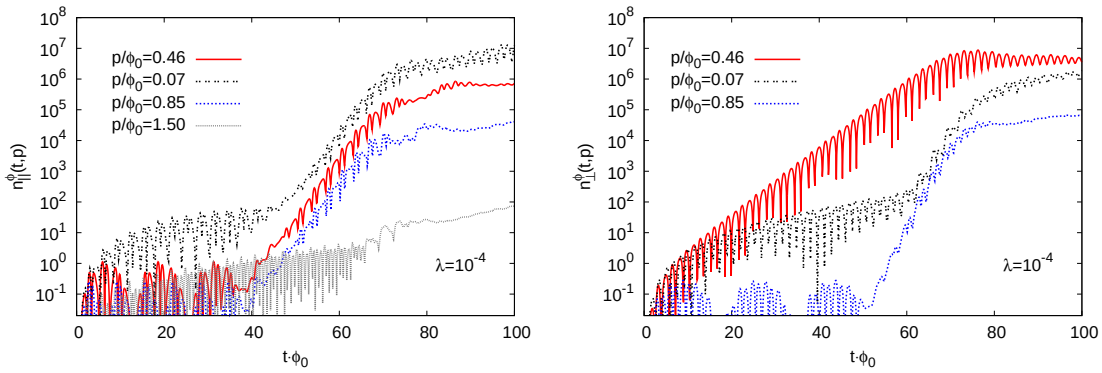

Figure 5.2: Time evolution of different modes of the longitudinal (left plot) and transversal components of $n_\phi(t,\mathbf{p})$. The typical characteristics of the dynamics are observable.

a "secondary" exponential growth period with a growth rate of multiples of the maximum primary growth rate. It ends at t_ϕ after which the system enters the slow evolution.

The maximal growth rate of the transversal components is by the above analytical considerations given by the value $\gamma_0^{\text{analyt}}/\phi_0 = 0.14$ for the maximally amplified mode with $|\mathbf{p}_0|/\phi_0 = 0.5$. In Fig. 5.2 the fastest growing mode ($|\mathbf{p}_0|/\phi_0 = 0.46$) has a growth rate of $\gamma_0/\phi_0 \approx 0.13$ which is in good agreement with the analytical value. The secondaries of $n_\perp^\phi$ have a rate which is three times as large as γ_0 and the one of $n_\parallel^\phi$ grow with a rate which is twice as large as γ_0. This structure is the same as was found in Ref. [BS03, Ber05]. We emphasize that the structure of the dynamics described above is independent of λ.

The unstable evolution of modes stop if all higher order processes included in the effective action become of order one. The time at which this happens can be determined by analytical estimations of the full nonlinear equations. Following the lines in Ref. [Ber05, BPR09] we obtain an equation for t_ϕ which is

$$t_\phi - \frac{1}{4\gamma_0}\ln(t_\phi\,\phi_0) = \frac{1}{2\gamma_0}\ln(\lambda^{-1}) + \frac{1}{4\gamma_0}\ln\left(\frac{(12N_s)^2\,\pi^3|\gamma_0''|\,\phi_0^3}{(N_s+1)^2 A_0^2\,|\mathbf{p}_0|^4}\right)\,, \tag{5.4}$$

where A_0 is the initial amplitude of $F_\perp^\phi(t,t;\mathbf{p})$ with $A_0\,\phi_0 \simeq 1/2$ and the absolute value $|\gamma_0''|$ is the second derivative of the growth rate with respect to the momentum evaluated at $\mathbf{p}_0$. In our case we have $|\gamma_0''|\phi_0 \approx 0.47$, for details see [Ber05]. If we now apply this formula to the example evolution above with $\lambda = 10^{-4}$ we get $t_\phi\phi_0 \simeq 72$ which describes the end of the exponential growth quite well, as can

beginning on might lie between two modes of our grid.

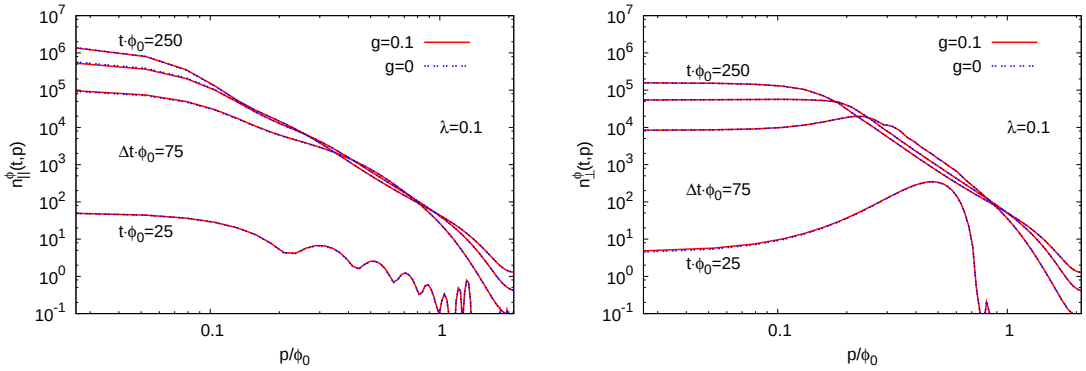

Figure 5.3: Demonstration of the fermion impact on the spectra of $n_{\parallel}^{\phi}(t,\mathbf{p})$ and $n_{\perp}^{\phi}(t,\mathbf{p})$ at different times. There is no significant difference visible.

be seen in Fig. 5.2. The other time scales, namely $s_{\phi}^{\parallel}$ and $s_{\phi}^{\perp}$, are fractions of t_{ϕ}, more precisely they can be approximated by $s_{\phi}^{\parallel} \simeq \frac{1}{2}t_{\phi}$ and $s_{\phi}^{\perp} \simeq \frac{2}{3}t_{\phi} + \frac{\ln N_s}{6\gamma_0}$ [Ber05], which is confirmed in Fig. 5.2[9]. The smaller λ (for fixed γ_0), the larger becomes t_{ϕ} and so $s_{\phi}^{\perp}$ and $s_{\phi}^{\parallel}$, thus the whole process becomes slower for smaller self-couplings. However for small λ the features of the dynamics are clearly observable.

So far we only set the frame of the boson sector, however, one might ask if the presence of fermions changes the dynamics significantly. Simulations of the model (3.1), in the approximation used in this work, are able to judge whether this is the case or not for not too strongly coupled fermions. In the next subsection we are going to answer this question.

5.1.2 Fermion Impact

In Fig. 5.3 we present a comparison of the boson dynamics with ($g=0.1$) and without ($g=0$) fermion interaction in the case of $\lambda = 0.1$, i.e. $\xi = 0.1$ and $\xi = 0$. The plots show the longitudinal and transversal components of the occupation number $n_{\phi}(t,\mathbf{p})$ as a function of $|\mathbf{p}|$ on a double logarithmic plot at different times. The simulation shows different times starting at $t\phi_0 = 25$ with $\Delta t\phi_0 = 25$ up to $t\phi_0 = 250$. For $t\phi_0 > 100$ a power-law behavior with $1/|\mathbf{p}|^4$ emerges in both components. This is a typical property of systems out of equilibrium where an instability acts in the beginning of the evolution. This prevents a fast thermalization. The exponent four was not observed before in the ultraviolet regime. The origin of the specific value is so far not known. Well known methods to determine ultraviolet exponents yield other values, see e.g. Refs. [MT04, BH09a]. The difference between the simulations with

[9]These approximations become better for smaller self-couplings λ.

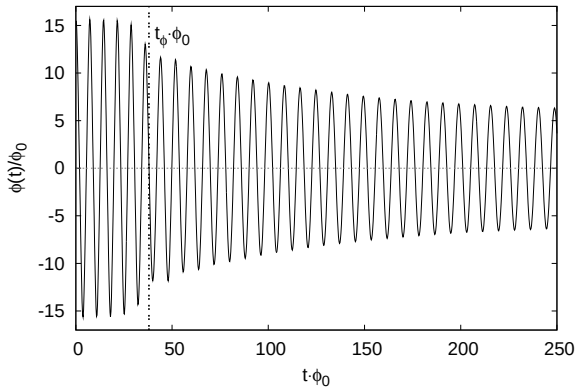

Figure 5.4: Time evolution of $\phi(t)$ for $\lambda = 0.1$ and $g = 0.1$. The vertical line indicates the time scale t_ϕ where the unstable evolution of boson fluctuations stops. There is no change if $g < 0.1$.

a vanishing Yukawa coupling and $g = 0.1$ is almost not visible and thus we conclude that in this parameter regime there is no significant impact on the boson evolution coming from the fermion interaction. However, this statement does not hold in both directions. We will see in Sec. 5.2 that the dynamics of the fermions is always affected considerably. Simulations with $\xi \lesssim 1$ do not show a significant difference in general. A larger Yukawa coupling ($g \approx 1$) may lead to substantial changes in the dynamics of the boson occupation number, however, together with large boson fluctuations and large background field amplitudes the equations of motion require an extremely small time discretization[10] which, with a limited amount of computer memory, does not allow to reach times scales like t_ϕ. Moreover it is questionable if our approximation is reliable for $\xi \gtrsim 1$. Hence we cannot judge in the strong Yukawa coupling regime whether or not the fermions have a large impact. It is expected that for sufficiently high g the impact starts to be significant.

The subsequent evolution of the system after the instability acts is an actively discussed topic. The known facts from the literature claim that there is no fast thermalization with a reheating temperature known from standard hot Big Bang calculations. Since our simulations do not reach extremely late times we are not able to analyze thermalization. However, the information gained from the simulations like the one in Fig. 5.3 suggest that there is no change of this picture if the fermions are weakly coupled.

Important for considerations concerning the fermion dynamics in the forthcoming Sec. 5.2 is the time evolution of the macroscopic field $\phi(t)$. In Fig. 5.4 we display

[10]This was different in the case of a spinodal instability in Sec. 4.1 where $\phi(t) = 0$ for all times and thus a high frequency contribution to the equations of motion was absent.

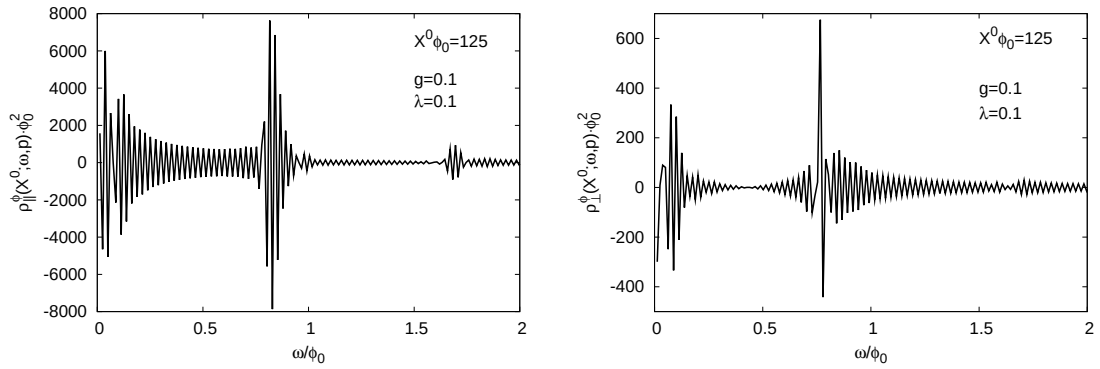

Figure 5.5: Boson spectral function for the smallest momentum available at the latest time accessible indicated in the figure. Despite finite time effects the spectral functions exhibit a peak structure.

$\phi(t)/\phi_0$ as a function of time for $\lambda = 0.1$ and $g = 0.1$. The evolution is the same for vanishing g. At the time scale t_ϕ, defined in Eq. (5.4), indicated by the vertical line, the amplitude is for a short time period exponentially damped. Afterwards the amplitude decreases with a polynomial behavior with a small exponent. The exponential damping comes from the infinite many order one processes at t_ϕ where the fluctuations become of order $1/\lambda$.

Another important quantity is the spectral function. In Fig. 5.5 the spectral functions for the longitudinal (left) and transversal components in the Wigner representation are displayed. We consider the smallest available momentum, i.e. $|\mathbf{p}| \approx 0$, at the latest accessible time. Despite large finite time effects a peak structure emerges. The right peak of $\rho_\parallel^\phi(X^0;\omega,|\mathbf{p}|)$ has the position $\omega/\phi_0 \simeq 0.83$. This fits with the oscillation frequency of the macroscopic field $\phi(t)$, thus the physical mass. The right peak of $\rho_\parallel^\phi(X^0;\omega,|\mathbf{p}|)$ has the position $\omega/\phi_0 \simeq 0.76$. Within our numerical accuracy, together with the finite time effects we can say that the positions are approximately the same, i.e. $\omega/\phi_0 \approx 0.8$, and reflect the value of the physical mass of the macroscopic field. This becomes important when we consider fermion production in the next section. The lower but broader peak at very low energies remains to be interpreted.

5.2 Fermion Dynamics

The goal of this section is to point out whether the fluctuation interaction due to the fermion-boson loop changes the fermion production obtained by an interaction with a macroscopic classical background field like in Refs. [GK99, GK00]. The description of the production mechanism of fermions due to an oscillating homogeneous

macroscopic field was developed in Refs. [GK99, GK00]. In the beginning the dynamics was analyzed by using a periodic time dependence of the background field. This allows for a discussion of the main characteristics of the mechanism. In the first subsection we review the key features of the corresponding dynamics and comment on extensions like introducing an expanding space-time. Since the equations of motions are Dirac equations we refer to those approaches as the "Dirac-type approximations". In the subsequent section we analyze the dynamics in the presence of the fermion-boson loop shown in Fig. 3.2.

5.2.1 Dirac-Type Approximations

The key point of the production mechanism via a macroscopic field $\phi(t)$ is the violation of the so called adiabaticity condition. It states that $\dot{\omega}_{\mathbf{p}} < \omega_{\mathbf{p}}^2$ where $\omega_{\mathbf{p}}$ is the frequency of the mode functions of fermionic quantum fields[11] which is time dependent due to $\phi(t)$. At certain time points the condition is maximally violated which causes an increasing occupation number [GK99, GK00].

Typical time evolutions of fermion occupation numbers in the Dirac-type approximation in the model (3.1) are shown in the left plot of Fig. 5.6. This kind of dynamics were observed in several publications, see e.g. [GK99, GK00, BHP98, GBMR00, GPS04] and the main characteristics we are going to discuss are independent of the specific classical potential of ϕ. The different behavior is governed by the resonance parameter[12] $\xi = g^2/\lambda$ as well as by the momentum $|\mathbf{p}|$. The scale is set by ϕ_0, in this chapter we will express all quantities in units of ϕ_0. Depending on the values of ξ and $|\mathbf{p}|$ the evolution of $n_\psi(t, \mathbf{p})$ shows different characteristics. Universal is the fact that every mode oscillates everlasting with its own amplitude and frequency if not the background field changes its periodicity or amplitude. It is important to note that there are three time-scales on which the fermion dynamics takes place. The first is the period T of the background oscillation, the second is the period of each mode depending on the frequency $\omega_{\mathbf{p}}(t)$ which is time dependend due to $\phi(t)$, the third scale is the modulation period which is larger than the others. The mode frequency changes throughout and can become very large if the amplitude of $\phi(t)$ is very large,thus this might be the smallest time scale. A change of $n_\psi(t, \mathbf{p})$ always occurs if $m_\psi(t) = 0$ where the adiabaticity condition is maximally violated, see the right plot in Fig. 5.6. The occurrence of this time point, t_*, depends on the background period T. The amount of change of $n_\psi(t, \mathbf{p})$ depends on ξ and the mass of the fermions, for instance in Fig. 5.7, which will be discussed below, ξ is not high but $m_\psi = 0$ so that at t_* the change is almost equal to one. Between two t_* n_ψ is constant up to an oscillation with frequency $\omega_{\mathbf{p}}(t)$ which becomes profound for high momenta as in the right plot of 5.6. The Pauli principle is always respected, hence a

[11] Actually the violation of the condition is also the origin of boson production [KLS97].
[12] In a $m^2\phi^2/2$ theory ($\lambda = 0$) it is defined by $\xi \equiv h^2\phi_0^2/m_\phi^2$ [GK00].

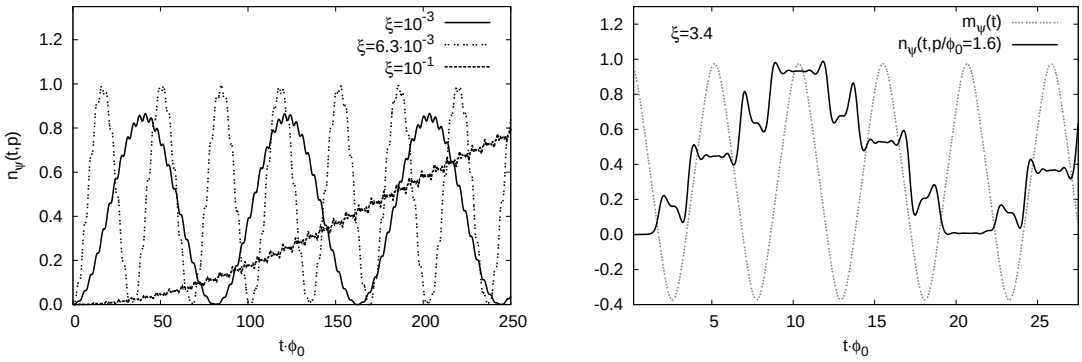

Figure 5.6: Left: Time evolution of $n_\psi(t, |\mathbf{p}|)$ for momenta $|\mathbf{p}|/\phi_0 = 0.4$(bold and double dashed) and $|\mathbf{p}|/\phi_0 = 0.8$(dashed) with masses $m_\psi/\phi_0 = 0.03$ and $m_\psi/\phi_0 = 2$, respectively. Right: Typical step-like evolution of $n_\psi(t, |\mathbf{p}|)$ for $\xi = 3.4$ together with $m_\psi(t)$ (amplitude scaled).

change in the particle number can also be negative. If ξ is very small it might takes several t_* till $n_\psi = 1$ (or equal to some other value between zero and one, depending on the momentum, which causes the shape of the spectrum, see below), afterwards n_ψ decreases again till $n_\psi \gtrsim 0$. These dynamics causes the modulation best seen in the examples in Fig. 5.6. There the case with $\xi = 6.3 \cdot 10^{-3}$ shows the change of n_ψ at t_* is small and not fast, therefore the high frequency oscillations are not observable. In the case of $\xi = 10^{-1}$ the modulation frequency is low, however the high frequency oscillations are observable. The beat in Fig. 5.7 is a reminiscence of the modulation, if ξ would be greater then the beat would be smaller. Note that for each momentum the characteristic changes.

A complete analytic description of this kind of dynamics is not known. There exist approximate descriptions which reproduce certain aspects. For instance, the authors in [GK99, GK00] found an analytical description for the case $\xi \gg 1$ by applying the method of parabolic scattering[13]. It describes the step-like evolution with constant time intervals, however there is no continuous time evolution. The modulation can also be described by a formula given in [GK99, GK00] and also in [GBMR00], there the authors apply an average over T in order to get rid of the high frequency dynamics. This methods also describes the shape of the ("maximal") spectrum, we consider this topic below when we discuss the spectra in general. The mechanism where $\xi \gg 1$ plays also an important role in the case of particle production in a single instance of time, see [FKL99, CKRT00]. If one would introduce a damped oscillation of ϕ by hand or by employing an expanding background metric, the resonance effect

[13]This method was first used in purely bosonic theories in Ref. [KLS97] and later applied to fermionic theories as well.

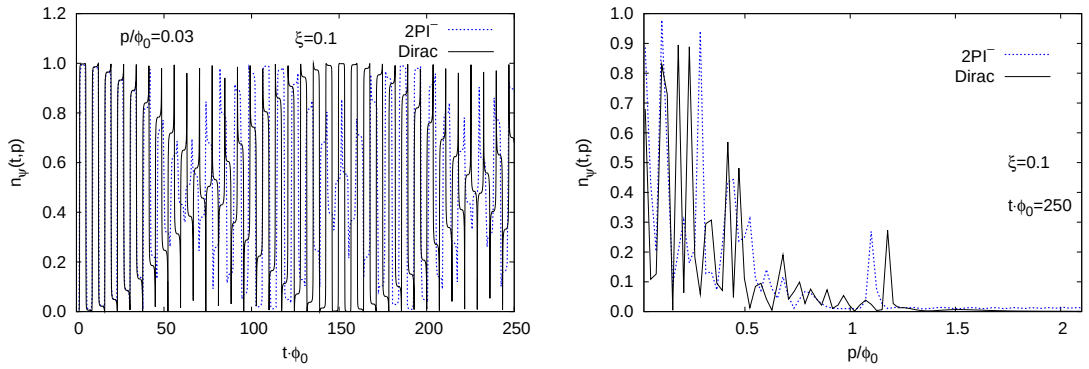

Figure 5.7: Comparison of a Dirac-type with a 2PI$^-$ simulation. Parameters are indicated in the figures. The spectrum represents a snapshot at $t\phi_0 = 250$. On the simulated time scale no big difference is observed. The damping behavior of the 2PI$^-$ simulation is explained in the main text.

at some point becomes inefficient, since then $\xi = \xi(t)$ decreases, and the production would be stopped. That means at some time point $n_\psi(t, \mathbf{p})$ would be constant with different values for different modes, this leads to a certain shape of the spectrum [GK99, GK00]. This brings us to the discussion of the spectra.

The spectra of the occupation number n_ψ typically look like the one in the right plot of Fig. 5.7 where we compare a Dirac-type simulation with a 2PI$^-$ simulation. The corresponding time evolution for the smallest momentum is shown in the left plot. The characteristic properties of these spectra are the multiple peak structure arising due to resonance bands. The strength of the resonance in each band depend on the parameters of the theory, this determines the value up to which a certain mode can grow, see above description of the time evolution. Note the time dependence of the amplitude (which cannot observed in the snapshot in Fig. 5.7) due to the oscillatory behavior of modes, see left plot. The difference of these two approximations is not big, however the time evolution exhibits a weak damping which comes from the damping of the background field due to the interaction with its fluctuations, i.e. due to the nonlinearity. If we could follow the evolution till $\phi(t)$ is completely damped and thus $\phi \approx 0$ the spectrum would be well defined. If the amplitude of the background oscillation does not decrease, as in the Dirac-type approximation, there exists no unique final spectrum. To be able to speak about "the" spectrum in the literature often an envelope function is defined which describes the maximal amplitude of each mode during the time evolution, see e.g. [GK00]. Or there is a "mean" function defined which interpolates the spectrum between the different peaks [PS00]. Efficient fermion production[14] occurs only up to a certain

[14]This terminology is often used while speaking about an amplitude of the occupation number of

momentum $|\mathbf{p}|_{max} \sim \xi^{1/4}\phi_0$ [GK99], thus depends on the resonance parameter[15]. The $\sim \xi^{1/4}$ property follows from the non-adiabaticity condition and was also found in Ref. [GBMR00].

The inclusion of an expanding background in a $m^2\phi^2/2$ theory changes the dynamics in a way that the oscillatory behavior of n_ψ becomes stochastic and the peak structured spectrum becomes broader up to a certain momentum $|\mathbf{p}|_{max} \sim \xi^{1/3}(t = 0)m_\phi$ [GPRT99, GK00] and falls off exponentially for $|\mathbf{p}| > |\mathbf{p}|_{max}$. In Ref. [PS00] a slightly different scaling of $|\mathbf{p}|_{max}$ was found, with an additional factor of the square root of the logarithm of ξ, however qualitatively there is no difference. The parametric resonant production there ends at some point because in that case the resonant parameter depends on the inverse scale factor, thus at some point the parameter becomes too small for an efficient production of fermions, for details see [GK00]. We will not include the expansion of the background in our investigations. Up to now the technique of solving equations of motion in a 2PI framework beyond LO is less developed. There are first results of such studies in pure bosonic theories [Tra08]. A similar construction in a theory considered here lies beyond the scope of this work. However, due to the nonlinear dynamics in the boson sector the amplitude of the background field decreases and eventually the spectrum would converge against a certain state, as mentioned above.

A slightly different approach compared to what was reported above was followed in Ref. [AS00]. The authors considered a coupling of fermions to an inhomogeneous classical background field in $1 + 1$ dimensions. They find an approximately thermalized fermion occupation number due to the inhomogeneity of the classical field. If this property also holds in $3 + 1$ dimensions is unclear. Such a calculation is not known.

In the following subsection we will go beyond such Dirac-type approximations. We will focus on the difference to the production mechanism reported above.

5.2.2 Including Quantum Corrections

Time Evolution

Fig. 5.8 shows the time evolution of the fermion occupation number (3.82) for couplings $\lambda = 0.1$, $g = 0.1$, i.e. $\xi = g^2/\lambda = 0.1$, momentum $|\mathbf{p}|/\phi_0 = 0.03$ (left plot) and $|\mathbf{p}|/\phi_0 = 1.3$ (right plot). We consider massless fermions, i.e. $m_\psi = 0$. The bold line represents the evolution with the fermion-boson loop from Fig. 3.2 ($2PI^+$) whereas the dotted line corresponds to the evolution neglecting the loop ($2PI^-$). Consider first the left plot. One clearly observes the difference of the two results. Without loop the occupation number oscillates with approximately the same ampli-

$n_\psi \gtrsim 0.5$. We will see later that this might not be complete appropriate.

[15] A $\xi^{1/4}$ behavior was also found in the case of bosons, see e.g. [GKLS97].

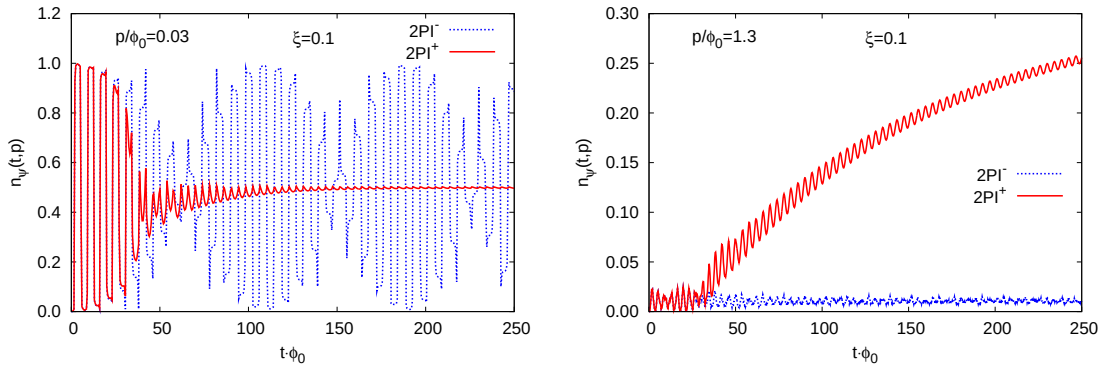

Figure 5.8: Time evolution of $n_\psi(t, |\mathbf{p}|)$ in two different approximations with $\xi = 0.1$ for two different momenta indicated in the plots. The loop including approximation (2PI^+) changes the dynamics tremendously.

tude over the whole simulation time. The loop causes a strong damped oscillation where $n_\psi(t, \mathbf{p})$ quickly approaches the value $1/2$, which corresponds to a thermal occupancy for massless infrared fermion modes, cf. Sec. 4.1.2.3. Note that in the deep infrared the time average of the oscillations of the 2PI^- results corresponds as well to $\simeq 1/2$, however 2PI^+ does not represent the time average of 2PI^-, this becomes clear when we consider the momentum dependence of $n_\psi(t, |\mathbf{p}|)$ below. In the case of $\xi \gtrsim 0.05$ the fast approach to $1/2$ is common for modes smaller than a certain momentum $|\mathbf{p}_*|$. We find $|\mathbf{p}_*| \approx \phi_0$. The simulation of a higher momentum mode ($|\mathbf{p}|/\phi_0 = 1.3$) is given in the right plot of Fig. 5.8. At early times again both simulations agree and show an oscillation with a rather small amplitude. After a certain time point the dynamics start to differ. If the fermion-boson loop is present those higher modes get amplified significantly, due to nonlinear effects. The larger the momentum the less the modes become amplified which leads to a special momentum dependence of $n_\psi(t, |\mathbf{p}|)$. Without loop the oscillation around a small value continues. The corresponding spectrum is presented in the left plot of Fig. 5.10, we will consider the momentum dependence of $n_\psi(t, |\mathbf{p}|)$ in detail in the next section. We do not observe an exponential growth as it was the case in Sec. 4.1. However, the mechanism observed in Sec. 4.1.2 takes place as well, it only plays a subdominant role.

In Fig. 5.9 a time evolution of $n_\psi(t, |\mathbf{p}|)$ for different momenta with $\xi = 0.01$ is shown which displays the loop effect for a low ξ. If $\xi \lesssim 0.05$ the large amplitude oscillation are not strongly damped, i.e. the modes of a resonance band are not extremely affected by the loop. This is different for modes out of a resonance band, there the loop causes an amplification which is absent in the 2PI^- simulation, see right plot of Fig. 5.9.

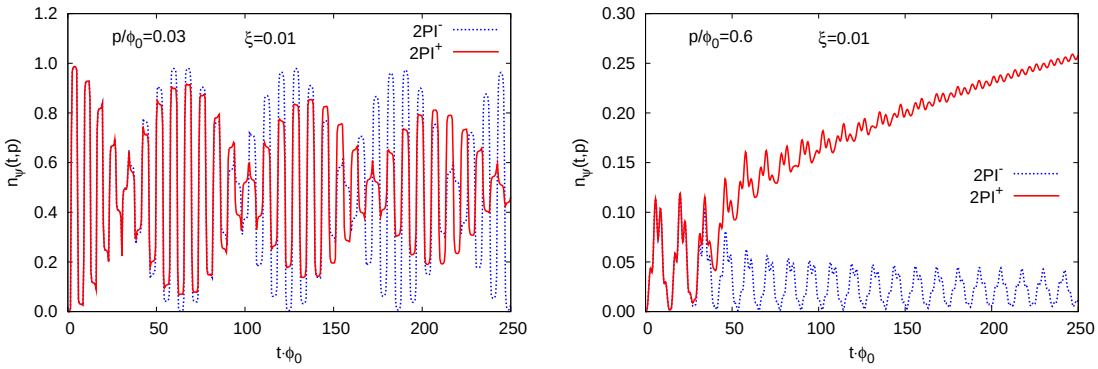

Figure 5.9: Time evolution of $n_\psi(t, |\mathbf{p}|)$ with (2PI$^+$) and without loop (2PI$^-$), with $\xi = 0.01$ for two different momenta indicated in the figure. The 2PI$^+$ approximation leads to a strong amplification of modes.

For extremely small ξ, i.e. $\xi \ll 10^{-3}$ the dynamics is not affected considerably by the loop. And a 2PI$^+$ approximation for not to large times can be described without including the loop. At late times when $\phi(t) \to 0$, the fluctuation start to dominate the dynamics and a description without quantum corrections would fail. We emphasize that the most interesting cases are $\xi \gg 1$ and in this regime the loop effect is maximally pronounced.

Let us now turn to the discussion of the occupation number as a function of momentum.

Spectrum

In Fig. 5.10 we present $n_\psi(t, |\mathbf{p}|)$ as a function of momentum corresponding to the simulations showed in Fig. 5.8 and Fig. 5.9. We compare the results where the loop is included (2PI$^+$) with those neglecting it (2PI$^-$) at our latest accessible time. In addition we plotted in both cases the time average of $n_\psi^{2PI^-}$, which clearly shows that the 2PI$^+$ simulation does not reproduce the time average of 2PI$^-$. We took the time average over approximately twenty oscillations of $\phi(t)$. The momentum regime where the time average leads to $\simeq 1/2$ can be referred to as strong (broad) resonance bands.

The left plot states one of our main results of this chapter. Due to the fermion-boson loop the spectrum gets high occupation numbers in a large range of momenta. Within the small region of the strong resonance band the time average produces a similar occupation, however, the rest of the spectrum is totally different. The peak in $n_\psi^{2PI^-}$ at $|\mathbf{p}|/\phi_0 \approx 1.1$ corresponds to a weak (narrow) resonance band which plays a subdominant role. The spectrum which results if quantum corrections are included exhibits a special shape. We observe the occupation $n_\psi(t, |\mathbf{p}|) \simeq 1/2$ in a

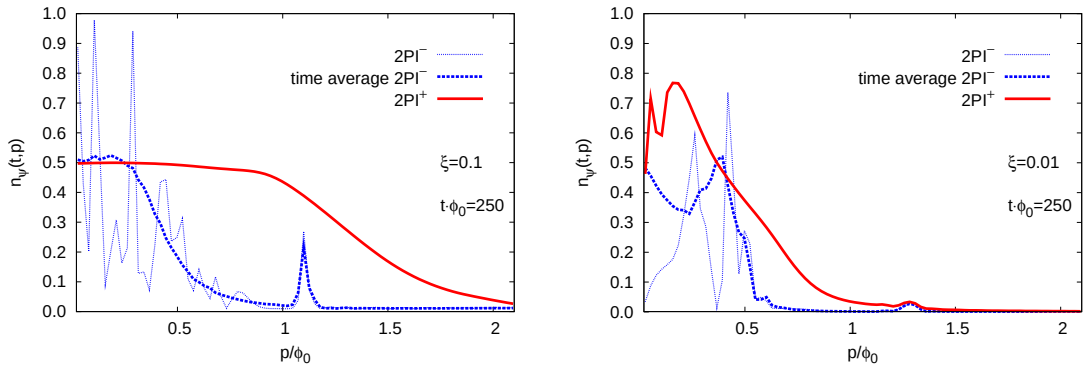

Figure 5.10: Spectra of $n_\psi(t, |\mathbf{p}|)$ for $\xi = 0.1$ (left) and $\xi = 0.01$ at $t\phi_0 = 250$. The left plot shows the sizable difference if the loop is included (2PI$^+$). For $\xi = 0.01$ the difference between the two approximations becomes less but still exists.

momentum range starting in the deep infrared up to momenta with $|\mathbf{p}| \approx \phi_0$. For higher momenta the occupation falls off with a shape reminiscent of a Fermi-Dirac distribution. However, since we have a vanishing chemical potential a corresponding Fermi-Dirac statistics does not have such a form.

The right plot illustrates the situation if $\xi = 0.01$. The huge difference becomes smaller and the wide range of maximal occupation is not observable, the 2PI$^+$ spectrum rather shows signatures from the 2PI$^-$ spectrum. Nevertheless one observes a higher occupation with loop. That means the total particle number produced can become larger as without loop, thus always a more efficient fermion production occurs if quantum corrections like the loop in Fig. 3.2 are respected. This is most pronounced for $\xi \gtrsim 0.05$.

The more efficient fermion production is best visualized if one considers the integrated particle number

$$N_\psi(t) = 8 \int \frac{d^3p}{(2\pi)^3}\, n_\psi(t, \mathbf{p})\,, \tag{5.5}$$

where the eight counts the degrees of freedom in our system, flavor ($N_f = 2$), spin and charge. In Fig. 5.11 we show the time evolution of $N_\psi(t)/\phi_0^3$ for neglecting (2PI$^-$) compared to including the loop interaction (2PI$^+$). The difference is remarkable. Taking the loop into account leads to an enormously enhancement of fermion production. The time evolution in Fig. 5.11 reflects the difference between the spectra observed above. Interesting is that the impact of the loop starts to become significantly around the time scale $t = t_\phi$. We already know t_ϕ from the boson dynamics in Sec. 5.1. It describes the time at which the boson fluctuations become of the order $1/\lambda$, thus the time at which the instability terminates. It can be calculated by Eq. (5.4) and for our parameters here we find $t_\phi\phi_0 \simeq 38$. This

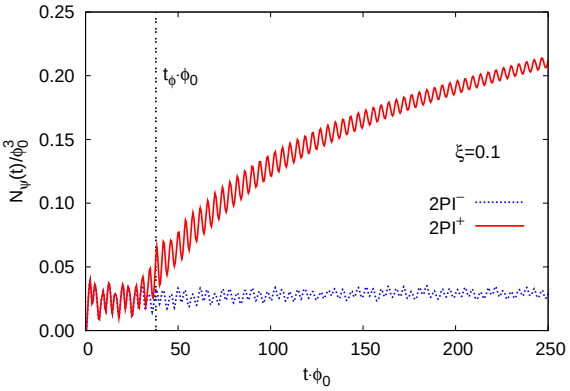

Figure 5.11: Comparison of the time evolution of $N_\psi(t)$ where the loop is included (2PI^+) and where not (2PI^-). The difference becomes pronounced at $t = t_\phi$.

corresponds to the vertical line in Fig. 5.11. If the boson fluctuations are $\sim 1/\lambda$ the fermion self-energies in the equations of motion for the fermion correlators become dominant. As we saw in Sec. 5.1, around t_ϕ the evolution of $\phi(t)$ shows a characteristic behavior, see Fig. 5.4. It gets exponentially damped for a short amount of time and the amplitude starts to decrease. At the same time the damping (left) and the amplification (right) in Fig. 5.8 is developed. It is important to note that in the parametric resonance evolution considered here the loop effect starts after the instability acts. This is in contrast to what was observed in Sec. 4.1.2.

In the following we will describe the effect which yields an amplification of occupation number modes. We make some estimates which leads us to an interpretation of the dynamics. Around t_ϕ the field $\phi(t)$ is exponentially damped and the amplitude decreases afterwards and it oscillates around zero, i.e. on average $\phi(t) \approx 0$. Since $m_\psi = 0$ we then have $F_S \approx 0$. Thus the occupation number (3.82) is determined by F_V. If there is no symmetry breaking macroscopic field we know from Sec. 4.1.2 that the equation of motion can be simplified by

$$\partial_t F_V(t,t;|\mathbf{p}|) + K(t) F_V(t,t;|\mathbf{p}|) \simeq 0\,, \tag{5.6}$$

during the unstable evolution. Note that also in parametric resonance $F_\phi \sim e^{\gamma\, t}$ with some growth rate γ which explicit value is not necessary here. Now, after t_ϕ the unstable evolution is no longer existent and we can approximate $F_\phi(t,t,|\mathbf{p}|) \approx$ const.. Further we know from (4.16) that $K(t) \sim g^2$ and after t_ϕ it holds that $F_\phi \sim 1/\lambda$, hence we estimate $K(t) \approx K \sim g^2/\lambda = \xi$, for $t > t_\phi$. In the following we define $K \equiv \xi\, \mathcal{K}$, and are not interested in the exact value of $\mathcal{K}$. The Eq. (5.6) then acquires the form

$$\partial_t F_V(t,t;|\mathbf{p}|) + \xi\, \mathcal{K}\, F_V(t,t;|\mathbf{p}|) \simeq 0\,, \tag{5.7}$$

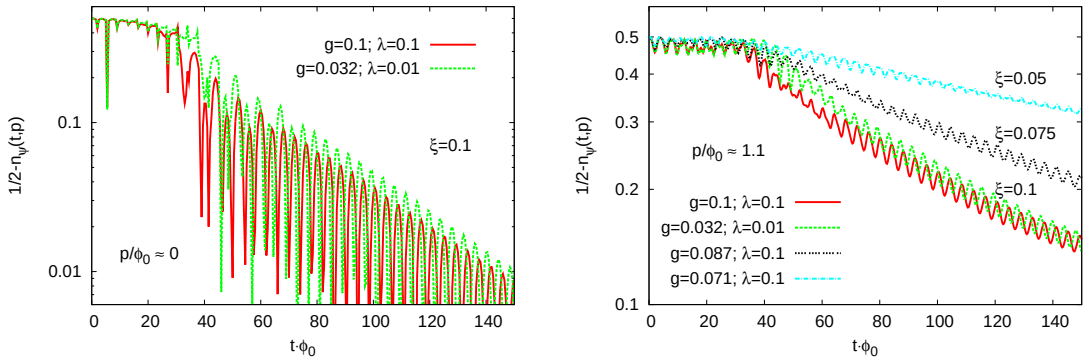

Figure 5.12: Confirmation that $1/2 - n_\psi(t, |\mathbf{p}|)$ approaches zero with a rate $\sim \xi$. The plots state in addition that for equal ξ the dynamics is approximately the same.

with the solution

$$F_V(t, t; |\mathbf{p}|) = \frac{1}{2} e^{-\xi \mathcal{K} t}\,, \tag{5.8}$$

where we used the initial condition $F_V(0, 0; |\mathbf{p}|) = 1/2$. Accordingly the fermion occupation number yields

$$n_\psi(t, |\mathbf{p}|) = \frac{1}{2} - \frac{1}{2} e^{-\xi \mathcal{K} t}\,, \tag{5.9}$$

thus it approaches the value $1/2$ with a rate proportional to ξ. We emphasize that the above argumentation is rather rough and the only purpose is to show that the growth of occupation number modes after t_ϕ depends on ξ. For instance, we neglect a momentum dependence of $\mathcal{K}$ and the existence of $\phi(t)$. Accordingly, (5.9) is not valid for all momenta and times.

In order to show that the increase in the occupation number is proportional to ξ we display in Fig. 5.12 the time evolution of $1/2 - n_\psi(t, |\mathbf{p}|)$ which is supposed to approach zero with a rate $\sim \xi$. In the left figure we plotted the time evolution on a logarithmic plot for a small momentum, $|\mathbf{p}|/\phi_0 \approx 0$, for two different combinations of g and λ with the same ξ. We observe that there is an exponential decrease. In the right plot we consider the same quantity, but with a higher momentum, $|\mathbf{p}|/\phi_0 \approx 1.1$, and together with two different ξ, i.e. $\xi = 0.05$ and $\xi = 0.075$. We observe that with higher ξ the approach towards zero is faster, i.e. performs with a higher rate. The same can be inferred from lower momenta. We took a larger momentum than ϕ_0 in order to show that the part of the spectrum of $n_\psi(t, |\mathbf{p}|)$ with $|\mathbf{p}| > \phi_0$ becomes more occupied with larger ξ. Moreover, the total particle number $N_\psi(t)$ is dominated by not too small momenta and thus the increase of $N_\psi^{2PI^+}(t)$ in Fig. 5.11 becomes larger for larger ξ. Note that there is no such increase of the total

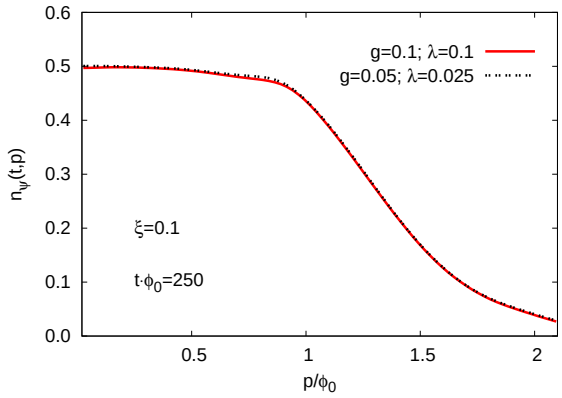

Figure 5.13: Fermion occupation number spectrum for $\xi = 0.1$ with two different pairs of g and λ indicated in the figure. The agreement of the spectra is remarkable.

particle number if we neglect the loop, irrespective for which ξ. The value around which $N_\psi^{2PI^-}(t)$ oscillates might become higher, however there is no slope such as in $N_\psi^{2PI^+}(t)$ starting on top of the oscillations.

The left plot in Fig. 5.12 contains an addition information. The dynamics for equal ξ is approximately the same. This is in contrast to what was observed in the case of spinodal instability [BPR09] where only the late time was described by ξ. At late times the dynamics even become indistinguishable. This results into equal occupation number spectra and thus to an equal efficient fermion production. In Fig. 5.13 we present two spectra with equal ξ, however the specific values of the couplings λ and g are different. The results are taken at our latest accessible time. The agreement of both spectra is excellent, this coincides with what was already observed in [BPR09] in the case of vanishing background field and a spinodal instability.

In summary, the fermion-boson loop causes a very efficient fermion production not observed before. The production rate is proportional to ξ. This is phenomenologically interesting since even for very small Yukawa couplings there can be an efficient fermion production as long as λ is small enough. Small λ, e.g. $\lambda \sim 10^{-13}$ is typical in preheating scenarios [GK99].

Now we know that there is a fermion production mechanism governed by ξ. Since this happens after the instability exists an instability-induced process is not the reason. We get more insight into the observed process if we consider the fermionic spectral functions. The anticommutation rules of the spectral functions yield the sum rule $i = \int \frac{d\omega}{2\pi} \rho_V^0(\omega, |\mathbf{p}|)$ where $\omega = p^0$ is the zeroth component of the

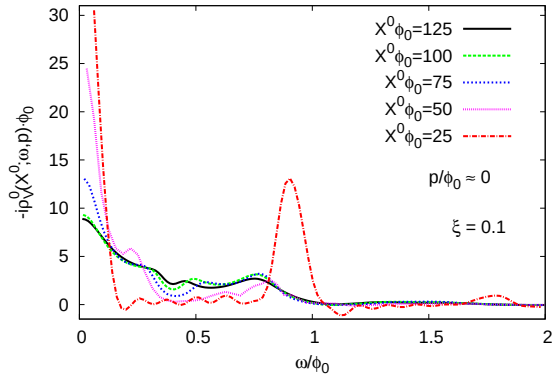

Figure 5.14: The spectral function $\rho_V^0(X^0;\omega,|\mathbf{p}|)$ as a function of ω for $|\mathbf{p}|/\phi_0 \approx 0$ at different center of mass times X^0. A "melting" of the peak structure, due to the nonequilibrium evolution with quantum correction, is visible.

four-momentum. With this we know that we have a normalized[16] ρ_V^0. Analyzing $\rho_V^0(\omega,|\mathbf{p}|)$ tells us which states can be occupied. Note that we cannot integrate from $-\infty$ to $+\infty$. Thus the spectral function depends on time, i.e. on the center of mass coordinate $X^0 = (t+t')/2$, see Appendix D for details of the computation technique. In Fig. 5.14 we present the spectral function ρ_V^0 as a function of the energy at different times X^0 for our smallest available momentum $|\mathbf{p}|/\phi_0 \approx 0$.

The time $X^0\phi_0 = 25$ corresponds to a time $t < t_\phi$ whereas all other times correspond to $t > t_\phi$. This plot explicitly shows the complex structure of spectral functions out of equilibrium. For $t < t_\phi$ we observe two pronounced peaks at $\omega/\phi_0 = 0$ and $\omega/\phi_0 = 0.9$. For a free-field theory one would have approximately δ-function peaks. Since our theory without loop can be interpreted as a free theory with time dependend background field ϕ, the width of the peaks at $X^0\phi_0 = 25$ comes from the virtue of the loop, cf. Sec. 4.1. After t_ϕ the peaks vanish and the spectrum acquires a broad shallow shape with its middle point around $\omega/\phi_0 \simeq 0.45$. The peaks at early times are interpreted as states with masses $m_\psi^{\text{eff}} = 0$ and $m_\psi^{\text{eff}} = 0.9$. The mass parameter m_ψ is zero. From the oscillation frequency from $F_V^0(t,0,|\mathbf{p}|)$ we measure the physical mass $m_\psi^{\text{eff}}/\phi_0 = 0.87 \approx 0.9$ at early times. The vanishing of the peak structure is caused by the loop, without loop the structure remains a peak structure with a smaller width. We observe that the effective mass m_ψ^{eff} is time dependent. Till the latest time point at which we calculated the spectral function the effective mass changed to $m_\psi^{\text{eff}}/\phi_0 \approx 0.4$. At that time point the initially clear oscillations become irregular and the value 0.4 has to be taken with care. In Sec. 5.1 we saw that the boson spectral functions exhibits a peak at $\omega/\phi_0 \approx 0.8$ which coincides

[16] This can be used to check the numerical accuracy of the computation of $\rho_V^0(\omega,|\mathbf{p}|)$. In our case deviations did not exceed one percent.

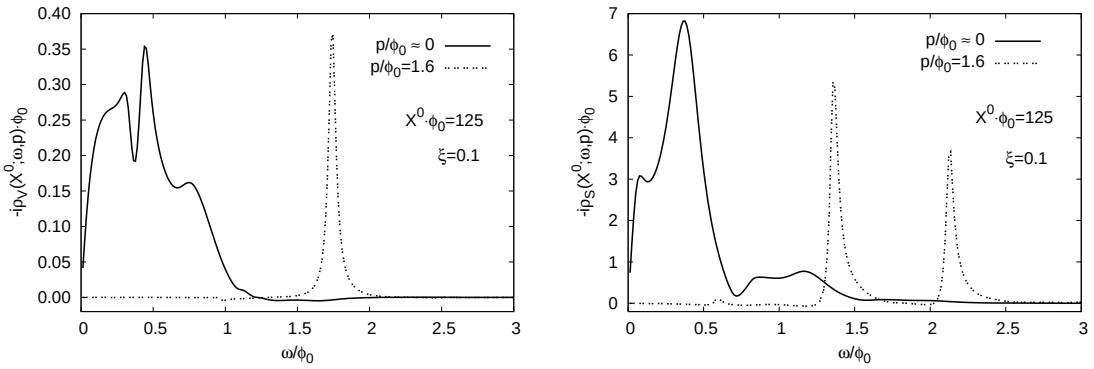

Figure 5.15: Left: Result of the fermion spectral function $\rho_V(X^0;\omega,|\mathbf{p}|)$ at center of mass time coordinate $X^0\phi_0 = 125$ for different $|\mathbf{p}|$ (The amplitude of the $|\mathbf{p}|/\phi_0 = 1.6$ spectrum is scaled down by a factor of 10^{-2}, otherwise the $|\mathbf{p}|/\phi_0 \approx 0$ result is not clearly visible). Right: the same as left for $\rho_S(X^0;\omega,|\mathbf{p}|)$ but without scaled high momentum peak.

with the physical mass of $\phi(t)$ taken from its oscillations. The boson mass changes from $m_\phi^{\text{eff}}/\phi_0 = 0.89$ to $m_\phi^{\text{eff}}/\phi_0 = 0.75$ over the whole simulation time. At the time point $t\phi_0 = 125$ we measure $m_\phi^{\text{eff}}/\phi_0 = 0.76$ thus the change after the instability is rather slow.

If we consider the spectral functions $\rho_V(X^0;\omega,|\mathbf{p}|)$ and $\rho_S(X^0;\omega,|\mathbf{p}|)$ at $X^0\phi_0 = 125$ we obtain the peak structure displayed in Fig. 5.15. We plotted two different modes indicated in the figure. Note that the high-momentum peak in the left plot is scaled for illustrative reasons. We first concentrate on the left plot. We observe two peaks at $\omega/\phi_0 \simeq 0.45$ and $\omega/\phi_0 \simeq 1.74$. Since the former corresponds to vanishing momenta and the latter to $|\mathbf{p}|/\phi_0 = 1.6$ we infer[17] with $\omega_{|\mathbf{p}|} = \sqrt{|\mathbf{p}|^2 + (m_\psi^{\text{eff}})^2}$ a fermion mass $m_\psi^{\text{eff}}/\phi_0 \approx 0.5$. This fits, within the expected error bounds, with the measured value mentioned above. Interesting is the peak structure of the high-momentum mode of $\rho_S(X^0;\omega,|\mathbf{p}|)$. It is a double peak structure visible whereas the distance of the peaks is $\omega/\phi_0 \simeq 0.77$. The mid point position is $\omega_{|\mathbf{p}|} = \sqrt{|\mathbf{p}|^2 + (m_\psi^{\text{eff}})^2}$ with $m_\psi^{\text{eff}}/\phi_0 \approx 0.5$ and the distance correspond to m_ϕ^{eff}, i.e. we observe peaks at positions $\omega_{|\mathbf{p}|} \pm m_\phi^{\text{eff}}/2$. This is a signal of chiral symmetry breaking due to the oscillating field ϕ. We also checked the shape of the low-momentum peak at early times and found a double peak with the same characteristics as explained above. The nonequilibrium evolution with the loop causes a

[17] Note that the high-momentum peaks are slightly shifted by a systematic numerical inaccuracy, see Appendix D for details. This means the actual peak position for $|\mathbf{p}|/\phi_0 = 1.6$ is not $\omega/\phi_0 \simeq 1.74$, rather a few percent smaller.

"melting" of this structure. So the peak at $\omega/\phi_0 \simeq 0.37$ with a hill at $\omega/\phi_0 \simeq 1.17$ is a relic of a double peak structure, thus it is difficult to gain a mass value from it. For higher Yukawa couplings the clear peak structure gets more and more lost even at high momenta. Consequently, we find a complex structure for the spectral function with interesting features.

The melting of the spectral function is interpreted as approving new states. Since the occupation number increases if the loop impact becomes most efficient we conclude that new generated states (decay channels) are the origin of the amplification of occupation number modes, thus of more particles. For this it needs a nonvanishing boson mass. This is typically the case in parametric resonance settings. With the definition of $n_\psi(t, |\mathbf{p}|)$ we cannot judge which states are occupied, however it is remarkable that an occupation of $n_\psi(t, |\mathbf{p}|) \simeq 1/2$ occurs in a momentum regime from zero to $|\mathbf{p}| \approx \phi_0$ which is the favored regime of states given by $\rho_V^0(\omega, |\mathbf{p}|)$.

Interesting is that, despite the fact that we observe massive fermions, the fermion occupation number is occupied in the infrared like a thermal spectrum for massless fermions, cf. Sec. 4.1.2.3. That the occupation number is insensitive to effective masses generated by nonlocal self-energies was also observed in Ref. [BBS03]. Our findings confirm this behavior so that it seems to be a general property of those fermion occupation numbers used here.

Chapter 6

Conclusions and Outlook

In this thesis we investigated nonequilibrium fermion production in a Yukawa-type model out of equilibrium in $3+1$ dimensions where scalar boson fields interact with Dirac fermion fields. We used the $1/N$-expansion of the 2PI effective action up to next-to-leading order in the boson sector and have applied a loop-expansion in the fermion sector up to two-loop order. This yields an interaction of both kinds of fluctuations, i.e. scattering and off-shell effects are included. We analyzed different initial conditions which lead to the phenomenon of nonequilibrium instabilities. In our case we studied spinodal instabilities and parametric resonance. We focused on the resulting fermion production mechanism and its impact on the boson dynamics.

The inclusion of the fermion-boson loop in Fig. 3.1 turned out to yield a dramatic impact of the fermion production in the presence of large boson fluctuations. We found two different mechanisms of efficient fermion production which are absent without quantum corrections.

In the case of spinodal instabilities we found a new mechanism for fermion production. Fermions are produced exponentially fast over the whole spectrum with approximately the same rate as the maximal primary boson growth rate. This shows a specific character of the mechanism, i.e. the fermion production is induced by unstable boson fluctuations. This could not have been observed before because of the lack of the fermion-boson loop.

We derived an analytic expression for the fermion occupation number as a function of time which serves for a complete understanding of the mechanism. The efficiency is controlled by the coupling ratio $\xi = g^2/\lambda$. The production ends if the maximal thermal occupancy of low-momentum modes is reached or if the instability terminates beforehand. Thus the fermions are driven towards thermal equilibrium. Hence, we find fast thermalizing fermions interacting with bosons which are still far from equilibrium. A fermionic "heat bath" in nonequilibrium evolutions could have interesting consequences in phenomenological applications.

The momentum dependence of the fermion occupation number shows interesting features. Whereas an infrared power-law behavior is forbidden by the Pauli principle, we found an ultraviolet power-law behavior with an exponent $\kappa_\psi = 2$. The origin is quite different from what is known from bosonic ultraviolet power-laws (turbulence).

Analytical considerations showed that the former appears rather early in time and is explained by a retardation effect due to the memory integrals in the equations of motion. It is rather stable. However, eventually nonlinear effects will drive the system into thermal equilibrium. The presence of such an ultraviolet excess compared to a thermal spectrum could have important consequences in different applications. Not only because the energy is dominated by this momentum regime, furthermore, because bosons typically have a low occupation in the high-momentum regime.

We observed that the same production mechanism approximately holds for massive fermions. For heavier fermions a larger ξ is required to get an equal efficient production.

A nonvanishing expectation value of a boson field (macroscopic field) does not change the dynamics qualitatively if the amplitude of this field is not large. If there exists a large initial value for the macroscopic field we found that the loop plays a subdominant role during the early time evolution.

In the case of parametric resonance we found a different kind of mechanism caused by the fermion-boson loop. Since the initial conditions require a large macroscopic field in order to induce the resonance effect, initially the fermion dynamics is completely governed by the interaction term $\sim g\phi(t)$. The resulting production mechanism, till the instability ends, was already observed in literature and is known as the nonadiabatic excitation of fermion modes.

However, at the end of the unstable evolution phase, i.e. when the boson fluctuations become of the order $1/\lambda$, the loop starts to dominate the dynamics and leads to a very efficient fermion production compared to the nonadiabatic excitation. This mechanism is completely different to what was observed in the spinodal instability case and is interpreted as an efficient decay of particles. The fermion production is amplified by the loop with a rate proportional to ξ. The analysis of the fermion spectral function showed that the quantum corrections yield more accessible fermion states. If the boson mass is large enough many decay processes can occur and an efficient fermion production is possible. Since the boson mass after the spinodal instability almost vanishes no efficient decay was observed. The possibility of post-instability decays makes sure that the parametric resonance mechanism tends to be more efficient.

The analysis of spectral functions showed interesting features like signatures of symmetry breaking. Such investigations should be followed in the future in order to get a comprehensive understanding of spectral functions out of equilibrium.

In both kinds of initial conditions the shape of the spectrum after the instability is governed by ξ. For each combination of the Yukawa coupling g and boson self-coupling λ which yields the same ξ, we obtain the same spectrum. For the parametric resonance initial conditions there is even at early times an approximate coincidence of the dynamics. The implication of an efficiency proportional to ξ has important

consequences. Even if g is small the production is very efficient if λ is sufficiently small, which is usually the case as inferred from cosmic microwave background measurements.

In the boson dynamics we observed typical properties of an evolution with an instability. In the fast unstable regime primary and secondary growth rates appear before the system enters a slow evolution phase. The quasi-stationary regime exhibits typical signatures like self-similarity and power-law behavior. This holds for both kinds of instability. In the case of spinodal instability classical-statistical simulations show that the boson sector approaches a nonthermal infrared fixed point with an exponent $\kappa_{\mathrm{IR}} = 4$ which means there are strongly enhanced fluctuations compared to thermal equilibrium. The same exponent was also observed in an earlier work [BRS08] in the case of a purely scalar field theory with a parametric resonance. This shows that subsequent evolutions are insensitive against different initial conditions and gives a notion of universality far from equilibrium. In the 2PI (quantum) evolution with parametric resonance we found an ultraviolet power-law with an exponent $\kappa_{\mathrm{UV}} = 4$. This is connected to the phenomenon of turbulence. To our knowledge there is no connection between both power-law behaviors.

The impact of the fermions on the boson dynamics is rather small. In the coupling regime considered here almost no change is observable. The bosonic scaling behavior is not affected by the inclusion of fermions. This is important for applications in reheating and/or heavy-ion collisions. The hope that fermions change the current known picture is diminished.

Our study represents a small step towards more realistic applications. It shows interesting phenomena which may have important implications. Nevertheless, of course, there is still a lot which has to be understood, e.g.:

What yields a fast thermalization? Since we have shown that fermions do not change the slow thermalization after instabilities in set-ups used in this work there might be some other mechanism. The first step beyond our work should be a proof of the statement (e.g. by numerical simulations) that strongly coupled fermions really have a large impact.

Concerning cosmology, long time simulations may have a different outcome if the expansion of space-time is included. There exists attempts to implement 2PI evolution equations with expanding metric on a computer [Tra08], however, for a model with different kinds of fields there still have to be a development and the lack of sufficient computer resources limits the applicability so far.

Another interesting application is the physics of core-collapse supernovae. Different kinds of instabilities play an important role [JLM$^+$07, KPJM03] and a microphysical description of the dynamics is not known yet.

So far only toy models have been investigated in out-of-equilibrium settings. It is not excluded that a realistic model with different types of fields (may be even a supersymmetric extension of it) shows new phenomena, so far unknown, if quantum

corrections are included. With the efficient fermion production mechanisms found in this work the resulting consequences may help to understand open questions in applications of nonequilibrium quantum field theory.

Appendix A

Fermion Two-Point Functions in the Chiral Basis

In this Appendix we are going to present the decomposition of the fermion two-point functions in the chiral basis. We will restrict the consideration on the, in our model, nonvanishing fermion components, i.e. the scalar, vector and the "temporal-spatial" tensor components of $F(x,y)$ and $\rho(x,y)$. The aim is to show which of these functions are chiral-invariant and which not.

In the chiral basis Dirac spinors can be written as $\psi(x) = \psi_L(x) + \psi_R(x)$ (we omit Dirac indices throughout the whole Appendix). Where

$$\psi_L(x) = \begin{pmatrix} \chi_L(x) \\ 0 \end{pmatrix} \quad \text{and} \quad \psi_R(x) = \begin{pmatrix} 0 \\ \chi_R(x) \end{pmatrix}. \tag{A.1}$$

The $\chi_{L/R}(x)$ are two component Weyl-Spinors. This decomposition is done by projections (P_L and P_R) given as

$$\begin{aligned} \psi(x) &= P_L\psi(x) + P_R\psi(x) \\ &\equiv \frac{1}{2}\left(1-\gamma_5\right)\psi(x) + \frac{1}{2}\left(1+\gamma_5\right)\psi(x). \end{aligned} \tag{A.2}$$

The γ-matrices in this basis are given by

$$\gamma_0 = \begin{pmatrix} 0 & \mathbb{1}_{2\times2} \\ \mathbb{1}_{2\times2} & 0 \end{pmatrix}, \quad \gamma_i = \begin{pmatrix} 0 & \sigma_i \\ -\sigma_i & 0 \end{pmatrix}, \quad \gamma_5 = \begin{pmatrix} -\mathbb{1}_{2\times2} & 0 \\ 0 & \mathbb{1}_{2\times2} \end{pmatrix}. \tag{A.3}$$

The adjoint spinor $\bar{\psi}(x)$ can be written as

$$\bar{\psi}(x) \equiv \psi^\dagger(x)\gamma_0 = \left(\psi_L^\dagger(x) + \psi_R^\dagger(x)\right)\gamma_0 = \bar{\psi}_L(x) + \bar{\psi}_R(x), \tag{A.4}$$

with

$$\bar{\psi}_L(x) = \begin{pmatrix} 0, & \chi_L^\dagger(x) \end{pmatrix} \quad \text{and} \quad \bar{\psi}_R(x) = \begin{pmatrix} \chi_R^\dagger(x), & 0 \end{pmatrix}. \tag{A.5}$$

Having the spinor representation prepared we can build the two-point functions. In the next two sections we will consider the statistical and spectral components respectively.

Statistical Two-Point Function

The statistical two-point function is defined by

$$F(x,y) = \frac{1}{2}\left\langle [\psi(x), \bar{\psi}(y)] \right\rangle. \tag{A.6}$$

where the expectation value has to be taken with respect to the initial density matrix. Inserting the spinors defined above into the definition of $F(x,y)$ yields

$$F(x,y) = \frac{1}{2}\begin{pmatrix} \left\langle \left[\chi_L(x), \chi_R^\dagger(y)\right] \right\rangle & \left\langle \chi_L(x)\chi_L^\dagger(y) - \chi_R^\dagger(y)\chi_R(x) \right\rangle \\ \left\langle \chi_R(x)\chi_R^\dagger(y) - \chi_L^\dagger(y)\chi_L(x) \right\rangle & \left\langle \left[\chi_R(x), \chi_L^\dagger(y)\right] \right\rangle \end{pmatrix}. \tag{A.7}$$

Now we can calculate each Lorentz component by use of Eqs. (3.13). For the temporal component of the vector part we find

$$F_V^0(x,y) = \frac{1}{8}\left[\mathrm{tr}\left(\left\langle \left[\chi_R(x), \chi_R^\dagger(y)\right] \right\rangle\right) + \mathrm{tr}\left(\left\langle \left[\chi_L(x), \chi_L^\dagger(y)\right] \right\rangle\right)\right], \tag{A.8}$$

and for the spatial components we find

$$\mathbf{F}_V(x,y) = \frac{1}{8}\left[\mathrm{tr}\left(\boldsymbol{\sigma}\left\langle \left\{\chi_R(x), \chi_R^\dagger(y)\right\} \right\rangle\right) - \mathrm{tr}\left(\boldsymbol{\sigma}\left\langle \left\{\chi_L(x), \chi_L^\dagger(y)\right\} \right\rangle\right)\right]. \tag{A.9}$$

We observe that terms in which either only left- or only right-handed spinors arises. This indicates the chiral-invariance of these two-point functions. The scalar part results into

$$F_S(x,y) = \frac{1}{8}\left[\mathrm{tr}\left(\left\langle \left[\chi_L(x), \chi_R^\dagger(y)\right] \right\rangle\right) + \mathrm{tr}\left(\left\langle \left[\chi_R(x), \chi_L^\dagger(y)\right] \right\rangle\right)\right], \tag{A.10}$$

which demonstrates the expected information that this two-point function is not invariant under a chiral transformation. Consequently in a model with broken chiral symmetry those two-point functions are nonvanishing. The nonvanishing tensor components of the statistical function in the chiral basis have the form

$$\mathbf{F}_T^0(x,y) = \frac{i}{8}\left[\mathrm{tr}\left(\boldsymbol{\sigma}\left\langle \left[\chi_R(x), \chi_L^\dagger(y)\right] \right\rangle\right) - \mathrm{tr}\left(\boldsymbol{\sigma}\left\langle \left[\chi_L(x), \chi_R^\dagger(y)\right] \right\rangle\right)\right], \tag{A.11}$$

which also mixes left and right components and thus have to be respected in calculations where no chiral symmetry is imposed. We conclude that whenever an equation of motion consists out of vector components of two-point correlation functions it is chirally invariant.

Spectral Two-Point Function

The spectral function $\rho(x,y)$ is defined by

$$\rho(x,y) = i\Big\langle \left\{\psi(x), \bar{\psi}(y)\right\} \Big\rangle , \tag{A.12}$$

which leads in term of the two-component spinors

$$\rho(x,y) = i \begin{pmatrix} \Big\langle \left\{\chi_L(x), \chi_R^\dagger(y)\right\} \Big\rangle & \Big\langle \chi_L(x)\chi_L^\dagger(y) + \chi_R^\dagger(y)\chi_R(x) \Big\rangle \\ \Big\langle \chi_R(x)\chi_R^\dagger(y) + \chi_L^\dagger(y)\chi_L(x) \Big\rangle & \Big\langle \left\{\chi_R(x), \chi_L^\dagger(y)\right\} \Big\rangle \end{pmatrix} .$$

For the temporal and spatial component of the vector part we have

$$\rho_V^0(x,y) = \frac{i}{4}\left[\mathrm{tr}\left(\Big\langle \left\{\chi_R(x), \chi_R^\dagger(y)\right\} \Big\rangle \right) + \mathrm{tr}\left(\Big\langle \left\{\chi_L(x), \chi_L^\dagger(y)\right\} \Big\rangle \right) \right] , \tag{A.13}$$

and

$$\boldsymbol{\rho}_V(x,y) = \frac{i}{4}\left[\mathrm{tr}\left(\boldsymbol{\sigma} \Big\langle \left[\chi_R(x), \chi_R^\dagger(y)\right] \Big\rangle \right) - \mathrm{tr}\left(\boldsymbol{\sigma} \Big\langle \left[\chi_L(x), \chi_L^\dagger(y)\right] \Big\rangle \right) \right] . \tag{A.14}$$

As for the statistical functions, these components are chiral invariant. The scalar component in turn mixes left- and right-handed components, i.e. we have

$$\rho_S(x,y) = \frac{i}{4}\left[\mathrm{tr}\left(\Big\langle \left\{\chi_L(x), \chi_R^\dagger(y)\right\} \Big\rangle \right) + \mathrm{tr}\left(\Big\langle \left\{\chi_R(x), \chi_L^\dagger(y)\right\} \Big\rangle \right) \right] , \tag{A.15}$$

as well does the tensor part

$$\boldsymbol{\rho}_T^0(x,y) = \frac{1}{4}\left[\mathrm{tr}\left(\boldsymbol{\sigma} \Big\langle \left\{\chi_L(x), \chi_R^\dagger(y)\right\} \Big\rangle \right) - \mathrm{tr}\left(\boldsymbol{\sigma} \Big\langle \left\{\chi_R(x), \chi_L^\dagger(y)\right\} \Big\rangle \right) \right] . \tag{A.16}$$

We infer from these results, as in the last section for the statistical part, whenever an equation of motion is made out of vector parts of correlation functions such equations are chirally invariant. We emphasize that our applied symmetries, cf. Sec. 3.1, restrict the number of nonvanishing components. For instance, in a model without spatial isotropy the "spatial-spatial" tensor components not necessarily vanish.

Appendix B

Energy-Momentum Tensor

In this Appendix we present an explicit calculation of the energy-momentum tensor $T_{\mu\nu}(x)$.

There are two ways often used in literature in calculating $T_{\mu\nu}(x)$. One way considers a general coordinate transformation $x^\mu \longrightarrow x^\mu + \epsilon^\mu(x)$ in the effective action and defines the tensor as a conserved current under this transformation, for details of this approach see e.g. [AST05, Nis08]. The second way, which we will follow, defines the tensor by the variation of the effective action with respect to the metric $g_{\mu\nu}(x)$ which is assumed to be a general space-time dependend metric with x as the space-time coordinates, see e.g. [BD82, CHR00, C$^+$94]. That means we have to calculate the functional derivative

$$T_{\mu\nu}(x) = \frac{2}{\sqrt{-g(x)}} \left. \frac{\delta\Gamma[\phi, G, D, g^{\mu\nu}]}{\delta g^{\mu\nu}(x)} \right|_{g_{\mu\nu}=\eta_{\mu\nu}} , \tag{B.1}$$

where $-g(x) \equiv \det(g_{\mu\nu}(x))$. The result will be evaluated at $g_{\mu\nu} = \eta_{\mu\nu}$ the Minkowski metric with $\mathrm{diag}(+1, -1, -1, -1)$. The effective action in (B.1) is the one defined in Sec. 2.2 in Eq. (2.10) with the classical part and propagators introduced in Sec. 3.1. Here we explicitly show the dependence on the metric which emerges due to space-time integrals and scalar-products. Consequently we have in (2.10) $\Gamma_2[\phi, D, G] = \Gamma_2[\phi, D, G, g^{\mu\nu}]$. In the following we will omit the metric dependence indication for convenience. For the calculation of $T_{\mu\nu}(x)$ the following rules might be helpful

$$\begin{aligned}
&\frac{\delta g^{\mu\nu}(x)}{\delta\, g_{\kappa\lambda}(y)} = -g^{\mu\kappa}(x)g^{\nu\lambda}(x)\delta(x-y)\,; \quad \frac{\delta g^{\mu\nu}(x)}{\delta\, g^{\kappa\lambda}(y)} = \delta^\mu_\kappa \delta^\nu_\lambda \delta(x-y)\,; \\
&\frac{\delta g(x)}{\delta\, g_{\mu\nu}(y)} = g(x)g^{\mu\nu}(x)\delta(x-y)\,; \quad \frac{\delta g(x)}{\delta\, g^{\mu\nu}(y)} = -g(x)g_{\mu\nu}(x)\delta(x-y)\,; \\
&\frac{\delta\sqrt{-g(x)}}{\delta\, g_{\mu\nu}(y)} = \frac{1}{2}\sqrt{-g(x)}g^{\mu\nu}(x)\delta(x-y)\,; \quad \frac{\delta\sqrt{-g(x)}}{\delta\, g^{\mu\nu}(y)} = -\frac{1}{2}\sqrt{-g(x)}g_{\mu\nu}(x)\delta(x-y)\,.
\end{aligned} \tag{B.2}$$

It is convenient to divide the energy-momentum tensor into three parts representing a fermionic, bosonic and classical part. The sum of these three parts results

in $T_{\mu\nu}(x)$. In the following we will present a detailed calculation of each part separately. In the two subsequent sections we will focus on the energy density and pressure respectively.

Fermion Part of Quantum Fluctuations

The fermionic part of the effective action is given by

$$\Gamma^{\psi}[\phi, D, G] = \underbrace{-i\mathrm{Tr}\log D^{-1}(x,y)}_{A}\underbrace{-i\mathrm{Tr}D_0^{-1}(x,y)D(y,x)}_{B}\underbrace{+\Gamma_2^{\psi}[D,G]}_{C} \quad \text{(B.3)}$$

We labeled each term for later reference. The 2PI part Γ_2^{ψ} is the fermion part of (3.44), i.e.

$$\Gamma_2^{\psi}[D,G] = -ih^2\frac{N_f}{2}\int_c d^4x d^4y\,\mathrm{tr}[D(x,y)D(y,x)]G_{aa}(x,y)\,. \quad \text{(B.4)}$$

This definition is plausible since also without fermion interaction the boson and classical energy density would be determined with the remaining terms in (3.44). In general there is no clear rigorous separation of different parts of the tensor the only well defined quantity is the total energy density. In the following we will discuss the functional derivative of each term in detail.

Term A This "one-loop term"[1] with the resummed propagator $D(x,y)$ is independent of the metric $g_{\mu\nu}(x)$, see e.g. [CHR00, PS95]. Consequently term A vanishes due to the variation with respect to the metric.

$$T^{\psi}_{\mu\nu}(x)|_A = \frac{2}{\sqrt{-g}}\frac{\delta}{\delta g^{\mu\nu}(x)}\left[-i\mathrm{Tr}\log D^{-1}(y,z)\right] = 0\,. \quad \text{(B.5)}$$

Term B Here we have to consider

$$T_{\mu\nu}(x)|_B = \frac{2}{\sqrt{-g}}\frac{\delta}{\delta g^{\mu\nu}(x)}\left[-i\mathrm{Tr}D_0^{-1}(z,y)D(y,z)\right]. \quad \text{(B.6)}$$

The trace corresponds to the integration over space-time and summation over Dirac and flavor indices. Since we are dealing with a space-time dependend metric $g^{\mu\nu}(x)$ we have to use invariant integral measures $d^4x = d^4x\sqrt{-g}(x)$. The calculation looks

[1] This term can be rewritten in such a way that "trace log" yields "log det", which does not contain a single space-time integration and thus no metric dependence.

as follows[2]

$$
\begin{aligned}
&T^{\psi}_{\mu\nu}(x)|_B \\
&= \frac{2}{\sqrt{-g}}\frac{\delta}{\delta g^{\mu\nu}(x)}\left(-2i\int d^4z\int d^4y\sqrt{-g(z)}\sqrt{-g(y)}\,\mathrm{tr}D_0^{-1}(z,y)D(y,z)\right) \\
&= \frac{-4}{\sqrt{-g}}\frac{\delta}{\delta g^{\mu\nu}(x)}\int_z\int_y\sqrt{-g(z)}\sqrt{-g(y)}\,\mathrm{tr}\left[[\left(i\gamma^\alpha\partial^z_\alpha - M_\psi(z)\right)\delta(z-y)]D(y,z)\right] \\
&= \frac{-4}{\sqrt{-g}}\frac{\delta}{\delta g^{\mu\nu}(x)}\int_z\sqrt{-g(z)}\,\mathrm{tr}\left[\left(-i\gamma^\alpha\partial^{z'}_\alpha - M_\psi(z)\right)D(z,z')\right]\Big|_{z'=z} \\
&= \frac{-4}{\sqrt{-g}}\left\{\int_z -\frac{1}{2}\sqrt{-g(z)}g_{\mu\nu}(z)\delta(x-z)\mathrm{tr}\left[\left(-i\gamma^\alpha\partial^{z'}_\alpha - M_\psi(z)\right)D(z,z')\right]\right. \\
&\left.+\int_z\sqrt{-g(z)}\mathrm{tr}\left[-\delta^\alpha{}_\mu\delta^\beta{}_\nu\delta(x-z)i\gamma_\alpha\partial^{z'}_\beta D(z,z')\right]\right\}\Big|_{z'=z}
\end{aligned}
\tag{B.7}
$$

In the second step we applied an integration by parts and evaluated the y-integral. Evaluating the last integral at $g^{\mu\nu}=\eta^{\mu\nu}$ we end up with

$$
\begin{aligned}
&T^{\psi}_{\mu\nu}(x)|_B \\
&= 4\left\{\frac{1}{2}\eta_{\mu\nu}\mathrm{tr}\left[\left(-i\gamma^\alpha\partial^{x'}_\alpha - M_\psi(x)\right)D(x,x')\right] + \mathrm{tr}\left(i\gamma_\mu\partial^{x'}_\nu D(x,x')\right)\right\}\Big|_{x'=x}
\end{aligned}
\tag{B.8}
$$

After a Lorentz decomposition the propagator $D(x,x')$ in our approximation only contains scalar D_S, vector D_V and tensor components D_T. Terms in the inverse free propagator thus acts like a projector on the vector and scalar components respectively. With the identity $\mathrm{tr}\,(\gamma^\mu\gamma^\nu)=4g^{\mu\nu}$ we have got

$$
\begin{aligned}
&T^{\psi}_{\mu\nu}(x)|_B \\
&= 16\left[\frac{1}{2}\eta_{\mu\nu}\left(-i\partial^{x'}_\alpha D^\alpha_V(x,x') - M_\psi(x)D_S(x,x')\right) + i\partial^{x'}_\nu D_{V,\mu}(x,x')\right]\Big|_{x'=x}
\end{aligned}
\tag{B.9}
$$

Inserting now the statistical and spectral part of the propagators and applying $x'=x$ we find

$$
\begin{aligned}
&T^{\psi}_{\mu\nu}(x)|_B \\
&= 16\left[\frac{1}{2}\eta_{\mu\nu}\left(-i\partial^{x'}_\alpha F^\alpha_V(x,x') - M_\psi(x)F_S(x,x')\right) + i\partial^{x'}_\nu F_{V,\mu}(x,x')\right]\Big|_{x'=x}
\end{aligned}
\tag{B.10}
$$

This is our final version of the term B contribution.

[2]The additionally factor of two in the first line arises due to the flavor trace part and "tr" denotes the Dirac trace part, evaluated at the end. We will abbreviate integrals by $\int d^4x \to \int_x$ throughout this chapter, if not stated otherwise.

Term C This term provides the most sophisticated part of the calculation. The starting point is

$$T^{\psi}_{\mu\nu}(x)|_C = \frac{2}{\sqrt{-g}(x)}\frac{\delta}{\delta g^{\mu\nu}(x)}\left[-ih^2\frac{N_f}{2}\int_z\int_y\sqrt{-g(z)}\sqrt{-g(y)}\,\mathrm{tr}\,[D(z,y)D(y,z)]\,G^{\phi}_{aa}(z,y)\right]. \tag{B.11}$$

where the trace has to be calculated with respect to the Dirac space. The variation only acts on the product of integral measures, thus we get two identical terms which yields a factor of two. Note that there is a factor 1/2 coming from the corresponding derivative in (B.2).

$$T^{\psi}_{\mu\nu}(x)|_C = \eta_{\mu\nu}\,i\,h^2N_f\int d^4y\,\mathrm{tr}\,[D(x,y)D(y,x)]\,G^{\phi}_{aa}(x,y)\,. \tag{B.12}$$

The next step is to express this result in terms of the statistical and spectral parts of the propagators. Since there is a closed time path integral[3] we have to be careful with the different terms which arises if we decompose the two-point functions. Because of the $\mathrm{sign}(x^0-y^0)$ function in the correlators only certain terms contribute to the time integral. The decomposition leads to the following expression, where we indicate in the second equation the trace by the implicit summation over the Dirac indices α,β.

$$\begin{aligned}T^{\psi}_{\mu\nu}(x)|_C &= +\eta_{\mu\nu}\,i\,h^2N_f\int_c d^4y\,\mathrm{tr}\left\{\left[F(x,y)-\frac{i}{2}\rho(x,y)\mathrm{sign}(x^0-y^0)\right]\right.\\ &\qquad\left.\times\left[F(y,x)-\frac{i}{2}\rho(y,x)\mathrm{sign}(y^0-x^0)\right]\right\}\\ &\qquad\times\left(F^{\phi}_{aa}(x,y)-\frac{i}{2}\rho^{\phi}_{aa}(x,y)\mathrm{sign}(x^0-y^0)\right)\end{aligned}$$

$$\begin{aligned}= +\eta_{\mu\nu}\,i\,h^2N_f\int_c d^4y\,\Big[&F_{\alpha\beta}(x,y)F_{\beta\alpha}(y,x)F^{\phi}_{aa}(x,y)\\ &+\frac{i}{8}\rho_{\alpha\beta}(x,y)\rho_{\beta\alpha}(y,x)\rho^{\phi}_{aa}(x,y)\mathrm{sign}(y^0-x^0)\\ &-\frac{i}{2}F_{\alpha\beta}(x,y)\rho_{\beta\alpha}(y,x)F^{\phi}_{aa}(x,y)\mathrm{sign}(y^0-x^0)\\ &-\frac{i}{2}\rho_{\alpha\beta}(x,y)F_{\beta\alpha}(y,x)F^{\phi}_{aa}(x,y)\mathrm{sign}(x^0-y^0)\\ &-\frac{i}{2}F_{\alpha\beta}(x,y)F_{\beta\alpha}(y,x)\rho^{\phi}_{aa}(x,y)\mathrm{sign}(x^0-y^0)\end{aligned} \tag{B.13}$$

[3] We use a compact notation with $\int_c dx^0\int d^3x = \int_c d^4x$, where c indicates the closed time path prescription

$$
\begin{aligned}
&- \frac{1}{4}\rho_{\alpha\beta}(x,y)\rho_{\beta\alpha}(y,x)F^{\phi}_{aa}(x,y)\mathrm{sign}(x^0-y^0)\mathrm{sign}(y^0-x^0) \\
&- \frac{1}{4}F_{\alpha\beta}(x,y)\rho_{\beta\alpha}(y,x)\rho^{\phi}_{aa}(x,y)\mathrm{sign}(x^0-y^0)\mathrm{sign}(y^0-x^0) \\
&- \frac{1}{4}\rho_{\alpha\beta}(x,y)F_{\beta\alpha}(y,x)\rho^{\phi}_{aa}(x,y)\mathrm{sign}(x^0-y^0)\mathrm{sign}(y^0-x^0)\Big] \, .
\end{aligned}
$$

For the evaluation of the time integration we have to keep in mind that

$$
\begin{aligned}
\int_c dy^0 \cdots \mathrm{sign}(y^0-x^0) &= \int_0^{x^0} dy^0(-1)\cdots + \int_{x^0}^{0} dy^0(+1)\cdots \\
&= -2\int_0^{x^0} dy^0 \cdots \, ,
\end{aligned} \tag{B.14}
$$

in the case of $\mathrm{sign}(x^0-y^0)$ there is a plus sign in front. If there are two sign functions the integral vanish because $\mathrm{sign}(x^0-y^0)\mathrm{sign}(y^0-x^0)=1$ and the integration over a closed path vanishes. Note that here a special case arises in which the two sign function contain the same arguments. In general it does not have to vanish (see e.g. [Ber05] for details). With this we see that only the second, third, fourth and fifth term contribute. If we sort the remaining terms we find

$$
\begin{aligned}
&T^{\psi}_{\mu\nu}(x)|_C \\
&\quad = -\eta_{\mu\nu}\, h^2 N_f \int_0^{x^0} d^4y \, \Big[-\Big(F_{\alpha\beta}(x,y)F_{\beta\alpha}(y,x) + \frac{1}{4}\rho_{\alpha\beta}(x,y)\rho_{\beta\alpha}(y,x)\Big)\rho^{\phi}_{aa}(x,y) \\
&\qquad\qquad + \Big(F_{\alpha\beta}(x,y)\rho_{\beta\alpha}(y,x) - \rho_{\alpha\beta}(x,y)F_{\beta\alpha}(y,x)\Big)F^{\phi}_{aa}(x,y)\Big] \, ,
\end{aligned} \tag{B.15}
$$

where we explicitly wrote the closed time path limits. Now we insert the Lorentz decomposition of the propagators with respect of the symmetries employed here. The Dirac traces lead to a factor of 4 because of

$$
\begin{aligned}
F_{\alpha\beta}(x,y)F_{\beta\alpha}(y,x) &= 4\Big[F_S(x,y)F_S(y,x) \\
&\qquad + F_{V,\mu}(x,y)F^{\mu}_V(y,x) + F_{T,\mu\nu}(x,y)F^{\mu\nu}_T(y,x)\Big] \, .
\end{aligned} \tag{B.16}
$$

In the following we will show for the vector part the next steps explicitly, the other terms are obtained analogously. We find for the vector part

$$\begin{aligned} &T^{\psi}_{\mu\nu}(x)|_{C,\mathrm{V}} \\ &\quad = -\eta_{\mu\nu}\, 4h^2 N_f \int_0^{x^0} d^4y \left\{ \left[F_{V,\mu}(x,y)F^{\phi}_{aa}(x,y) - \frac{1}{4}\rho_{V,\mu}(x,y)\rho^{\phi}_{aa}(x,y) \right] \rho^{\mu}_V(y,x) \right. \\ &\qquad\qquad \left. - \left[F_{V,\mu}(x,y)\rho^{\phi}_{aa}(x,y) + \rho_{V,\mu}(x,y)F^{\phi}_{aa}(x,y) \right] F^{\mu}_V(y,x) \right\} \end{aligned} \tag{B.17}$$

If we now use the Fourier expansion of the two-point functions we get rid of the spatial integral and we will see that each term corresponds to a part of a fermionic self-energy. As an example we consider the first term in (B.17)[4]

$$\begin{aligned} &-\eta_{\mu\nu}\, 4h^2 N_f \int_0^{x^0} d^4y \left[F_{V,\mu}(x,y)F^{\phi}_{aa}(x,y)\rho^{\mu}_V(y,x) \right] \\ = \; &-\eta_{\mu\nu}\, 4h^2 N_f \int_0^{x^0} d^4y \left[\int \frac{d^3k}{(2\pi)^3} e^{i\mathbf{k}(\mathbf{x}-\mathbf{y})} F_{V,\mu}(x^0,y^0;\mathbf{k}) \int \frac{d^3q}{(2\pi)^3} e^{i\mathbf{q}(\mathbf{x}-\mathbf{y})} F^{\phi}_{aa}(x^0,y^0;\mathbf{q}) \right. \\ &\qquad \left. \times \int \frac{d^3p}{(2\pi)^3} e^{-i\mathbf{p}(\mathbf{x}-\mathbf{y})} \rho^{\mu}_V(y^0,x^0;\mathbf{p}) \right] \\ = \; &-\eta_{\mu\nu}\, 4h^2 N_f \int_0^{x^0} dy^0 \int_{\mathbf{y},\mathbf{k},\mathbf{q},\mathbf{p}} e^{i(\mathbf{k}+\mathbf{q}-\mathbf{p})(\mathbf{x}-\mathbf{y})} F_{V,\mu}(x^0,y^0;\mathbf{k}) F^{\phi}_{aa}(x^0,y^0;\mathbf{q}) \rho^{\mu}_V(y^0,x^0;\mathbf{p}) \\ = \; &-\eta_{\mu\nu}\, 4h^2 N_f \int_0^{x^0} dy^0 \int_{\mathbf{k},\mathbf{q},\mathbf{p}} e^{i(\mathbf{k}+\mathbf{q}-\mathbf{p})\mathbf{x}} \delta(\mathbf{k}+\mathbf{q}-\mathbf{p}) \\ &\qquad \times F_{V,\mu}(x^0,y^0;\mathbf{k}) F^{\phi}_{aa}(x^0,y^0;\mathbf{q}) \rho^{\mu}_V(y^0,x^0;\mathbf{p}) \\ = \; &-\eta_{\mu\nu}\, 4h^2 N_f \int_0^{x^0} dy^0 \int_{\mathbf{k},\mathbf{p}} F_{V,\mu}(x^0,y^0;\mathbf{k}) F^{\phi}_{aa}(x^0,y^0;\mathbf{p}-\mathbf{k}) \rho^{\mu}_V(y^0,x^0;\mathbf{p}) \end{aligned} \tag{B.18}$$

The $\mathbf{k}$-integral has exactly the form of an integral in the fermionic self-energy (3.48). If we take the second term in (B.17) and do the same steps, in combination with (B.18)

[4]Note that we indicate spatial integrals with a bold face letter.

we end up with the following expression

$$
\begin{aligned}
&-\eta_{\mu\nu}\,4h^2N_f\int_0^{x^0}dy^0\int_{\mathbf{p}}\int_{\mathbf{k}}\Big[F_{V,\mu}(x^0,y^0;\mathbf{k})F^{\phi}_{aa}(x^0,y^0;\mathbf{p}-\mathbf{k})\\
&\qquad\qquad -\frac{1}{4}\rho_{V,\mu}(x^0,y^0;\mathbf{k})\rho^{\phi}_{aa}(x^0,y^0;\mathbf{p}-\mathbf{k})\Big]\rho^{\mu}_V(y^0,x^0;\mathbf{p})\\
=\;&\eta_{\mu\nu}\,4N_f\int_0^{x^0}dy^0\int_{\mathbf{p}}C^{\mu}_V(x^0,y^0;\mathbf{p})\rho_{V,\mu}(y^0,x^0;\mathbf{p})
\end{aligned}
\tag{B.19}
$$

The last two terms in (B.17) give

$$
-\eta_{\mu\nu}\,4N_f\int_0^{x^0}dy^0\int_{\mathbf{p}}A^{\mu}_V(x^0,y^0;\mathbf{p})F_{V,\mu}(y^0,x^0;\mathbf{p})\,. \tag{B.20}
$$

Alltogether we have got

$$
\begin{aligned}
T^{\psi}_{\mu\nu}(x)|_{C,V} \;=\;&-\eta_{\mu\nu}\,4N_f\int_0^{x^0}dy^0\int_{\mathbf{p}}\big[A^{\mu}_V(x^0,y^0;\mathbf{p})F^{(f)}_{\mu}(y^0,x^0;\mathbf{p})\\
&\qquad -C^{\mu}_V(x^0,y^0;\mathbf{p})\rho_{V,\mu}(y^0,x^0;\mathbf{p})\Big]\,.
\end{aligned}
\tag{B.21}
$$

If we write the scalar product explicitly and use $N_f = 2$ we find

$$
\begin{aligned}
&T^{\psi}_{\mu\nu}(x)|_{C,V}\\
&\quad=-8\,\eta_{\mu\nu}\int_{\mathbf{p}}\int_0^{x^0}dy^0\Big[A^0_V(x^0,y^0;\mathbf{p})F^0_V(y^0,x^0;\mathbf{p})-A^i_V(x^0,y^0;\mathbf{p})F_{V,i}(y^0,x^0;\mathbf{p})\\
&\qquad\qquad -C^0_V(x^0,y^0;\mathbf{p})\rho^0_V(y^0,x^0;\mathbf{p})+C^i_V(x^0,y^0;\mathbf{p})\rho_{V,i}(y^0,x^0;\mathbf{p})\Big]\,.
\end{aligned}
\tag{B.22}
$$

All steps from (B.15) to (B.22) can also be made for the scalar and tensor part of (B.15). The expression (B.22) is a part of the right hand side of the equation of motion for $F^0_V(t,t';\mathbf{p})$ (3.31), more precisely it is a part of the memory integrals. The manipulations of the scalar and tensor parts in (B.15) would lead to the remaining terms in the memory integrals in (3.31) so that we get the complete memory integral

structure of the equation of motion. [5] The final expression of $T^{\psi}_{\mu\nu}(x)|_{C,V}$ accordingly is

$$\begin{aligned}
&T^{\psi}_{\mu\nu}(x)|_C \\
&= -8\eta_{\mu\nu}\int_{\mathbf{p}}\int_0^{x^0} dy^0 \Big[A_S(x^0,y^0;\mathbf{p})F_S(y^0,x^0;\mathbf{p}) - A^{0i}_T(x^0,y^0;\mathbf{p})F^{0i}_T(y^0,x^0;\mathbf{p}) \\
&\qquad\qquad + A^0_V(x^0,y^0;\mathbf{p})F^0_V(y^0,x^0;\mathbf{p}) - A^i_V(x^0,y^0;\mathbf{p})F^i_V(y^0,x^0;\mathbf{p})\Big] \\
&+8\eta_{\mu\nu}\int_{\mathbf{p}}\int_0^{x^0} dy^0 \Big[C_S(x^0,y^0;\mathbf{p})\rho_S(y^0,x^0;\mathbf{p}) - C^{0i}_T(x^0,y^0;\mathbf{p})\rho^{0i}_T(y^0,x^0;\mathbf{p}) \\
&\qquad\qquad + C^0_V(x^0,y^0;\mathbf{p})\rho^0_V(y^0,x^0;\mathbf{p}) - C^i_V(x^0,y^0;\mathbf{p})\rho^i_V(y^0,x^0;\mathbf{p})\Big] \\
&\equiv -8\eta_{\mu\nu}\int_{\mathbf{p}} R(x^0;\mathbf{p})\,,
\end{aligned} \tag{B.23}$$

where we defined the memory integral contribution by $R(x^0;\mathbf{p})$.

Total Fermion Part

The final expression of the complete fermion part of the energy-momentum tensor is

$$\begin{aligned}
T^{\psi}_{\mu\nu}(x) \;=\; 8\Bigg[\eta_{\mu\nu}\left(-i\partial^{x'}_{\alpha}F^{\alpha}_V(x,x')\Big|_{x'=x} - M_{\psi}(x)F_S(x,x) - \int_{\mathbf{p}} R(x^0;\mathbf{p})\right) \\
+2i\partial^{x'}_{\nu}F_{V,\mu}(x,x')\Big|_{x'=x}\Bigg]\,.
\end{aligned} \tag{B.24}$$

Boson Part of Quantum Fluctuations

The bosonic part of the effective action is defined by

$$\Gamma^{\phi}[\phi,G] \;=\; \underbrace{\frac{i}{2}\mathrm{Tr}\log G^{-1}(x,y)}_{A} + \underbrace{\frac{i}{2}\mathrm{Tr}G_0^{-1}(x,y)G(y,x)}_{B} + \underbrace{\Gamma^{\phi}_2[\phi,G]}_{C}\,, \tag{B.25}$$

[5] In the expression derived here the momentum arguments of the self-energies and propagators do not contain the absolute value of the momentum, however, $\mathbf{p}\cdot\mathbf{p}/(|\mathbf{p}||\mathbf{p}|) = 1$ and thus our results agrees with the right hand side of the equation of motion.

with the labels A, B and C for later reference. $\Gamma_2^\phi[\phi, G]$ is the quantum bosonic part of (3.44), i.e.

$$\begin{aligned}\Gamma_2^\phi[\phi,G] &= -\frac{\lambda}{4!N_s}\int_x G_{aa}(x,x)G_{bb}(x,x) \\ &\quad +\frac{i}{2}\mathrm{Tr}\ln\left[\delta^{(4)}(x-y)+i\frac{\lambda}{6N_s}G_{ab}(x,y)G_{ab}(x,y)\right] \\ &\quad +i\frac{\lambda}{6N_s}\int_x\int_y I(x,y;G)\phi(x)G_{\|}(x,y)\phi(y) \end{aligned} \tag{B.26}$$

In the following we will consider the different terms A, B, and C separately.

Term A The first term in the boson effective action vanishes for the same reason as in the fermion part, that means it is independent of the metric. Thus we have

$$T^\phi_{\mu\nu}(x)|_A = \frac{2}{\sqrt{-g}}\frac{\delta}{\delta g^{\mu\nu}(x)}\left[\frac{i}{2}\mathrm{Tr}\log G^{-1}(x,y)\right] = 0\,. \tag{B.27}$$

Term B This term has to calculated carefully. The key ingredient of this calculation is the fact that the derivative-operator in G_0^{-1} only acts on the delta function in G_0^{-1}. Hence we apply an integration by parts in order to have derivatives of the resummed propagator present. Further we note the use of the identity $\int_{x,y}\partial_x^2\,\delta(x-y) = -\int_{x,y}\partial_x\partial_y\,\delta(x-y)$. Explicitely this means

$$\begin{aligned} &T^\phi_{\mu\nu}(x)|_B \\ &= \frac{2}{\sqrt{-g}}\frac{\delta}{\delta g^{\mu\nu}(x)}\left\{\frac{i}{2}\int_z\int_y\sqrt{-g(z)}\sqrt{-g(y)}\right. \\ &\quad \left.\times\mathrm{tr}\left[\left[i\left(\Box_z\delta_{ab}+M^2_{ab}(z^0)\right)\delta(z-y)\right]G(y,z)\right]\right\} \\ &= \frac{2}{\sqrt{-g}}\frac{\delta}{\delta g^{\mu\nu}(x)}\left\{\frac{i}{2}\int_z\int_y\sqrt{-g(z)}\sqrt{-g(y)}\right. \\ &\quad \left.\times\mathrm{tr}\left[\left[i\left(-\partial^\mu_z\partial^y_\mu\delta_{ab}+M^2_{ab}(z^0)\right)\delta(z-y)\right]G(y,z)\right]\right\} \\ &= \frac{-1}{\sqrt{-g}}\frac{\delta}{\delta g^{\mu\nu}(x)}\left\{\int_z\sqrt{-g(z)}\mathrm{tr}\left[\left(-(-1)^2\partial^\mu_{z'}\partial^z_\mu\delta_{ab}+M^2_{ab}(x^0)\right)G(z,z')\right]\Big|_{z'=z}\right\} \\ &= \frac{-1}{\sqrt{-g}}\left\{\int_z -\frac{1}{2}g_{\mu\nu}(z)\sqrt{-g(z)}\delta(x-z)\mathrm{tr}\left[\left(-\partial^\mu_{z'}\partial^z_\mu\delta_{ab}+M^2_{ab}(x^0)\right)G(z,z')\right]\right. \end{aligned}$$

$$+\int_z \sqrt{-g(z)}\mathrm{tr}\left[\left(-\delta^\alpha_\mu\,\delta^\beta_\nu\,\partial^{z'}_\alpha\,\partial^{z'}_\beta\right)\delta_{ab}\delta(x-z)G(z,z')\right]\Big\}\Big|_{z'=z}.$$

So we end up with

$$T^\phi_{\mu\nu}(x)|_B = \left[\frac{1}{2}\eta_{\mu\nu}\left(-g^{\alpha\beta}\,\partial^x_\alpha\,\partial^{x'}_\beta\,\delta_{ab}\,+M^2_{ab}(x^0)\right)G_{ba}(x,x')+\partial^x_\mu\,\partial^{x'}_\nu\,G_{aa}(x,x')\right]\Big|_{x'=x}. \tag{B.28}$$

In terms of the statistical propagator this simply reads

$$T^\phi_{\mu\nu}(x)|_B = \left[\frac{1}{2}\eta_{\mu\nu}\left(-g^{\alpha\beta}\,\partial^x_\alpha\,\partial^{x'}_\beta\,\delta_{ab}\,+M^2_{ab}(x^0)\right)F^\phi_{ba}(x,x')+\partial^x_\mu\,\partial^{x'}_\nu\,F^\phi_{aa}(x,x')\right]\Big|_{x'=x}, \tag{B.29}$$

because the spectral propagator vanishes at $x'=x$.

Term C This term is worth to divide into three parts. We will call the first, second and third term in (B.26) C1, C2, C3, respectively. The calculation of part C1 is quite simple, we have a variation with respect to the metric due to the integral measure thus C1 becomes:

$$T^\phi_{\mu\nu}(x)|_{\mathrm{C1}} = \eta_{\mu\nu}\frac{\lambda}{4!N_s}\,G_{aa}(x,x)G_{bb}(x,x)\,. \tag{B.30}$$

The part C2 has to be treated in a special way. First we expand the logarithm and then apply the variation with respect to the metric. We observe the following structure. The only metric dependence parts are the integral measures. Depending on the order of the expansion we have one integral measure $\sqrt{-g}$, a product of two,a product of three, etc.. The different terms which arises due to the product rule can be combined because of $G(x,x') = G(x',x)$. Thus we have factors like $\frac{\delta}{\delta g^{\mu\nu}}(\sqrt{-g})^n = -n\frac{1}{2}(\sqrt{-g})^n g_{\mu\nu}$, the factor $1/2$ cancel with the factor of two in the definition of the energy-momentum tensor. The factor n cancels with the Taylor expansion coefficients. What remains is exactly the function $I(x,x,G)$ (3.46) times $1/2$. Hence we have

$$T^\phi_{\mu\nu}(x)|_{\mathrm{C2}} = \eta_{\mu\nu}\frac{1}{2}I(x,x;G)\,, \tag{B.31}$$

which is the final expression for the C2 part.

The calculation of the part C3 requires some effort. It starts with

$$T^\phi_{\mu\nu}(x)|_{\mathrm{C3}} = \frac{2}{\sqrt{-g}}\frac{\delta}{\delta g^{\mu\nu}(x)}\left\{\frac{i\lambda}{6N_s}\int_z\int_y\sqrt{-g(z)}\sqrt{-g(y)}I(z,y;G)\phi(z)G_\parallel(z,y)\phi(y)\right\}, \tag{B.32}$$

note that in $I(z,y;G)$ additional space-time integrations appear and thus additional dependencies on the metric. For convenience we recall that

$$I(z,y;G) = \frac{\lambda}{6N_s} G_{ab}(z,y)G_{ab}(z,y) - \frac{i\lambda}{6N_s}\int_w \sqrt{-g(w)} I(z,w;G)G_{ab}(w,y)G_{ab}(w,y)\,. \tag{B.33}$$

In (B.32) we apply the product rule for the variation, if the variation acts on the product of integral measures we get two terms which can be added due to the symmetry relation of $G(z,y)$. With what we end up after the first step is

$$\begin{aligned} T^{\phi}_{\mu\nu}(x)|_{C3} &= \frac{-2i\lambda}{6N_s\sqrt{-g}}\left\{ g_{\mu\nu}(x)\int_y \sqrt{-g(y)} I(x,y;G)\phi(x)G_{\parallel}(x,y)\phi(y) \right. \\ &\quad \left. - \int_z\int_y \sqrt{-g(z)}\sqrt{-g(y)}\left[\frac{\delta I(z,y;G)}{\delta g^{\mu\nu}(x)}\right]\phi(z)G_{\parallel}(z,y)\phi(y)\right\}. \end{aligned} \tag{B.34}$$

It is worth to have a detailed look on the variation of the function $I(z,y;G)$ emerging in the second term of (B.34). The first term in (B.33) vanishes and the second term generates two terms, i.e.

$$\begin{aligned} \frac{\delta I(z,y;G)}{\delta g^{\mu\nu}(x)} &= \frac{\lambda}{6N_s}\left\{ +i\frac{g_{\mu\nu}(x)}{2} I(z,x;G)G_{ab}(x,y)G_{ab}(x,y) \right. \\ &\quad \left. -i\int_w \sqrt{-g(w)}\left[\frac{\delta I(z,w;G)}{\delta g^{\mu\nu}(x)}\right] G_{ab}(w,y)G_{ab}(w,y)\right\}. \end{aligned} \tag{B.35}$$

This can be viewed as a recursive definition of a new quantity, namely the derivative of the resummation function $I(z,y;G)$. However, we can rewrite this expression into a form which consits purely out of $I(z,y;G)$ itself. We will now first describe the structure in words before we will present the mathematical expression. The second term in (B.35) produces a factor $g_{\mu\nu}(x)I(z,x;G)/2$ under the w-integral as in the first term in (B.35), thus can be pulled out of the integration and one is left with a product of four bosonic propagators G. The reiteration of the second term in (B.35) produces a new integral, we call it u-integral, with a new function $I(z,u;G)$ and a product of $G(u,x)$. Inserting an additional reiteration leads again to a factor $g_{\mu\nu}(x)I(z,x;G)/2$ which can again be pulled out of the two integrations. This structure turns up on each iteration level, thus we end up with a common factor in front of nested integrals. Luckily these nested integrals are exactly a resummation function $I(x,y;G)$, however with different arguments. Mathematically this looks

like (we abbreviate the derivative with a prime)

$$\begin{aligned} I'_x(z,y;G) &= +i\frac{\lambda}{6N_s}\frac{g_{\mu\nu}(x)}{2}I(z,x;G)G^2_{ab}(x,y) - i\frac{\lambda}{6N_s}\int_w I'_x(z,w;G)G^2_{ab}(w,y) \\ &= +i\frac{\lambda}{6N_s}\frac{g_{\mu\nu}(x)}{2}I(z,x;G)G^2_{ab}(x,y) \\ &\quad -i\frac{\lambda}{6N_s}\int_w \left[\frac{i\lambda}{6N_s}\frac{g_{\mu\nu}(x)}{2}I(z,x;G)G^2_{ab}(x,w)\right] G^2_{ab}(w,y) \\ &\quad \frac{-i\lambda}{6N_s}\int_w \left[\frac{-i\lambda}{6N_s}\int_u \left[\frac{i\lambda}{6N_s}\frac{g_{\mu\nu}(x)}{2}I(z,x;G)G^2_{ab}(x,u)\right] G^2_{ab}(u,w)\right] G^2_{ab}(w,y) + ... \\ &= \frac{ig_{\mu\nu}(x)}{2}I(z,x;G)\left\{\frac{\lambda}{6N_s}G^2_{ab}(x,y) - i\left(\frac{\lambda}{6N_s}\right)^2\int_w G^2_{ab}(x,w)G^2_{ab}(w,y)\right. \\ &\quad \left. -\left(\frac{\lambda}{6N_s}\right)^3\int_w\int_u G^2_{ab}(x,u)G^2_{ab}(u,w)G^2_{ab}(w,y) + ...\right\}. \end{aligned}$$

The expression in braces is nothing but (B.33) with the corresponding arguments after one complete iteration. Consequently the result is

$$\frac{\delta I(z,y;G)}{\delta g^{\mu\nu}(x)} = \frac{i}{2}I(z,x;G)I(x,y;G)g_{\mu\nu}(x)\,. \tag{B.36}$$

Inserting this into (B.34) leads to

$$\begin{aligned} T^{\phi}_{\mu\nu}(x)|_{C3} &= -\eta_{\mu\nu}\frac{2i\lambda}{6N_s}\left\{\int_y I(x,y;G)\phi(x)G_{\parallel}(x,y)\phi(y)\right. \\ &\quad \left. -\frac{i}{2}\int_z\int_y I(z,x;G)I(x,y;G)\phi(z)G_{\parallel}(z,y)\phi(y)\right\}. \end{aligned} \tag{B.37}$$

So alltogether we have for the term C

$$\begin{aligned} T^{\phi}_{\mu\nu}(x)|_{C} &= \eta_{\mu\nu}\left\{\frac{\lambda}{4!N_s}G_{aa}(x,x)G_{bb}(x,x) + \frac{1}{2}I(x,x;G)\right. \\ &\quad -\frac{2i\lambda}{6N_s}\left[\int_y I(x,y;G)\phi(x)G_{\parallel}(x,y)\phi(y)\right. \\ &\quad \left.\left. -\frac{i}{2}\int_z\int_y I(z,x;G)I(x,y;G)\phi(z)G_{\parallel}(z,y)\phi(y)\right]\right\}. \end{aligned} \tag{B.38}$$

Now, this has to be expressed in terms of the statistical and spectral part of the boson propagator $G_{ab}(x,y)$ (3.7). First of all we have to note that $G_{aa} = G_{\parallel} + (N_s -$

1)$G_\perp$ and recall that the bosonic spectral function vanishes at equal arguments. Accordingly the results of the first two terms in (B.38) are easily obtained. We will list them in the complete final version below.

The last two terms require more attention. The macroscopic field has no decomposition and thus will not changed. We use the notation introduced in (3.61) and (3.62) for the products of the form $\phi(x)G(x,y)\phi(y)$, which are denoted by $H_F(x,y)$ or $H_\rho(x,y)$ for the statistical and spectral part of $G(x,y)$ respectively. Further we have to respect the time integration over the closed time path, as was done in the case of the fermion part. In (B.38) the third term contains only one time integration whereas the last term contains two. Terms which contain no/two or one sign-function vanish due to the integration over one/one or two time path, respectively. The product in the third term in (B.38) leads to

$$\begin{aligned} I(x,y;G)\phi(x)G_\parallel(x,y)\phi(y) &= -I(x,y;G)H(x,y) \\ &= -\Big\{ I_F(x,y;G)H_F(x,y) \\ &\quad -\frac{1}{4}I_\rho(x,y;G)H_\rho(x,y)\,\mathrm{sign}(x^0-y^0)\,\mathrm{sign}(x^0-y^0) \\ &\quad -\frac{i}{2}I_F(x,y;G)H_\rho(x,y)\,\mathrm{sign}(x^0-y^0) \\ &\quad -\frac{i}{2}I_\rho(x,y;G)H_F(x,y)\,\mathrm{sign}(x^0-y^0)\Big\}\,. \end{aligned} \tag{B.39}$$

The integration over y^0 (B.38) forces the first two terms to vanish. Recalling the closed time path properties we find the result for this term

$$\begin{aligned} -\eta_{\mu\nu}\frac{2i\lambda}{6N_s}\int_y I(x,y;G)\sigma(x)G_\parallel(x,y)\sigma(y) = \\ \eta_{\mu\nu}\frac{2\lambda}{6N_s}\int_0^{x^0} d^4y\,[I_F(x,y;G)H_\rho(x,y)+I_\rho(x,y;G)H_F(x,y)]\,. \end{aligned} \tag{B.40}$$

This expression is a part of the definition of the function $P_F(x,y)$ given in (3.59). We now turn to the last term in (B.38). Doing the same kind of decomposition as in (B.39) we find terms with no, one and two sign-functions. As mentioned above

only terms with two sign-functions survive two time integrations. We find

$$
\begin{aligned}
-\eta_{\mu\nu}\frac{2i\lambda}{6N_s}\frac{-i}{2}\int_z\int_y I(z,x;G)I(x,y;G)\sigma(z)G_{\parallel}(z,y)\sigma(y) = \\
-\eta_{\mu\nu}\frac{\lambda}{6N_s}\frac{1}{4}\int_z\int_y\Big\{ I_F(z,x)H_\rho(z,y)I_\rho(x,y)\,\mathrm{sign}(x^0-y^0)\,\mathrm{sign}(z^0-y^0) \\
+I_\rho(z,x)H_\rho(z,y)I_F(x,y)\,\mathrm{sign}(z^0-x^0)\,\mathrm{sign}(z^0-y^0) \\
+I_\rho(z,x)H_F(z,y)I_\rho(x,y)\,\mathrm{sign}(z^0-x^0)\,\mathrm{sign}(x^0-y^0)\Big\}. \qquad \text{(B.41)}
\end{aligned}
$$

Now the important part of the time integration turns up. Due to the special arguments of the sign-functions we get special integration limits We start in all cases with the y-integration. The close time path integration leads for each integral to a factor of two, thus the 1/4 cancels. Explicitely we find

$$
\begin{aligned}
-\eta_{\mu\nu}\frac{\lambda}{6N_s}\Big\{-\int_0^{x^0}\int_0^{x^0} I_\rho(x,z)H_F(z,y)I_\rho(y,x) \\
+\int_0^{x^0}\int_0^{z^0} I_\rho(x,z)H_\rho(z,y)I_F(y,x) \\
+\int_0^{x^0}\int_{z^0}^{x^0} I_F(x,z)H_\rho(z,y)I_\rho(y,x)\Big\}. \qquad \text{(B.42)}
\end{aligned}
$$

Note that some arguments of functions in (B.42) are interchanged for convenience, this results in additional minus signs. If we compare (B.40) and (B.42) with the definition of $P_F(x,x)$ in Eq. (3.59) we observe that the last two terms in (B.38) can be expressed by

$$
+\frac{\eta_{\mu\nu}}{2}\left[P_F(x,x)+\frac{\lambda}{3N_s}H_F(x,x)\right]. \qquad \text{(B.43)}
$$

Total Boson Part of Quantum Fluctuations

Now we are able to write down the complete expression of the bosonic part of the energy-momentum tensor

$$
\begin{aligned}
T^\phi_{\mu\nu}(x) \;=\; & \left[\frac{1}{2}\eta_{\mu\nu}\left(-g^{\alpha\beta}\,\partial^x_\alpha\,\partial^{x'}_\beta\,\delta_{ab}\;+M^2_{ab}(x^0)\right)F^\phi_{ba}(x,x')+\partial^x_\mu\,\partial^{x'}_\nu\,F^\phi_{aa}(x,x')\right]\Big|_{x'=x} \\
& +\eta_{\mu\nu}\frac{\lambda}{4!N_s}\,\left[F^\phi_{aa}(x,x)\right]^2+\eta_{\mu\nu}\frac{1}{2}I_F(x,x;G) \\
& +\eta_{\mu\nu}\frac{1}{2}\left[P_F(x,x)+\frac{\lambda}{3N_s}H_F(x,x)\right]. \qquad \text{(B.44)}
\end{aligned}
$$

Classical Part

The classical part of the energy-momentum tensor is defined by the variation with respect to the metric of the classical action $\mathcal{S}$ in (2.10). The classical action in which only the nonvanishing macroscopic field $\phi(x)$ enters is defined by

$$\mathcal{S}[\phi] = \int d^4x \left[\frac{1}{2}\partial_\mu\phi(x)\partial^\mu\phi(x) - \frac{1}{2}m_\phi^2\,\phi^2(x) - \frac{\lambda}{4!N_s}\phi^4(x)\right], \tag{B.45}$$

We will keep all terms of the potential together in $V(\phi)$ for an organized notation. Applying the variation (B.1) we find the solution for the classical energy-momentum tensor to be

$$\begin{aligned} T_{\mu\nu}^{\text{class}}(x) &= \frac{2}{\sqrt{-g}}\frac{\delta}{\delta g^{\mu\nu}}\left\{\int_z \sqrt{-g(z)}\left[\frac{1}{2}g^{\alpha\beta}\partial_\alpha\phi(x)\partial_\beta\phi(x) - V(\phi)\right]\right\} \\ &= \frac{2}{\sqrt{-g}}\left\{\int_z \frac{-1}{2}\sqrt{-g(z)}g_{\mu\nu}\delta(x-z)\left[\frac{1}{2}g^{\alpha\beta}\partial_\alpha\phi(x)\partial_\beta\phi(x) - V(\phi)\right]\right. \\ &\quad \left. + \int_z \sqrt{-g(z)}\left[\frac{1}{2}\delta_\mu^\alpha\,\delta_\nu^\beta\,\partial_\alpha\,\phi(x)\partial_\beta\phi(x)\delta(x-z)\right]\right\} \\ &= \partial_\mu\,\phi(x)\partial_\nu\,\phi(x) - \eta_{\mu\nu}\left[\frac{1}{2}g^{\alpha\beta}\partial_\alpha\phi(x)\partial_\beta\phi(x) - V(\phi)\right]. \end{aligned} \tag{B.46}$$

Energy Density

In the last section we calculated the energy-momentum tensor $T_{\mu\nu}(x)$ for the fermionic and bosonic fluctuations as well as for the classical, macroscopic field. With these results it is simple to determine the energy density and pressure of the corresponding parts. In this section we list the results of the energy densities $T_{00}(x)$. We will present the results in terms of Fourier modes since these expressions are the ones used in the numerical codes. That means we insert a Fourier expansion like the one in Eq. (3.14) into the expressions (B.24) and (B.44). The macroscopic field has no Fourier expansion since we consider spatial homogeneous fields.

Fermion Part of Quantum Fluctuations

The fermion energy density in terms of Fourier modes is given by

$$\begin{aligned} T_{00}^{\psi}(t) = -8\int \frac{d^3p}{(2\pi)^3}\Bigg[-i\partial_{t'}F_V^0(t,t';|\mathbf{p}|)\Big|_{t=t'} + |\mathbf{p}|F_V(t,t;|\mathbf{p}|) + M_\psi(t)\,F_S(t,t;|\mathbf{p}|) \\ + R(t;|\mathbf{p}|)\Bigg], \end{aligned} \tag{B.47}$$

or by using the equation of motion for $F_V^0(t,t';|\mathbf{p}|)$ (3.31)

$$T_{00}^{\psi}(t) \;=\; -16\int\frac{d^3p}{(2\pi)^3}\Big[|\mathbf{p}|F_V(t,t;|\mathbf{p}|)+M_\psi(t)\,F_S(t,t;|\mathbf{p}|)+R(t;|\mathbf{p}|)\Big]\,. \tag{B.48}$$

Boson Part of Quantum Fluctuations

The complete boson energy density in terms of Fourier modes results in

$$\begin{aligned}T_{00}^{\phi}(t) \;=\;& \frac{1}{2}\int\frac{d^3p}{(2\pi)^3}\Big\{\partial_t\,\partial_{t'}\,F_{aa}(t,t';\mathbf{p})|_{t'=t}+\;\mathbf{p}^2\,F_{aa}(t,t;\mathbf{p})+M_{ab}^2(t)F_{ba}(t,t;\mathbf{p})\Big\}\\ &+\frac{\lambda}{4!N_s}\left(\int\frac{d^3p}{(2\pi)^3}F_{aa}(t,t;\mathbf{p})\right)^2+\frac{1}{2}\int\frac{d^3p}{(2\pi)^3}I_F(t,t;\mathbf{p})\\ &+\frac{1}{2}\int\frac{d^3p}{(2\pi)^3}\left[P_F(t,t;\mathbf{p})+\frac{\lambda}{3N_s}H_F(t,t;\mathbf{p})\right]\,.\end{aligned} \tag{B.49}$$

Classical Part

For the classical energy density we consequently obtain,

$$T_{00}^{\text{class}}(t)=\frac{1}{2}\dot{\phi}^2(t)+\frac{1}{2}m_\phi^2\,\phi^2(t)+\frac{\lambda}{4!N_s}\phi^4(t)\,. \tag{B.50}$$

Pressure

Since we already know the complete expression of $T_{\mu\nu}(x)$ it is easy to determine the pressure. The pressure was defined in (3.91). Thus we need to sum the spatial diagonal components before we divide by three. In the case of the classical part of the tensor this results just in minus sign in from of the potential. The terms proportional to $\eta_{\mu\nu}$ in (B.24) and (B.44) also just get a minus sign. The terms which contain the derivative operators require some care, since not all are proportional to the metric. In the following we will present the results for each part separately.

Fermion Part of Quantum Fluctuations

The fermion pressure in terms of Fourier modes is given by

$$\begin{aligned}\frac{P^{\psi}(t)}{V} \;=\;& 8\int\frac{d^3p}{(2\pi)^3}\Big\{+i\partial_{t'}F_V^0(t,t';|\mathbf{p}|)|_{t'=t}+\frac{1}{3}|\mathbf{p}|F_V(t,t;|\mathbf{p}|)\,.\\ &+M_\psi(t)\,F_S(t,t;|\mathbf{p}|)+R(t;|\mathbf{p}|)\Big\}\,,\end{aligned} \tag{B.51}$$

as expected the pressure is independent of spatial coordinates, therefore we put the volume V on the left hand side. If we use the equation of motion for $F_V^0(t,t';|\mathbf{p}|)$ and put it into (B.51) as we did for the energy density we get

$$\frac{P^\psi(t)}{V} = 16 \int \frac{d^3p}{(2\pi)^3} \frac{|\mathbf{p}|}{3} F_V(t,t;|\mathbf{p}|)\,. \tag{B.52}$$

Boson Part of Quantum Fluctuations

The spatial homogeneous boson pressure divided by the spatial volume V results in

$$\begin{aligned}\frac{P^\phi(t)}{V} &= \frac{1}{2}\int \frac{d^3p}{(2\pi)^3}\left\{\partial_t\,\partial_{t'}\,F_{aa}(t,t';\mathbf{p})|_{t'=t} + \frac{\mathbf{p}^2}{3}\,F_{aa}(t,t;\mathbf{p}) - M^2_{ab}(t)F_{ba}(t,t;\mathbf{p})\right\} \\ &\quad -\frac{\lambda}{4!N_s}\left(\int \frac{d^3p}{(2\pi)^3}F_{aa}(t,t;\mathbf{p})\right)^2 - \frac{1}{2}\int \frac{d^3p}{(2\pi)^3} I_F(t,t;\mathbf{p}) \\ &\quad -\frac{1}{2}\int \frac{d^3p}{(2\pi)^3}\left[P_F(t,t;\mathbf{p}) + \frac{\lambda}{3N_s}H_F(t,t;\mathbf{p})\right]\,. \end{aligned} \tag{B.53}$$

Classical Part

For the classical pressure density we obtain

$$\frac{P^{\rm class}(t)}{V} = \frac{1}{2}\dot{\phi}^2(t) - \frac{1}{2}m_\phi^2\,\phi^2(t) - \frac{\lambda}{4!N_s}\phi^4(t)\,. \tag{B.54}$$

Appendix C

Particle Number in Terms of Mode Functions

In this section we are going to show that (3.82) coincides with the particle number definition used in Ref. [GK00] where a mode function analysis was done. Hence we have to determine the connection between the 2PI two-point correlation functions with the corresponding mode functions. This allows us to show that both expressions agree.

The statistical two-point function is defined by (α and β represent Dirac indices)

$$\begin{aligned} F_{\alpha\beta}(x,y) &= \frac{1}{2}\Big\langle \big[\psi_\alpha(x), \bar{\psi}_\beta(y)\big] \Big\rangle \\ &= \frac{1}{2}\Big(\Big\langle \psi_\alpha(x)\bar{\psi}_\beta(y) \Big\rangle - \Big\langle \bar{\psi}_\beta(y)\psi_\alpha(x) \Big\rangle \Big) . \end{aligned} \tag{C.1}$$

For the quantum fields ψ we use the following decomposition into mode-functions

$$\psi_\alpha(x) = \sum_{s=1,2} \int \frac{d^3p}{(2\pi)^3} \left[a_{\mathbf{p},s} U^s_{\mathbf{p},\alpha}(t) e^{i\mathbf{px}} + b^\dagger_{\mathbf{p},s} V^s_{\mathbf{p},\alpha}(t) e^{-i\mathbf{px}} \right] , \tag{C.2}$$

with the usual anticommutation rules for the creation and annihilation operators $b^\dagger_{\mathbf{p},s}$ and $a_{\mathbf{p},s}$. For the spinors it is common to use the ansatz

$$U^s_{\mathbf{p},\alpha}(t) = \mathcal{N}_0 \left[i\gamma_0\partial_t - \vec{\gamma}\cdot\mathbf{p} + M_\psi(t) \right] f_{\mathbf{p}}(t) u^s_\alpha , \tag{C.3}$$

$$V^s_{\mathbf{p},\alpha}(t) = \mathcal{N}_0 \left[i\gamma_0\partial_t + \vec{\gamma}\cdot\mathbf{p} + M_\psi(t) \right] f^*_{\mathbf{p}}(t) v^s_\alpha , \tag{C.4}$$

with the norm of these spinors given by

$$\mathcal{N}_0 = \frac{1}{\sqrt{2\omega_{\mathbf{p}}(\omega_{\mathbf{p}} + M_\psi(t=0))}} , \qquad \omega_{\mathbf{p}} = \sqrt{\mathbf{p}^2 + M^2_\psi(t)} , \tag{C.5}$$

and the complex valued mode-functions $f_{\mathbf{p}}(t)$ which now describe the time evolution. The spinor character is given by u^s_α and v^s_α with the spin index s. They are defined

by

$$u^1_\alpha = \begin{pmatrix}1\\0\\0\\0\end{pmatrix} \equiv \begin{pmatrix}\chi^1\\0\end{pmatrix} \quad , \quad u^2_\alpha = \begin{pmatrix}0\\1\\0\\0\end{pmatrix} \equiv \begin{pmatrix}\chi^2\\0\end{pmatrix} \quad , \tag{C.6}$$

$$v^1_\alpha = \begin{pmatrix}0\\0\\1\\0\end{pmatrix} \equiv \begin{pmatrix}0\\\chi^1\end{pmatrix} \quad , \quad v^2_\alpha = \begin{pmatrix}0\\0\\0\\1\end{pmatrix} \equiv \begin{pmatrix}0\\\chi^2\end{pmatrix} \quad . \tag{C.7}$$

The $f_{\mathbf{p}}(t)$ accordingly have to fulfill the equation of motion

$$\left[\partial_t^2 + \mathbf{p}^2 + M_f^2(t) - i\dot{M}_\psi(t)\right] f_{\mathbf{p}}(t) \;=\; 0\,. \tag{C.8}$$

Thus the problem to solve the first order Dirac equation is transformed to a problem to solve a second order differential equation with an imaginary mass-like term[1], reminiscence of the original Dirac equation. If we now calculate the statistical two-point function in vacuum we get

$$F_{\alpha\beta}(t,t',|\mathbf{p}|) = \frac{1}{2}\sum_s \left[\left\langle U^s_{\mathbf{p},\alpha}(t)\bar{U}^s_{\mathbf{p},\beta}(t')\right\rangle - \left\langle \bar{V}^s_{-\mathbf{p},\beta}(t')V^s_{-\mathbf{p},\alpha}(t)\right\rangle\right]. \tag{C.9}$$

We emphasize that this expression has a matrix structure, so the second term has to be understood as a direct product[2].

Inserting the spinors $U^s_{\mathbf{p},\alpha}(t)$ and $V^s_{\mathbf{p},\alpha}(t)$ into (C.9) would lead to the complete expression of $F_{\alpha\beta}(t,t';\mathbf{p})$ in terms of the mode functions $f_{\mathbf{p}}(t)$. The result is a rather lengthy matrix expressions and we prefer to present the results for the equal time Lorentz-components we need to use:

$$\begin{aligned} F_S(t,t;|\mathbf{p}|) \;&=\; \frac{\mathcal{N}_0^2}{2}\Big[|\dot{f}_{\mathbf{p}}(t)|^2 - |f_{\mathbf{p}}(t)|^2\left(\mathbf{p}^2 - M_\psi^2(t)\right) \\ &\quad + iM_\psi(t)\left(f^*_{\mathbf{p}}(t)\dot{f}_{\mathbf{p}}(t) - \dot{f}^*_{\mathbf{p}}(t)f_{\mathbf{p}}(t)\right)\Big]\,, \end{aligned} \tag{C.10}$$

$$F_V(t,t;|\mathbf{p}|) \;=\; \frac{\mathcal{N}_0^2|\,\mathbf{p}|}{2}\left[i\left(f^*_{\mathbf{p}}(t)\dot{f}_{\mathbf{p}}(t) - \dot{f}^*_{\mathbf{p}}(t)f_{\mathbf{p}}(t)\right) + 2M_\psi(t)|f_{\mathbf{p}}(t)|^2\right], \tag{C.11}$$

$$F_T(t,t;|\mathbf{p}|) \;=\; \frac{\mathcal{N}_0^2\,|\mathbf{p}|}{2}\left[\left(f^*_{\mathbf{p}}(t)\dot{f}_{\mathbf{p}}(t) + \dot{f}^*_{\mathbf{p}}(t)f_{\mathbf{p}}(t)\right)\right], \tag{C.12}$$

$$F^0_V(t,t;|\mathbf{p}|) \;=\; 0\,. \tag{C.13}$$

[1]The dot denote the derivative with respect to the time t.

[2]The difference to the nonvanishing temperature expression is not large, there we would have two additional terms with a Fermi-Dirac distribution $n_{\mathbf{p}}$ in front and the factors of the terms given here would be modified by $(1-n_{\mathbf{p}})$.

With these expressions we are able to find the solution for the particle number used in [GK00] in terms of the 2PI two-point correlation functions. The way we get this expression is the following. We first rewrite the scalar component F_S with the use of a conserved quantity, the so called Wronskian

$$|\dot{f}_{\mathbf{p}}(t)|^2 + \left[\mathbf{p}^2 + M_\psi^2(t)\right] |f_{\mathbf{p}}(t)|^2 + iM_\psi(t)\left(\dot{f}_{\mathbf{p}}(t) f^*_{\mathbf{p}}(t) - \dot{f}^*_{\mathbf{p}}(t) f_{\mathbf{p}}(t)\right) = 2\omega_{\mathbf{p}}(\omega_{\mathbf{p}} + M_\psi(t_0))\,. \tag{C.14}$$

Using this equation we find

$$F_S(t,t;|\mathbf{p}|) = \frac{\mathcal{N}_0^2}{2}\left[2\omega_{\mathbf{p}}(\omega_{\mathbf{p}} + M_\psi(t_0)) - 2\mathbf{p}^2|f_{\mathbf{p}}(t)|^2\right]\,. \tag{C.15}$$

Now we express $|f_{\mathbf{p}}(t)|^2$, $|\dot{f}_{\mathbf{p}}(t)|^2$ and $i\left(f^*_{\mathbf{p}}(t)\dot{f}_{\mathbf{p}}(t) - \dot{f}^*_{\mathbf{p}}(t) f_{\mathbf{p}}(t)\right)$ in terms of the two-point functions by using the equations (C.10)–(C.13). Note

$$\begin{aligned} i\left(f^*_{\mathbf{p}}(t)\dot{f}_{\mathbf{p}}(t) - \dot{f}^*_{\mathbf{p}}(t) f_{\mathbf{p}}(t)\right) &= 2Im\left[\dot{f}^*_{\mathbf{p}}(t) f_{\mathbf{p}}(t)\right] \\ &= -Im(\dot{f}_{\mathbf{p}}(t))Re(f_{\mathbf{p}}(t)) + Re(\dot{f}_{\mathbf{p}}(t))Im(f_{\mathbf{p}}(t))\,. \end{aligned} \tag{C.16}$$

The solutions are

$$|f_{\mathbf{p}}(t)|^2 = \frac{1}{2\mathcal{N}^2|\mathbf{p}|}\left(1 - 2F_S(t,t;|\mathbf{p}|)\right)\,, \tag{C.17}$$

$$2Im\left[\dot{f}^*_{\mathbf{p}}(t) f_{\mathbf{p}}(t)\right] = \frac{2F_V(t,t;|\mathbf{p}|)}{\mathcal{N}^2|\mathbf{p}|} - \frac{M_\psi(t)}{\mathcal{N}^2|\mathbf{p}|}\left(1 - 2F_S(t,t;|\mathbf{p}|)\right)\,, \tag{C.18}$$

$$\begin{aligned} |\dot{f}_{\mathbf{p}}(t)|^2 &= \frac{2F_S(t,t;|\mathbf{p}|)}{\mathcal{N}^2} + \frac{1 - 2F_S(t,t;|\mathbf{p}|)}{\mathcal{N}^2}\left(\frac{M_\psi^2(t)}{2|\mathbf{p}|^2} + \frac{1}{2}\right) \\ &\quad - \frac{2F_V(t,t;|\mathbf{p}|)M_\psi(t)}{\mathcal{N}^2|\mathbf{p}|}\,. \end{aligned} \tag{C.19}$$

The definition of the occupation number in [GK99] results in the following expression

$$n_\psi(t;\mathbf{p}) = \mathcal{N}^2\mathcal{N}_0^2|\mathbf{p}|^2\left[\omega_{\mathbf{p}}^2|f_{\mathbf{p}}(t)|^2 + |\dot{f}_{\mathbf{p}}(t)|^2 - 2\omega_{\mathbf{p}} Im\left[\dot{f}^*_{\mathbf{p}}(t) f_{\mathbf{p}}(t)\right]\right]\,. \tag{C.20}$$

Note that there is a factor $\mathcal{N}^2$, the normalization factor (C.5) at time t, and a factor $\mathcal{N}_0^2$, that means the mode functions do not contain a normalization and we can directly insert the expressions (C.17)-(C.19) into (C.20) and find a connection between this special definition of the occupation number and the 2PI correlation functions, which is

$$n_\psi(t;\mathbf{p}) = \frac{1}{2} - \frac{1}{\omega_{\mathbf{p}}}\left[M_\psi(t)\, F_S(t,t;|\mathbf{p}|) + |\mathbf{p}|\, F_V(t,t;|\mathbf{p}|)\right]\,. \tag{C.21}$$

This is exactly the expression introduced in (3.82). In the massless (chiral) case (C.21) reduces to the particle number (3.84) also used in [BPR09].

Appendix D

Calculation of the Spectral Function

The study of the spectral function out of equilibrium is of great interest in current research regarding transport and/or kinetic processes. For example, in the early universe a proper description of leptogenesis requires the inclusion of off-shell effects which could change the standard picture of the evolution [GHKL09]. Having tools available which allow to study those dynamics from first principles we will consider in this chapter an analysis of the spectral function out of equilibrium in the presence of an instability. We use our generic model introduced in Sec. 3.1. The main features might be transferred to more phenomenological models. Another interesting property of the spectral function is the scaling behavior in the four dimensional Fourier space. The exponent of the scaling behavior is connected to the so called anomalous dimension [PS95]. Such scaling solutions play an important role in studying critical phenomena in and out of equilibrium. The emergence of critical phenomena out of equilibrium gained recently a lot attention [BRS08, BSS09b]. The anomalous dimension is typically chosen to be zero as it is expected in relativistic scalar field theories. Till now there exist no numerical determination of the exponent out of equilibrium in the 2PI framework. With the method presented in this chapter it is possible to attack this problem. However, we will left this out and refere to future studies.

D.1 Wigner Transformation

In this appendix we describe the method we used for the calculation of spectral functions in four-dimensional Fourier space, like $\rho_V(\omega;\mathbf{p})$. Moreover we will check our routine by comparison of numerical results with analytical solutions.

First we will present the definition of the Wigner transformation. Consider an arbitrary correlation function $C(x,y)$ which describes the correlation between two arbitrary variables x and y. The Wigner transformation of $C(x,y)$ is defined by a Fourier transformation with respect to the relative variable $r \equiv x-y$, where the

center of mass variable $z = \frac{x+y}{2}$ is held fixed. Consequently the first step of the calculation is a variable transformation $C(x,y) \to C(z+\frac{r}{2}, z-\frac{r}{2})$. The Fourier transformation[1]

$$C(z,u) = \int_{-\infty}^{+\infty} dr\, e^{iur}\, C(z+\frac{r}{2}, z-\frac{r}{2}) \tag{D.1}$$

leads to the Wigner function of the correlation.

Practically we are interested in the Wigner transformation of a spectral function $\rho(t,t';\mathbf{p})$[2] during a numerical simulation. That means the integration limits cannot be $\pm\infty$. Accordingly the relative variable is the relative time coordinate $s \equiv t - t'$, whereas the center of mass variable becomes $X^0 \equiv \frac{t+t'}{2}$. The transformation of the spectral function, $\rho(t,t';\mathbf{p}) = -\rho(t',t;\mathbf{p})$, then may defined by

$$\rho(X^0;\omega,\mathbf{p}) = \int_{-2X^0}^{2X^0} ds\, e^{i\omega s} \rho(X^0+\frac{s}{2}, X^0-\frac{s}{2};\mathbf{p})\,, \tag{D.2}$$

where now the integral limits are given by the center of mass coordinate[3]. The integral limits naturally occur if one integrates over the relative coordinate in a finite volume. The integration path can be easily visualized in the (t,t')-plane, as in Fig. D.1 shown. Each antidiagonal line corresponds to different X^0 which are constant along the antidiagonal line whereas s varies from $-2X^0$ to $+2X^0$. The diagonal line crosses the antidiagonal lines at $s = 0$. Having presented the definition of the Wigner transformation we can proceed and report about checks of the routine used in the simulations. We will consider two examples. The first will be a transformation of an analytical function which describes a damped oscillation. This gives us the opportunity to discuss the influence of different damping rates. Further we can compare a finite time calculation with an exact result and learn something about signatures of finite times. The second example is a transformation out of a free-field theory, where the Wigner transformation of a spectral function is analytically known. We will simulate a free-field spectral function and thus can check the accuracy of our program by comparison with the analytical results. A further check of the accuracy is obtained by the confirmation of the sum rule. The sum rule is an identity following from the (anti-) commutatorelation of the quantum

[1] We omit possible constant factors which may appear in certain definitions.

[2] This ρ could be a boson as well as a fermion spectral function.

[3] The resulting $\rho(X^0;\omega,\mathbf{p})$ in general can be imaginary, depending on the symmetry. In order to deal with real numbers one might defines the transformation including an imaginary unit on the left-hand side.

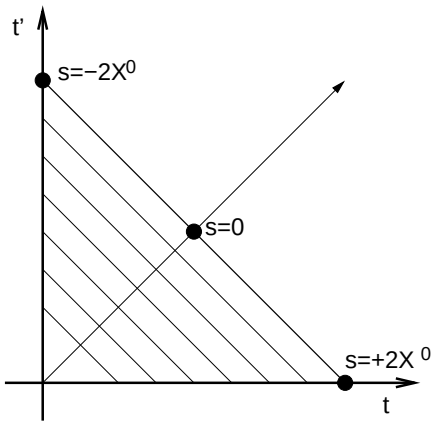

Figure D.1: Visualization of the (t, t')-plane. The antidiagonal lines represent the s-integration paths. The end points of a symmetric interval around $s = 0$ are given by $-2X^0$ and $+2X^0$.

fields. For the bosonic spectral function the sum rule reads

$$\int_{-\infty}^{+\infty} \frac{d\omega}{2\pi}\, \omega\, \rho_\phi(X^0; \omega, \mathbf{p}) = 1\,, \tag{D.3}$$

whereas for the fermion quantum fields it is

$$\int_{-\infty}^{+\infty} \frac{d\omega}{2\pi} \rho_V^0(X^0; \omega, \mathbf{p}) = i\,. \tag{D.4}$$

In our calculations the deviation from the identities did not exceed the order of one percent, in most cases the deviations were even smaller.

Damped Oscillation

Consider a damped oscillation which typically arises in an interacting theory

$$f(t, t'; \mathbf{p}) = e^{-\gamma|t-t'|}\, \frac{\sin\left[E_\mathbf{p}(t-t')\right]}{E_\mathbf{p}}\,. \tag{D.5}$$

For the sake of simplicity we assumed that the damping rate γ and the energy $E_\mathbf{p} = \sqrt{\mathbf{p}^2 + m^2}$ are time independent which in general does not have to be the case. Applying a Wigner transformation yields

$$f_{\mathrm{WT}}(\omega, \mathbf{p}) = \frac{2\,\gamma\,\omega}{(\omega^2 - E_\mathbf{p}^2)^2 + 2\gamma^2\omega^2 + \gamma^2(\gamma^2 + 2E_\mathbf{p}^2)}\,. \tag{D.6}$$

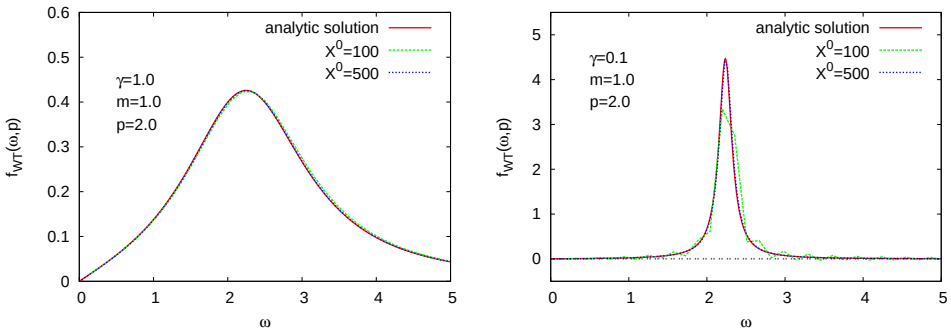

Figure D.2: Comparison between analytical and numerical Wigner transformed spectral function.

Note that if we would have allowed for X^0-dependent damping rate and energy, together with finite integral limits we would have a time dependence of f_{WT}. Further additional terms $\sim e^{-2\gamma X^0}$ would appear. Consequently, in order to reproduce (D.6) numerically one should have $X^0 \gg 1/\gamma$. The additional time dependencies lead to a deformation of the actual solution. In the above example this results in an oscillatory behavior of the amplitude which acts like a modulation. It is well known that finite-time effects cause such an oscillating behavior of the transformed quantity as well as a possible non-positivity [AB01].

In the following we will present results of a comparison of the analytical solution with numerical calculations. In the left panel of Fig. D.2 we display $f_{\mathrm{WT}}(\omega, \mathbf{p})$ (D.6) as a function of ω with $\gamma = 1$, $m = 1$ and $|\mathbf{p}| = 2.0$ together with the corresponding numerical results. We plotted the latter for two different X^0 indicated in the figure. We observe a remarkably good agreement. Finite-time effects are hardly visible. In the right panel in Fig. D.2 we present a similar comparison with $\gamma = 0.1$. There the typical oscillations due to finite time effects are visible, however for $X^0 = 500$ they almost vanish and a good agreement is obtained. Note that those oscillations may cause negative values of the result. We infer from these findings that for large damping rates the result is closer to the exact solution at fixed X^0, since γX^0 is larger. This may be important if we consider nonequilibrium simulations with instabilities.

Free-Field Example

In order to show that our numerical Wigner transformation works well we will consider in this section the case of a free fermion field. In this situation we are able to determine the Wigner transformation analytically, and thus get the information whether or not the numerics yields correct results. We will consider the vector

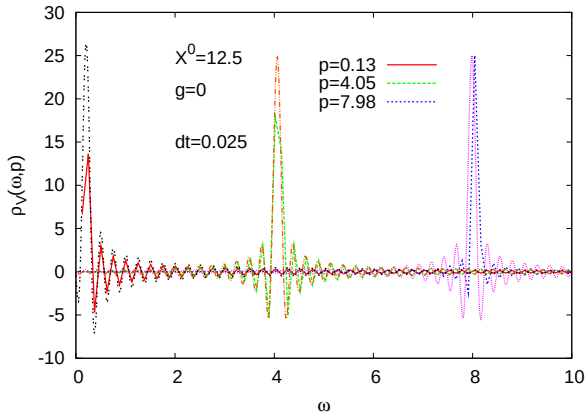

Figure D.3: Comparison between analytics and numerics

component of a free-field fermion spectral function which has the form

$$\rho_V(x^0, y^0; \mathbf{p}) = \sin[E^\psi_{\mathbf{p}}(x^0 - y^0)]\,, \tag{D.7}$$

with $E^\psi_{\mathbf{p}} = \sqrt{\mathbf{p}^2 + m^2_\psi}$. The Wigner transformation leads to the result

$$\rho_V(X^0; \omega, \mathbf{p}) = \frac{\sin[2X^0(E^\psi_{\mathbf{p}} - \omega)]}{E^\psi_{\mathbf{p}} - \omega} - \frac{\sin[2X^0(E^\psi_{\mathbf{p}} + \omega)]}{E^\psi_{\mathbf{p}} + \omega}\,. \tag{D.8}$$

We directly observe the dependence on X^0. Numerically we get (D.7) from the solution of the equation of motion for ρ_V. In Fig. D.3 we show a comparison between the analytical result (D.8) and the corresponding numerical solution for three different momenta indicated in the figure. The position of the peaks for not too large momenta agree and coincide with the expected position. Remarkably is that the oscillations are reproduced quite well. Finite time effects are pronounced because X^0 is not very large. The plot confirms the reliability of the calculation.

For large momenta, i.e. high frequencies, the position of the peak from numerical results, is not exactly the correct one. In Fig. D.3 the numerical peak with $|\mathbf{p}| = 7.98$ is slightly shifted to the right. This shortcoming is due to the limited accuracy of solving the equations for highly oscillating modes. For a better discretization one would find the peaks to be at the expected position. However, the deviation of high-frequency peak positions in all calculations does not exceed the order of one percent. Furthermore, we are mainly interested in the spectrum for low momenta (see main text) thus those results are trustworthy. A better time discretization would imply a smaller X^0 with equal computer resources, thus there have to be a compromise.

The same analysis presented in this section could also be made for boson spectral functions. A difference would be a constant factor $1/E^\phi_{\mathbf{p}}$ in (D.7). We found that the results are qualitatively the same.

Appendix E

Calculation of Self-Energy Contributions

In this Appendix we are going to present a detailed calculation of the fermionic part of the self-energies in the model (3.1). The formal definition of the self-energy was already given in (2.11) and (2.12). In the first section we consider the fermion self-energy Σ, subsequently the fermion part of the boson self-energy Π is calculated. Starting point in both sections is the functional derivative of the Γ_2 part of the effective action. Since we are only interested in the fermionic part we consider the functional derivative of

$$\Gamma_2^{\psi}[D,G] = -i\left(\frac{g}{N_f}\right)^2 \frac{N_f}{2}\int_x\int_y \mathrm{tr}\left[D(x,y)D(y,x)\right] G_{aa}(x,y)\,, \tag{E.1}$$

cf. (3.44).

Fermion Self-Energy

We have to consider the functional derivative of (E.1) with respect to $D(x,y)$. This means, with kl as Dirac indices,

$$\begin{aligned}
-i\frac{\delta\Gamma_2^{\psi}}{\delta D_{kl}(z,w)} &= -\left(\frac{g}{N_f}\right)^2\frac{N_f}{2}\int_x\int_y \frac{\delta}{\delta D_{kl}(z,w)} D_{ij}(x,y)D_{ji}(y,x)G_{aa}(x,y) \\
&= -\left(\frac{g}{N_f}\right)^2\frac{N_f}{2}\int_x\int_y \{\delta_{ik}\delta_{jl}\delta(x-z)\delta(y-w)D_{ji}(y,x)G_{aa}(x,y) \\
&\quad +\delta_{jk}\delta_{il}\delta(y-z)\delta(x-w)D_{ij}(x,y)G_{aa}(x,y)\} \\
&= -\left(\frac{g}{N_f}\right)^2\frac{N_f}{2}\{D_{lk}(w,z)G_{aa}(z,w) + D_{lk}(w,z)G_{aa}(w,z)\} \\
&= -\left(\frac{g}{N_f}\right)^2 N_f D_{lk}(w,z)G_{aa}(w,z)\,,
\end{aligned} \tag{E.2}$$

the N_f in front comes from the trace in flavor space. The self-energy for each flavor hence does not contain this factor. The product of the fermion and boson two-point

function can be decomposed first before one projects outs the specific (Lorentz) components of the fermion self-energies. So the general structure becomes

$$\begin{aligned}\Sigma_{ij}(x,y) &= -\left(\frac{g}{N_f}\right)^2 \Big\{ F_{ij}(x,y)F^{\phi}_{aa}(x,y) - \frac{1}{4}\rho_{ij}(x,y)\rho^{\phi}_{aa}(x,y) \\ &\quad -\frac{i}{2}\mathrm{sign}(x^0-y^0)\left[F_{ij}(x,y)\rho^{\phi}_{aa}(x,y) + \rho_{ij}(x,y)F^{\phi}_{aa}(x,y)\right]\Big\}\end{aligned} \tag{E.3}$$

To get the real or imaginary part of the self-energies we simply have to take the real or imaginary part out of this expression, cf. (3.8). Respecting the factor $-\frac{i}{2}\mathrm{sign}(x^0-y^0)$ in front of the imaginary part we end up with

$$C_{ij}(x,y) = -\left(\frac{g}{N_f}\right)^2 \left\{ F_{ij}(x,y)F^{\phi}_{aa}(x,y) - \frac{1}{4}\rho_{ij}(x,y)\rho^{\phi}_{aa}(x,y)\right\}, \tag{E.4}$$

for the statistical (real) part and with

$$A_{ij}(x,y) = -\left(\frac{g}{N_f}\right)^2 \left\{ F_{ij}(x,y)\rho^{\phi}_{aa}(x,y) + \rho_{ij}(x,y)F^{\phi}_{aa}(x,y)\right\}, \tag{E.5}$$

for the spectral (imaginary) part. To obtain the Lorentz components one simply projects out the required component as usual and gets the corresponding Lorentz component for the self-energy.

Boson Self-Energy

In this section we calculate the expression for the fermion part Π^{ψ} of the boson self-energy. We have to apply a functional derivative of (E.1) with respect to the boson propagator, we find

$$2i\frac{\delta\Gamma_2}{\delta G^{\phi}_{bc}(z,w)} = 2\left(\frac{g}{N_f}\right)^2 \frac{N_f}{2}\int_x\int_y \mathrm{tr}D(x,y)D(y,x)\delta(z-x)\delta(w-y)\delta_{bc}\,. \tag{E.6}$$

this means

$$\Pi^{\psi}_{bc}(x,y) = \left(\frac{g}{N_f}\right)^2 N_f\,\mathrm{tr}D(x,y)D(y,x)\delta_{bc}\,. \tag{E.7}$$

We are left with the trace over the two fermion propagators which we will consider in detail in the following.

In the trace we use the decomposition of D into its Lorentz components, i.e. we insert

$$D(x,y) = D_S(x,y) + \gamma_\mu D^{\mu}_V(x,y) + \frac{1}{2}\sigma_{\mu\nu}D^{\mu\nu}_T(x,y)\,, \tag{E.8}$$

which leads to

$$\begin{aligned}\mathrm{tr}\left[D(x,y)D(y,x)\right] &= \mathrm{tr}\left[D_S(x,y)D_S(y,x)\right. \\ &\left. +\gamma_\mu\gamma_\nu D_V^\mu(x,y)D_V^\nu(y,x)+\frac{1}{4}\sigma_{\mu\nu}\sigma_{\alpha\beta}D_T^{\mu\nu}(x,y)D_T^{\alpha\beta}(y,x)\right],\end{aligned} \tag{E.9}$$

where we need to know

$$\mathrm{tr}\left[\sigma_{\mu\nu}\sigma_{\alpha\beta}D_T^{\mu\nu}(x,y)D_T^{\alpha\beta}(y,x)\right]=\frac{-1}{4}\cdot(-4)\cdot 8\cdot\left(D_T(x,y)\right)_\mu{}^\nu\left(D_T(y,x)\right)^\mu{}_\nu\,. \tag{E.10}$$

The product of the tensor components can be rewritten with the use of isotropy into

$$\left(D_T(x,y)\right)_\mu{}^\nu\left(D_T(y,x)\right)^\mu{}_\nu=-2D_T^{0i}(x,y)D_T^{0i}(y,x)\,, \tag{E.11}$$

this is at best seen if one writes the D_T's in matrix form. This gives us

$$\begin{aligned}\mathrm{tr}\left[D(x,y)D(y,x)\right] &= 4\left[D_S(x,y)D_S(y,x)+D_V^0(x,y)D_V^0(y,x)\right. \\ &\left. -D_V^i(x,y)D_V^i(y,x)-D_T^{0i}(x,y)D_T^{0i}(y,x)\right].\end{aligned} \tag{E.12}$$

Using the decomposition like the one in Eq. (3.6) then we observe that

$$\begin{aligned}D_S(x,y)D_S(y,x) &= F_S(x,y)F_S(y,x)+\frac{1}{4}\rho_S(x,y)\rho_S(y,x) \\ &-\frac{i}{2}\mathrm{sign}(x^0-y^0)\left[\rho_S(x,y)F_S(y,x)-F_S(x,y)\rho_S(y,x)\right].\end{aligned} \tag{E.13}$$

and equivalently for the other components. Now we use symmetry relations of the real and imaginary parts under interchanging the space-time arguments in order to have the same order of arguments in each factor. We find

$$F_V^0(x,y) = -F_V^0(y,x)\,, \tag{E.14}$$
$$F_V^i(x,y) = -F_V^i(y,x)\,, \tag{E.15}$$
$$F_S(x,y) = +F_S(y,x)\,, \tag{E.16}$$
$$F_T^{0i}(x,y) = -F_T^{0i}(y,x)\,. \tag{E.17}$$

for the symmetry relations of the statistical parts and

$$\rho_V^0(x,y) = +\rho_V^0(y,x)\,, \tag{E.18}$$
$$\rho_V^i(x,y) = +\rho_V^i(y,x)\,, \tag{E.19}$$
$$\rho_S(x,y) = -\rho_S(y,x)\,, \tag{E.20}$$
$$\rho_T^{0i}(x,y) = +\rho_T^{0i}(y,x)\,. \tag{E.21}$$

for the spectral parts. Using this in (E.13) leads to the following products:

$$\begin{aligned} D_V^0(x,y)D_V^0(y,x) &= -F_V^0(x,y)F_V^0(x,y) + \frac{1}{4}\rho_V^0(x,y)\rho_V^0(x,y) \\ &\quad -\frac{i}{2}\mathrm{sign}(x^0-y^0)\left[-\rho_V^0(x,y)F_V^0(x,y) - F_V^0(x,y)\rho_V^0(x,y)\right], \end{aligned} \tag{E.22}$$

$$\begin{aligned} D_V^i(x,y)D_V^i(y,x) &= -F_V^i(x,y)F_V^i(x,y) + \frac{1}{4}\rho_V^i(x,y)\rho_V^i(x,y) \\ &\quad -\frac{i}{2}\mathrm{sign}(x^0-y^0)\left[-\rho_V^i(x,y)F_V^i(x,y) - F_V^i(x,y)\rho_V^i(x,y)\right], \end{aligned} \tag{E.23}$$

$$\begin{aligned} D_S(x,y)D_S(y,x) &= F_S(x,y)F_S(x,y) - \frac{1}{4}\rho_S(x,y)\rho_S(x,y) \\ &\quad -\frac{i}{2}\mathrm{sign}(x^0-y^0)\left[\rho_S(x,y)F_S(x,y) + F_S(x,y)\rho_S(x,y)\right], \end{aligned} \tag{E.24}$$

$$\begin{aligned} D_T^{0i}(x,y)D_T^{0i}(y,x) &= -F_T^{0i}(x,y)F_T^{0i}(x,y) + \frac{1}{4}\rho_T^{0i}(x,y)\rho_T^{0i}(x,y) \\ &\quad -\frac{i}{2}\mathrm{sign}(x^0-y^0)\left[-\rho_T^{0i}(x,y)F_T^{0i}(x,y) - F_T^{0i}(x,y)\rho_T^{0i}(x,y)\right], \end{aligned} \tag{E.25}$$

which now can be inserted into (E.7) by using (E.12). With this we find for the fermion part of the boson self-energy

$$\begin{aligned} \Pi_{bc}^{\psi}(x,y) &= 4\left(\frac{g}{N_f}\right)^2 N_f \left[D_S(x,y)D_S(y,x) + D_V^0(x,y)D_V^0(y,x)\right. \\ &\quad \left. -D_V^i(x,y)D_V^i(y,x) - D_T^{0i}(x,y)D_T^{0i}(y,x)\right]\delta_{bc} \\ &= 4\left(\frac{g}{N_f}\right)^2 N_f \left\{F_S(x,y)F_S(x,y) - \frac{1}{4}\rho_S(x,y)\rho_S(x,y)\right. \\ &\quad -F_V^0(x,y)F_V^0(x,y) + \frac{1}{4}\rho_V^0(x,y)\rho_V^0(x,y) \\ &\quad +F_V^i(x,y)F_V^i(x,y) - \frac{1}{4}\rho_V^i(x,y)\rho_V^i(x,y) \\ &\quad +F_T^{0i}(x,y)F_T^{0i}(x,y) - \frac{1}{4}\rho_T^{0i}(x,y)\rho_T^{0i}(x,y) \\ &\quad -\frac{i}{2}\mathrm{sign}(x^0-y^0)2\left[\rho_S(x,y)F_S(x,y) + \rho_T^{0i}(x,y)F_T^{0i}(x,y)\right. \\ &\quad \left.\left. -\rho_V^0(x,y)F_V^0(x,y) + \rho_V^i(x,y)F_V^i(x,y)\right]\right\}\delta_{bc} \end{aligned} \tag{E.26}$$

With this expression it is easy to determine the statistical (real) and spectral (imaginary) part of the self-energy. We find

$$\begin{aligned}\Pi_{bc}^{F,\psi}(x,y) &= 4\left(\frac{g}{N_f}\right)^2 N_f \Big\{ F_S(x,y)F_S(x,y) \\ &\quad -F_V^0(x,y)F_V^0(x,y) + F_V^i(x,y)F_V^i(x,y) + F_T^{0i}(x,y)F_T^{0i}(x,y) \\ &\quad +\frac{1}{4}\Big[-\rho_S(x,y)\rho_S(x,y) + \rho_V^0(x,y)\rho_V^0(x,y) - \rho_V^i(x,y)\rho_V^i(x,y) \\ &\quad -\rho_T^{0i}(x,y)\rho_T^{0i}(x,y)\Big]\Big\}\delta_{bc}\end{aligned} \tag{E.27}$$

for the real part and

$$\begin{aligned}\Pi_{bc}^{\rho,\psi}(x,y) &= 8\left(\frac{g}{N_f}\right)^2 N_f \Big\{ \rho_S(x,y)F_S(x,y) + \rho_T^{0i}(x,y)F_T^{0i}(x,y) \\ &\quad -\rho_V^0(x,y)F_V^0(x,y) + \rho_V^i(x,y)F_V^i(x,y)\Big\}\delta_{bc}\end{aligned} \tag{E.28}$$

for the imaginary part.

Appendix F

Numerical Implementation and Stability

In this appendix we are going to present the methods we used to solve the evolution equations of our systems and check the sensibility of the results against infrared and ultraviolet cut-off changes. First we consider the implementation of the equations of motion, after that we discuss the discretized Fourier transformation which is used to determine the Fourier modes of the two-point correlation functions as well as the modes of the self-energies whose numerical computation is considered in Sec. F.1. In Sec. F.2 we will consider the sensitivity against cut-off changes of typical time evolutions and spectra out of Chapter 4 and Chapter 5.

F.1 Numerical Methods

Time Evolution

The equations of motion for the fermionic and bosonic two-point functions, (3.30)–(3.37) and (3.38)–(3.41) respectively, are solved in Fourier space. This simplifies the calculation significantly since we do not have to deal with a spatial derivative operator. Further this prevents the user from calculating a spatial integral at each time-step in the integrals on the right hand side of the equations of motions. The functions are discretized in two time-directions and one (spatial) momentum-direction. This is possible because we apply spherical symmetry and thus only need to discretize the absolute value of the momentum. It is important to note that the equations are causal (explicit) in time. We stored memory only in the lower part of the array $[t][t']$, with $t = i\,dt$ and $t' = j\,dt$ for $i, j = 1, 2, 3, ...T_{\max}$, where the half is defined by the diagonal line in the (t, t')-plane. Thus the second entry is smaller or equal to the first. With this there is no loss of information because we can use the symmetry relations (3.18)–(3.25) and (3.26)–(3.29) with which we get the whole information. At each t we have to solve the equations for every $t' \leq t$. The numerical method we used for solving the differential equations is the so called

Euler-rule in the case of the boson evolution and a leap-frog type algorithm for the fermion first-order differential equations. The Euler rule is defined by the following discretization of the Laplace operator

$$\frac{\partial}{\partial t^2} f(t,t';\mathbf{p}) \longrightarrow \frac{f(i+1,j;\mathbf{p}) + f(i-1,j;\mathbf{p}) - 2f(i,j;\mathbf{p})}{dt^2}\,, \tag{F.1}$$

where, here and below, $f(t,t';\mathbf{p})$ stands for each two-point function. This is the typical "forward-backward" lattice discretization [MM94]. The leap-frog type algorithm is characterized by the way the data is stored. We use one array for two functions, thus the fermions are discretized with a time-step dt_f twice as large as the one of the bosons. Practically one has two time arrays, with double time-step width, stored in one array shifted against each other by dt. That this is possible is due to the structure of the equations together with the symmetries we applied. It follows that one stores one function at a grid point where $t - t' =$ even and the other at $t - t' =$ odd. A consequence is that the shape of the right hand side of the equations of motion changes during the t'-loop. Moreover the memory integration automatically results in a discretized sum with $2dt$. This results in an algorithm which uses many if-conditions. In connection with this, one important fact is that by calculating the fermion part of the boson self-energy one has to introduce a factor of two in order to have a double time-step while calculating the memory-integral in the equation of motion[1]. For the first order derivative in the fermion equations we use the central derivative

$$\frac{\partial}{\partial t} f(t,t';\mathbf{p}) \longrightarrow \frac{f(i+1,j;\mathbf{p}) - f(i-1,j;\mathbf{p})}{2dt}\,. \tag{F.2}$$

In each time step one has to solve the memory-integral which is done by the trapezoidal rule, which is defined by

$$\int_a^b dt\, f(t,t';\mathbf{p}) \longrightarrow dt \left[\frac{1}{2} f(a,j;\mathbf{p}) + \sum_{i=1}^{b-1} f(i,j;\mathbf{p}) + \frac{1}{2} f(b,j;\mathbf{p})\right]. \tag{F.3}$$

The time-derivative operator only acts on one time-component. Because of the two time arguments of the correlation functions one is confronted in the last forward-time-step, $t' \to t+1$, with functions with a larger second argument than the first, e.g. $f(t,t+1) = \pm f(t+1,t)$, depending on their symmetry relation. This makes it complicated to use more sophisticated methods than Euler, as for instance, fourth order Runge-Kutta where one has to deal with velocities of those functions. Moreover our

[1] In the boson equations there is only "dt" used, not "$2dt$", but this is required by the way the fermions are treated. This is one way of implementation, of course there exist alternative formulations.

method needs initial conditions for $f(0,0)$, $f(0,1)$, $f(1,0)$, and $f(1,1)$, starting at $t = 1$. We stress that, by discretizing the theory on the level of the equations of motions the problem of fermion doublers [MM94] does not occur.

Our numerical calculations for the equations of motion are carried out on a single personal computer with 8Gb RAM. In our simulations we used up to $T_{\max} = 1850$ time steps with a width of $dt \leq 0.05$, depending on the coupling constants and/or the needed time resolution of a physical process like high frequencies.

Fourier Transform

Because of spatial isotropy the Fourier modes of each two-point function only depends on the absolute value of the momentum. Therefore it is possible to calculate the angular part analytically and just discretize the absolute momentum, which is one dimensional. This saves a significant amount of memory. That this also holds for the convolutions is not obvious. We will describe the method below after we presented the explicit discretization of the Fourier space.

The transformation from the coordinate space into the momentum space can be calculated in the case of an isotropic system in the following way[2].

$$\begin{aligned}
\tilde{f}(|\mathbf{p}|) &= \int d^3x\, f(\mathbf{x}) e^{-i\mathbf{px}} \\
&= \int_0^{2\pi} d\varphi \int_0^{\pi} d\theta \int_0^{\infty} d|\mathbf{x}|\, \sin(\theta) |\mathbf{x}|^2 f(|\mathbf{x}|) e^{-i\mathbf{px}} \\
&= \frac{4\pi}{|\mathbf{p}|} \int_0^{\infty} d|\mathbf{x}|\, |\mathbf{x}| f(|\mathbf{x}|) \sin(|\mathbf{p}||\mathbf{x}|)\,. \qquad \text{(F.4)}
\end{aligned}$$

The back transformation consequently takes the form

$$\begin{aligned}
\tilde{f}(|\mathbf{x}|) &= \int \frac{d^3p}{(2\pi)^3} f(\mathbf{p}) e^{i\mathbf{px}} \\
&= \frac{1}{(2\pi)^3} \int_0^{2\pi} d\varphi \int_0^{\pi} d\theta \int_0^{\infty} d|\mathbf{p}|\, \sin(\theta) |\mathbf{p}|^2 f(|\mathbf{p}|) e^{i\mathbf{px}} \\
&= \frac{4\pi}{(2\pi)^3 |\mathbf{x}|} \int_0^{\infty} d|\mathbf{p}|\, |\mathbf{p}| f(|\mathbf{p}|) \sin(|\mathbf{p}||\mathbf{x}|)\,. \qquad \text{(F.5)}
\end{aligned}$$

We use the following discretized momenta and coordinates

$$|\mathbf{p}| \quad \longrightarrow \quad |\mathbf{p}|_i = \frac{\pi}{a_s N}(i+1)\,, \qquad \text{(F.6)}$$

$$|\mathbf{x}| \quad \longrightarrow \quad |\mathbf{x}|_i = a_s(i+1/2)\,, \qquad \text{(F.7)}$$

[2]Here is no factor of $1/(2\pi)^3$ because it is taken into account in the inverse transformation.

where a_s is the spatial lattice spacing and N the number of grid points. Accordingly $d|\mathbf{x}| = a_s$ and $d|\mathbf{p}| = \frac{\pi}{a_s N}$. Note that for specific values of a_s and N a certain infrared and ultraviolet cut-off is chosen. The special (different) start points of the discretization for $|\mathbf{p}|$ and $|\mathbf{x}|$ is chosen in that way, that we can apply the fastest Fourier transform routines for 1 dimension by using the FFTW library[3]. With (F.6) and (F.7) the discretized versions of the Fourier transformations are

$$\tilde{f}(|\mathbf{p}|_j) = \frac{2a_s^3 N}{(j+1)} \sum_{i=0}^{N-1} (i+1/2) f(|\mathbf{x}|_i) 2 \sin\left[\frac{\pi}{N}(j+1)(i+1/2)\right], \quad \text{(F.8)}$$

for (F.4) and

$$\tilde{f}(|\mathbf{x}|_j) = \frac{1}{a_s(j+\frac{1}{2})} \frac{1}{4(a_s N)^2} \sum_{i=0}^{N-1} (i+1) f(|\mathbf{p}|_i) 2 \sin\left[\frac{\pi}{N}(i+1)(j+1/2)\right]. \quad \text{(F.9)}$$

for (F.5).

In our numerical calculations the momentum grid has $N = 40 - 256$ discretization points and a spatial lattice spacing of $a_s = 0.15 - 1$. The different values were taken in order to check the independence of the results on the cut-off.

Self-Energies

The self-energies enter the equations of motion in Fourier space, however the self-energies are calculated in coordinate space via the fast Fourier transformation algorithm introduced above. A product in coordinate space which has to be Fourier transformed corresponds to a convolution integral. One has to distinguish the different kinds of two-point functions which enter the products and thus the integrand of the convolution. The integrand of fermion self-energies can build out of either two scalar-valued functions or one scalar and one vector-valued function, see (3.50)–(3.48). The fermion part of the boson self-energies are build out of either two scalar-valued functions or two vector-valued functions, see (3.53) and (3.54). To show the explicit way how to calculate the self-energies we take the two following examples[4] of a fermion self-energy (A_V^μ) and a fermion part of a boson self-energy

[3] These routines are called ROD10 for the transformation $|\mathbf{x}| \to |\mathbf{p}|$ and ROD10 for the transformation $|\mathbf{p}| \to |\mathbf{x}|$ provided on http://www.fftw.org/.

[4] They correspond to two examples out of the chiral linear-sigma-model, the calculation shown here transfers to the more general case of the non-chiral model in a trivial way.

(Π_ρ^ψ),

$$A_V^\mu(t,t';\mathbf{p}) = -g^2\int\frac{d^3q}{(2\pi)^3}\Big[F_V^\mu(t,t';\mathbf{q})\rho_\phi(t,t';\mathbf{p}-\mathbf{q}) + \rho_V^\mu(t,t';\mathbf{q})F_\phi(t,t';\mathbf{p}-\mathbf{q})\Big], \tag{F.10}$$

$$\Pi_\rho^\psi(t,t';\mathbf{p}) = -4g^2\int\frac{d^3q}{(2\pi)^3}\Big\{\rho_V^\mu(t,t';\mathbf{q})F_{V,\mu}(t,t';\mathbf{p}-\mathbf{q})\Big\}. \tag{F.11}$$

The complication of calculating these integral with the discretization shown above arises due to the differences of momenta in one argument under the integral. In general this would involve angular dependencies. Depending on the kind of functions under the integral one can avoid this complication by rewriting the integral in a certain way, respectively use expressions in the coordinate space. In (F.10) we have two types of integrands. It depends on the space-time index μ with which structure we are confronted. For the time component ($\mu = 0$) we have an integrand where two scalar functions are multiplied ("scalar-scalar"). For $\mu = 1,2,3$ we have a scalar and a vector valued function under the integral ("scalar-vector"). In (F.11) we have in the first term the "scalar-scalar" structure whereas in the second term a "vector-vector" structure arises which is absent in the fermion self-energies. The easiest case is of course the "scalar-scalar" integrand. We just have to Fourier transform the two functions and multiply the transformed quantities and transform this product back, this leads exactly to the convolution shown in (F.10) and (F.11). This method is applied in the purely bosonic sector where all functions are scalar valued. For the "vector-scalar" or the "vector-vector" integrand we have to have a detailed look at the integrals. The way we are going to show how one can calculate the self-energies by only using absolute values of momenta, is a way backwards from a certain combination of integrals to the expression in (F.10) or (F.11). That means in practice we use the special combinations of integrals in order to compute the convolutions which arises in the self-energies. First we consider the spatial part of the first term in (F.10) which corresponds to a "vector-scalar" integral. There we have

$$\begin{aligned}
&\frac{1}{2}\int_{\mathbf{x}}\Big\{\int_{\mathbf{q}}|\mathbf{q}|F_V(t,t';|\mathbf{q}|)e^{-i\mathbf{q}(\mathbf{x}-\mathbf{y})}\int_{\mathbf{k}}\frac{1}{|\mathbf{p}|}\rho_\phi(t,t';|\mathbf{k}|)e^{-i\mathbf{k}(\mathbf{x}-\mathbf{y})}\\
&-\int_{\mathbf{q}}\frac{1}{|\mathbf{q}|}F_V(t,t';|\mathbf{q}|)e^{-i\mathbf{q}(\mathbf{x}-\mathbf{y})}\int_{\mathbf{k}}\frac{|\mathbf{k}|^2}{|\mathbf{p}|}\rho_\phi(t,t';|\mathbf{k}|)e^{-i\mathbf{k}(\mathbf{x}-\mathbf{y})}\\
&+\int_{\mathbf{q}}\frac{1}{|\mathbf{q}|}F_V(t,t';|\mathbf{q}|)e^{-i\mathbf{q}(\mathbf{x}-\mathbf{y})}\int_{\mathbf{k}}|\mathbf{p}|\rho_\phi(t,t';|\mathbf{k}|)e^{-i\mathbf{k}(\mathbf{x}-\mathbf{y})}\Big\}e^{+i\mathbf{p}(\mathbf{x}-\mathbf{y})}\\
&=\frac{1}{2}\int_{\mathbf{x}}\int_{\mathbf{q}}\int_{\mathbf{k}}\left[\frac{|\mathbf{q}|}{|\mathbf{p}|}-\frac{|\mathbf{k}|^2}{|\mathbf{q}|\,|\mathbf{p}|}+\frac{|\mathbf{p}|}{|\mathbf{q}|}\right]F_V(t,t';|\mathbf{q}|)\rho_\phi(t,t';|\mathbf{k}|)e^{-i(\mathbf{x}-\mathbf{y})(\mathbf{q}+\mathbf{k}-\mathbf{p})}
\end{aligned}$$

$$
\begin{aligned}
&= \frac{1}{2}\int_{\mathbf{q}}\int_{\mathbf{k}}\left[\frac{|\mathbf{q}|}{|\mathbf{p}|} - \frac{|\mathbf{k}|^2}{|\mathbf{q}|\,|\mathbf{p}|} + \frac{|\mathbf{p}|}{|\mathbf{q}|}\right] F_V(t,t';|\mathbf{q}|)\rho_\phi(t,t';|\mathbf{k}|)\delta(\mathbf{q}+\mathbf{k}-\mathbf{p}) \\
&= \frac{1}{2}\int_{\mathbf{q}}\left[\frac{|\mathbf{q}|}{|\mathbf{p}|} - \frac{|\mathbf{p}-\mathbf{q}|^2}{|\mathbf{q}|\,|\mathbf{p}|} + \frac{|\mathbf{p}|}{|\mathbf{q}|}\right] F_V(t,t';|\mathbf{q}|)\rho_\phi(t,t';|\mathbf{p}-\mathbf{q}|) \\
&= \frac{1}{2}\int_{\mathbf{q}}\left[\frac{|\mathbf{q}|}{|\mathbf{p}|} - \frac{|\mathbf{p}|^2+|\mathbf{q}|^2-2\mathbf{p}\cdot\mathbf{q}}{|\mathbf{q}|\,|\mathbf{p}|} + \frac{|\mathbf{p}|}{|\mathbf{q}|}\right] F_V(t,t';|\mathbf{q}|)\rho_\phi(t,t';|\mathbf{p}-\mathbf{q}|) \\
&= \int \frac{d^3q}{(2\pi)^3}\frac{\mathbf{p}\cdot\mathbf{q}}{|\mathbf{p}|\,|\mathbf{q}|} F_V(t,t';|\mathbf{q}|)\rho_\phi(t,t';|\mathbf{p}-\mathbf{q}|) = -g^{-2}A_V(t,t';|\mathbf{p}|)|_{1.\text{term}}. \qquad \text{(F.12)}
\end{aligned}
$$

The last equality corresponds to the first term in (F.10) after multiplying with $-g^2\mathbf{p}/|\mathbf{p}|$. This result tells us that we are able to calculate the self-energy convolution, by taking the left hand side of (F.12), without explicitly dealing with vector differences rather with absolute values of vectors. This simplifies the computation and makes it numerical cheaper. The same steps could be done for the second term in (F.10).

For a "vector-vector" integrand we take (as an example) the second term in (F.11), here we have

$$
\begin{aligned}
&\frac{1}{2}\int_{\mathbf{x}}\Bigg\{-\int_{\mathbf{q}}|\mathbf{q}|F_V(t,t';\mathbf{q})e^{-i\mathbf{q}(\mathbf{x}-\mathbf{y})}\int_{\mathbf{k}}\frac{1}{|\mathbf{k}|}\rho_V(t,t';|\mathbf{k}|)e^{-i\mathbf{k}(\mathbf{x}-\mathbf{y})} \\
&\quad -\int_{\mathbf{q}}\frac{1}{|\mathbf{q}|}F_V(t,t';|\mathbf{q}|)e^{-i\mathbf{q}(\mathbf{x}-\mathbf{y})}\int_{\mathbf{k}}|\mathbf{k}|\rho_V(t,t';|\mathbf{k}|)e^{-i\mathbf{k}(\mathbf{x}-\mathbf{y})} \\
&\quad +\int_{\mathbf{q}}\frac{1}{|\mathbf{q}|}F_V(t,t';|\mathbf{q}|)e^{-i\mathbf{q}(\mathbf{x}-\mathbf{y})}\int_{\mathbf{k}}\rho_V(t,t';|\mathbf{k}|)\frac{|\mathbf{p}|^2}{|\mathbf{k}|}e^{-i\mathbf{k}(\mathbf{x}-\mathbf{y})}\Bigg\}e^{+i\mathbf{p}(\mathbf{x}-\mathbf{y})} \\
&= \frac{1}{2}\int_{\mathbf{x}}\int_{\mathbf{q}}\int_{\mathbf{k}}\left[-\frac{|\mathbf{q}|}{|\mathbf{k}|} - \frac{|\mathbf{k}|}{|\mathbf{q}|} + \frac{|\mathbf{p}|^2}{|\mathbf{k}|\,|\mathbf{q}|}\right] F_V(t,t';|\mathbf{q}|)\rho_V(t,t';|\mathbf{k}|)e^{-i(\mathbf{x}-\mathbf{y})(\mathbf{q}+\mathbf{k}-\mathbf{p})} \\
&= \frac{1}{2}\int_{\mathbf{q}}\int_{\mathbf{k}}\left[-\frac{|\mathbf{q}|}{|\mathbf{k}|} - \frac{|\mathbf{k}|}{|\mathbf{q}|} + \frac{|\mathbf{p}|^2}{|\mathbf{k}|\,|\mathbf{q}|}\right] F_V(t,t';|\mathbf{q}|)\rho_V(t,t';|\mathbf{k}|)\delta(\mathbf{q}+\mathbf{k}-\mathbf{p}) \\
&= \frac{1}{2}\int_{\mathbf{q}}\left[-\frac{|\mathbf{q}|}{|\mathbf{p}-\mathbf{q}|} - \frac{|\mathbf{p}-\mathbf{q}|}{|\mathbf{q}|} + \frac{|\mathbf{p}|^2}{|\mathbf{p}-\mathbf{q}|\,|\mathbf{q}|}\right] F_V(t,t';|\mathbf{q}|)\rho_V(t,t';|\mathbf{p}-\mathbf{q}|) \\
&= \frac{1}{2}\int_{\mathbf{q}}\left[\frac{-|\mathbf{q}|^2-|\mathbf{p}-\mathbf{q}|^2+|\mathbf{p}|^2}{|\mathbf{p}-\mathbf{q}|\,|\mathbf{q}|}\right] F_V(t,t';|\mathbf{q}|)\rho_V(t,t';|\mathbf{p}-\mathbf{q}|) \\
&= \frac{1}{2}\int_{\mathbf{q}}\left[\frac{-2|\mathbf{q}|^2+2\mathbf{p}\cdot\mathbf{q}}{|\mathbf{p}-\mathbf{q}|\,|\mathbf{q}|}\right] F_V(t,t';|\mathbf{q}|)\rho_V(t,t';|\mathbf{p}-\mathbf{q}|) \\
&= \int\frac{d^3q}{(2\pi)^3}\frac{\mathbf{q}\cdot(\mathbf{p}-\mathbf{q})}{|\mathbf{q}|\,|\mathbf{p}-\mathbf{q}|}F_V(t,t';|\mathbf{q}|)\rho_V(t,t';|\mathbf{p}-\mathbf{q}|) \\
&= -(-4g^{-2})\Pi^\psi_\rho(t,t';|\mathbf{p}|)|_{2.\text{term}}. \qquad \text{(F.13)}
\end{aligned}
$$

In the last line we explicitly wrote down the minus sign coming from the four-vector

product in (F.11). Hence, also for the "vector-vector" integrals we are able to avoid handling with vector differences, by taking the left hand side of (F.13). Here is important to note that the calculations are strongly depend on the assumption of isotropy, however, for all other self-energies, not shown here, the same method applies.

For the calculation of the boson part of the bosonic self-energies we need the $I(x,y)$-functions (3.57) and (3.58) as well as the $P(x,y)$-functions (3.59) and (3.60). In order to calculate $I(x,y)$ we introduce numerically auxiliary functions which represent the product $F^{\phi}_{ab}(x,y)\rho^{\phi}_{ba}(x,y)$ and $F^{\phi}_{ab}(x,y)F^{\phi}_{ba}(x,y) - \frac{1}{4}\rho^{\phi}_{ab}(x,y)\rho^{\phi}_{ba}(x,y)$ and determine the corresponding modes. In this way we can calculate the modes of $I(x,y)$ in Fourier space by just multiplying the corresponding modes of the auxiliary functions with the I's and with themselves and build the sum in order to account for the memory integrals, thus there is no need for an integral over coordinate space. However it is worth to stress that these equations are also explicit in time as the equations of motions are. This is not obvious but true, we refere the reader to Ref. [Ber05] for further details. For the same reasons as for $I(x,y)$ we calculate $P(x,y)$ in Fourier space. It is useful to treat the double time-integrals in a certain way, in which we prefer to spend memory and obtain a faster code by calculating the inner time-integrals first and save their results into an array so that the data is allocated for the outer integrals. This is numerically expensive since there is no symmetry information present regarding the inner integrals, that means we have to save the whole time array, i.e. $T_{\max} \times T_{\max}$, however this accelerates the calculation enormously.

F.2 Numerical Stability

In this section we are going to discuss the insensitivity against infrared and ultraviolet cut-off changes. In Sec. F.2 we consider simulations out of Sec. 4.1. In the subsequent section we turn to the simulations out of Sec. 4.2. In Sec. F.2 we check the results in Sec. 5.1 and 5.2.

Production of Massless Fermions in the Presence of a Spinodal Instability

The following considerations concern the simulations out of Sec. 4.1. We present findings of the occupation numbers $n_{\psi}(t,\mathbf{p})$ and $n_{\phi}(t,\mathbf{p})$ defined in (3.84) and (3.85). We consider simulations with $g\sqrt{2} = 0.01$ and $\lambda = 0.01$. In Sec. F.1 we introduced the discretization we use. Note that for a given lattice spacing a_s and number of discretization points N the radius L of the sphere is fixed, thus the volume is. The parameter sets comprise $a_s = 0.15/m, 0.3/m, 0.6/m$ and $N = 40, 80, 160$. The

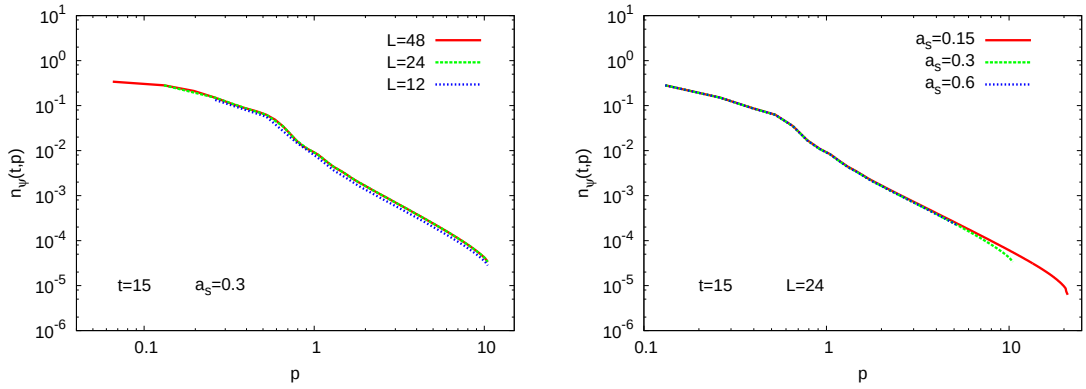

Figure F.1: Left: Λ_{IR} dependence, without significant changes with larger volumes. Right: Λ_{UV} dependence, the power-law continues with larger cut-offs, the sharp fall of at Λ_{UV} is an artifact without consequences.

results in Sec. 4.1 have $L = 0.3 \cdot 80/m = 24/m$. As in the main text all quantities shown in plots have to be understood in units of the mass m.

In Fig. F.1 we show two plots which display the infrared (left plot) and ultraviolet cut-off (Λ_{IR} and Λ_{UV} respectively) insensitivity of $n_\psi(t, \mathbf{p})$. We took three different radii, i.e. $L = 12/m, 24/m, 48/m$ to check the volume dependence and $a_s = 0.15/m, 0.3/m, 0.6/m$ for different ultraviolet cut-offs. The plots correspond to those in Fig. 4.17 at time $t = 15/m$. We choose $t = 15/m$ since the spectrum shows all its main features and afterwards it does not change a lot due to the quasi-stationary evolution. We discuss the time evolution below. Increasing the volume exhibits modes with larger amplitudes without exceeding $1/2$ as expected (left plot). The spectrum as a whole is not changed qualitatively. Consequently the main characteristics are insensitive against changing Λ_{IR}. Increasing the ultraviolet cut-off (right plot) yields a larger range with power-law $|\mathbf{p}|^{-2}$, this was mentioned already in Sec. 4.1.2. The sharp fall-off at Λ_{UV} is a numerical artifact which has no consequences, it could be removed by using a better time discretization. Hence the spectrum as a whole is not altered qualitatively when changing Λ_{UV}.

In Fig. F.2 we present spectra of the boson occupation number where we varied the infrared cut-off. We do not consider the ultraviolet cut-off dependence since it is obvious that the results are independent in the case of $n_\phi(t, \mathbf{p})$. As for the fermion results we do not observe qualitative changes in the spectrum.

In order to show that our findings are not specific for $t = 15/m$ we show in Fig. F.3 a time evolution of $n_\psi(t, \mathbf{p})$ for $|\mathbf{p}| = 0.26$ as an example. In the left plot we changed Λ_{IR} according to the radii indicated in the figure, all lines lie on top of each other, which perfectly shows that with our chosen discretization in Sec. 4.1 the infinite volume limit is arrived. In the right plot we changed the Λ_{UV} as above. There we observe changes in the very early time evolution. However with $a_s = 0.3/m$ and

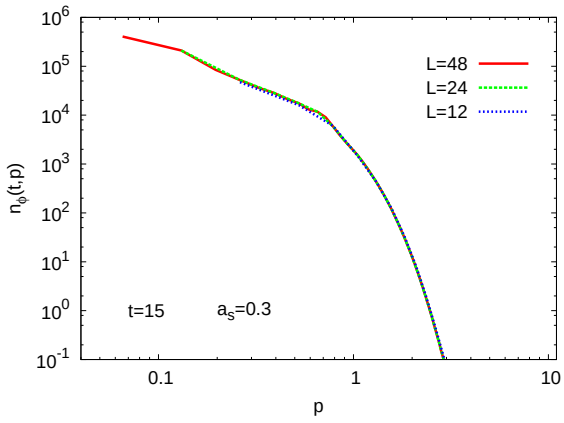

Figure F.2: Λ_{IR} dependence of the boson occupation number. With larger volumes the new included modes show larger amplitudes, however the spectrum as a whole is not changed qualitatively.

$N = 80$ a large enough cut-off is obtained. The difference to $a_s = 0.15/m$ with $N = 160$ is negligible. Same findings are valid for all other modes.

A time evolution of $n_\phi(t, \mathbf{p})$ for a certain $|\mathbf{p}|$ would show again three lines on top of each other, as in Fig. F.3. We skip the presentation of this plot.

As a summary we can say that our results for fermion and boson occupation numbers are rather stable against cut-off changes as it should be.

Production of Massive Fermions due to a Spinodal Instability

In this section we concentrate on the fermion occupation number as examples of the numerical stability. We showed in the main text that the boson dynamics is not affected by the dynamics of massive fermions. This was also the case for massless fermion in the last section, accordingly the boson spectra here are as well not sensitive against cut-off changes and we skip the presentation of redundant plots. However, we mentioned in Sec. 4.2 that the late time evolution of the macroscopic field becomes infrared cut-off dependent. Therefore we think it is necessary to demonstrate that on the time scales we investigated the evolution is insensitive against cut-off changes.

The parameter sets shown here comprise $a_s = 0.25/m, 0.5/m, 1/m$ and $N = 64, 128, 256$. The results in Sec. 4.2 have $L = 1 \cdot 256/m$. As in the main text all quantities shown in plots have to be understood in units of the mass m. We take a specific parameter set out of Sec. 4.2 as an example. We emphasize that all other sets have the same insensitivity. Here we consider simulations with couplings $\lambda = 0.01$ and $g = 0.01$. The fermion mass was taken to be $m_\psi = 0.15m$ and for the initial

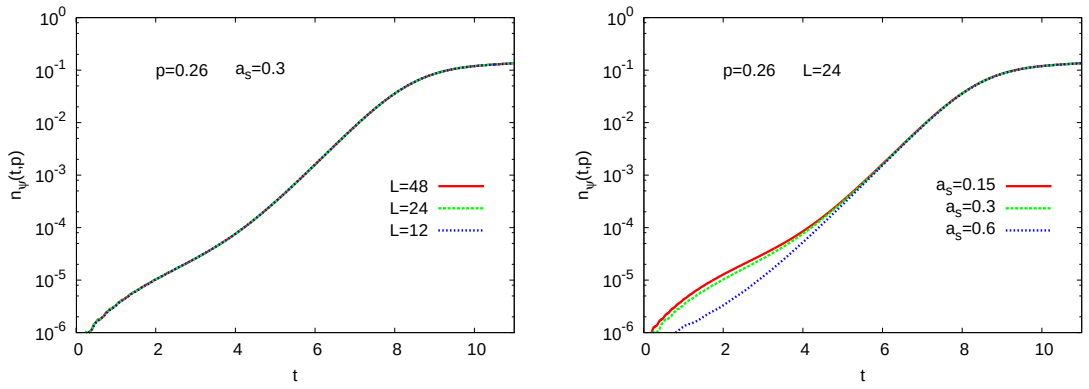

Figure F.3: Left: variation of the volume does not change the time evolution. Right: same time evolution as in the left plot but Λ_{UV} is changed with a fixed volume. The early time deviations are discussed in the text.

value of the macroscopic field we chose $\phi_0 = 0.1m$.

In the left plot of Fig. F.4 we present spectra of $n_\psi(t, \mathbf{p})$ at $t = 10/m$ where we changed the infrared cut-off Λ_{IR} with fixed spacing $a_s = 1/m$. The right plot displays the corresponding results where we varied the ultraviolet cut-off Λ_{UV} with fixed radius $L = 64$[5]. We observe that there is no qualitatively difference for different Λ_{IR}. In the large-momentum regime the stable power-law with exponent minus two is present. For small values of the momentum the amplitude saturates at a nonvanishing value as was already mentioned in the main text. Here we consider $t = 10/m$ which corresponds to the transition regime between the end of exponential growth and the quasi-stationary evolution. Therefore the amplitude is larger and the hill in the middle is more pronounced. In total we infere that the results are insensitive against the infrared cut-off change and thus we are in the infinite volume limit with $L = 256/m$ which was used in Sec. 4.2.

The right plot of Fig. F.4 shows that the results are insensitive against Λ_{UV} changing. The qualitatively shape of the spectrum remains the same while changing from $\Lambda_{\mathrm{UV}} = \pi$ to $\Lambda_{\mathrm{UV}} = 4\pi$. The power-law continues till larger momenta as mentioned in the main text. The little fall-off at the ultraviolet cut-off is a numerical artifact, it can be removed by using a better time discretization.

In order to show that this holds for all times in our simulations we present in Fig. F.5 time evolutions of $n_\psi(t, \mathbf{p})$ with $|\mathbf{p}| = 0.1m$. In the left plot we varied Λ_{IR}

[5]In the main text we have simulations with $L = 256/m$ which does not appear in the Λ_{UV} check. The reason is that for $L = 256/m$ with increasing cut-offs we need more than $N = 256$ grid points in order to fix the infrared cut-off. With this the time memory would be strongly limited and would not reach required time scales. So there have to be a compromise. However our results show that even for $N = 64$ there is no cut-off dependence and thus we belief that there is non for even larger volumes.

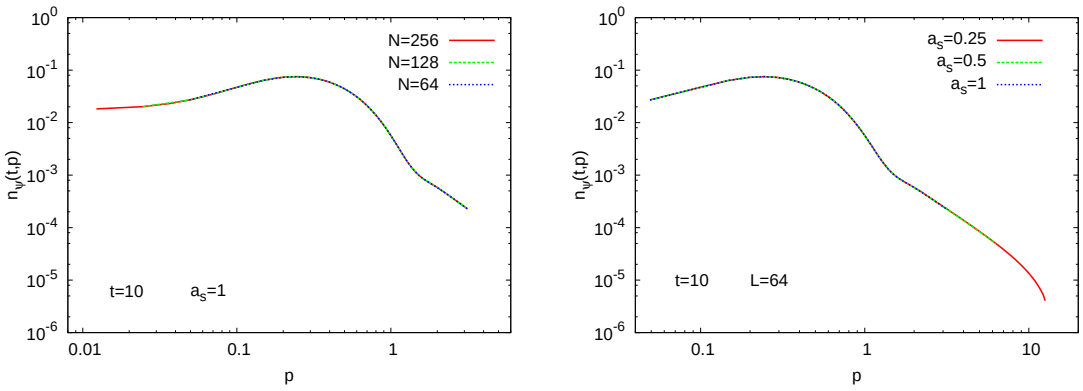

Figure F.4: Left: variation of the volume does not change the major aspects of the spectrum, the saturation for small momenta becomes more pronounced. Right: Λ_{UV} is changed with a fixed volume, qualitatively no difference occurs.

and in the right plot Λ_{UV}. Whereas in the left plot all curves lie on top of each other, in the right plot there are small deviations at early times. In all cases the exponential growth has the same rate and the end of the unstable evolution phase is the same in each case too. Qualitatively the same is observed for other momentum modes. Consequently the physics is not changed and all our results are safe.

Now we turn to the evolution of the macroscopic field $\phi(t)$. As stated in the main text the late time ($t \gtrsim 15/m$) evolution is infrared cut-off dependent. In order to show that on smaller time scales everything is independent of Λ_{IR} we plotted in Fig. F.6 the time evolution of $\phi(t)$ for the same parameters as given above. The cut-off was changed in the same manner as in the left plot of Fig. F.5. We observe that no changes at all are visible and all curves lie on top of each other. The same result is obtained if we change the ultraviolet cut-off, therefore we did not present the plot, it would look exactly the same.

The mentioned infrared cut-off dependence at late times is not observed for the parametric resonance case which we will consider in the next section.

Fermion Production due to Parametric Resonance

In this section we will present a study of the insensitivity of the fermion occupation number to changing the infrared (Λ_{IR}) and ultraviolet (Λ_{UV}) cut-off. We skip a detailed discussion of the boson sector. We checked that the results are insensitive to cut-off changes. Since the dynamics we found is the same already reported about in earlier works, e.g. [BS03], there is no need to confirm explicitly that the findings are physical and free from artifacts. At the end we will confirm the choice of ϕ_0 as our scale, as it was done in Chapter 5.

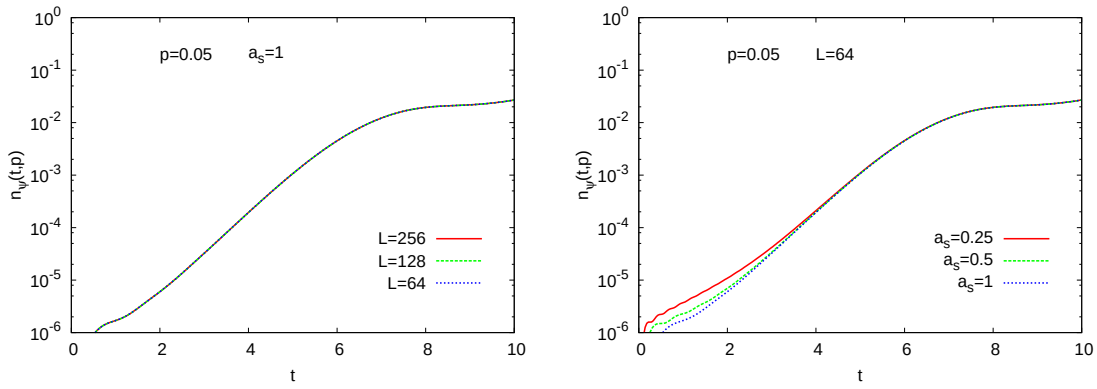

Figure F.5: Left:variation of the volume does not change the time evolution. Right: same time evolution as in the left plot but $\Lambda_{\rm UV}$ is changed with a fixed volume. The early time deviations are discussed in the text.

We consider simulations with coupling parameters $g = 0.1$ and $\lambda = 0.1$, i.e. $\xi = 0.1$. We will express every dimensionful quantity in units of ϕ_0 since this sets the scale in the dynamics[6], cf. Sec. 5.2. We consider massless fermions and $m/\phi_0 = 0.2$, hence the physical situation corresponds to one example given in Sec. 5.2. We have chosen three different values of a_s and L. They are $a_s\phi_0 = 1, 1.5, 2$ and $L\phi_0 = 90, 120, 180$ with $N = 60, 80\,120$, and $a_s\phi_0 = 1.5$. We emphasize that for parametric resonance the equations are more sensitive against time discretization compared to spinodal instability. This is due to the oscillatory behavior of the macroscopic field, its signature is observable in each quantity.

In Fig. F.7 we show the results of the fermion occupation number as a function of the momentum. The left plot considers the $\Lambda_{\rm IR}$ and the right the $\Lambda_{\rm UV}$ insensitivity. For the $\Lambda_{\rm IR}$-check the radius of the sphere was changed from $L\phi_0 = 90 - 180$ with a fixed spacing $a_s\phi_0 = 1.5$. For the $\Lambda_{\rm UV}$-check the spacing was changed from $a_s\phi_0 = 1 - 2$ with a fixed radius $L\phi_0 = 120$. The time was chosen to be $t\phi_0 = 175$.

We observe in the left plot that all simulations lie on top of each other which displays the stability of the results. In the right plot there are deviations at the corresponding ultraviolet cut-offs. They have no consequences on the qualitatively shape of the spectrum and thus no impact on physical conclusions made in Sec. 5.2. The deviations vanish if one uses a small enough time discretization, here we used $dt\phi_0 = 0.25$. This is a compromise between reaching a reasonable "late" time and a high precision calculation.

In order to check that the time evolution is not affected by cut-off changes we present in Fig. F.8 two time evolutions of $n_\psi(t, \mathbf{p})$ for $|\mathbf{p}|/\phi_0 = 0.03$. The left plot

[6]We did various simulations with different numerical values of ϕ_0 the results shown here were obtained with $\phi_0 = 5$.

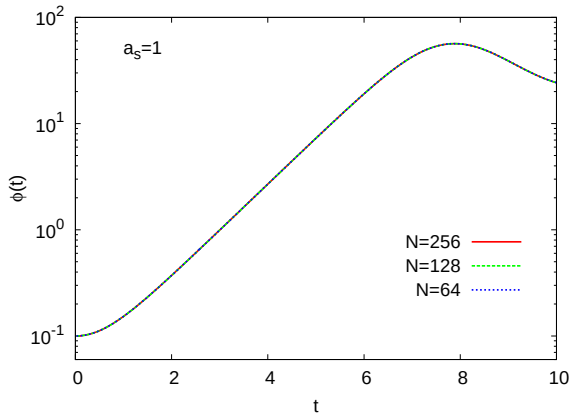

Figure F.6: Demonstration of the insensitivity of $\phi(t)$ against Λ_{IR} changes. All three curves lie on top of each other. The same results would be obtained for the ultraviolet cut-off check.

considers the Λ_{IR} dependence and the right plot the Λ_{UV} dependence. In the left plot small deviations at early times are visible in the case of $L\phi_0 = 120$. This is just due to practical circumstances. With the discretization parameters we have chosen we cannot exactly calculate in the case $L\phi_0 = 120$ the same momentum as in the other cases. That means in the two cases $L\phi_0 = 180$ and $L\phi_0 = 90$ we have $|\mathbf{p}|/\phi_0 = 0.034$ and in the case $L\phi_0 = 120$ we have $|\mathbf{p}|/\phi_0 = 0.026$, this causes the difference. Most important there is no qualitatively difference in the dynamics over the whole simulation time. This is also observed in the right plot where the ultraviolet cut-off was changed according to the values given in the figure. Qualitatively the same is observed for all other values of momentum.

In summary we can say that our results for the fermion dynamics are stable against cut-off changes and thus trustworthy.

Choice of ϕ_0 as a scale

In Chapter 5 we use the parameter ϕ_0 as our scale. In this section we argue that this is a reasonable choice. The parameter ϕ_0 fixes the initial value of the macroscopic field $\phi(t)$. Hence, for not too small ϕ_0 the initial classical energy is essentially given by ϕ_0^4. This sets the scale in the dynamics. Fig. F.9 states that this is indeed the case. There we present fermion occupation number spectra for different ϕ_0 at fixed times $t \cdot \phi_0$. We display the snapshots at $t \cdot \phi_0 = 60, 90, 120, 150$ which correspond to intermediate times out of the simulations shown in the main text.

We observe that the spectra qualitatively agree with each other at the same time. Consequently there is no specific information for a certain value of ϕ_0. Qualitatively the same is obtained for results of the boson sector.

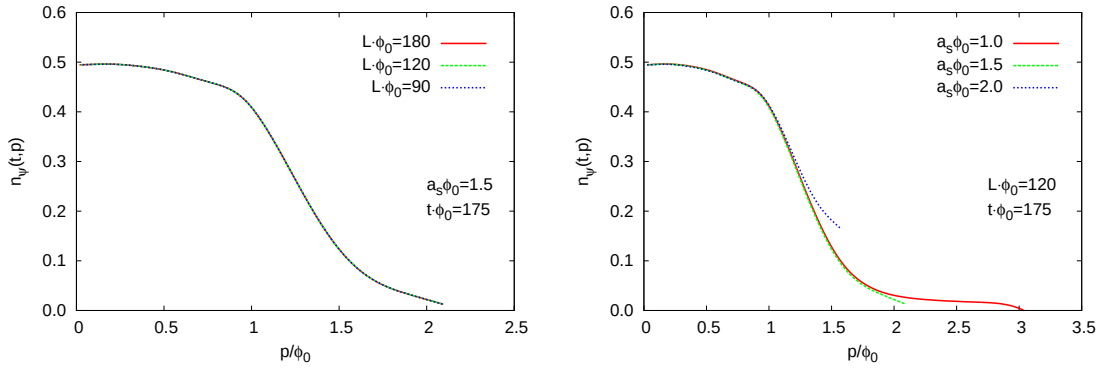

Figure F.7: Left: Λ_{IR} independence of $n_\psi(t, \mathbf{p})$ all curves lie on top of each other. Right: Λ_{UV} independence of $n_\psi(t, \mathbf{p})$. The general shape is conserved, the small deviation at the cut-offs have no consequences.

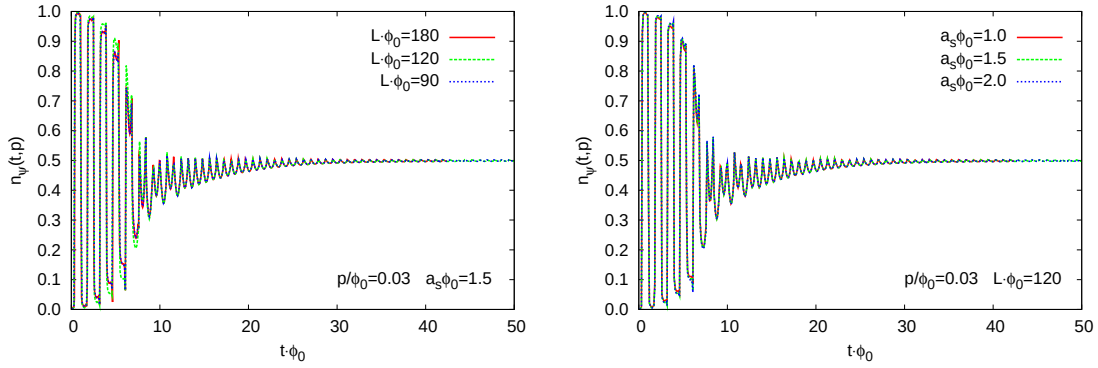

Figure F.8: Left: Λ_{IR} independence of $n_\psi(t, \mathbf{p})$ all curves lie on top of each other except for small deviations at early times. Right: Λ_{UV} independence of $n_\psi(t, \mathbf{p})$ with a perfectly agreement of the dynamics.

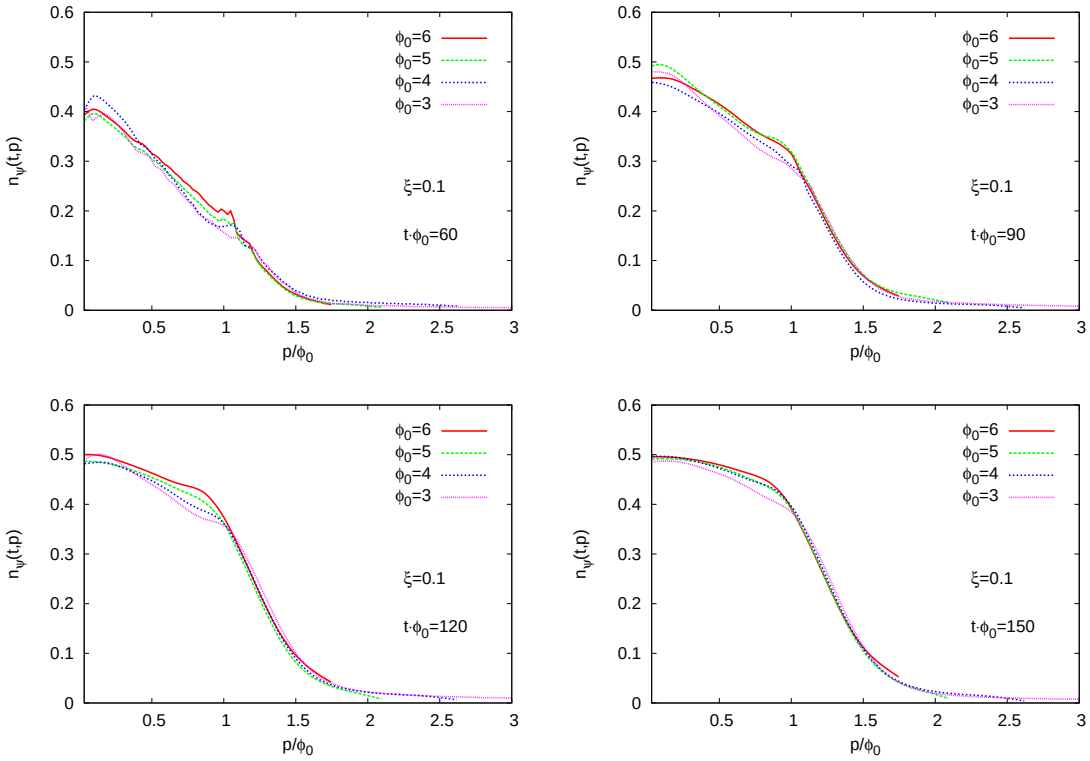

Figure F.9: Fermion occupation number spectra for different ϕ_0 at fixed times $t \cdot \phi_0$. These results state that ϕ_0 can be used as a scale.

Bibliography

[AAB+02] G. Aarts, D. Ahrensmeier, R. Baier, J. Berges, and J. Serreau, *Far-from-equilibrium dynamics with broken symmetries from the 2PI-1/N expansion*, Phys. Rev. **D66** (2002), 045008.

[Aar09] G. Aarts, *Can stochastic quantization evade the sign problem? – the relativistic Bose gas at finite chemical potential*, Phys. Rev. Lett. **102** (2009), 131601.

[AB01] G. Aarts and J. Berges, *Nonequilibrium time evolution of the spectral function in quantum field theory*, Phys. Rev. **D64** (2001), 105010.

[AB02] ———, *Classical aspects of quantum fields far from equilibrium*, Phys. Rev. Lett. **88** (2002), 041603.

[ABCRM10] R. Allahverdi, R. Brandenberger, F.-Y. Cyr-Racine, and A. Mazumdar, *Reheating in Inflationary Cosmology: Theory and Applications*.

[AFW82] L. F. Abbott, E. Farhi, and M. B. Wise, *Particle Production in the New Inflationary Cosmology*, Phys. Lett. **B117** (1982), 29.

[ALM03] P. Arnold, J. Lenaghan, and G. D. Moore, *QCD plasma instabilities and bottom-up thermalization*, JHEP **08** (2003), 002.

[ALMY05] P. Arnold, J. Lenaghan, G. D. Moore, and Laurence G. Yaffe, *Apparent thermalization due to plasma instabilities in quark gluon plasma*, Phys. Rev. Lett. **94** (2005), 072302.

[AM06a] P. Arnold and G. D. Moore, *QCD plasma instabilities: The nonabelian cascade*, Phys. Rev. **D73** (2006), 025006.

[AM06b] ———, *The turbulent spectrum created by non-Abelian plasma instabilities*, Phys. Rev. **D73** (2006), 025013.

[AMPEC08] P. R. Anderson, C. Molina-Paris, D. Evanich, and G. B. Cook, *Study of the preheating phase of chaotic inflation*, Phys. Rev. **D78** (2008), 083514.

[AS64] M. Abramowitz and I. A. Stegun, *Handbook of mathematical functions with formulas, graphs, and mathematical tables.*

[AS99] G. Aarts and J. Smit, *Real-time dynamics with fermions on a lattice*, Nucl. Phys. **B555** (1999), 355–394.

[AS00] ———, *Particle production and effective thermalization in inhomogeneous mean field theory*, Phys. Rev. **D61** (2000), 025002.

[AST04] A. Arrizabalaga, J. Smit, and A. Tranberg, *Tachyonic preheating using 2PI - 1/N dynamics and the classical approximation*, JHEP **10** (2004), 017.

[AST05] ———, *Equilibration in phi**4 theory in 3+1 dimensions*, Phys. Rev. **D72** (2005), 025014.

[Bay62] G. Baym, *Selfconsistent approximation in many body systems*, Phys. Rev. **127** (1962), 1391–1401.

[BBS03] J. Berges, S. Borsanyi, and J. Serreau, *Thermalization of fermionic quantum fields*, Nucl. Phys. **B660** (2003), 51–80.

[BBW04] J. Berges, S. Borsanyi, and C. Wetterich, *Prethermalization*, Phys. Rev. Lett. **93** (2004), 142002.

[BC01] J. Berges and J. Cox, *Thermalization of quantum fields from time-reversal invariant evolution equations*, Phys. Lett. **B517** (2001), 369–374.

[BCdV+98] D. Boyanovsky, D. Cormier, H. J. de Vega, R. Holman, and S. P. Kumar, *Non-perturbative quantum dynamics of a new inflation model*, Phys. Rev. **D57** (1998), 2166–2185.

[BD82] N. D. Birrell and P. C. W. Davies, *QUANTUM FIELDS IN CURVED SPACE*, Cambridge, Uk: Univ. Pr. (1982) 340p.

[BDdV+95] D. Boyanovsky, M. D'Attanasio, H. J. de Vega, R. Holman, and D. S. Lee, *Reheating and thermalization: Linear versus nonlinear relaxation*, Phys. Rev. **D52** (1995), 6805–6827.

[BdVH+95] D. Boyanovsky, H. J. de Vega, R. Holman, D. S. Lee, and A. Singh, *Dissipation via particle production in scalar field theories*, Phys. Rev. **D51** (1995), 4419–4444.

[BdVHS96] D. Boyanovsky, H. J. de Vega, R. Holman, and J. F. J. Salgado, *Analytic and numerical study of preheating dynamics*, Phys. Rev. **D54** (1996), 7570–7598.

[Ber02] J. Berges, *Controlled nonperturbative dynamics of quantum fields out of equilibrium*, Nucl. Phys. **A699** (2002), 847–886.

[Ber04] ———, *n-PI effective action techniques for gauge theories*, Phys. Rev. **D70** (2004), 105010.

[Ber05] ———, *Introduction to nonequilibrium quantum field theory*, AIP Conf. Proc. **739** (2005), 3–62.

[BG07] J. Berges and T. Gasenzer, *Quantum versus classical statistical dynamics of an ultracold Bose gas*, Phys. Rev. **A76** (2007), 033604.

[BGM00] M. Bastero-Gil and A. Mazumdar, *Gravitino production in hybrid inflationary models*, Phys. Rev. **D62** (2000), 083510.

[BGSS09] J. Berges, D. Gelfand, S. Scheffler, and D. Sexty, *Simulating plasma instabilities in SU(3) gauge theory*, Phys. Lett. **B677** (2009), 210–213.

[BH04] J. Baacke and A. Heinen, *Out-of-equilibrium evolution of quantum fields in the hybrid model with quantum back reaction*, Phys. Rev. **D69** (2004), 083523.

[BH09a] J. Berges and G. Hoffmeister, *Nonthermal fixed points and the functional renormalization group*, Nucl. Phys. **B813** (2009), 383–407.

[BH09b] S. Borsanyi and M. Hindmarsh, *Low-cost fermions in classical field simulations*, Phys. Rev. **D79** (2009), 065010.

[BHP97] J. Baacke, K. Heitmann, and C. Patzold, *Nonequilibrium dynamics: A renormalized computation scheme*, Phys. Rev. **D55** (1997), 2320–2330.

[BHP98] ———, *Nonequilibrium dynamics of fermions in a spatially homogeneous scalar background field*, Phys. Rev. **D58** (1998), 125013.

[BJW99] J. Berges, D. U. Jungnickel, and C. Wetterich, *Two flavor chiral phase transition from nonperturbative flow equations*, Phys. Rev. **D59** (1999), 034010.

[BKP07] J. Baacke, N. Kevlishvili, and J. Pruschke, *Quantum back-reaction of the superpartners in a large-N supersymmetric hybrid model*, JCAP **0706** (2007), 004.

[BM63a] P. M. Bakshi and K. T. Mahanthappa, *Expectation value formalism in quantum field theory. 1*, J. Math. Phys. **4** (1963), 1–11.

[BM63b] ———, *Expectation value formalism in quantum field theory. 2*, J. Math. Phys. **4** (1963), 12–16.

[BPR09] J. Berges, J. Pruschke, and A. Rothkopf, *Instability-induced fermion production in quantum field theory*, Phys. Rev. **D80** (2009), 023522.

[BR05] A. Berera and R. O. Ramos, *Dynamics of interacting scalar fields in expanding space- time*, Phys. Rev. **D71** (2005), 023513.

[Bra10] R. H. Brandenberger, *Cosmology of the Very Early Universe*, arXiv:1003.1745 (2010).

[BRS08] J. Berges, A. Rothkopf, and J. Schmidt, *Non-thermal fixed points: effective weak-coupling for strongly correlated systems far from equilibrium*, Phys. Rev. Lett. **101** (2008), 041603.

[BS03] J. Berges and J. Serreau, *Parametric resonance in quantum field theory*, Phys. Rev. Lett. **91** (2003), 111601.

[BS05] J. Berges and I. O. Stamatescu, *Simulating nonequilibrium quantum fields with stochastic quantization techniques*, Phys. Rev. Lett. **95** (2005), 202003.

[BSS08] J. Berges, S. Scheffler, and D. Sexty, *Bottom-up isotropization in classical-statistical lattice gauge theory*, Phys. Rev. **D77** (2008), 034504.

[BSS09a] ———, *Turbulence in nonabelian gauge theory*, Phys. Lett. **B681** (2009), 362–366.

[BSS09b] J. Berges, S. Schlichting, and D. Sexty, *Dynamic critical phenomena from spectral functions on the lattice*.

[BTW02] J. Berges, N. Tetradis, and C. Wetterich, *Non-perturbative renormalization flow in quantum field theory and statistical physics*, Phys. Rept. **363** (2002), 223–386.

[BTW06] B. A. Bassett, S. Tsujikawa, and D. Wands, *Inflation dynamics and reheating*, Rev. Mod. Phys. **78** (2006), 537–589.

[BW98] L. M. A. Bettencourt and C. Wetterich, *Time evolution of correlation functions in non-equilibrium field theories*, Phys. Lett. **B430** (1998), 140–150.

[C+94] F. Cooper et al., *Nonequilibrium quantum fields in the large N expansion*, Phys. Rev. **D50** (1994), 2848–2869.

[Cas09] W. Cassing, *From Kadanoff-Baym dynamics to off-shell parton transport*, Eur. Phys. J. ST **168** (2009), 3–87.

[CCR04] P. Chomaz, M. Colonna, and J. Randrup, *Nuclear spinodal fragmentation*, Phys. Rept. **389** (2004), 263–440.

[CH87] E. Calzetta and B. L. Hu, *Closed Time Path Functional Formalism in Curved Space- Time: Application to Cosmological Back Reaction Problems*, Phys. Rev. **D35** (1987), 495.

[CH08] E. A. Calzetta and B.-L. Hu, *Nonequilibrium quantum field theory*, Cambridge University Press, (2008).

[CHKM97] F. Cooper, S. Habib, Y. Kluger, and E. Mottola, *Nonequilibrium dynamics of symmetry breaking in lambda Phi**4 field theory*, Phys. Rev. **D55** (1997), 6471–6503.

[CHR00] E. A. Calzetta, B. L. Hu, and S. A. Ramsey, *Hydrodynamic transport functions from quantum kinetic field theory*, Phys. Rev. **D61** (2000), 125013.

[CJP74] S. R. Coleman, R. Jackiw, and H. D. Politzer, *Spontaneous Symmetry Breaking in the O(N) Model for Large N**, Phys. Rev. **D10** (1974), 2491.

[CJT74] J. M. Cornwall, R. Jackiw, and E. Tomboulis, *Effective Action for Composite Operators*, Phys. Rev. **D10** (1974), 2428–2445.

[CKRT00] D. J. H. Chung, E. W. Kolb, A. Riotto, and I. I. Tkachev, *Probing Planckian physics: Resonant production of particles during inflation and features in the primordial power spectrum*, Phys. Rev. **D62** (2000), 043508.

[CPR02] E. J. Copeland, S. Pascoli, and A. Rajantie, *Dynamics of tachyonic preheating after hybrid inflation*, Phys. Rev. **D65** (2002), 103517.

[CSHY85] K.-c. Chou, Z.-b. Su, B.-l. Hao, and L. Yu, *Equilibrium and Nonequilibrium Formalisms Made Unified*, Phys. Rept. **118** (1985), 1.

[DFK+06] J. F. Dufaux, G. N. Felder, L. Kofman, M. Peloso, and D. Podolsky, *Preheating with Trilinear Interactions: Tachyonic Resonance*, JCAP **0607** (2006), 006.

[DFKL05] M. Desroche, G. N. Felder, J. M. Kratochvil, and A. D. Linde, *Preheating in new inflation*, Phys. Rev. **D71** (2005), 103516.

[DJ74] L. Dolan and R. Jackiw, *Symmetry Behavior at Finite Temperature*, Phys. Rev. **D9** (1974), 3320–3341.

[DL82] A. D. Dolgov and A. D. Linde, *Baryon Asymmetry in Inflationary Universe*, Phys. Lett. **B116** (1982), 329.

[DN05] A. Dumitru and Y. Nara, *QCD plasma instabilities and isotropization*, Phys. Lett. **B621** (2005), 89–95.

[DNS07] A. Dumitru, Y. Nara, and M. Strickland, *Ultraviolet avalanche in anisotropic non-Abelian plasmas*, Phys. Rev. **D75** (2007), 025016.

[F+01] Gary N. Felder et al., *Dynamics of symmetry breaking and tachyonic preheating*, Phys. Rev. Lett. **87** (2001), 011601.

[FI08] H. Fujii and K. Itakura, *Expanding color flux tubes and instabilities*, Nucl. Phys. **A809** (2008), 88–109.

[FII09] H. Fujii, K. Itakura, and A. Iwazaki, *Instabilities in non-expanding glasma*, Nucl. Phys. **A828** (2009), 178–190.

[FK01] G. N. Felder and L. Kofman, *The development of equilibrium after preheating*, Phys. Rev. **D63** (2001), 103503.

[FKL99] G. N. Felder, L. Kofman, and A. D. Linde, *Instant preheating*, Phys. Rev. **D59** (1999), 123523.

[FKL01] ———, *Tachyonic instability and dynamics of spontaneous symmetry breaking*, Phys. Rev. **D64** (2001), 123517.

[FKYY96a] H. Fujisaki, K. Kumekawa, M. Yamaguchi, and M. Yoshimura, *Particle production and dissipative cosmic field*, Phys. Rev. **D53** (1996), 6805–6812.

[FKYY96b] ———, *Particle Production and Gravitino Abundance after Inflation*, Phys. Rev. **D54** (1996), 2494–2503.

[Fri95] U. Frisch, *Turbulence: the legacy of A. N. Kolmogorov* , Cambridge University Press, UK (1995).

[GBFR09] J. Garcia-Bellido, D. G. Figueroa, and J. Rubio, *Preheating in the Standard Model with the Higgs-Inflaton coupled to gravity*, Phys. Rev. **D79** (2009), 063531.

[GBL98] J. Garcia-Bellido and A. D. Linde, *Preheating in hybrid inflation*, Phys. Rev. **D57** (1998), 6075–6088.

[GBMR00] J. Garcia-Bellido, S. Mollerach, and E. Roulet, *Fermion production during preheating after hybrid inflation*, JHEP **02** (2000), 034.

[GC02] M. Grana and E. Calzetta, *Reheating and turbulence*, Phys. Rev. **D65** (2002), 063522.

[GHKL09] M. Garny, A. Hohenegger, A. Kartavtsev, and M. Lindner, *Systematic approach to leptogenesis in nonequilibrium QFT: vertex contribution to the CP-violating parameter*, Phys. Rev. **D80** (2009), 125027.

[GK99] P. B. Greene and L. Kofman, *Preheating of fermions*, Phys. Lett. **B448** (1999), 6–12.

[GK00] ———, *On the theory of fermionic preheating*, Phys. Rev. **D62** (2000), 123516.

[GKL06] F. Gelis, K. Kajantie, and T. Lappi, *Chemical thermalization in relativistic heavy ion collisions*, Phys. Rev. Lett. **96** (2006), 032304.

[GKLS97] P. B. Greene, L. Kofman, A. D. Linde, and A. A. Starobinsky, *Structure of resonance in preheating after inflation*, Phys. Rev. **D56** (1997), 6175–6192.

[GML60] M. Gell-Mann and M. Levy, *The axial vector current in beta decay*, Nuovo Cim. **16** (1960), 705.

[GP08] T. Gasenzer and J. M. Pawlowski, *Towards far-from-equilibrium quantum field dynamics: A functional renormalisation-group approach*, Phys. Lett. **B670** (2008), 135–140.

[GPRT99] G. F. Giudice, M. Peloso, A. Riotto, and I. Tkachev, *Production of massive fermions at preheating and leptogenesis*, JHEP **08** (1999), 014.

[GPS04] B. Garbrecht, T. Prokopec, and M. G. Schmidt, *Particle number in kinetic theory*, Eur. Phys. J. **C38** (2004), 135–143.

[GRT99] G. F. Giudice, A. Riotto, and I. Tkachev, *Thermal and non-thermal production of gravitinos in the early universe*, JHEP **11** (1999), 036.

[GTR99] G. F. Giudice, I. Tkachev, and A. Riotto, *Non-thermal production of dangerous relics in the early universe*, JHEP **08** (1999), 009.

[Gut81] A. H. Guth, *The Inflationary Universe: A Possible Solution to the Horizon and Flatness Problems*, Phys. Rev. **D23** (1981), 347–356.

[Hei01] U. W. Heinz, *The little bang: Searching for quark-gluon matter in relativistic heavy-ion collisions*, Nucl. Phys. **A685** (2001), 414–431.

[Hei05] ———, *Thermalization at RHIC*, AIP Conf. Proc. **739** (2005), 163–180.

[JLM+07] H.-T. Janka, K. Langanke, A. Marek, G. Martinez-Pinedo, and B. Mueller, *Theory of Core-Collapse Supernovae*, Phys. Rept. **442** (2007), 38–74.

[Jor86] R. D. Jordan, *Effective Field Equations for Expectation Values*, Phys. Rev. **D33** (1986), 444–454.

[Kai96] D. I. Kaiser, *Post inflation reheating in an expanding universe*, Phys. Rev. **D53** (1996), 1776–1783.

[Kai97] ———, *Preheating in an expanding universe: Analytic results for the massless case*, Phys. Rev. **D56** (1997), 706–716.

[Kai98] ———, *Resonance structure for preheating with massless fields*, Phys. Rev. **D57** (1998), 702–711.

[Kel64] L. V. Keldysh, *Diagram technique for nonequilibrium processes*, Zh. Eksp. Teor. Fiz. **47** (1964), 1515–1527.

[KES+92] Y. Kluger, J. M. Eisenberg, B. Svetitsky, F. Cooper, and E. Mottola, *Fermion pair production in a strong electric field*, Phys. Rev. **D45** (1992), 4659–4671.

[Kha08] V. Khachatryan, *Modified Kolmogorov Wave Turbulence in QCD matched onto "Bottom-up" Thermalization*, Nucl. Phys. **A810** (2008), 109–141.

[KLS94] L. Kofman, A. D. Linde, and A. A. Starobinsky, *Reheating after inflation*, Phys. Rev. Lett. **73** (1994), 3195–3198.

[KLS97] ———, *Towards the theory of reheating after inflation*, Phys. Rev. **D56** (1997), 3258–3295.

[KPJM03] K. Kifonidis, T. Plewa, H. Th. Janka, and E. Mueller, *Non-spherical core collapse supernovae. I: Neutrino-driven convection, Rayleigh-Taylor instabilities, and the formation and propagation of metal clumps*, Astron. Astrophys. **408** (2003), 621–650.

[KT90] E. W. Kolb and M. S. Turner, *The Early universe*, Front. Phys. **69** (1990), 1–547.

[KT96] S. Y. Khlebnikov and I. I. Tkachev, *Classical decay of inflaton*, Phys. Rev. Lett. **77** (1996), 219–222.

[Kub57] R. Kubo, *Statistical mechanical theory of irreversible processes. 1. General theory and simple applications in magnetic and conduction problems*, J. Phys. Soc. Jap. **12** (1957), 570–586.

[Lin83] A. D. Linde, *Chaotic Inflation*, Phys. Lett. **B129** (1983), 177–181.

[Lin94] ———, *Hybrid inflation*, Phys. Rev. **D49** (1994), 748–754.

[LL62] L.D. Landau and E.M. Lifschiz, *Lehrbuch der Theoretischen Physik: Band I*, Akademie Verlag Berlin, (1962).

[LW60] J. M. Luttinger and John C. Ward, *Ground state energy of a many fermion system. 2*, Phys. Rev. **118** (1960), 1417–1427.

[MDC97] B. Mihaila, J. F. Dawson, and F. Cooper, *Order 1/N corrections to the time-dependent Hartree approximation for a system of N+1 oscillators*, Phys. Rev. **D56** (1997), 5400–5412.

[MM94] I. Montvay and G. Munster, *Quantum fields on a lattice*, Cambridge, UK: Univ. Pr. (1994) 491 p. (Cambridge monographs on mathematical physics).

[Mro88] S. Mrowczynski, *Stream Instabilities of the Quak-Gluon Plasma*, Phys. Lett. **B214** (1988), 587.

[Mro02] ———, *Quasiquarks in two stream system*, Phys. Rev. **D65** (2002), 117501.

[Mro06] ———, *Early stage thermalization via instabilities*, PoS **CPOD2006** (2006), 042.

[MS59] P. C. Martin and J. S. Schwinger, *Theory of many particle systems. I*, Phys. Rev. **115** (1959), 1342–1373.

[MSW07] A. H. Mueller, A. I. Shoshi, and S. M. H. Wong, *On Kolmogorov wave turbulence in QCD*, Nucl. Phys. **B760** (2007), 145–165.

[MT03] R. Micha and I. I. Tkachev, *Relativistic turbulence: A long way from preheating to equilibrium*, Phys. Rev. Lett. **90** (2003), 121301.

[MT04] ———, *Turbulent thermalization*, Phys. Rev. **D70** (2004), 043538.

[Nis08] A. Nishiyama, *Entropy production in 2D $\lambda\phi^4$ theory in the Kadanoff-Baym approach.*

[NO78] N. K. Nielsen and P. Olesen, *An Unstable Yang-Mills Field Mode*, Nucl. Phys. **B144** (1978), 376.

[NPS01a] H. P. Nilles, M. Peloso, and L. Sorbo, *Coupled fields in external background with application to nonthermal production of gravitinos*, JHEP **04** (2001), 004.

[NPS01b] ———, *Nonthermal production of gravitinos and inflatinos*, Phys. Rev. Lett. **87** (2001), 051302.

[PFKP06] D. I. Podolsky, G. N. Felder, L. Kofman, and M. Peloso, *Equation of state and beginning of thermalization after preheating*, Phys. Rev. **D73** (2006), 023501.

[PR97] T. Prokopec and T. G. Roos, *Lattice study of classical inflaton decay*, Phys. Rev. **D55** (1997), 3768–3775.

[PS95] M. E. Peskin and D. V. Schroeder, *An Introduction to quantum field theory*, Reading, USA: Addison-Wesley (1995) 842 p.

[PS00] M. Peloso and L. Sorbo, *Preheating of massive fermions after inflation: Analytical results*, JHEP **05** (2000), 016.

[RH97] S. A. Ramsey and B. L. Hu, *Nonequilibrium inflaton dynamics and reheating: Back reaction of parametric particle creation and curved spacetime effects*, Phys. Rev. **D56** (1997), 678–705.

[RHS98] S. A. Ramsey, B. L. Hu, and A. M. Stylianopoulos, *Nonequilibrium inflaton dynamics and reheating. II: Fermion production, noise, and stochasticity*, Phys. Rev. **D57** (1998), 6003–6021.

[RS03] P. Romatschke and M. Strickland, *Collective Modes of an Anisotropic Quark-Gluon Plasma*, Phys. Rev. **D68** (2003), 036004.

[RV06a] P. Romatschke and R. Venugopalan, *Collective non-Abelian instabilities in a melting color glass condensate*, Phys. Rev. Lett. **96** (2006), 062302.

[RV06b] ———, *The unstable Glasma*, Phys. Rev. **D74** (2006), 045011.

[RW93] K. Rajagopal and F. Wilczek, *Emergence of coherent long wavelength oscillations after a quench: Application to QCD*, Nucl. Phys. **B404** (1993), 577–589.

[Sch61] J. S. Schwinger, *Brownian motion of a quantum oscillator*, J. Math. Phys. **2** (1961), 407–432.

[Sch74] H. J. Schnitzer, *Nonperturbative Effective Potential for Lambda phi**4 Theory in the Many Field Limit*, Phys. Rev. **D10** (1974), 1800.

[SFR07] C. Sasaki, B. Friman, and K. Redlich, *Density fluctuations in the presence of spinodal instabilities*, Phys. Rev. Lett. **99** (2007), 232301.

[Son96] D. T. Son, *Reheating and thermalization in a simple scalar model*, Phys. Rev. **D54** (1996), 3745–3761.

[SS06] B. Schenke and M. Strickland, *Fermionic collective modes of an anisotropic quark-gluon plasma*, Phys. Rev. **D74** (2006), 065004.

[TBV00] S. Tsujikawa, B. A. Bassett, and F. Viniegra, *Multi-field fermionic preheating*, JHEP **08** (2000), 019.

[Tra08] A. Tranberg, *Quantum field thermalization in expanding backgrounds*, JHEP **11** (2008), 037.

[WW58] E.T. Whittaker and G.N. Watson, *A course of modern analysis*, Cambridge University Press, Chapter 23.

[XG05] Z. Xu and C. Greiner, *Thermalization of gluons in ultrarelativistic heavy ion collisions by including three-body interactions in a parton cascade*, Phys. Rev. **C71** (2005), 064901.

[Yos95] M. Yoshimura, *Catastrophic particle production under periodic perturbation*, Prog. Theor. Phys. **94** (1995), 873–898.

[ZH98] P.-f. Zhuang and U. W. Heinz, *Equal-time hierarchies for quantum transport theory*, Phys. Rev. **D57** (1998), 6525–6543.

[ZLF92] V.E. Zakharov, V.S. L'Vov, and G. Falkovich, *Kolmogorov spectra of turbulence 1. Wave turbulence.*, Berlin, Germany: Springer (1992) 275p.

Danksagung

Es war für mich persönlich ein herausforderndes Projekt nach Darmstadt zu ziehen und eine Doktorarbeit zu schreiben. Zum Glück bin ich auf viele nette und hilfsbereite Menschen gestoßen, die mir dabei geholfen haben, das Projekt durchzuziehen und abzuschließen. Ich habe viel von ihnen gelernt und ich danke allen. Einige davon möchte ich explizit erwähnen:

Ich danke meinem Doktorvater Prof. Dr. Jürgen Berges für die Aufnahme als Doktorand in seine Arbeitsgruppe und die interessanten Fragestellungen, die zu dieser Arbeit geführt haben, sowie für die damit verbundene Betreuung. Des Weiteren bin ich für die Teilnahme an einem internationalen Workshop am KITP in Kalifornien dankbar, bei dem eine produktive Atmosphäre herrschte. Ich möchte mich insbesondere für die Motivation bedanken die ich durch Gespräche mit ihm erhalten habe, in Phasen, in denen ich zweifelte, bis hierher zu kommen.

Zu großem Dank bin ich Dr. Sebastian Scheffler verpflichtet. Mit einem solch hilfsbereiten und kompetenten Kollegen ein Büro teilen zu dürfen war sehr wertvoll. Er hat mir bei vielen Dingen geholfen, die ich hier nicht alle aufzählen kann.

Dipl.-Phys. Alexander Rothkopf danke ich für die sehr angenehme und erfolgreiche Zusammenarbeit, sowie für viele erleuchtende Gespräche, auch nachdem er in weite Ferne gezogen ist.

Dankbar bin ich Dipl.-Phys. Thorsten Zöller für zahlreiche interessante Gespräche und fachliche Unterstützung, aber auch für das sehr sorgfältige Korrekturlesen großer Teile dieser Arbeit. Wobei ich gleich anmerken möchte, dass selbstverständlich alle verbliebenen Merkwürdigkeiten auf meine Kappe gehen.

Ich danke Dr. Felix Schmitt, Dr. Markus Hild, Dipl.-Phys. Jens Müller, Dr. Richard Williams, Dr. Dominik Nickel und Dr. Jean-Sébastien Gagnon für viele nette gemeinsame Stunden. So etwas ist unschätzbar.

Das Institut für Kernphysik, insbesondere die Theoriegruppe, habe ich als angenehmen Arbeitsplatz empfunden, wofür ich sehr dankbar bin. Hier möchte ich unsere Sekretärin Genette Kluckner erwähnen, die bei verwaltungstechnischen Fragen immer hilfsbereit zur Seite stand.

Meine Arbeit verlangte es, die ein oder andere Simulation auf einem Rechner zu machen, der zur “Farm” gehört. Dass das immer einwandfrei funktionierte ist Prof. Dr. Robert Roth und seinen Mitarbeitern zu verdanken. Für die Administration der Rechner unserer Gruppe danke ich Dr. Denes Séxty und Dipl.-Phys. Stefan Roth.

Ich danke Herrn Prof. Dr. Christian Fischer, Frau Prof. Dr. Barbara Drossel und Herrn Prof. Dr. Thomas Walther, für die Bereiterklärung als Korreferent, bzw. Prüfer zur Verfügung zu stehen.

Ich danke dem Odenwald für die Bereitstellung einer leicht erreichbaren, exzellenten "Radfahrumgebung", die einen nicht unerheblichen Teil dazu beigetragen hat, dass ich mich in Darmstadt wohl fühle. Einige Stunden auf dem Rad in wunderbarer Natur lassen auch, zeitweise, einen "Faktor 2" oder Vorzeichen, vergessen.

Ich danke all meinen Freunden, besonders meinen Besten, für viel Verständnis und Rückhalt. Dazu gehört Ralf Burek dem ich auch für die vielen erfrischenden Anrufe im Büro, am Abend oder am Wochenende, in der Endphase des Zusammenschreibens, danke.

Ich komme nun zu den Menschen, die eigentlich an erster Stelle stehen sollten. Ich danke meiner Familie, die es mir ermöglicht hat meinen Weg zu gehen, ohne ihn in Frage zu stellen.

Insbesondere meinem Vater danke ich für umfassende Unterstützung in jeglicher Hinsicht. Auch für den, nicht absichtlich vollzogenen Anstoß, viele Jahre zurück, mich für Physik zu interessieren.

Ich danke meinem Bruder, der bei mir, durch seinen Erfolg in seinem Arbeitsgebiet, eine indirekte Motivation erzeugt hat.

Meiner Mutter danke ich für alles was sie je für mich getan hat und auch jetzt noch tut. Sie hat in Gedanken für viel Liebe, Kraft und Zuversicht gesorgt. Danke.

Darmstadt, 17. Mai 2010

Lebenslauf

Vorname:	Jens
Nachname:	Pruschke
Geburtsdatum:	17.01.1981
Geburtsort:	Dortmund
Staatsangehörigkeit:	deutsch
Familienstand:	ledig

Schulische und universitäre Ausbildung

1987 - 1991:	Uhland-Grundschule in Dortmund
1991 - 1997:	Ricarda-Huch-Realschule in Dortmund
1997 - 2000:	Max-Planck-Gymnasium in Dortmund
2000 - 2001:	Zivildienst in den Städtischen Kliniken Dortmund
2001 - 2007:	Studium der Physik an der Universität Dortmund
seit 2007:	Wissenschaftlicher Mitarbeiter am Institut für Kernphysik der Technischen Universität Darmstadt

Veröffentlichungen

1. J. Baacke, N. Kevlishvili and J. Pruschke, "*Quantum back-reaction of the superpartners in a large-N supersymmetric hybrid model*", JCAP **0706** (2007) 004, arXiv:hep-th/0702009.

2. J. Berges, J. Pruschke and A. Rothkopf, "*Instability-induced fermion production in quantum field theory*", Phys.Rev. **D80** (2009), arXiv:0904.3073[hep-ph].

Eidesstattliche Erklärung

Hiermit erkläre ich eidesstattlich, dass ich die vorliegende Dissertation selbständig verfasst, keine anderen als die angegebenen Hilfsmittel verwendet und noch kein Promotionsversuch unternommen habe.

Darmstadt, 18. Mai 2010,

..... gez. Jens Pruschke

Unterschrift